APPLICATION OF FEMTOSECOND LASERS IN CONFOCAL AND SCANNING TUNNELLING MICROSCOPY

BY

OWAIN DAVIES

A thesis submitted to
The University of Birmingham
for the degree of
DOCTOR OF PHILOSOPHY

Nanoscale Physics Research Laboratory
School of Physics & Astronomy
The University of Birmingham
May 2010

UNIVERSITY OF BIRMINGHAM

University of Birmingham Research Archive

e-theses repository

Abstract

This thesis reports the use of a Ti:sapphire ultrafast laser with a confocal microscope to precisely induce DNA damage in the nuclei of live cells by multi-photon absorption, the development and comparison of foci counting algorithms for the quantitative assessment of radiation damage and work towards the development of an ultrafast Scanning Tunnelling Microscopy (STM) technique, employing a Ti:sapphire pulsed laser, called Shaken Pulse Pair eXcitation (SPPX) STM.

Measurements of the laser intensity, pulse duration and point spread function are used to estimate the peak intensity at the focus of the confocal microscope. A UV absorption in DNA is excited by the simultaneous absorption of three IR photons (3P). This process leads to the formation of cyclobutane pyrimidine dimmers (CPDs) in the DNA chain. Proliferating Cell Nuclear Antigen (PCNA), involved in the repair of these lesions is tagged with Green Fluorescent Protein (GFP) to visualise the repair process. Damage is detected at peak intensities as low as 23 ± 3 GW/cm^2 which is lower than previous studies. PCNA localises at the DNA damage sites with an exponential localisation.

Three foci counting algorithms were implemented: a simple intensity threshold algorithm; a Compact Hough transform and Radial Mapping (CHARM) algorithm and a watershed algorithm. The watershed algorithm was particularly effective for the assessment of foci in 3D datasets, providing counts and other properties relating to the foci. It is applied to a study of γ-H2AX foci in radiation dosed cells to assess various properties of γ-H2AX foci as a function of radiation.

Work on the SPPX-STM apparatus led to the development of a novel high frequency translation stage, allowing a retro-reflector to be periodically oscillated without coupling the vibration into the optical table.

Dedication

This thesis is dedicated to my parents, Kathryn and Julian Davies, who have provided unfailing support and encouragement throughout my education and academic career. I would especially like thank my mother for proof reading countless copies of this thesis, and my fiancée, Helen, who has put up with me throughout the writing process and still agreeing to marry me.

Acknowledgments

Contents

Abbreviations and Definitions

Abbreviation	Definition
2D	Two Dimensions
3D	Three Dimensions
3P	Three Photons
AOTF	Acousto-Optic Tuneable Filter
CHARM	Compact Hough Transform and Radial Mapping algorithm
CPD	Cyclobutane Pyrimidine Dimer
CW	Continuous Wave – refers to a mode of operation in lasers
DSB	Double Strand Break in the DNA chain.
FITC	Fluorescein Isothiocyanate, a functionalised Fluorescein derivative
FRAC	Fringe Resolved Auto Correlation
FWHM	Full Width at Half of Maximum
GFP	Green Fluorescent Protein
H2AX	The histone groups around which DNA is wrapped.
IR	InfraRed
LSCM	Laser Scanning Confocal Microscopy
PCNA	Proliferating Cell Nuclear Antigen
PSF	Point Spread Function
RMS	Root Mean Square
SPPX	Shaken Pulse Pair Excitation
STM	Scanning Tunnelling Microscope
γ-H2AX	Phosphorylated H2AX, forms in response to DSBs in DNA.

CHAPTER 1.

1. Introduction

This thesis is concerned with the application of an ultrafast femtosecond laser to confocal microscopy providing a novel multi-photon technique which can accurately induce precise DNA damage in live cells. The high peak intensities of ultrashort pulses are utilised in these non-linear studies whilst the temporal resolution that femtosecond lasers deliver is exploited in work towards combining femtosecond pump-probe spectroscopic techniques with the unparalleled spatial resolution that can be obtained by scanning tunnelling microscopy (STM).

Ultrafast lasers can produce pulses on the femtosecond time scale, simultaneously delivering high peak intensities and femtosecond time resolution. Femtosecond pulse lasers have already found many applications in ultrafast optical spectroscopy[1] where the short duration of the pulses has enabled the time resolved study of the fast carrier dynamics in novel semiconductors, whilst access to extremely high peak intensities have been separately utilised elsewhere in laser ablation studies[2]. These high intensities were also the key to verifying the theoretical work, performed by Maria Göppert-Mayer [3] in 1931, on multiphoton interactions. Only with the advent of ultrafast lasers could the intensities required be achieved to experimentally verify her theories on the absorption cross sections for multi-photon absorption events. Today those theories underpin modern multi-photon excitation microscopy. In this work the high intensities available through ultrashort pulses are exploited to excite multiphoton absorption in DNA to accurately induce precise localised targeted damage within the nucleus.

The confocal microscope has been used extensively to obtain high quality images with superior axial resolution when compared with wide-field microscopes, allowing detailed sections through living cells and tissue to be acquired. The acquisition of multiple sections enables detailed 3D reconstructions of cells and sub-cellular structures. This work allowed the cellular response to the induced damage to be observed by high resolution 3D time lapse confocal

microscopy, allowing direct measurement of the dynamics of the proteins involved in the repair process.

Multiphoton microscopy is a technique that is closely related to confocal microscopy. By using the high intensities inherent to picosecond and femtosecond pulses multiphoton excitation of fluorophores can be achieved at the focus of a microscope with modest average laser powers. Multi-photon excitation and absorption is a non-linear process and objects smaller than the excitation wavelength of the laser can be resolved. Multiphoton excitation also has non-imaging applications such as photolysis of caged compounds, accurate localised photobleaching and induction of highly localised DNA damage in cells with interaction volumes smaller than the wavelength of the light.

Even given the benefits of multiphoton imaging the spatial resolution of optical microscopy and spectroscopy are fundamentally limited by the wavelength of the excitation light. However, the Scanning Tunnelling Microscope (STM) exploits the quantum mechanical phenomenon of tunnelling to obtain sub-nanometer resolution necessary to resolve atoms. The STM was developed by G. Binnig and W. Rohrer in 1981 [4]. It could be argued that the ability to directly observe and manipulate, in real space, surfaces and molecules on the nanometer and sub-nanometer scale triggered the growth of the field that is now called nanotechnology. In subsequent years, modifications and improvements have been made to the STM and new techniques such as Scanning Tunnelling Spectroscopy (STS) have allowed the electronic structure of many surface reconstructions and adsorbed molecules to be analysed. However, the small tunnelling currents involved require very high gain amplification and generally the bandwidth of any direct measurement is limited to a maximum of about 100kHz.

A number of attempts have been made to combine ultrafast lasers and STMs to improve the temporal resolution of the STM, but it was the work of Takeuchi et al [5-7] that first detected a femtosecond time resolved signal with its origins in the tunnelling current. They employed a pump probe arrangement and modulated delay between the pulses whilst the detecting the signal at the modulation frequency. The technique was called Shaken Pulse Pair eXcitation STM (SPPX-STM) and it was used to measure transient ultrafast photo induced processes in GaN_xAs_{1-x}, (x=0.36%). In this thesis work towards the development of such an apparatus is started and the progress in this area is reported.

This thesis details the implementation of multiphoton imaging and excitation systems in a commercial confocal microscope which allow precisely controlled DNA damage to be inflicted by a 3-photon interaction at target locations within the nuclei of live cells and collect real-time images of cells as they respond to the inflicted damage. This thesis will also document the

development of an SPPX-STM apparatus, analyse the technical and practical challenges associated with designing and building such an instrument and provide a roadmap to the completion of this task.

The remainder of the thesis is structured as follows: In chapter 2 the key topics of femtosecond optics, confocal microscopy and scanning tunnelling microscopy are introduced as well as some background on the biological DNA damage process and the cellular response that the multi-photon confocal microscope system was used to study.

Chapter 3 outlines precise details of the systems and methods used. It details the alignment of the femtosecond laser with the confocal microscope and how the confocal microscope may be used in multi-photon mode. It provides recommendations and guidance on how to configure and align the specific systems. Procedures are developed to perform accurate measurements of the point spread function of the microscope and the actual duration of the femtosecond pulse at the focus of the microscope objective after broadening by the microscope optics.

Chapters 4 and 5 present the results of the investigations with the confocal microscope. In Chapter 4 the confocal microscope is used to image live ovarian cells of Chinese hamster and target sub nuclear structures for irradiation with the femtosecond laser to induce DNA damage by a 3-photon absorption. DNA has a broad absorption resonance at 250nm which can be accessed by the simultaneous absorption of three 750nm photons leading to the formation of cyclobutane pyrimidine dimmers (CPDs). There is a detailed calculation of the peak laser intensity and cells were irradiated with a range of laser powers to attempt to identify a threshold intensity below which DNA damage would not occur. DNA damage and repair in the nuclei of the cells was visualised in real-time by tagging Proliferating Cell Nuclear Antigen (PCNA) with Green Fluorescent Protein (GFP) by transfection. PCNA is one of about 30 proteins involved with the replication and repair of DNA. Following irradiation by the femtosecond laser the PCNA protein kinetics were studied.

Chapter 5 reports the development of software for the automated counting of fluorescence foci in 3D. Three popular 2D segmentation techniques are analysed and the algorithms extended to operate in 3D. An algorithm was developed to operate in 3D, based on the Fernand Mayer watershed algorithm, to count foci and obtain distributions for foci size, intensity and distribution with respect of neighbouring foci. This algorithm was applied to cells that were treated with varying amounts of gamma radiation which causes the double strand breaks (DSBs) in the DNA. These DSBs are marked by γ-H2AX protein which binds to DSBs in response to damage. The γ-H2AX was immunostained with the fluorescent marker, Alexa 488,

allowing the foci to be imaged in the confocal microscope. The foci were counted and analysed by the algorithm developed in this chapter.

Chapter 6 reports ongoing efforts toward the development of an SPPX-STM apparatus which couples the femtosecond pulse with the STM junction. There is also a review of previous attempts to develop ultrafast STM including the work of Takeuchi et al. Attention is particularly directed to the development of a delay stage controller as one of the central components in a Laser Assisted STM controller (LA-STM). A high frequency mechanical shaker stage is developed which it is hoped may improve the lock-in detection of the time dependant signal whilst preventing coupling of vibrations to the STM. Finally a data acquisition environment is developed to record data from and control the LA-STM equipment.

Chapter 7 provides a summary and highlights possible improvements that could be made to the systems used in this work.

CHAPTER 2.

2. Background

This work is the result of the fusion of several technologies and fields of research and this chapter serves to provide grounding in the physics and technologies that underpin the methods developed and the results presented in subsequent chapters. Initially the femtosecond optics and the generation of femtosecond pulses by a titanium:sapphire (Ti:sapphire) laser are described, and consideration is given to the meteorology and control of ultrashort pulses. The focus then shifts to the operational principles of the laser scanning confocal microscope with specific attention to multi-photon imaging, which is a precursor to understanding the 3-photon DNA absorption damage process studied in Chapter 3. Finally, the concepts behind scanning tunnelling microscopy (STM) are introduced as a precursor to the time resolved STM work studied later in Chapter 6.

2.1.   FEMTOSECOND OPTICS

Lasers provide a source of intense coherent light across a multitude of wavelengths. They produce beams of light with very low divergences and minimal wave front distortion allowing the efficient operation of lenses as focusing elements at or very close to the physical diffraction limit. In these situations very high intensities can develop at the focus of the lens. A laser beam of a centimetre or more in diameter can be focused to a spot with a size of the order of the wavelength of the light, concentrating all the power from the beam into a very small area. In this example a lens is used to focus light spatially. The use of pulses enables the average energy of the laser to be concentrated in to a short period of time, thus increasing the peak intensity. For example, a laser producing pulses of 100×10^{-15}s (100 femtoseconds) duration with a repetition rate of 100MHz, the peak intensity is 100,000 times higher than if it was operating in continuous wave mode only. The exceptionally high peak intensities generated when the light is focused both spatially and temporally readily facilitate access to multi-photon interactions whilst maintaining a relatively low average power. In addition to providing a high intensity light source, when used in a pump-probe configuration, the ultrashort pulses provide high temporal resolution. These capabilities allow researchers to probe the electron dynamics of processes on a femtosecond time scale.

2.1.1.   ULTRASHORT PULSES

One of the simplest models of a laser beam is a propagating plane polarised wave oscillating at a single frequency. The beam may be defined to be travelling along the z-axis with a wave number k. The electric field will be perpendicular to the direction of travel, and the y-axis can be chosen to coincide with the direction of the electric field. The electric field in the y-direction, E_y, is described, using complex notation, by (2-1).

$$E_y(z,t) = E_0 e^{i(\omega_0 t - kz)} + C.C. \qquad (2\text{-}1)$$

The wave exists over all space and all time and, if one was to calculate the Fourier transform into the frequency domain, it would consist simply of a delta function at ω_0. Considering only the temporal dependence of (2-1); a pulse can be mathematically constructed by multiplying a Gaussian function onto it leading to a pulse with a width related to $\Gamma \propto t_0^{-2}$, where t_0, is the temporal width of the pulse.

$$E_y = E_0 e^{-\Gamma t^2 + i\omega_0 t} + C.C. \qquad (2\text{-}2)$$

The Fourier transform of any Gaussian function is also a Gaussian with inverse width. The frequency spectrum can be obtained by taking the Fourier transform of (2-2), yielding (2-3).

$$E_0(\omega) = \exp\left[\frac{-(\omega - \omega_0)^2}{4\Gamma}\right] \tag{2-3}$$

It can be seen that short pulses, with large Γ, result in the broad spectra in the frequency domain. This property of Fourier transforms is a classical illustration of the uncertainty principle; there is a fundamental limit to the duration bandwidth product of a pulse. There are several definitions of pulse duration Δt and spectral bandwidth $\Delta\omega$, as these quantities for ultrashort pulses are dependant on their pulse shape. The experimentally measurable quantity is the full width at half of maximum of the intensity auto-correlation. Using these definitions, the inequality for the duration bandwidth is described by (2-4) where c_B is a numerical constant dependant on pulse shape [8].

$$\Delta t \cdot \Delta\omega \geq 2\pi \cdot c_B \qquad \text{, where}$$

c_B	Pulse Shape
0.441	Gaussian
0.315	Sech

(2-4)

For the equality in (2-4) to hold it must be symmetrical regardless of pulse shape; the pulse is then considered to be transform limited. The symmetry of a pulse is controlled by the relative phase of each of the frequency components and how the phase evolves with time. Consider again (2-2); the instantaneous frequency is given by the time derivative of the phase, which for (2-2) is constant with a value ω_0. Suppose that a quadratic term was added to the phase function, $\Phi(t)$, as shown below in (2-5):

$$\begin{aligned} E_y &= E_0 e^{-\Gamma t^2 + i\left(\omega_0 t + \alpha t^2\right)} + C.C. \\ &= E_0 e^{-\Gamma t^2 + i\Phi(t)} + C.C. \end{aligned} \tag{2-5}$$

In this case, the instantaneous frequency of (2-5) is given by (2-6) and results in a waveform similar to that shown in Figure 2-1 which exhibits higher instantaneous frequency at long times, corresponding to the trailing edge of the pulse. Pulses possessing such a quadratic dependence on time in the phase of the pulse are known as *chirped pulses*.

$$\frac{\partial\Phi}{\partial t} = \omega_0 + \alpha t \tag{2-6}$$
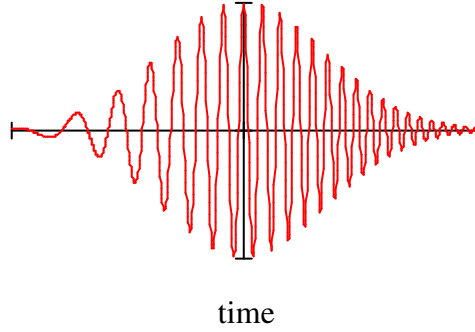
time

Figure 2-1 **Chirped Gaussian pulse with a quadratic time dependence of the phase**
Pulses where the instantaneous frequency varies over time are said to be chirped. The longer wavelengths arrive at an earlier time than the shorter wave lengths, such pulses are said to be positively chirped. In negatively chirped pulses, the shorter wavelengths precede the longer ones, whilst unchirped pulses are symmetric about the pulse centre and represent the shortest pulse for the available bandwidth and are thus referred to as diffraction limited.

Physically, chirping can occur in a number of ways, both intentional and unavoidable. The most common is the result of unavoidable dispersion caused by the optics that focus and manipulate the laser beam on the optical table.

2.1.2. DISPERSION AND COMPENSATION

The refractive indices of all transparent media vary with frequency. It is this property that allows a prism to split white light into its constituent colours. All glasses create this effect to different extents. As previously mentioned, ultrashort pulses require large bandwidths. As such a pulse passes through the optics or the air the blue components of the light are slowed down with respect to the red components, causing the pulse to become increasingly chirped and broadened. This phenomenon is called *dispersion* and such materials are said to be *dispersive*.

Consider the spectrum of a simple unchirped Gaussian pulse, as has already been described in (2-3). As the pulse passes through the material phase shifts are applied to the different frequency components resulting in a new spectrum:

$$E(\omega, x) = E_0(\omega) \cdot e^{-ik(\omega)x} \, , \qquad k(\omega) = \frac{n\omega}{c} \qquad (2\text{-}7)$$

Where $k(\omega)$ is the wave number for a wave propagating in a medium with a refractive index of n. In general the refractive index, n, is frequency dependent. Consequently, the dispersion curve is not linear as it is in a vacuum, but possesses some curvature. To facilitate further analytical treatment one can perform a Taylor expansion about the central pulse frequency ω_0 to quadratic order

$$k(\omega) \cong k(\omega_0) + k'(\omega - \omega_0) + \tfrac{1}{2}k''(\omega - \omega_0)^2 \, , \qquad (2\text{-}8)$$

Where k' and k'' are the first and second derivatives of $k(\omega)$ with respect ω evaluated at ω_0 respectively. Combining (2-3), (2-7) and (2-8) one can obtain an expression for the pulse spectrum as it propagates through the medium.

$$E(\omega, x) = \exp\left[-ik(\omega_0)x - ik'x(\omega - \omega_0) - \left(\frac{1}{4\Gamma} + \frac{i}{2}k''x\right)(\omega - \omega_0)^2\right] \qquad (2\text{-}9)$$

In the modified spectrum, the same frequencies are present but their phases have been modified. The effect of these phase shifts in the pulse spectrum on the temporal evolution of the pulse can be readily obtained by taking the inverse Fourier transform of (2-9).

$$\varepsilon(t, x) = \frac{1}{2\pi}\int_{-\infty}^{\infty} E(\omega, x) \cdot e^{i\omega t}\, d\omega$$

$$\varepsilon(t, x) = \sqrt{\frac{\Gamma(x)}{\pi}}\underbrace{\exp\left[i\omega_0\left(t - \frac{x}{v_\phi}\right)\right]}_{\substack{\text{Delay in phase term of}\\ \text{pulses' carrier wave}}} \cdot \exp\left[\underbrace{-\Gamma(x)}_{\text{Gaussian Envelope}}\underbrace{\left(t - \frac{x}{v_g}\right)^2}_{\text{Delay to pulse}}\right] \qquad (2\text{-}10)$$

where,

$$v_\phi = \left(\frac{\omega}{k}\right)_{\omega_0} \quad , \quad v_g = \left(\frac{d\omega}{dk}\right)_{\omega_0} = \frac{1}{k'} \quad , \quad \frac{1}{\Gamma(x)} = \frac{1}{\Gamma} + i \cdot 2k''x \qquad (2\text{-}11)$$

Compare (2-10) with (2-2); for any given value of x they share a similar structure. There is an oscillatory factor that provides a pure carrier wave, modulated by a Gaussian envelope. In (2-10) there is a delay to the phase of the carrier wave. The magnitude of this delay is determined by the phase velocity, v_ϕ, which is related to the refractive index of the material at ω_0. As this term only affects the overall phase of the carrier it has no measurable effect on the pulse. Similarly, the delay caused by the group velocity determines the arrival time of the pulse at a position x. Neither of these effects has substantially changed the structure of the pulse. The structure of the pulse is contained in the factor $\Gamma(x)$. In (2-2), Γ was real and constant, but in (2-10) $\Gamma(x)$ is complex and evolves as the pulse travels through the medium. It can be seen from (2-12) that $\Gamma(x)_{x=0} = \Gamma$ so the pulse is initially an unchirped Gaussian pulse. To examine how $\Gamma(x)$ changes as the pulse propagates through the medium, we can write $\Gamma(x)$ explicitly as:

$$\Gamma(x) = \frac{\Gamma}{1 + \xi^2 x^2} - i\frac{\Gamma\xi x}{1 + \xi^2 x^2}, \qquad \xi = 2\Gamma k'' \qquad (2\text{-}12)$$

The real part of (2-12) defines the form factor of the pulse after travelling some distance, x. Notice that it can only get smaller; as a result the pulse is always broadened. The imaginary part, when substituted into (2-11) leads to a quadratic dependence of phase on time. In addition to being broadened by the real part of $\Gamma(x)$, the imaginary part leads to a chirp in the pulse. This is called *group velocity dispersion (GVD)* and is present in all optics used to manipulate pulses. Its effects are cumulative and must be compensated for, in the course of an experiment, if the properties of the ultrashort pulses are to be preserved. This is especially true in laser cavities where pulses may make many thousands of passes. In this treatment, the dispersion relation, $k(\omega)$, was only expanded to quadratic order. Higher order expansions yield results for high order dispersions such as cubic dispersion. These effects become more important as the pulse duration drops and must also be compensated to achieve pulse durations shorter than 25fs. This was not necessary in the system used for this work as its bandwidth limited pulses were only 80-100fs at peak performance.

Prism Dispersion Compensation

The shortest possible pulse for a given spectral bandwidth $\Delta\omega$, is given by the equality in (2-4). This is achievable only in an unchirped symmetrical pulse spectrum. In the previous section it was seen that any element will cause dispersion and several arrangements have been found which possess negative dispersion. This permits the phase of the frequency components to be corrected either before or after other dispersing optics. This reduces the duration of a stretched pulse to the ideal unchirped duration in the interaction region where the experiment is being performed. One such arrangement is shown below in Figure 2-2.
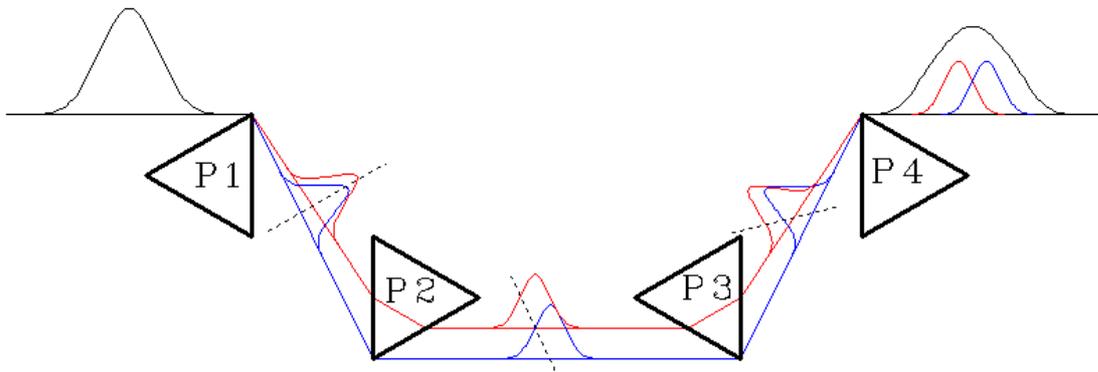
Figure 2-2   4 Prism Dispersion Compensation
This arrangement of prisms possesses negative group velocity dispersion. The red path passes through more glass than the blue path and slows the blue components in relation to the red components.

An unchirped pulse is incident on P1, which causes angular dispersion of the pulse spectrum with the higher frequencies (blue) experiencing greater refraction than lower

frequencies (red). In addition to compensating the angular dispersion of the pulse, it delays the low frequency components more than the high frequency components. The red path traverses more of the prism than the blue path even though the blue path is actually longer. The refractive index of the glass slows the red path more. Consequentially, the pulse emerging from P2 possesses a chirp such that the leading edge of the pulse has a higher frequency than the trailing edge. P3 further delays the low frequency components before traversing P4, which corrects the angular dispersion resulting in a broadened pulse without transverse spectral separation. The pulse broadening is a result of the angular dispersion of passing through this system. In this system the lower frequency components lag the higher frequency components and it is said to have negative group velocity dispersion. This is in direct contrast to the dispersion effect of a pulse propagating through transparent media discussed previously. Such arrangements can be incorporated into experiments to compensate for the positive dispersion introduced by the other optical elements such as mirrors and lenses.

2.1.3.   PULSE CHARACTERISATION

A pulse is fully characterised by its spectral intensity and spectral phase. The first is easily obtained from a regular spectrometer provided that it has enough range to accommodate the bandwidth of the pulse. Unfortunately, this yields no information about the phase relationship between the frequencies in the pulse which, in previous sections, has been shown to be important in maintaining short pulses. A technique is needed to directly measure the pulse duration. Conventionally this would be achieved with a cross-correlation to shorter reference pulse. This leads to a correlation function $G(\tau)$ of two time dependant functions, the signal under analysis $F(t)$ and a well known comparatively short reference signal $R(t)$:

$$G(\tau) = \int\limits_{-\infty}^{\infty} R(t) F(t - \tau)\, \mathrm{d}t \qquad\qquad (2\text{-}13)$$

For ultrafast pulses, this approach has a limited applicability in that there is rarely a shorter distinctively characterised pulse available. This has led to the development of a technique called autocorrelation in which the pulse under investigation is correlated with itself.

Field Autocorrelation

In an interferometric autocorrelation, the laser pulse is split into two pulses and recombined but separated by a delay, τ. The electric fields interfere with each other and the intensity is measured at the output of the interferometer. The measured intensity is given by

equation (2-14) which is shown in the form of an autocorrelation of the electric field. This sort of measurement is often called a field correlation.

$$I(\tau) = \int_{-\infty}^{\infty} |E(t) + E(t-\tau)|^2 dt$$
$$\propto 2\int_{-\infty}^{\infty} E(t)^2 dt + 2\int_{-\infty}^{\infty} E(t)E(t-\tau)dt \tag{2-14}$$

If one assumes that the electric field can be decomposed into a carrier and complex envelope as in equation (2-15), and that the pulse envelope varies slowly compared to the period of the carrier oscillation then the correlation integral in (2-14) reduces to a correlation of the envelopes modulated by carrier at the laser's central frequency.

$$E(t) = \varepsilon(t)e^{i\omega t} + \varepsilon^*(t)e^{-i\omega t} \tag{2-15}$$

$$\int_{-\infty}^{\infty} E(t)E(t-\tau)dt = e^{i\omega\tau}\int_{-\infty}^{\infty} \varepsilon(t)\varepsilon^*(t-\tau)dt + c.c. \tag{2-16}$$

Without considering any specific waveform, it is clear from convolution theory that the Fourier transform of (2-16) would only yield the spectral intensity of the pulse and provide no information about the phase. The width of the auto-correlation itself is simply a measurement of coherence length rather that pulse duration.

Second Harmonic Field Autocorrelation

Higher order auto-correlations are required to extract useful information regarding the phase and pulse duration. Experimentally these are accessible by multiphoton interactions such as multi-photon absorption and second harmonic generation. A second harmonic generation (SHG) crystal may be placed at the output of the interferometer and the fundamental frequency filtered. The various implementations of this technique are discussed in section 0. The resulting signal for a second order autocorrelation is given by;

$$I_2(\tau) = \int_{-\infty}^{\infty} \left| [E(t) + E(t-\tau)]^2 \right|^2 dt \tag{2-17}$$

Or more generally for the Nth order autocorrelations as;

$$I_N(\tau) = \int_{-\infty}^{\infty} \left| [E(t) + E(t-\tau)]^2 \right|^N dt \tag{2-18}$$

The fields in (2-17) are substituted for the complex representation $E(t) = \varepsilon(t)e^{i\omega t}e^{i\phi(t)}$, where in this case $\varepsilon(t)$ is the real pulse envelope and the phase variation has been separated into

the function $\phi(t)$. Assuming that the slowly varying envelope approximation can be applied, the laser oscillation period can be averaged to obtain the following signal from the detector [9].

$$I_2(\tau) = A_0(\tau) + \Re\left[A_1(\tau)e^{-i\omega\tau}\right] + \Re\left[A_2(\tau)e^{-i2\omega\tau}\right] \tag{2-19}$$

where,

$$A_0(\tau) = \int_{-\infty}^{+\infty}\left[\varepsilon^4(t) + \varepsilon^4(t-\tau) + 4\varepsilon^2(t)\varepsilon^2(t-\tau)\right]dt \tag{2-20}$$

$$A_1(\tau) = \int_{-\infty}^{+\infty}\varepsilon(t)\varepsilon(t-\tau)\left[\varepsilon^2(t) + \varepsilon^2(t-\tau)\right] \cdot e^{i[\phi(t-\tau)-\phi(t)]}dt \tag{2-21}$$

$$A_2(\tau) = \int_{-\infty}^{+\infty}\varepsilon^2(t)\varepsilon^2(t-\tau) \cdot e^{2i[\phi(t-\tau)-\phi(t)]}dt \tag{2-22}$$

In a fringe resolved measurement, the measured intensity signal as a function of the delay, shown in Eq. (2-19), possesses three components, at DC, ω and 2ω given by equations (2-20), (2-21), and (2-22) respectively. By Fourier transforming the signal and selecting the data clusters at these frequencies and then inverse Fourier transforming that data, it is possible to get individual components corresponding to A_0, A_1 and A_2. The DC component consists of a signal proportional to an intensity autocorrelation on a constant background. This provides some measurement of the pulse duration but usually a pulse shape needs to be assumed. The intensity autocorrelation provides no information about the phase or shape of the pulse however both A_1 and A_2 have phase terms $(\phi(t-\tau)-\phi(t))$.

For a Gaussian pulse with a linear chirp an exact solution is obtainable, and equation (2-19) becomes;

$$I_2(\tau) = 1 + 2e^{-\left(\frac{\tau}{\tau_G}\right)^2} + 4e^{-\frac{a^2+3}{4}\left(\frac{\tau}{\tau_G}\right)^2}\cos\left(\frac{a}{2}\left(\frac{\tau}{\tau_G}\right)^2\right)\cos(\omega\tau) + e^{-(1+a^2)\left(\frac{\tau}{\tau_G}\right)^2}\cos(2\omega\tau) \tag{2-23}$$

Where the pulse envelope is defined as;

$$\varepsilon(t) = e^{-(1+ia)\left(\frac{\tau}{\tau_G}\right)^2}. \tag{2-24}$$

It can clearly be seen from (2-23) that the DC component is independent of the chirp. The pulse duration can be obtained by measuring the width of the peak. Conventionally pulse duration (τ_p) is defined as the FWHM of the pulse's intensity profile. The relationship between the Gaussian parameter τ_G and the pulse duration is given by;

$$\tau_p = \sqrt{2\ln 2}\tau_G. \tag{2-25}$$

Experimentally, the FWHM of the autocorrelation is usually measured to obtain the pulse duration. Equation (2-26) applies;

$$\tau_p = \frac{\tau_{FWHM}}{\sqrt{2}}.$$ (2-26)

The oscillating terms also have an envelope related to the pulse duration but this is further modified by the chirp parameter *a*. As the magnitude of the chirp is increased the width of the envelope actually decreases. Consequentially heavily chirped pulses can have extremely narrow fringe resolved autocorrelations (see Figure 2-3), and care has to be taken to ensure that the intensity autocorrelation is observed as well. As the pulse's spectral phase becomes more complicated less fringe detail is available.
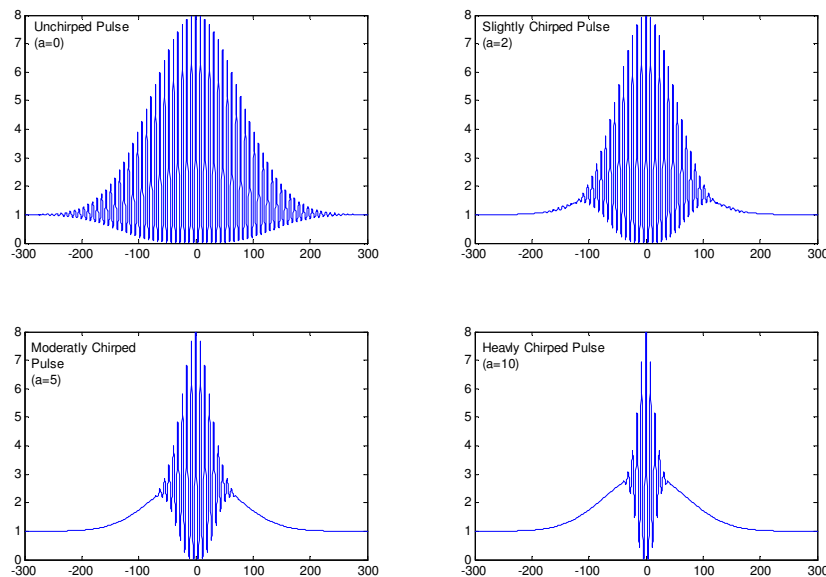
Figure 2-3 **The effects of pulse chirp on a second order autocorrelation.**
All the pulses have a duration of 100fs, with the amount of chirp varying between the graphs. As the level of chirp increases the fringe detail is no longer resolvable and only the intensity autocorrelation remains.

2.1.4. FEMTOSECOND LASER

In order to generate ultrashort pulses, positive gain is required across a broad range of wavelengths whilst maintaining control of the phase of each of the laser modes. The first ultrashort pulsed lasers that achieved 100fs pulses employed dye jets [10] which were both unstable and messy to maintain. These dye lasers have largely been replaced by solid state lasers. One of the most common gain mediums in use today is the titanium doped sapphire (Ti:sapphire) crystal. The Ti:sapphire crystal has a long lived excited state and a pair of vibrationally broadened levels. The fluorescence process is similar to that of the organic dyes discussed later in section 2.2.5, in that the fluorescence occurs due to a transition between the

bottom of the excited state and any one of the vibrationally excited ground state levels. This results in well separated absorption and emission spectra as shown in Figure 2-4. The excited level is quite long lived so a high inversion density can be readily achieved as the intra-band relation in the excited state is much faster than the inter-band transition rate.
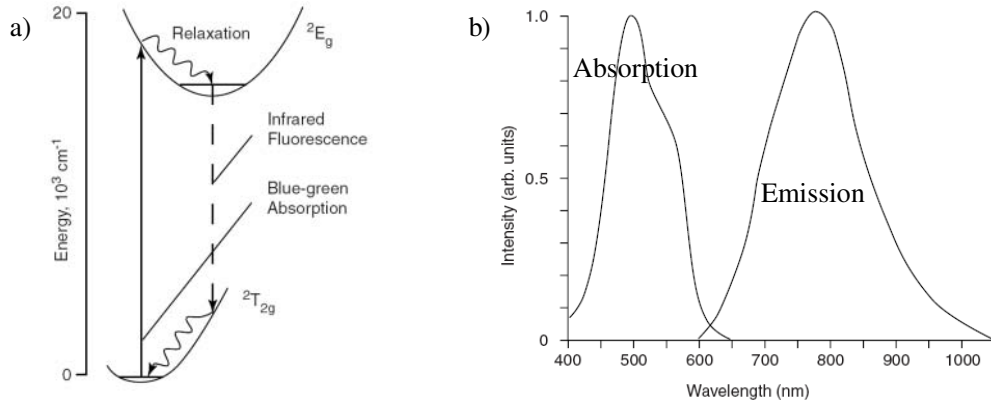
Figure 2-4   Energy levels in Ti^{3+} spectrum
Energy levels (a) and absorption and emission spectra (b) for Ti3+ ions. Adapted from [11].

The crystal is pumped by green continuous wave (CW) laser, either a Diode laser or an argon ion laser. Although emission occurs from 600nm-1100nm, in practise cavity losses and the tail in the absorption spectrum overlapping the emission spectrum reduce the useful spectrum over which gain can be achieved to above 670nm. The cavity losses are modified by the mirror sets installed as these are tuned for high reflectivity in specific regions.

The laser used in these experiments was a Spectra Physics Tsunami® Ti:sapphire laser pumped by a Coherent 5 watt Verdi® diode pumped solid state (DPSS) continuous wave (CW) laser. A schematic diagram of the Tsunami is included in Figure 2-5.
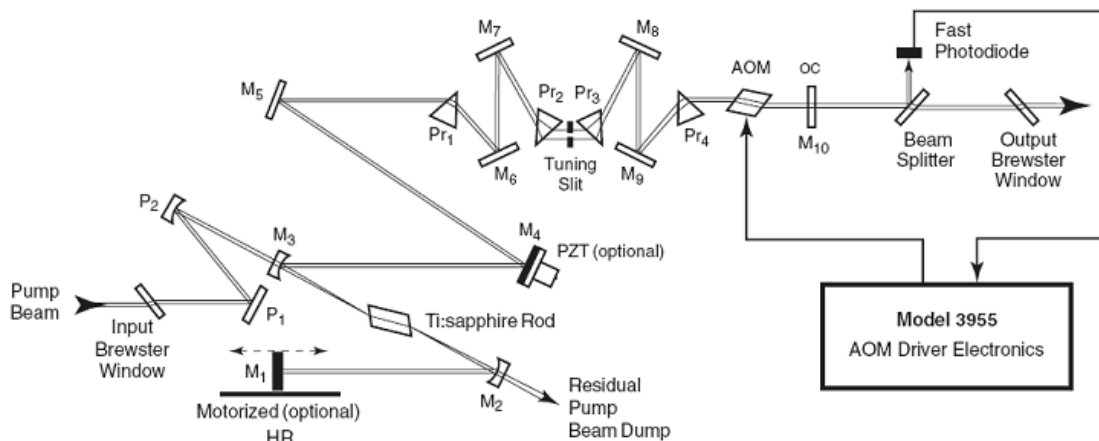
Figure 2-5   Schematic of Tsunami laser cavity configured for femtosecond pulses
[11]

The gain rod (Ti:sapphire) sits in a laser cavity. The simplest cavity consists of a confocal Fabry-Pérot etalon, but the additional components necessary to control intra-cavity dispersion

and control the phase of the pulses necessitates a larger cavity. The Ti:sapphire rod is quite long (a few cm) in comparison to a dye jet (~100 microns). This is necessary as solid state lasers generally have a smaller gain cross-section than organic dyes. The length of crystal also increases dispersion for which compensation must be made. In a laser, the light is reflected around the cavity repeatedly. A small fraction is emitted on each pass by an output coupler (M_{10}), but it is required that the waves from each pass of the cavity add in phase. As a result, only frequencies satisfying equation (2-27), that can fit an integer number of wavelengths into twice the cavity length will propagate.

$$f = \frac{nc}{2L} \qquad \text{, where, n is an integer.} \qquad (2\text{-}27)$$

At first it would seem that the broad frequency spectrum required for short pulses is unobtainable inside a cavity with such a narrow bandwidth. Indeed helium neon lasers frequently operate with only one or two longitudinal modes. For a particular mode to be amplified the gain on each pass of the cavity must exceed the losses. In a Ti:sapphire laser the gain curve is very broad allowing very many modes to simultaneously exist inside the cavity. The previous sections highlight the importance of the relative phase relationship. When all the modes beat together, the system is said to be mode-locked. There are several ways to achieve this condition in a Ti:sapphire laser. They fall into two categories. The first uses the intrinsic nonlinear properties of the gain medium and/or a saturable absorber and is referred to as passive mode locking. The other method involves inserting an element into the cavity which can be controlled by an external signal to modulate the loss or gain of the cavity and is known as active mode-locking. Shorter (few femtosecond) pulses are obtainable by passive mode locking, although the Tsunami used in these experiments uses active mode locking.

The Tsunami uses an acousto-optic modulator (AOM) to initiate a mode locking. An RF frequency signal is fed into a non-linear crystal by a piezoelectric transducer. The pressure waves in the crystal form a dynamic diffraction grating, causing a time dependent angular deviation to the beam. The effect is to modulate the losses in the cavity.

The effect of this on a signal mode is for the amplitude modulation to create sidebands in the frequency spectrum either side of the mode's frequency. The spacing of the sidebands from the mode's frequency is determined by the frequency of the amplitude modulation. In a multimode laser, when the frequency is chosen to be the same as the modal spacing of the cavity, the side bands of one mode will be at the same frequency as the adjacent mode. Once this situation occurs a competition ensues between the longitudinal modes of the cavity and the side bands. The most efficient situation is when the longitudinal modes phase lock to the side bands

of the adjacent mode. When this situation applies across all the modes in the laser cavity and a global phase lock exists, the laser is said to be *mode-locked*. All the energy is now in one pulse oscillating back and forth in the cavity. Once a mode-lock has been established the AOM is turned off as it is no longer required. The pulses should continue indefinitely as long as the cavity is not destabilised by retro-reflected light, pump-laser instability or mechanical shock.

The laser contains several optical components. There are several mirrors, a Ti:sapphire crystal and an AOM crystal. All these elements add group velocity dispersion to the system. This dispersion must be compensated or the pulse will broaden with each pass of the cavity. Ultimately a modal competition will cause a single mode to be prominent and the laser will operate in continuous wave mode. The system used in the Tsunami is a prism compressor consisting of four prisms like the one shown in Figure 2-2. The extra mirrors added between the Pr1 and Pr2 and also between Pr3 and Pr4 are only used to reduce the physical space required by the compressor.

The system described here can achieve minimum pulse durations of 100fs and average powers of ~600 mW, when pumped with a 5W diode laser. This provides more than enough power for the multi-photon microscopy described later in section 2.2.6, in fact the power has to be reduced and this is described in the experimental methods section.

2.2.   THE CONFOCAL MICROSCOPE

The confocal microscope was invented in the late 1950s by Marvin Minsky [12] at Harvard university. Although it has only a slightly improved lateral resolution over conventional wide field microscopy, what sets the confocal microscope apart from its wide field counterpart is its far superior axial resolution, allowing thin sections through a sample to be imaged. Additionally the confocal microscope has variable depth of field allowing almost all out of focus fluorescence to be omitted. This facilitates greatly improved image contrast as out of focus fluorescence does not wash out the fine detail of the image. Figure 2-6 below shows a comparison of wide field and confocal images.

The sectioning capability also permits 3D microscopy by sequentially capturing sections and reconstructing the 3D image on a computer. Combined with improvements in laser technology, the confocal microscope has allowed imaging of living samples that could not have been imaged by conventional optical microscopy or electron microscopy. It has been further exploited in multi-disciplinary sciences where it has been used to study photo-luminescence [13] in semi-conductor films, bioluminescent interaction with nanoparticles[14] and, with suitably sensitive detectors, single molecule detection is achievable [15].
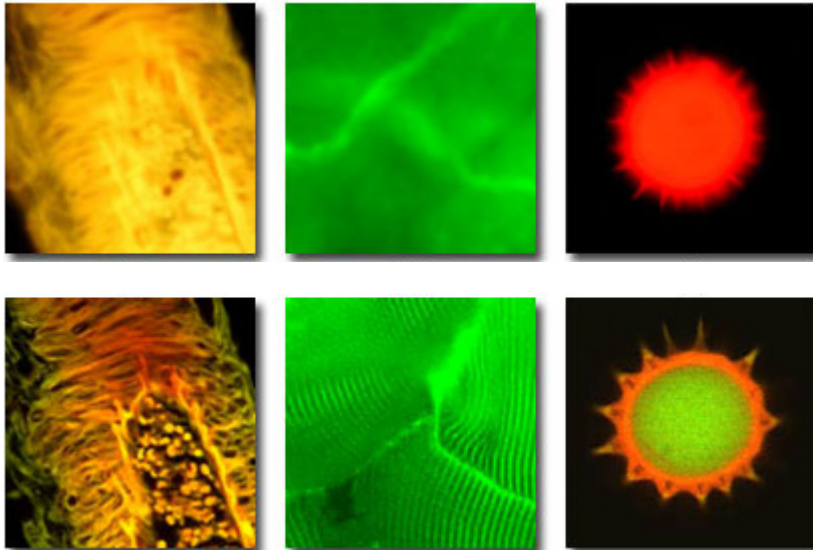
Figure 2-6   Comparison of confocal and wide field fluorescence images
Top: Images acquired in wide field mode. Bottom: A single section acquired in confocal mode showing the increased image detail achievable when the out of focus background is eliminated. Adapted from [16].

2.2.1.   OPERATIONAL PRINCIPLE

The improvements gained by the confocal microscope arise from its system of illumination and detection of fluorescence. In contrast to wide field where the entire field of view is illuminated, excitation in the confocal microscope is achieved by scanning a diffraction limited image of a point source.
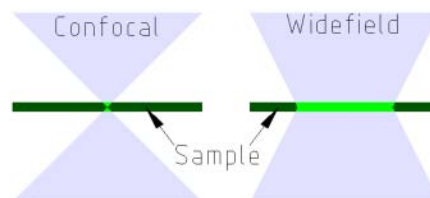
Figure 2-7   Illustration of confocal excitation and widefield illumination of a fluorescent sample
Confocal excitation illuminates only the diffraction limited spot whilst widefield illuminates the entire field. Fluorescence is generated in the bright green areas.

In addition to only having a small generation volume for fluorescence, a pinhole is placed in front of the detector in the conjugate focal plane of the excitation pinhole. Thus almost all the fluorescence that originated out of the focal plane is eliminated. Ray traces of in focus and out of focus fluorescence are show in Figure 2-8. It can be seen that only the in focus light from the excitation spot passes through the detection pinhole. Light from below the focal plane comes to a focus before the detection pinhole and then rapidly diverges with most of it being blocked. Light generated above the focal plane is divergent out of the objective, with most of it not even reaching the tube lens. The tube lens then focuses the remaining light far behind the pinhole, where most of it is blocked.
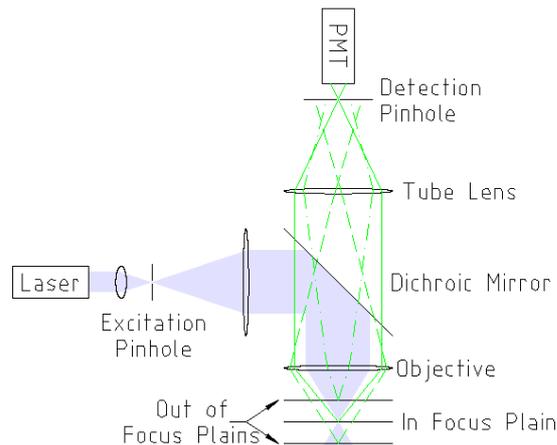
Figure 2-8   **Illustration of principle of operation of a confocal microscope**
Excitation light (blue shading), In focus fluorescence (solid green lines), Out of focus fluorescence (dashed and dot-dashed green lines). Note: for clarity the excitation light has not been shown to fill the objective

This arrangement has a curious consequence; one can never say that a confocal microscope is out of focus as if it is correctly aligned almost the light incident of the detector originates from the focal plane. Whilst it may not be the plane of interest, it is in focus. Consequentially one does not tend to talk about being in or out of focus in confocal microscopy but rather the "z-position".

2.2.2.   RESOLUTION AND THE POINT SPREAD FUNCTION OF A SINGLE LENS

The confocal microscope is an optical microscope and its resolution is limited by diffraction. In so far as imaging is concerned, this means a point source is not imaged to a single point in the image plane (or volume). As is the case with widefield microscopy, it is the objective that ultimately limits the resolution of the instrument. Before looking into the resolution and imaging properties of a confocal arrangement the characteristics of a single lens in a wide field configuration will be considered.

In Figure 2-9 the light emitted from point sources is spread out creating a set of overlapping diffraction patterns. The manner of the spreading is defined as the instrument's *Point Spread Function*[1] (PSF). There are many definitions of resolution in use in optical microscopy. Qualitatively it is the minimum separation of two point sources where they can still be distinguished.

---

[1] The point spread function is also known as the instrument function though this is more common in spectroscopy and astronomy circles.
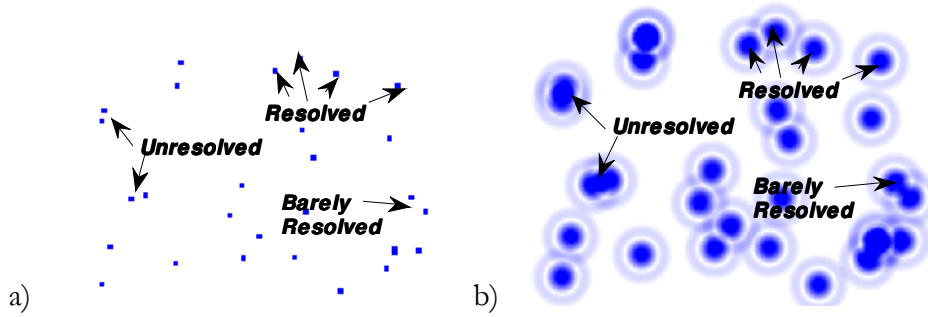
Figure 2-9   Point Spread Function and the Limit of resolution
Point sources of fluorescence (a) each have a diffraction pattern superimposed on them (b) causing the signal from the point sources to be spread over the image plane. Objects without sufficient separation can not be told apart, and are said to be unresolved.

A quantitative determination of resolution requires some knowledge of the PSF. A point light source will emit light in all directions (Figure 2-10) but only be collected by the lens within a finite focal cone. The size of the spot that is formed in the image plane is governed by the wavelength of the light, λ, and the numerical aperture (NA) of the lens. The NA is calculated from (2-28) and is governed by the semi-angle α on Figure 2-10 and the refractive index of the medium, *n*.

$$NA = n \cdot \sin \alpha \qquad (2\text{-}28)$$
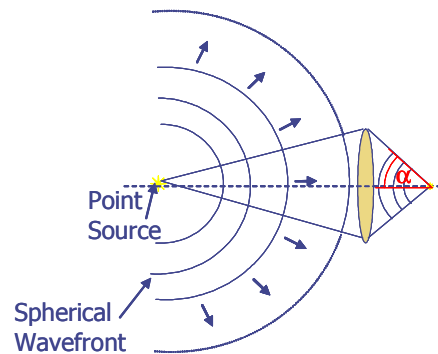
Figure 2-10   Ideal lens clipping a spherical wavefront.

Expressions for intensity can be obtained [17-19] in the focal plane (Eq.(2-29)) and along the optical axis (Eq.(2-30)) where *u* and *v* are the dimensionless axial and radial optical units. Optical units are used to represent spatial co-ordinates in dimensionless co-ordinates. Equations (2-31) and (2-32) define the relationship between the optical units and the real-space co-ordinates of a system with a numerical aperture, NA, operating at a specific wavelength, λ, in a medium with a refractive index, n.

$$I(0,v) \propto \left| \frac{2J_1(v)}{v} \right|^2 \qquad (2\text{-}29)$$

$$I(u,0) \propto \left(\frac{\sin(u/4)}{u/4} \right)^2 \tag{2-30}$$

$$v = r \cdot \frac{2\pi}{\lambda} NA \tag{2-31}$$

$$u = z \cdot \frac{2\pi}{\lambda} \frac{NA^2}{n} \tag{2-32}$$

The intensity distribution described by (2-29) and (2-30) are plotted in Figure 2-11.
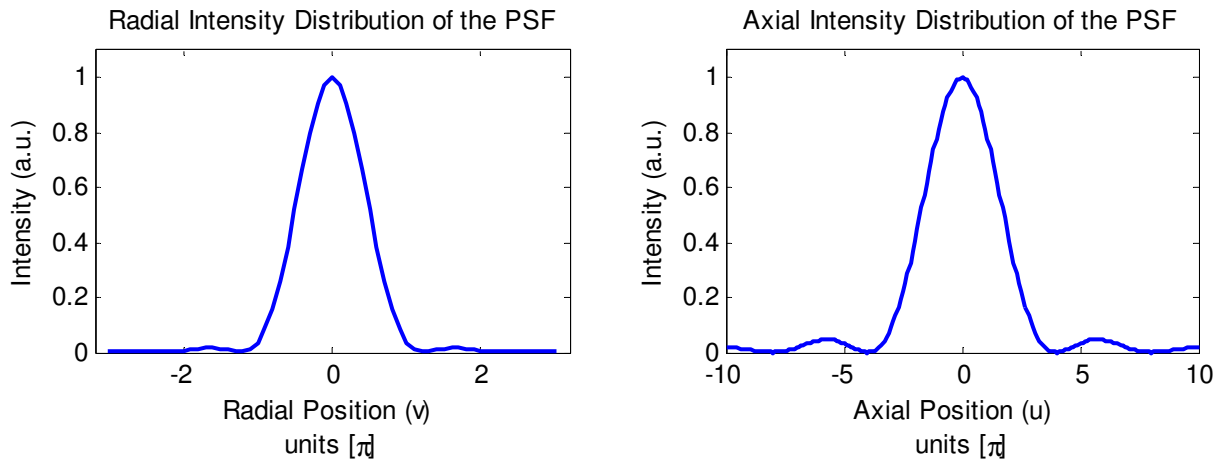
Figure 2-11   Intensity Distribution of the theoretical PSF
Radial side lobe relative intensity 3%. Axial Side Lobe intensity 5%.

It is the side lobes in the radial function that create the ring pattern shown in Figure 2-9b. The first zero in the radial distribution occurs at 1.22π leading to commonly quoted diffraction limited lateral resolution for optical microscopes. The Rayleigh criterion states that two objects are resolved if their separation is greater that r_0 given by (2-33). However it is shown in section 2.2.3 that this is not an appropriate definition for confocal microscopy.

$$v_0 = 1.22\pi$$
$$\therefore r_0 = \frac{0.61 \cdot \lambda}{NA} \tag{2-33}$$

In reality, the point spread function is a full 3D distribution and much work has been done to model its actual form [20-24] under a range of aberrations and real world complications for the purposes of deconvolution. Deconvolution is a post-processing step whereby the blurring caused by the PSF of the instrument can be compensated. This is usually only effective if the PSF of the instrument is well known. Although blind convolution is possible it is even more computationally expensive[25, 26].
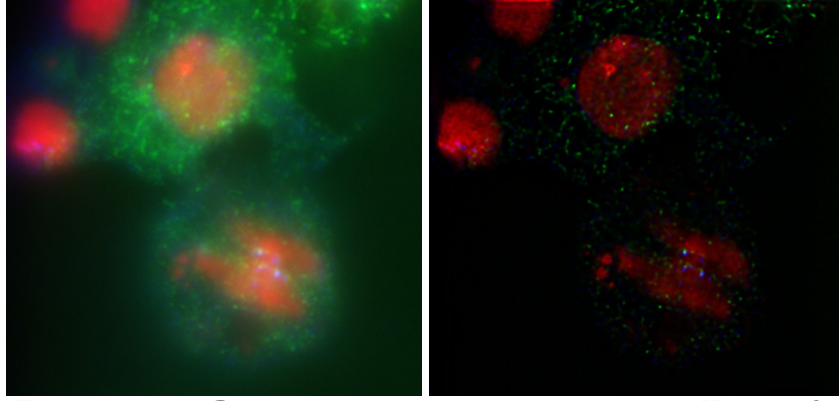
Figure 2-12 **Deconvolution of an image processed with Huygens Software[27] from Scientific Volume Imaging (SVI).**
Image before (left), deconvolved image (right). Images adapted from technical support pages of [27].

Excellent commercial software is available [27], and with increasing availability of high power computers and advances in deconvolution algorithms even widefield microscopy is now able to achieve high quality images that were once the preserve of confocal microscopy.

2.2.3. PINHOLES AND THE CONFOCAL PSF

It was shown in the previous section that the recorded image is a convolution of the actual object and the instrument's PSF. Mathematically this is expressed as,

$$I(X,Y,Z) = \iiint PSF(x', y', z') \cdot O(x'-X, y'-Y, z'-Z) \cdot dx' \cdot dy' \cdot dz'$$
$$\equiv (O * PSF)(X,Y,Z)$$

$$(2\text{-}34)$$

This assumes that PSF is translationally invariant and the image formation process is linear. However in confocal microscopy the PSF used in (2-34) is not the one derived in equations (2-29) & (2-30). The confocal PSF, PSF_{cf}, is the product of the excitation PSF, PSF_{ex}, and detection PSF, PSF_{det}, as given in (2-35) below:

$$PSF_{cf} = PSF_{ex} \cdot PSF_{det}$$

$$(2\text{-}35)$$

The excitation PSF is the diffraction limited spot formed by imaging the excitation pinhole into the sample through the microscope objective. Fluorescence from the excitation volume is captured by the microscope objective and imaged onto a photo detector. A pinhole is placed in front of the detector to exclude light not originating from the focal volume. The excitation and detection PSFs are overlapped and so the overall PSF is given by the product of these.

These PSFs are both similar and only vary in scale due to the different wavelengths of the excitation and fluorescence. In the simplified case, where both wavelengths are the same and the pinhole are infinitely small, this results in the confocal PSF being the square of the PSF already dealt with in equations (2-29) and (2-30). The axial confocal PSF is shown Figure 2-13. Notice

the narrowed central peak and the suppressed side lobes. This shows that confocal microscopy has an improved resolution due to the squared PSF. However, if the Rayleigh criterion was applied, that is to find the first zero in the PSF, we would show no improvement in resolution. Consequently the full width at half maxima (FWHM) of the PSF is often used as measure of resolution in the confocal microscopy. A similar reduction in the radial PSF is also observed although it is less pronounced.

A mono-mode fibre optic can be used to direct the light from the laser into the microscope. In this case the narrow fibre optic core provides the pinhole. The detection pinhole is provided by a small variable aperture. In Figure 2-13 it was assumed to be infinitely small. This of course is not practically possible and in reality there is always a trade off between obtaining a sufficient axial resolution and getting enough of a signal in the photodiode. Wilson and Carlini studied the effect of changing the detection pinhole size on the resolution of the confocal instrument [28]. They showed that a pinhole with a radius up to 0.5 optical units yielded similar lateral resolution to an infinitely small pinhole. As the pinhole increases in radius the lateral resolution is reduced. It approaches that of conventional microscopy at a pinhole size of about 4 optical units. However, even at these sizes the there is a considerable improvement in axial resolution compared to conventional microscopy. Using much smaller pinhole size does not greatly improve the axial resolution however axial resolution falls-off with increasing pinhole size.

Often the detection pinhole size is measured in Airy units, where 1 Airy unit (~3.8 optical units) is the diameter of the first zero of the theoretical radial PSF given by (2-33). To achieve true confocal resolution a pinhole of 0.13 Airy units or less should be used, however if the primary requirement is for depth discrimination a pinhole of 1 Airy unit can achieve similar axial resolution with considerably improved signal compared to operation with a very small pinhole, whilst retaining the lateral resolution of a conventional widefield microscope.
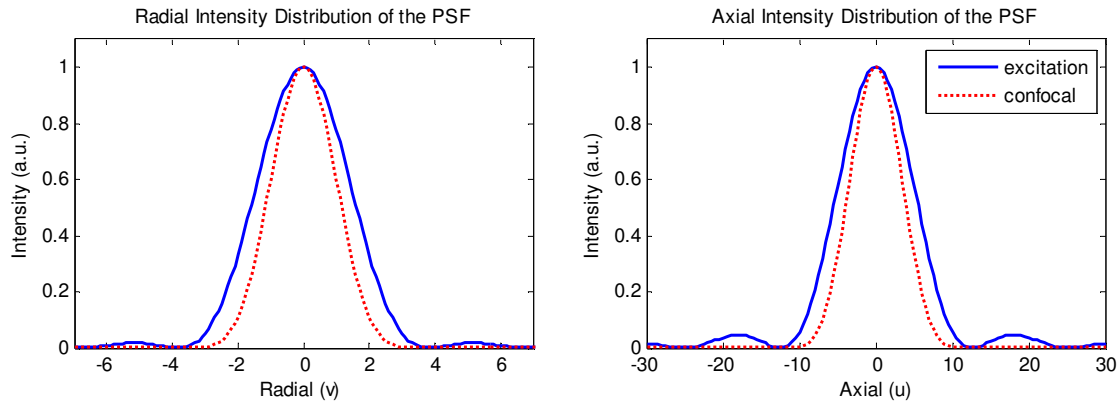
Figure 2-13   Excitation intensity distribution and confocal instrument PSF
The excitation PSF exhibits side lobes associated with a widefield PSF, however in the confocal detection PSF obtained by squaring the excitation PSF these side lobes have substantially reduced, additionally the central peak is slightly narrowed. The spatial co-ordinates measured in optical units.

2.2.4.   LASER ILLUMINATION

The laser provides an intense source of light at a specific wavelength and low divergence eliminating the requirement of the excitation pinhole with infinity corrected optics. Lasers suitable for confocal microscopy are available is a wide range of wavelengths[29] from near infrared to ultraviolet. The relatively new super-continuum[30] white light has provided single source that spans the entire visible and infrared spectrum[31]. Even the ultraviolet end of the spectrum has been reached by super-continuum sources[32] producing a spectral range from 331nm into the visible spectrum facilitating the use of UV excited dyes.

It should be clear why laser sources are the obvious choice in modern confocal microscopy but there are a few conditions to be satisfied. To obtain a diffraction limited excitation spot the whole of the back pupil of the objective must be uniformly (or close to uniformly) illuminated. Practically this is achieved by expanding the laser beam to completely fill the back pupil of the objective. When the beam is the same size as the back pupil the objective is said to be fully filled. The laser beam will not have a uniform beam profile though, it is more likely to be approximately Gaussian. By further expanding the beam and only using the central portion a more uniform beam profile is presented to the objective lens, although this is at the expense reduced transmitted light.

2.2.5.   FLUORESCENCE

The most common and useful imaging mode used in confocal microscopy is the fluorescence mode. Samples are stained or prepared to contain fluorescent tags or molecules. Whilst the biological methods of antibody tagging and genetic modification employed to mark samples are well beyond the scope of this work an understanding of the fluorescence process and

its role in acquiring high quality images is required. Fluorescent molecules tend to be relatively large bio-molecules that have origins in nature. Work done in the last few years has employed quantum dots and other synthetic fluorophores but most of the fluorophores in use today were is discovered over a hundred years ago.
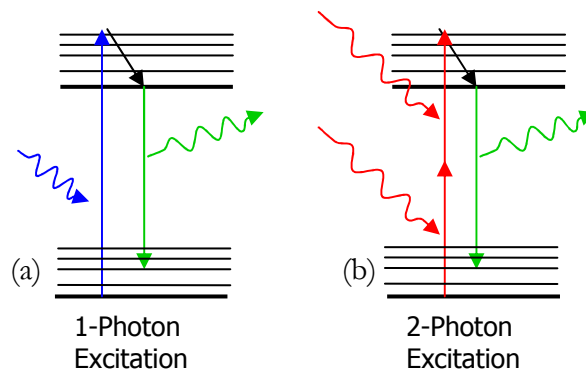
Figure 2-14   Energy level diagram illustrating the fluorescence process
The fluorescent molecule may be excited either by the absorption of a single high energy photon (blue) or two lower energy photons (red) arriving simultaneously. The intra-band relaxation is indicated by the black arrow prior to the fluorescent emission some time later depending on the lifetime of the fluorescence, which typically occurs on the nanosecond time scale.

The large bio-molecules possess, in addition to their electron energy levels, many vibrational and rotation energy levels. This band structure is responsible for broadness of the absorption and emission spectra of the biological molecules. Figure 2-14 shows an energy level diagram. Excitations generally occur almost instantaneously (the blue transition in Figure 2-14a) from the bottom of the ground state to one of the vibrational or rotational states in the band of excited electronic state. The electron then rapidly relaxes to the lowest energy state within that band before returning to the electronic ground state by the emission of a photon. On return to the ground state the electron may arrive in any of the vibrational or rotational sub levels of the ground state. The effect of these sub levels is to broaden the absorption and emission peaks. Furthermore, the intra-band relaxation within the excited electronic state causes the emission peak to be red-shifted with respect to the excitation peak. This red-shift in fluorescent molecules is known as the Stokes shift. Absorption and emission spectra for Fluorescein (FITC) are shown in Figure 2-15, and the Stokes shift is highlighted. The presence of a Stokes shift permits an extinction filter to be used to omit the excitation laser wavelength without significantly diminishing the fluorescence signal.
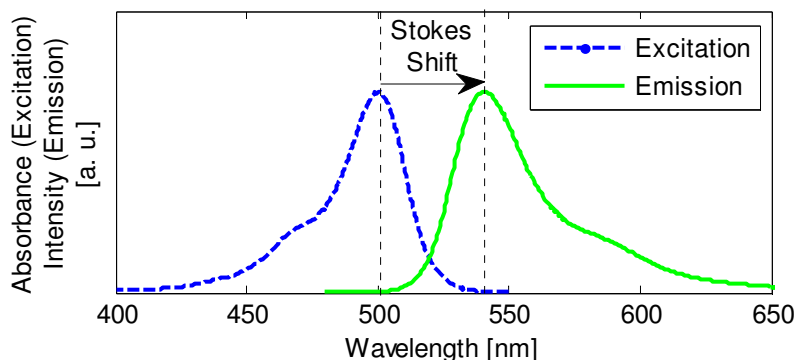
Figure 2-15 **Fluorescein (FITC) excitation and emission spectra**
Vibrational and rotational sublevels in the electronic structure cause broadening and a red shift in the emission spectrum known as the Stokes shift. (Source data for graph from [33])

2.2.6. MULTI-PHOTON EXCITATION

Instead of using a single high energy photon to achieve the excitation of the fluorophore two, or more, lower energy photons may be used as shown in Figure 2-14b. There is no electronic state corresponding to one of these lower energy red photons requiring that both photons arrive simultaneously. Obviously this is going to have a significantly lower probability than the 1 photon interaction. The probability of achieving an absorption event in a multi-photon process scales as the Nth power of intensity, where N is the number of photons involved in the process. So for two and three photon processes the excitation is quadratically and cubically related to intensity and the multi-photon (MP) absorption cross-sections are greatly reduced. This relationship was first shown by theorist Maria Göppert-Mayer[3] in 1931 some 30 years prior to the invention of the laser which would be required to prove the theory. Only since the relatively recent invention of ultrashort pulsed lasers have the high peak intensities, needed to achieve sufficient fluorescence signal to over come background noise, been available. Whilst it is theoretically possible to achieve the 2-photon signal from a continuous wave laser the power requirements are phenomenal and 1 photon heating would rapidly destroy any sample of interest.

The additional complications and equipment required to implement a 2-photon excitation are compensated for by significant benefits. These include an inherent sectioning capability without the need for spatial filtering at the detector, which greatly improves images from deep inside thick samples and reduces out of focus photobleaching. In addition to the imaging benefits of multiphoton interaction can be used to induce DNA damage by multiphoton absorption or ablation. High power lasers, combined with powerful microscopes, are being used to perform accurate and precise ablation of cells and structures and are increasingly finding applications in medicine[34] and dentistry [35].

The inherent sectioning ability arises from the non-linear excitation process. In the single photon fluorescence imaging, the PSF of the microscope is the product of the excitation and

detection PSFs, and these are almost identical, save for the small Stokes shift. To a reasonable approximation, the instrument function is the square of the excitation PSF. Squaring the PSF reduces the maxima in the side lobes of the axial PSF (see Figure 2-13) providing the sectioning capability. In two-photon microscopy the excitation PSF is the square of the one-photon excitation PSF because the fluorophore excitation goes as the square of the intensity. More generally the N photon excitation PSF can be expressed as:

$$PSF_{Np} = PSF_{1p}^{N} \tag{2-36}$$

The resulting generation of volumes for one, two and three-photon processes are progressively smaller for a given wavelength and are illustrated in Figure 2-16. The two and three photon excitation volumes are much more contained and have a much simpler structure. It may appear from this figure that multi photon imaging should be of inherently higher resolution. In practise, if you are using the same fluorophore, the two photon wavelength must be doubled in order excite the fluorophore.

If the laser wavelength is appropriately chosen so that it is not absorbed by the sample then greater sample penetration is achievable as absorption by the fluorophores only occurs within the focal volume. This is also why photo-bleaching does not occur out of the focal volume.
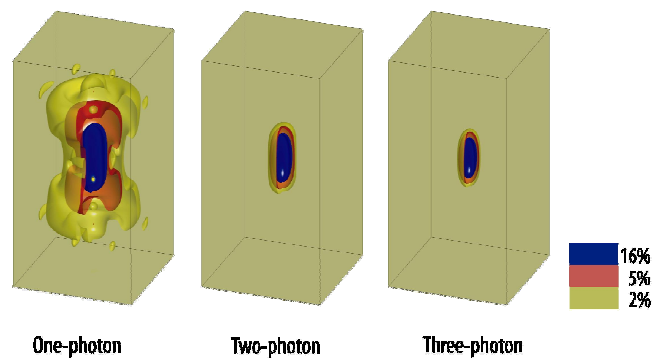
Figure 2-16   Multi-photon excitation generation volumes
Generation volumes for one-, two-, and three-photon fluorescence microscopy using wavelength of λ=750nm and a dry microscope objective lens of NA=0.9. The slabs are 4×4×8 μm along the lateral (×2) and axial directions, respectively. Isosurfaces are drawn at the given percentage values of the excitation intensity. [36]

2.2.7.   LIMITS OF CONFOCAL MICROSCOPY

Initially it may appear that confocal microscopy is a magic bullet for biological cell imaging. Unfortunately there are practical and fundamental limits imposed by the implementation of the confocal arrangement. The most apparent is the serial data acquisition process. The use of pinholes requires that the image is acquired in a point wise fashion. Either the sample or the point needs to be scanned. Sample scanning is simpler to implement and causes less aberration

but the inertia of the sample and stage ultimately limits the maximum scan rate. Beam scanning is potentially faster and a number of implementations have been developed that employ galvo-motor mounted mirrors to deflect the beam in the x and y directions whilst the z position is controlled by a micro-focusing stage attached to the objective. The scan rate here is also limited by inertia but the mirrors are smaller and so higher rates can be achieved than if sample scanning is employed. Petráñ[37] developed a method that used spinning a disc of apertures, called a Nipkow disc, in place of the pinhole parallelising the imaging process to some extent whilst the use of an array of microlenses in place of the apertures in the disc greatly increased the excitation efficiency[38]. The main drawback of this method is that the pinhole size is not variable so the user loses the option of trading off resolution for improved signal. Also even with the microlenses in place of the apertures in the spinning disc the microscope light transmittance is considerably less than a single pinhole confocal microscope. The next generation of microscopes that employ acousto-optic scanning are making video frame rates even at 3D a possibility.

At these high scanning rates, more problems become apparent. These include fluorophore saturation and photobleaching as well as problems of photon counting statistics. The photomultiplier tube (PMT) is a device that counts photons and is subject to multiplication noise and problems of quantum efficiency (Q_e). The Q_e is the fraction of photons incident on the detector that are converted to photoelectrons. These photoelectrons are multiplied in a dynode chain to obtain a detectable electronic signal which can either be counted or amplified by a trans-impedance amplifier. PMTs still show a signal in the absence of any light. This dark current is the dominating noise at low signal levels and is caused by thermionic electrons being released from the dynodes and cathode, in addition to regenerative effects caused by the glow of the dynodes and anode under electron bombardment. These photons can be incident on the photocathode and create after-pulses.

The number of events, n_E, detected is proportional to the photon flux, *I*, the quantum efficiency Q_e and the sampling period, τ.

$$n_E = I \cdot Q_e \cdot \tau \tag{2-37}$$

As the counting events are governed by Poisson statistics the variance, $\sigma(n_E)$, is also given by n_E with an additional term from the independent dark current noise n_D.

$$\sigma(n_E)^2 = n_E + n_D \tag{2-38}$$

This gives an overall signal to noise ratio, R_{SN}, of

$$R_{SN} = \frac{n_E}{\sqrt{n_E + n_D}} \, . \qquad\qquad (2\text{-}39)$$

At low signal levels the images become increasingly noisy and very short dwell times or high scan rates the signal is decreased. The only way to improve this is to increase the photon flux, I, or the quantum efficiency Q_e. As the user generally does not have the option of changing the PMT, the only way to increase the intensity is to increase the excitation laser intensity to create more fluorescence. This approach only works up to a certain point as can only be a finite number of fluorophores within the excitation volume, and assuming that it is strong enough to raise the entire population to an excited state the total amount of fluorescence is then limited by fluorescence lifetime. Furthermore, fluorescence is not the only relaxation pathway, there are at least two others, phosphorescence and photobleaching. The excited state can also relax to a triplet state by inter-system crossing. From here there is a radioactive decay path to the ground state called phosphorescence which has a longer lifetime due to the spin flip in the electron required to allow the transition. Alternatively, a photochemical reaction can occur that causes the molecule to lose its ability to fluoresce. This process is not well understood but photobleaching kinetics studies indicate that it is related to the triplet state and is dependent on the presence of oxygen[39]. Photobleaching has a probability of happening on any given excitation. Some fluorophores are more sensitive than others and the average number of fluorescence emissions that a fluorophore will make before bleaching occurs varies from a few 100 to ~ 100,000.

These effects limit the maximum intensity that can be used before the sample is lost to photobleaching. This in turn governs the maximum scan rates at which good quality images can be acquired.

2.3. DNA DAMAGE IN CELLS

In chapter 4 the femtosecond laser is used in conjunction with confocal microscope to induce ultraviolet (UV) photoproducts in the nuclei of live cells by the simultaneous absorption of three infra red (750nm) photons. This corresponds to an absorption by a single photon with a wavelength of 250nm which is in the UV spectrum. UV radiation, which can originate from harmful rays from the sun, has been the subject of cancer research for the last 40 years. Previous experiments used UV radiation to damage cells and the damage to the DNA was measured by biochemical methods which could detect the changes in the molecular weight of the DNA.

The advent of high resolution confocal microscopy has allowed these changes to be visualised in live cells without necessitating breaking up the cells for analysis. This combined with the discovery that ultraviolet type DNA damage could be induced by three photon infra-red

absorption, led to a unique experimental way of inducing highly resolved and precisely targeted areas of DNA damage in live cells [40].

The focus of this work is on the development of the methods required to perform these experiments, allowing cells to be targeted and the repair process visualised, in real time.

Whilst the full discussion of the cellular biology associated with these processes is beyond the scope of this work, a basic understanding of the fundamental damage process and the cell lifecycle is required for practical experimental reasons.

2.3.1.   UV INDUCED DNA DAMAGE IN CELLS

Ultraviolet light induces the formation of covalent linkages in the C=C bonds of two of the DNA bases, thymine and cytosine. Two common resulting UV products are cyclobutane pyrimidine dimmer (CPD) and 6,4 photoproduct. These create lesions in one strand of the double strand DNA and alter its structure. This can inhibit replicating and accurate transcription of the DNA and may lead to mutations in the DNA.

These lesions are repaired by a process called nucleotide excision repair. The pieces of DNA containing the UV photoproduct are cut out (excised) and then replicating polymerases use the other undamaged strand of the DNA as a template to replace the excised portion. There are over thirty proteins, including Proliferating Cell Nuclear Antigen (PCNA), involved in this process. Biochemical experiments using cell extracts and cells that have had portions of the DNA deliberately disabled have allowed the roles of the individual proteins involved in this process to be studied. However, less is known about the dynamics of these proteins and this work has attempted to design methods that can study the activity of these proteins in live cells to acquire greater knowledge of the protein kinetics in DNA repair.

2.3.2.   THE CELL DIVISION CYCLE

The division of cells is a vital process in multi cellular organisms, permitting their growth, renewal and repair. Cells are able to utilise check points throughout the process to arrest the propagation of mutated or damaged DNA. The cell cycle can be divided into four phases. These are listed below, with short descriptions of the activity that takes place in the cell and its appearance in Chinese Hamster Ovary (CHO9) cells transfected with GFP-PCNA. Figure 2-17 provides a schematic of the cell division cycle, with diagrams highlighting the characteristics of GFP-PCNA in CHO9 cells throughout the cell cycle.
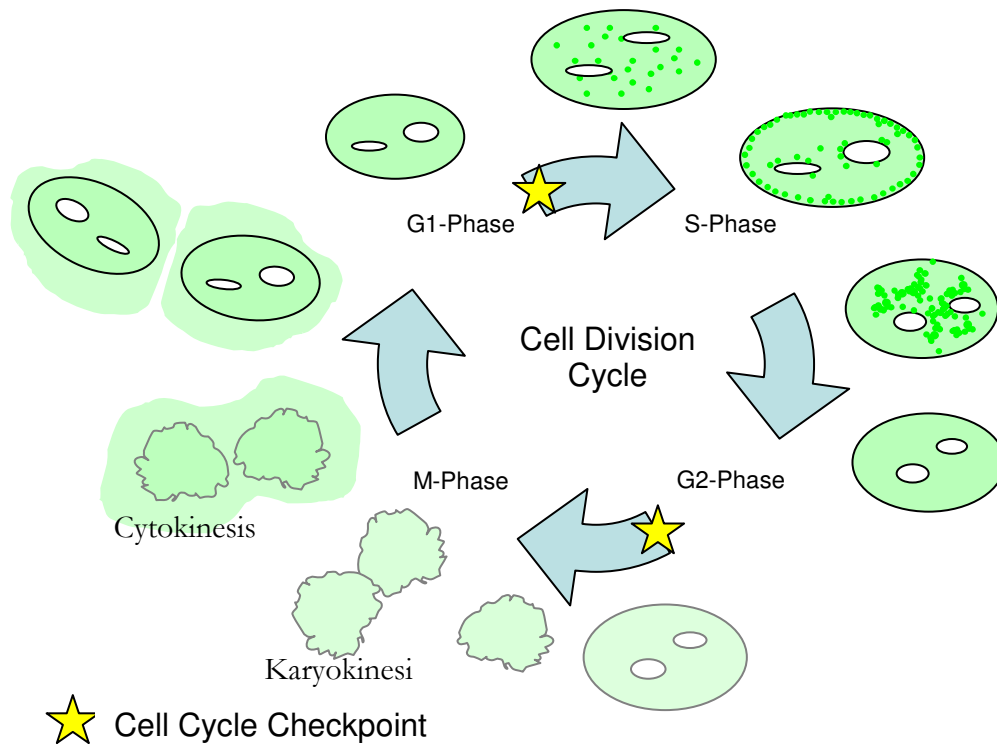
Figure 2-17   ***Schematic of the Cell Division Cycle***

Gap 1 (G1-Phase) – The cell produces enzymes and proteins required for DNA synthesis in the S-Phase. The PCNA is homogeneously distributed throughout the nucleus except in certain nucleoli which do not appear to contain PCNA. If the cell has only recently finished the M-Phase some fluorescence may be observed in the cytoplasm. The G1→S checkpoint ensures that the cell is ready to progress to the S-Phase. If the cell DNA is damaged or the environmental conditions are not suitable, the cell will not proceed and may enter the G0 or resting phase. An example of a G1-Phase cell transfected with GFP-PCNA is shown in Figure 2-19.

Synthesis (S-Phase) – The DNA is synthesised at replication centres within the nucleus. In early S-phase bright foci of PCNA are sparsely distributed throughout the nuclei. As the S-phase progresses PCNA localises in a foci around the perimeter of the nucleus and nucleoli. In the final stages of the S-Phase, large bright agglomerations of PCNA can be observed throughout the cell. Images of cells transfected with GFP-PCNA at different stages of the S-Phase are shown in Figure 2-18.

Gap 2 (G2-Phase) – Once DNA synthesis is complete, the cell enters G2-Phase. In the G2 further protein synthesis takes place prior to mitosis. The G2→M checkpoint will prevent the cell proceeding to Mitosis unless sufficient protein has been synthesised. In this phase the PCNA

is homogonously distributed thought the nucleus and is indistinguishable from the G1-phase. Examples of G2-Phase cells are shown in Figure 2-18 and Figure 2-19.

Mitosis (M-Phase) – The nuclei separate (Karyokinesis) and the cytoplasm is divided between the two daughter cells (Cytokinesis). During the M-Phase the PCNA is not clearly visible, and the nucleus boundary is less well defined. During Cytokinesis florescence is observed in the cytoplasm. Once cell division is complete the daughter cells will each enter the G1-Phase of the interphase and the process will repeat. Images of the progression of a cell from G2 through the M-Phase to G1 are shown in Figure 2-19.

The G1-Phase, S-Phase and G2-Phase are collectively referred to as the interphase, during which the cell is accumulating the necessary nutrients and preparing for division. Cells that are not in the cell division cycle are said to be a quiescent or senescent state which is also known as G0-Phase or resting phase. Quiescent cells may at some point enter the G1 phase when environmental conditions are appropriate and restart the cell division cycle whilst senescent cells have entered the G0 phase in response to DNA damage.
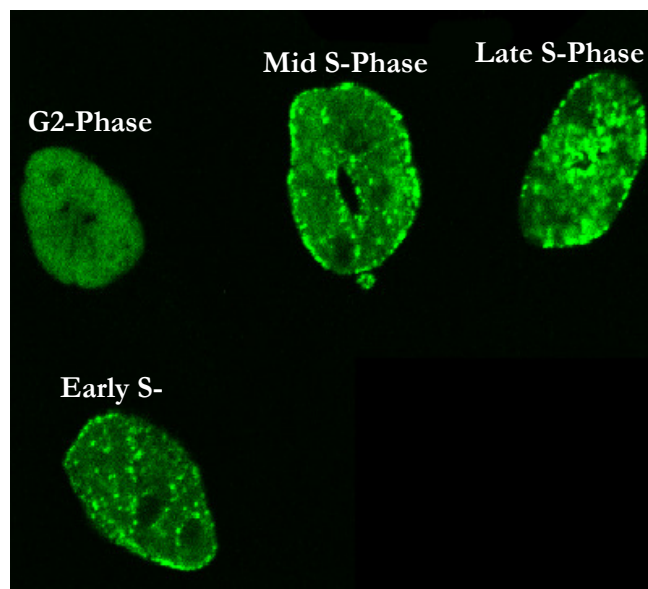
Figure 2-18   Progression through the S-Phase.
Cells exhibiting characteristic distributions of PCNA for the G2-Phase and throughout the S-Phase. These images were provided by Jeroen Essers [41]
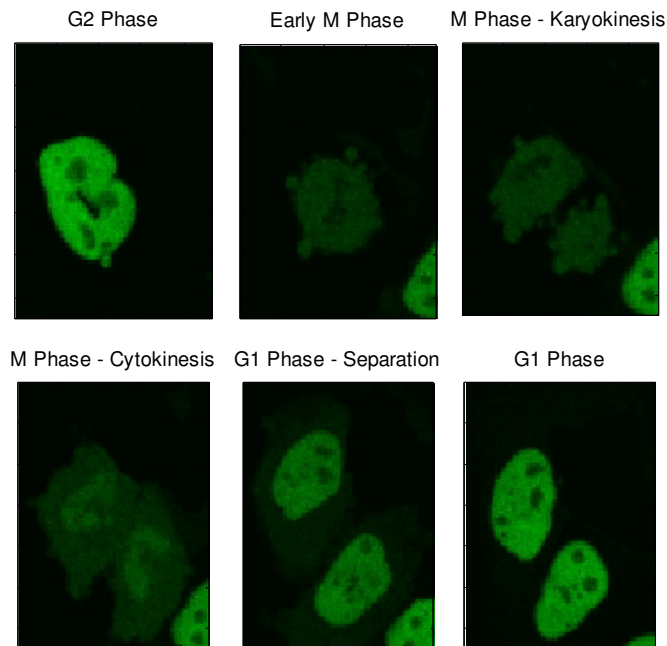
Figure 2-19   **Progression through the M-Phase.**
Portions of selected frames extracted from a time-lapse series of images showing a live cell undergoing mitosis.
Original movie provided by Jeroen Essers [41].

2.4. SCANNING TUNNELLING MICROSCOPY (STM)

2.4.1. OVERVIEW

The STM is one of the most critical components the in the SPPX-STM apparatus discussed in chapter 6. A brief overview of the principles of operation will be provided here.

It consists, essentially of a conducting sample and a conducting (usually metallic) probe (the tip) which comes to a sharp apex, ideally a single atom. The tip's position with respect to the sample can be precisely controlled, usually by a piezoelectric crystal which expands and contracts in response to an applied electric field. The tip is biased with respect to the sample and, through the quantum mechanical phenomenon of tunnelling, electrons are able to move across the gap between the sample and the tip. The signal is exponentially dependant on the tip's distance from the sample, providing a very sensitive measurement of any change in tip-sample separation.

Topographic images are acquired by specifying a current set-point and adjusting the separation of the tip and sample to maintain a constant height. This is controlled by a closed loop servo circuit. Simultaneously, the tip is scanned in the plane (x-y plane) of the sample and the servo continually adjusts the height to maintain the current set point. The height is measured at every position to obtain a topographic image.

2.4.2.   THE 1D TUNNELLING MODEL

In quantum mechanics the wavefunction $\psi(z)$, of an electron in a potential, $U(z)$, must satisfy the Schrodinger wave equation, given in (2-40), where m_e is the mass of an electron.

$$-\frac{\hbar}{2m_e}\frac{d^2}{dz^2}\psi(z) + U(z)\psi(z) = E\psi(z) \qquad (2\text{-}40)$$

Consider an electron represented as a plane wave incident on a rectangular barrier of finite height. Solutions can be found piecewise, for the region before, in and after the barrier. In the region before the barrier the energy of the electron, E, is greater than potential and so the electron has positive kinetic energy signified by its momentum. It travels as a propagating wave and the wave function in this region takes the form,

$$\psi(z) = Ae^{ikz} + Be^{-ikz} \qquad (2\text{-}41)$$

The positive and negative exponents represent right moving and left moving electron waves respectively. A and B are arbitrary constants that can be found by satisfying the boundary conditions. By differentiating (2-41) and substituting it into (2-40) it can be verified that this is a solution to the wave equation and the following expression for k is obtained.

$$k = \frac{\sqrt{2m_e(E-U)}}{\hbar} \qquad (2\text{-}42)$$

As long as the electron energy, E, is greater the potential, U, k is real and (2-41) yields a propagating wave. However, within the barrier, if E<U then k is imaginary. In this region a different wave function is required and a solution comprising a combination of growing and decay exponentials can be tried.

$$\psi(z) = Ce^{\kappa z} + De^{-\kappa z} \qquad (2\text{-}43)$$

This can be varied by substitution into the wave equation (2-40) which yields an expression for κ similar to that obtained for k in (2-42):

$$\kappa = \frac{\sqrt{2m_e(U-E)}}{\hbar} = ik \qquad (2\text{-}44)$$

Substituting (2-44) into (2-43), it can be seen that in the classically forbidden region of the barrier, where the electron energy is less than that of the barrier, an exponentially decaying

waveform is obtained. If the barrier were infinitely thick then C must be zero in order for the wave function to be finite and continuous over all space and a pure exponentially decaying waveform is obtained.

If an electron reaches the other side of the barrier then the potential becomes less than the electron energy and the wave function is of the same form as (2-41). This will only be a right travelling wave. The majority of the wave does not tunnel through the barrier and is reflected, leading to the left travelling wave in the region prior to the barrier. The electron on the other side of the barrier has the same energy as it did before it crossed the barrier. Only the probability density has been diminished by the barrier.

If this theory is applied to the STM, treating the STM as a 1D tunnelling problem, the potential barrier is the gap between the sample and the tip, as shown in Figure 2-20
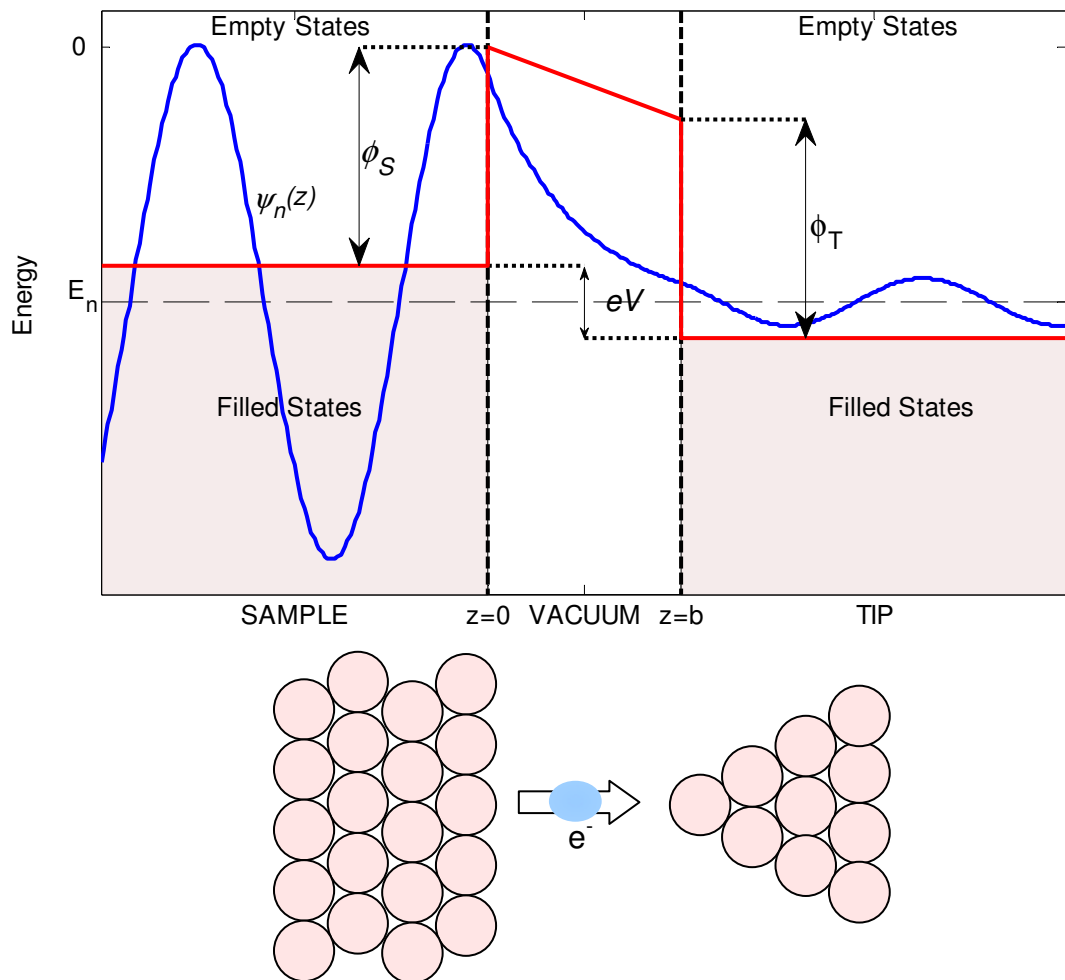
Figure 2-20   1D Energy Diagram of an STM Junction
The electron wavefunction (blue) tunnels across a vacuum gap with width b, overcoming the potential barrier (red) created by the work function of the sample ϕ_S. The electron tunnels from an occupied state in the sample to an unoccupied state in the tip.

The physical source of this potential is the work function which is defined as the minimum amount of energy required to extract the uppermost electron to vacuum. The work

function is a property of the metal. If the surface is contaminated the work function can be significantly lower. The work function of the sample and the tip will usually be different but for the purpose of this model they are assumed to be the same, that is to say:

$$\phi = \phi_S = \phi_T .$$
(2-45)

The choice of the zero point for the potential is arbitrary but by convention the vacuum level of the sample is defined as zero and all other energies are specified relative to this. In the abstract example considered previously it was stated that an electron was incident on the barrier, without consideration of where it originated. In STM, the electrons come from either the tip or sample depending on the bias applied. The case of an electron tunnelling from the sample into the tip must be considered. In the sample there are many electrons with discrete energy levels ranging from the ground state up to the Fermi level. The energy and wavefunction of these allowed states is denoted E_n and ψ_n respectively.

Having defined the vacuum potential as zero, the Fermi level defines the energy of the highest energy electron and is given by, $E_F = -\phi$, and substituting into (2-44) an expression for the κ in the tunnel gap is obtained.

$$\kappa = \frac{\sqrt{2 m_e \phi}}{\hbar}$$
(2-46)

In the absence of an applied bias, the electrons from the tip are as likely to tunnel into the sample as visa versa and there is no net current. Application of a bias is required for a tunnelling current to flow. In Figure 2-20 the tip has been positively biased with respect to the sample and electrons will tunnel from the sample to the tip. The applied bias is assumed to be small compared to the electron work function. This means the barrier can be assumed to be rectangular with constant potential, ϕ, and equation (2-46) is still valid for calculating the probability decay constant, κ. As the applied bias is small all the electrons tunnelling across the barrier can be considered to have energy of E_F, and the probability P_n of finding an electron from the nth sample state at the surface of the tip is given by:

$$P_n(b) = \left| \psi_n(b) \right|^2 = \left| \psi_n(0) \right|^2 e^{-2 \frac{\sqrt{2 m_e \phi}}{\hbar} b}$$
(2-47)

Contributions to the tunnel current come from all the electrons in the sample with energies in the range E_f to E_f-eV_b.

$$I \propto \sum_{E_n=E_F-eV_b}^{E_F} P_n(b) = \sum_{E_n=E_F-eV_b}^{E_F} |\psi_n(0)|^2 \, e^{-2\frac{\sqrt{2m_e\phi}}{\hbar}b} \qquad (2\text{-}48)$$

As the V_b is small compared to the work function ϕ, then rather than enumerate all the states in the range E_f to E_f-eV_b, it is convenient to define a density of samples states, $\rho_S(b,E_F)$, a distance of b from the sample surface at the energy E_f. Assuming that the $\rho_S(b,E_F)$ is constant over the interval eV_b wide at the Fermi level, then tunnelling current can be written as:

$$I \propto eV \cdot \rho_S(b, E_F) \qquad (2\text{-}49)$$

where, $\qquad \rho_S(z, E) \equiv \frac{1}{\in} \sum_{E_n=E-\in}^{E} |\psi_n(z)|^2 \qquad$ when $\in$ is small. $\qquad (2\text{-}50)$

From equation (2-49), it is clear that STM acts as probe of the Local Density Of States (LDOS) and in this simplified example it is implied that the sample and tip are both ideal free electron metals. What is not obvious from this model, although on consideration clearly true, is that for an electron to tunnel across the gap, initially it must be coming from an occupied state and going to suitable unoccupied state with the same energy in the tip. This has significant implications for semi-conductors and metals that have significant variations in their LDOS over the biases that may be applied to them.

2.4.3. STM PROBING LOCAL DENSITY OF STATES

When LDOS is flat with respect to change in the energy, then as the bias voltage is increased the tunnelling current rises linearly. However, if either the sample or the tip are semi-conductors, possessing an energy gap, then a sharp edge will be observed in the I/V curve near the energy of the gap. This indicates how the STM may be used to obtain spectra of the LDOS by varying the voltage. It also means that results must be interpreted with care as electronic features may be manifest in the samples topography. Also the I/V spectra obtained from an STM is usually not that of the isolated surface, but rather a convolution of the LDOS spectrum of the surface with the LDOS spectrum of the tip. To acquire a clean spectrum of the surface LDOS a tip must be made from a material closely resembling a free electron metal.

When both the tip and sample have structured LDOS spectra then the tunnelling current is better described by considering the overlap of the wavefunction of electron states from the tip and the sample and calculating the transition matrix element |M|. This was the approach suggested by Bardeen and ignoring any thermal effects, the current is given by:

$$I = \frac{4\pi e}{\hbar} \int_{E_F}^{E_F + eV} \rho_S(\in -eV) \cdot \rho_T(\in) \cdot |M|^2 \cdot d\in \qquad (2\text{-}51)$$

CHAPTER 3.

3. Experimental Techniques

This chapter deals with the experimental methods and techniques used in this work and it follows a similar structure to Chapter 1. It starts with an overview of the whole optical system and proceeds to describe the procedures for the use and alignment of the laser as well as measurement of the characteristics of the femtosecond pulses generated. The confocal microscope controls are explained and a procedure is provided for the alignment of the of femtosecond infrared (IR) laser to the confocal microscope for multiphoton experiments. The procedure for inflicting targeted DNA damage at specific points as well as the creation of patterned DNA damage is explained.

A method is presented for measuring the pulse duration and the point spread function at the focus of the microscope. This information is crucial in providing an accurate estimate of the peak laser intensity at the focus of the microscope.

The operation of the Scanning Tunnelling Microscope (STM) is described, including procedures for sample handling and basic imaging. Alignment of the IR laser with the STM is left until Chapter 6 which is devoted to the task of development of a time resolved shaken pulse pair excitation STM (SPPX-STM).

3.1. OVERVIEW OF THE OPTICAL SYSTEM

The optical system is split between two benches in different rooms. The Ti:sapphire laser is housed in one room (the laser room) and is shared between the systems detailed in this work and a regenerative amplifier system used by other groups for surface science and ablation measurements. Once the beam arrives in the microscopy lab it is distributed between three instruments on a vibrationally isolated optical table. These instruments consist of a scanning tunnelling microscope (STM) for the time resolved STM work, the confocal microscope for the 3-photon DNA absorption measurements and 2-photon imaging and a near-field scanning optical microscope (NSOM).

Figure 3-1 provides a diagram of the layout of the optical tables and positions of the key pieces of equipment. The table is laid out with a central beam path, defined by the apertures A3 and A4, forming a distribution backbone. Flip mirrors can be placed in the path to divert the beam to individual experiments. The half wave plate (WP1) and Glen Taylor polarising cube (PL1) allow continuously variable intensity control. When the delay stage is in use, the beam is incident on the beam splitter (BS2), which together with the retro-reflectors (M11, M10) forms a Michelson interferometer. M11 is mounted on a linear step motor driven translation stage with 4 inches (~10cm) travel, facilitating a change of delay of 666ps. The motor is controlled by a custom built microstep motor controller, the design of which is the subject of section 6.5. M5 is mounted on a Piezojena PX100 piezo translation stage with 100μm of travel. The piezo stage facilitates the precise delay variations over a range of 666fs and higher frequency oscillations of the mirror for the lock-in detection of signals up to few hundred hertz required for the Shaken Pulse Pair eXcitation (SPPX) equipment developed in Chapter 6.
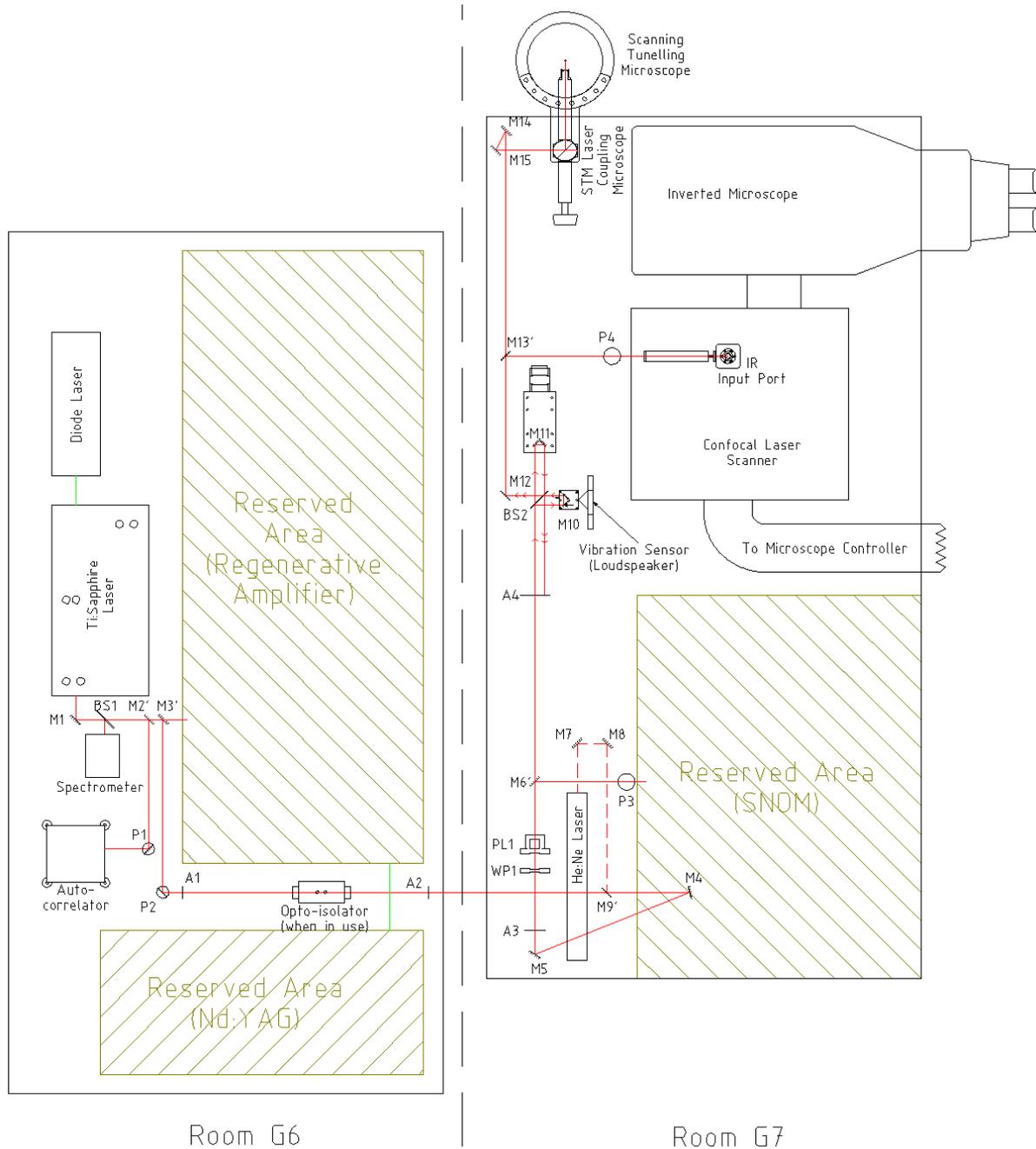
Figure 3-1   Overview of optical layout
Figure shows physical layout of the optical tables in the two rooms. The reserved areas are used by other experiments and placement of optics in these areas is complicated by additional equipment. M1-M15 are mirrors a ' symbol indicates a flip mirror, which may be up or down. BS1 is a 10:90 beam-splitter, and BS2 is a 50:50 beam-splitter. P1-4 are periscopes used to adjust the level of the beam. A1-A4 are adjustable apertures, and WP1 is a half-wave plate and PL1 is a Glen-Taylor polarising prism.

The use of retro-reflectors in the Michelson interferometer prevents the light being reflected back into the laser and destabilising the mode lock by translating the input and output beams. The output is directed into the confocal microscope and STM using mirror M12. Flip mirror M13', can be used to direct the laser to the confocal microscope and the final alignment is

achieved with the periscope (P4). When M13' is flipped down the laser beam continues onto mirrors M14 and M15 which allow precise alignment into the laser-STM coupling microscope.

3.1.1.   LASER OPERATION

The laser used in this work is a Spectra Physics Tsunami Ti:sapphire laser pumped by Coherent Verdi 5W diode pumped solid state laser.. Its external cooling system ensured both pump and oscillator operated at 19°C. The Verdi is a simple to operate turn key pump laser system. Details of the start up and optimisation procedure are described in Appendix B.1. During the start up procedure the power and pulse duration, as estimated from the pulse spectrum, is optimised. The performance of the laser systems varies as a function of central wavelength. Figure 3-2 below shows the experimentally measure maximum output from the Tsunami when pumped by the Verdi at 5W nominal power.
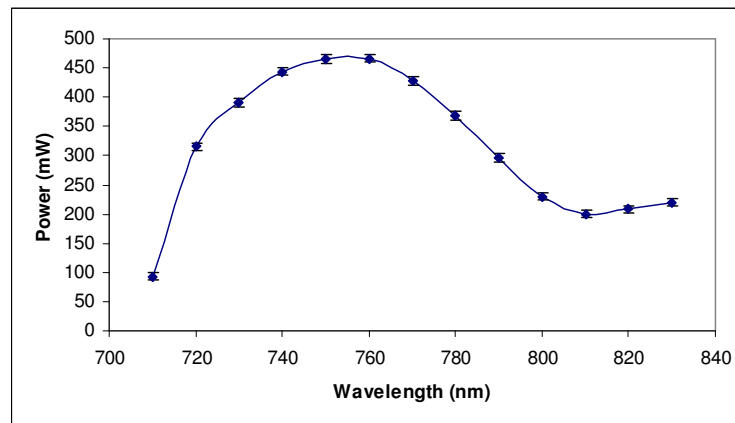
Figure 3-2   Typical maximum power available from the Tsunami
A measurement of the maximum power available from the Tsunami at each wavelength operating without mode locking. Intensity measured with a Model 407a power meter with a thermal expansion head.

3.1.2.   PULSE DURATION MEASUREMENTS

In addition to measuring the average pulse power and pulse spectrum during start up, a direct measurement of the pulse duration can be made by performing a fringe resolved 2nd order autocorrelation. Pulse durations are measured at the output of the laser, directly before the laser input port of the confocal laser scanner and at the focus of the microscope. The latter measurement is treated separately in section 3.2. The other measurements were performed using a commercial "Autocorrelator MINI 2000" manufactured by Angewandte Physik und Elektronik. The autocorrelator consists of an interferometer and a second harmonic generation crystal. A schematic of the APE MINI 2000 is shown in Figure 3-3. It can be operated in co-linear or non-co-linear modes. In co-linear mode the interferometer is a Michelson interferometer, and the 2nd order fringe resolved autocorrelation is superimposed on a background signal. In non-co-linear

form the focussing mirror brings the beam from the two arms of the interferometer together providing a spatial overlap within the second harmonic generation (SHG) crystal.

In SHG the two input waves create a second order oscillating polarisation wave in the material. This creates an electric field oscillation at twice the frequency of the input wave, with a corresponding wave vector related to the refractive index of the crystal at that frequency. In order to have constructive interface the second harmonic wave must have a wave vector equal to the sum of the contributing input wave vectors. This is called the phase matching condition. Due to dispersion this can be challenging as the refractive index varies with frequency. SHG Crystals are often strongly birefringent, possessing two optic axes, each with different refractive indices. Only by a careful choice of angle between the incident beams and the optic axis of the SHG crystal can the phase matching condition be satisfied.

The phase matching condition ensures the frequency double light propagates in the direction of the bisector of the two fundamental beams. The angle of the SHG crystal is adjusted electronically by the angular drive. This optimises the phase matching to maximise the second harmonic generation signal.
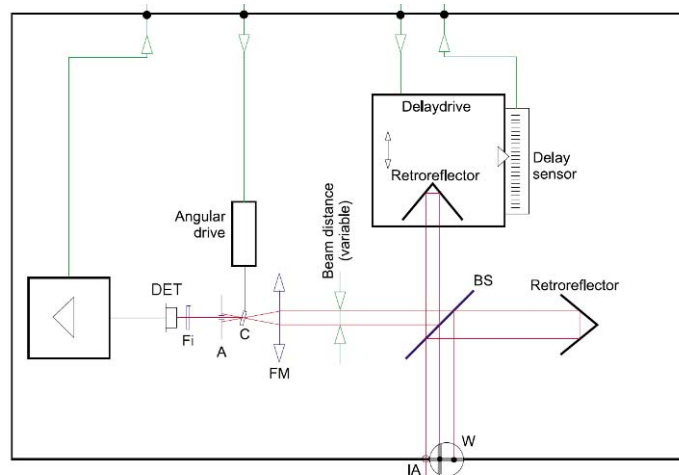
Figure 3-3   Schematic of the autocorrelator – Non-Collinear Mode
Figure showing how the autocorrelator can be used in non-co-linear mode. Laser is shown as red lines, whilst the green lines are electrical signals. IA – Input Aperture, W – Window, BS – Beam Splitter, FM - Focus Mirror, C – SHG-Crystal, A – Aperture, Fi – Filter and DET – Detector. (Reproduced from [42])

To satisfy the phase matching condition in the second harmonic crystal the light entering the autocorrelator has to be horizontally polarised. The laser output is vertically polarised and the beam's polarisation is rotated by using a periscope to adjust the height whilst simultaneously reflecting the beam through 90° in the plane of the optical table. The 2nd order autocorrelation trace is acquired using the autocorrelator's controller and the data output to a TEK digital oscilloscope from which it can be saved to disk allowing processing off line. The autocorrelator is capable of providing pulse duration measurements in real time, but this facility is not available for

measurement of the pulse duration at the focus. In order to make a fair comparison between these data and the data collected from the FRAC measurement at the microscope focus it is necessary to apply the same data processing to each data set.

Only the intensity of the signal from the detector is recorded against a time base. The autocorrelator has a facility to output the x position but this is almost linear over the whole scan range. Instead, the fringes are used as an intrinsic calibration. The laser's central wavelength is known from the spectrometer used when it is initialised. Knowing the wavelength and the speed of light it is a simple matter to establish a delay scale, although the choice of zero delay is an arbitrary one. It was shown in section 2.1.3 on the theory of second order autocorrelation that the signal can be decomposed into 3 components: The data clustered around the DC; the central laser frequency, ω_l and twice that $2\omega_l$. Figure 3-4 shows the autocorrelation of the pulse immediately after the laser output as well as the Fourier transform of the signal. It shows that the laser is producing pulses as short as 86fs. Furthermore the fringes are clearly resolvable over the entire trace and there is a significant signal component at $2\omega_l$. This indicates that pulse is most likely unchirped.

The short unchirped pulses from the laser must travel a significant distance through a number of optics as described at the beginning of this chapter to reach the experiment. These optics broaden the pulse. It is important to know what the actual pulse duration is at the interaction site whether that is the focus of the confocal microscope in fluorescence imaging and 3 photon DNA damage experiments or the STM junction in an SPPX measurement.

The pulse duration is also measured prior to the Michelson delay stage before it is directed into the STM and the confocal microscope. The light traverses a long path through air and is reflected from on a number of mirrors and passes through an optical isolator, a ½ wave plate and a polarising cube, all of which contribute to pulse broadening.
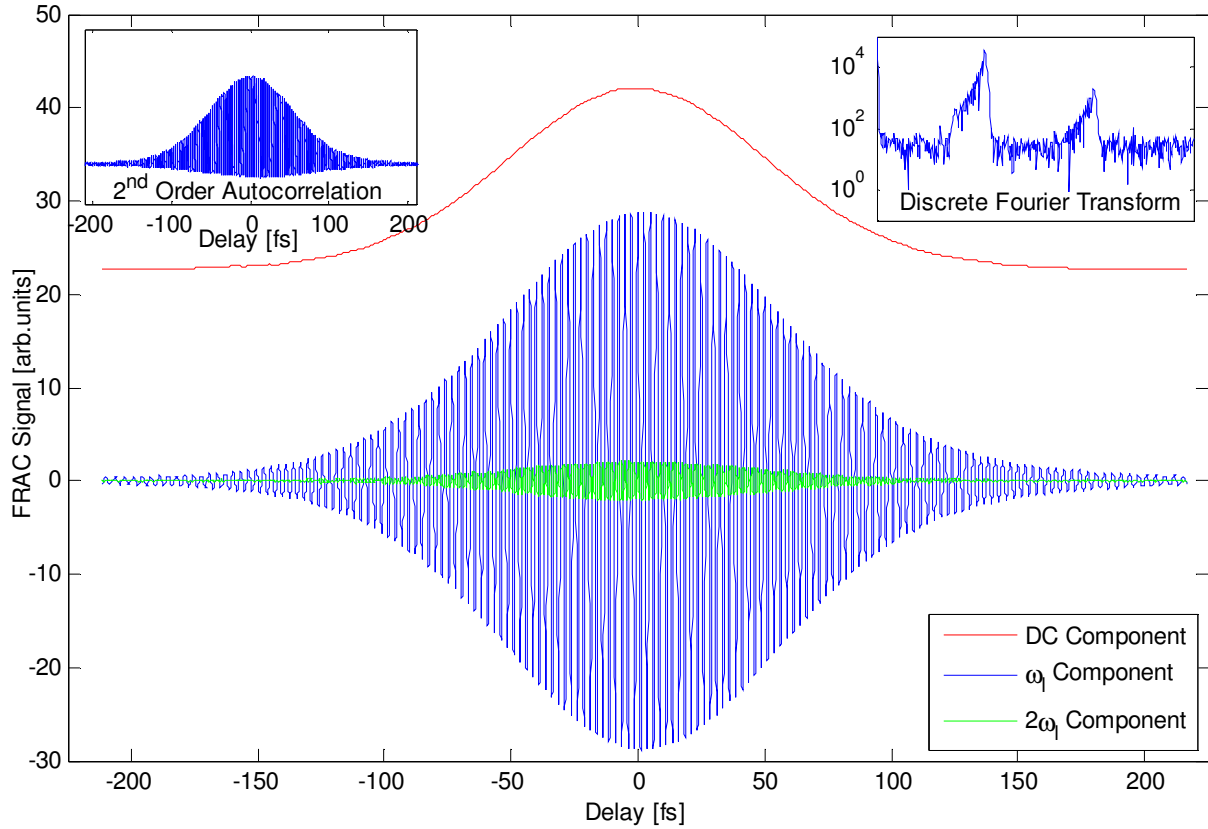
Figure 3-4 ***2nd Order Fringe Resolved Autocorrelation of the Laser Output***
Shows the experimentally measured fringe resolved autocorrelation from the laser output decomposed into the three components of the data. The Period of the ω_l Component (blue) defines the delay scale along the x-axis, and the zero delay is defined by the centroid of the Gaussian fit to the DC component (red). The $2\omega_l$ Component (green) is also clearly present. The Insets show the original signal (left) and the discrete Fourier transform(right) which is presented on a log scale. The DC component is well fitted to a Gaussian with a FWHM of 121fs corresponding to pulse duration of 86fs calculated using equation (2-26).
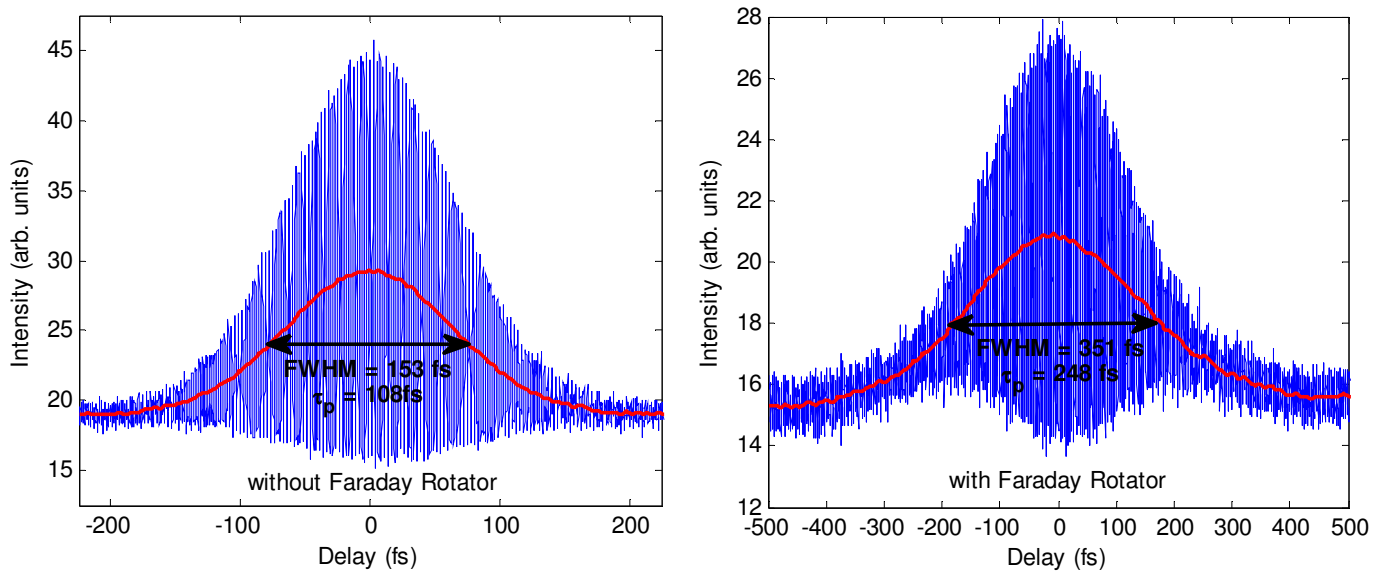
Figure 3-5 Pulse Duration Measurements before the microscope.
Autocorrelation traces of the femtosecond pulses prior to their use in the microscopes. The measurements where taken prior to the Michelson Interferometer. A Faraday rotator was available but significantly broadened the pulse. The pulse duration at this site was 108fs without the Faraday rotator in place compared to 248fs with it in place.

When the pulse duration was first measured it was found to be unacceptably broadened to 248fs, almost three times its original duration. The optical isolator was suspected due to the long distance of material (a few centimetres) required to get the magneto-optic effect. It had been installed to prevent reflections coupling back into the Ti:sapphire laser.

Once removed, a pulse duration of 108fs can be achieved which whilst still broader than the pulses generated is more acceptable. Figure 3-5 clearly illustrates that the Faraday Rotator had chirped the pulse. The autocorrelation measured shows that the fringe details at the edge of the autocorrelation trace have been washed-out and are only visible in a relatively narrow band at the centre. In comparison, the trace without the optical isolator shows a pulse possessing only a slight chirp with good fringe visibility most of the way to the edge on the pulse.

3.2. SCANNING TUNNELLING MICROSCOPE (STM)

3.2.1. INTRODUCTION

The STM used for this work was an Omicron micro H/LH UHV STM. It was operated in air as a bench top STM and was attached to the optical table using a custom designed mounting bracket. The omicron STM use a Viton stack for vibration isolation which is not usually adequate to obtain good quality images. However, when mounted on the optical table it benefits from the vibration isolation that its air legs provide.

The STM was controlled with an Omicron 2.0 STM controller and VME Workstation running Solaris 2.2 and the Omicron Scala software (version 2.3). Details of sample and tip loading procedures and a basic procedure for imaging are provided in Appendix B.2.

3.2.2. TIP PREPARATION

Arguably, the tip is the most important part of the STM [43] and many studies have been done into the best method of manufacturing tips that reliably produce repeatable results. As this STM was being used in air, the tungsten tips the manual suggested would not work because of the oxide layer that forms on them. Bench top STM is often successfully performed with freshly cut Platinum Iridium tips and atomic resolution on very flat surfaces such as HOGP is routinely achieved even in undergraduate experimental labs. Samples with high aspect ratio features such as the crevasse like valleys that can be observed in fast evaporated Au:Mica , large clusters on graphite and the meso-macroscopic structure of the tip can influence the measurement. When the sample has a higher curvature than the tip, the image will contain many replicas of the tip. Furthermore, a slowly tapering tip was required for the laser assisted STM measurements to avoid the problem of it shadowing the illuminated junction. These requirements can be satisfied with

an etched tip and procedures developed for etching and cutting Pt:Ir tips are provided in the following sections.

Cut Tips

Freshly cut Pt:Ir tips can by produced easily, quickly and inexpensively. They are routinely used to achieve atomic resolution and are satisfactory for most bench top applications. In addition, if the cut tip is not of an adequate quality another can quickly be produced.

All that is needed is a source of Pt:Ir wire of the appropriate diameter, a good pair of wire cutters, a pair of long nose pliers and pair of fine tweezers. The wire cutters are very important. The sharp edges must come together exactly on top of each other and there must no play in the hinge. Wire with a diameters of 0.25mm and 0.5mm were used to make tips in this work. The procedure is as follows:

1. Ensure the wire cutters and the end of the Pt:Ir wire are clean by swabbing them with a lint free swab moistened with acetone, followed by IsoPropyl Alcohol (IPA) and finally distilled water.

2. Cut a 1 cm length of Pt:Ir wire, place it in a bath of IPA and agitate it for several minutes.

3. Pick the wire up in the middle, using a pair of fine tweezers. With a pair of clean long nose pliers, firmly grasp one end of the wire, allowing the other to protrude from the tip of the long nose pliers.

4. Using the wire cutters, make an angle of 45° with wire and near the tip of the Pt:Ir wire cut away a small (1 or 2 mm) piece of the wire, to leave a behind sharp tip. As the cut is made being made, the wire cutters should be pulled in the direction of the tip and away from the pliers so that a tip is drawn from the Pt:Ir wire.

The tip can then be installed into the STM scanner using the method described in appendix B.2.

Etched Pt:Ir Tips

The etching process is time consuming but sometimes it is necessary to produce tips with the desired macroscopic shape which come to a sharp apex. PtIr is a noble metal and is usually etched using cyanide based chemicals which are extremely hazardous. PtIr tips can also be electrochemically etched with saturated solutions of $CaCl_2$ and HCl [44, 45]. Many of the reported methods in the literature for the production of sharp Pt:Ir tips require complicated electrical or mechanical arrangements. In this work, the method reported by Lindahl et al [45] was used as it could be implemented using the pre-existing tungsten tip etching apparatus.
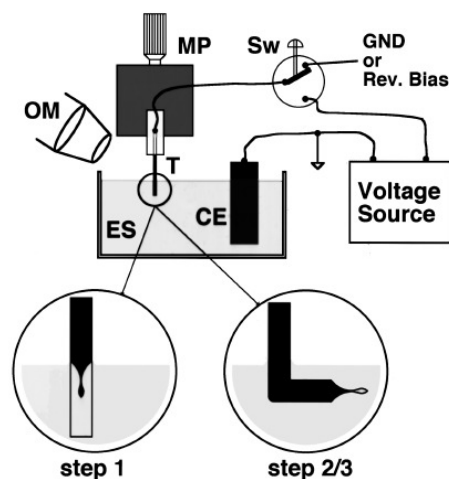
Figure 3-6 **Schematic of Pt:Ir tip etching arrangement**
CE – Carbon Electrode, ES – Electrolyte Solution, MP – Micropositioner, OM – Optical (inspection) microscope, Sw – Switch, T – Tip wire. (Reproduced from [45]).

The tips are formed in three steps. In preparation for the etching process Pt:Ir wire with a diameter of 0.25mm is cut into 20mm sections, and ultrasonically cleaned in acetone and IPA. The electrolyte for each of the steps is prepared as per Table 3-1.

Step 1 – Coarse Etching

A 100mL beaker containing the $CaCl_2/H_2O/HCl$ electrolyte is placed under the micropositioner and the carbon electrode inserted. The clean tip wire is inserted into the micropositioner's wire holder and the height adjusted so that the tip protrudes into the electrolyte by 1.5mm. The 21V AC power is provided by a Variac running from the mains. The current is measured using a multi-meter. Although, in our preparations, the directions of Lindahl et al were closely adhered to, the initial current measured was usually in the range of 1.2 A_{rms}, as opposed to the 100mA_{rms} reported. Despite this, the wire was still etched to the droplet shape shown in the step 1 inset of Figure 3-6 by the time the current had fallen to about 95-105 mA.

The wire with the droplet and the carbon electrode was removed from the electrolyte and rinsed in distilled water.

Step 2 – Polishing

After rinsing, the wire was bent to an angle of 90°, as shown in Figure 3-6, using two pairs of tweezers. It was replaced in the micropositioner and immersed in the H_2SO_4 electrolyte for the polishing stage.

Polishing happens at a higher frequency. A square wave rising to 10V and falling to -0.5V is used between the electrodes. It was generated by a signal generator buffered by a power audio

amplifier operated from a ±15V DC power supply[1]. This process usually takes about 10 minutes or until the tip drops off. Once it has dropped off, a further 10 seconds of etching is used to sharpen it.

Step 3 – Removal of Oxide Layer

In the final step, the oxide layer that is created by the electrochemical polishing in the H2SO4 electrolyte is removed. This is achieved by setting the DC bias to -1.1V for 2 minutes. The current observed usually drops to about $1/20^{th}$ of the initial current within 1 minute and 30 seconds.

The sharp tip is removed from the electrolyte and rinsed with distilled water and loaded into the STM scanner using the method described in Appendix B.2.

Step	Electrolyte	Waveform	Frequency	Stopping Condition
1	$CaCl_2$(sat.)/H_2O/HCl(conc.) (30/20/2 mL)	21VAC Sine wave	50Hz	Current reaches $I_0/10$
2	H_2SO_4/H_2O (45/5 mL)	+10V to -0.5V Square wave	4KHz	Tip Drop Off
3	H_2SO_4/H_2O (45/5 mL)	-1.1V DC	DC	Timed: 2 mins

Table 3-1   Etching Parameters for Pt:Ir Etching

This method consistently produces sharp tips. It was found that the same 50mL of electrolyte, used in step 1, could be used to make up to 10 tips after which the etching took longer and the droplet shape did not form consistently. SEM images of the tips produced show that they are smooth with a single apex of a small diameter (see Figure 3-7).
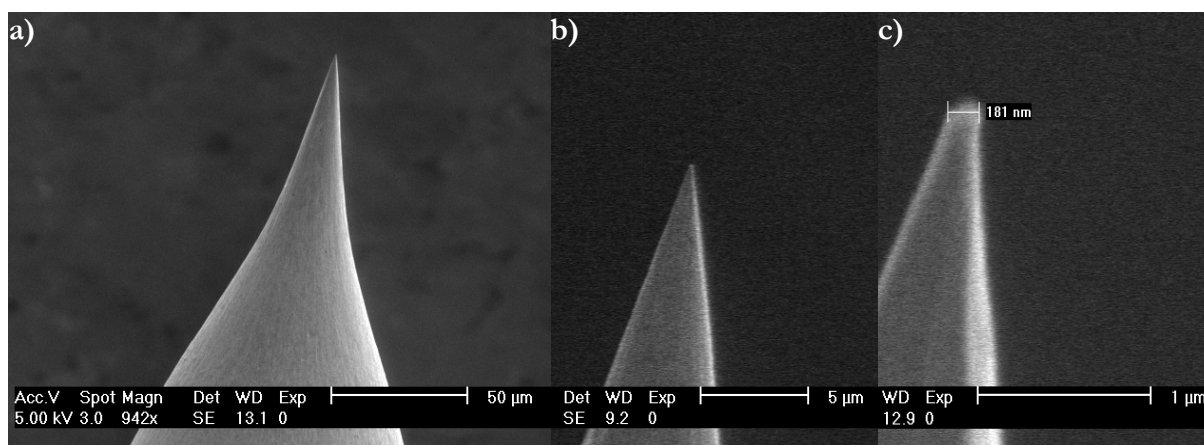
Figure 3-7   SEM Images of an Etch Pt:Ir Tip
Images of a tip prepared by this method are shown for 3 magnifications revealing the tip to have a single apex, with a diameter < 181nm. (Images and SEM microscopy by Mi Yeon Song of the Nanoscale Physics Laboratory at the University of Birmingham)

---

[1] The ac output coupling circuit of the amplifier was bypassed allowing the amplifier to provide a DC voltage offset. Audio power amplifiers usually ac couple the output to prevent damage to the speaker coils that could be caused by a DC offset.

3.3. THE CONFOCAL MICROSCOPE

The confocal microscope used in this work consisted of a Leica TCS SP2 confocal scanner attached to an IRE2 inverted microscope. The microscope has two oil immersion objective lenses with magnifications of 40x and 63x. It is equipped with an argon ion (Ar^+) laser for confocal excitation of fluorophores at 458nm, 476nm, 488nm, 514nm.
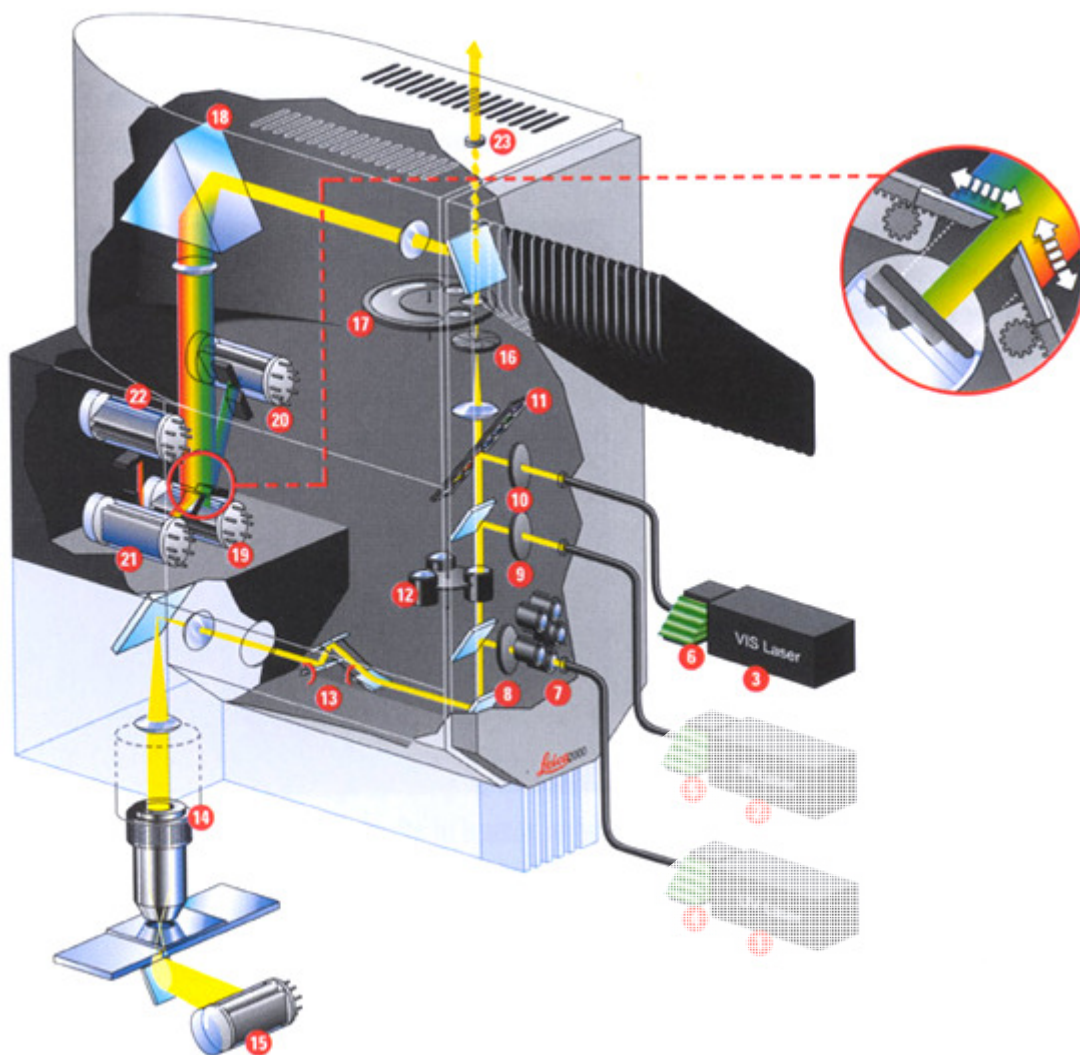
Figure 3-8   Detailed Schematic of the beam path in the Leica TCS SP2 Confocal Scanner.

This is the upright version of the microscope that was used in these experiments. It is essentially the same except that the scanner box is mounted horizontally besides an inverted microscope. The options that are not present in our system have been listed in grey in the legend below.

Ledgend: 1. UV Laser 2. IR Laser 3. Visible range Laser(s) 4. UV AOTF 5. IR EOM 6. Visible range AOTF 7. UV adaptation optics 8. UV excitation pinhole 9. IR excitation pinhole 10. VIS excitation pinhole 11. Primary beam splitter 12. Beam Expander(s) 13. "K"-Scanner with rotator 14. Microscope & objective 15. Transmitted light detector 16. Confocal detection pinhole 17. Analyzer wheel 18. Spectrophotometer prism 19. Photomultiplier channel 1 20. Photomultiplier channel 2 21. Photomultiplier channel 3 22. Photomultiplier channel 4 23. External optical port .

It has three detectors, two of which benefit from a spectrophotometer, and the third can be used for transmission microscopy. When operating in visual widefield mode (not confocal scanning mode), there is a mercury lamp. Using a range of beam splitting excitation and

fluorescence filters, the mercury lamp can be used to quickly search for the desired field before switching to confocal scanning mode. The microscope can be entirely controlled via the attached PC. A detailed description of the controls and procedure used for inflicting damage spots in the DNA of live cells is provided in Appendix B.3.

3.3.1. ALIGNMENT WITH IR LASER

In the DNA damage experiments, the ability to accurately target damage to specific structures within the nucleus is crucially dependant on a good alignment of the IR laser with the Ar+ laser integral to confocal microscope. What follows is a detailed procedure to ensure good alignment between the IR laser beam and the Ar^+ laser beam. The Ar^+ laser is assumed to be in good alignment, although this procedure does reveal that the Ar^+ laser is subject to alignment drift necessitating regular engineer visits.

Principles of laser alignment
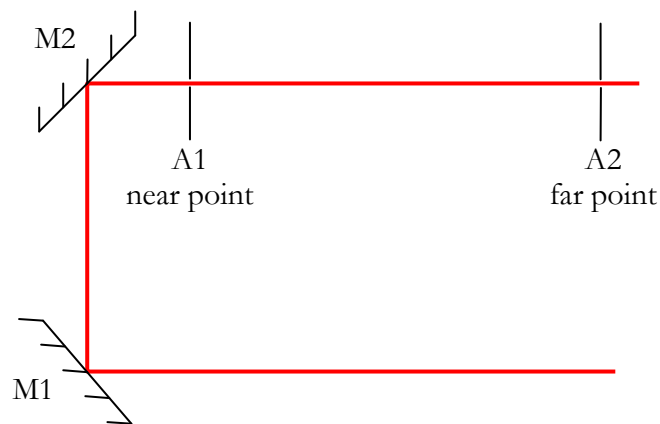
Figure 3-9   **Alignment of beam using two apertures.**

There is a common principle in aligning laser beams. If one wants the beam to travel along a specific line then it must pass through two points on that line. This can be achieved by using two mirrors. Apertures are placed at two points along the line. The line is most accurately defined if the apertures are small and spaced far apart. The first aperture that the laser is to pass through is called the near point and the second, the far point. This is illustrated in Figure 3-9. The laser is incident first on M1 which directs the beam to M2 which launches the beam along the line defined by the two apertures. Ideally you would use one mirror, M1, to define the start point of the line and the second mirror, M2, to define the direction. However, there is cross talk between these controls. Changing either mirror will cause a change in both the direction and position of the line.

Alignment to the line defined by the two apertures is achieved by using the controls for M1 to position the laser spot (reflected through M2) on the centre of the aperture, A1. Then the controls for M2 are used to adjust the direction of the beam so that the laser spot is centred on the aperture A2. It helps to slightly open the aperture of A1, whilst targeting the centre of A2 with mirror M2.

The aperture, A1, is closed down again. The previous adjustment of M2 will have slightly changed the position of the laser spot on A1. The laser spot is repositioned to the centre of A1 again using the mirror, M1. The process is iterated and with each iteration the size of the movement that is required is reduced, until the laser beam is able to pass through the centres of apertures A1 and A2.

The closer together M2 and A1 are positioned and the further apart A1 and A2 are, the fewer the number of iterations required to converge a solution as there is less cross talk between M1 and M2. This is an almost trivially simple alignment, but none the less practical and a useful illustration to define the term near point and far point in the alignment technique that follows.

The last example was conceptually simple and easy to implement, as both of the apertures and the position of the laser on them can be seen. When the same principle is applied to the alignment to the confocal microscope the concepts of the near and far point are more abstract.

Laser Alignment in the Microscope[1]

The Leica TCS2 allows a number of lasers to be used simultaneously for excitation of a broad range of fluorophores. It features a number of dielectric mirrors that reflect and transmit different parts of the spectrum. Figure 3-10a shows that the Ar^+ laser (visible) is transmitted through the IR-mirror whilst the IR is reflected allowing the IR and visible beams to be used simultaneously. In the ideally aligned case the IR beam is collinear with the Ar^+ laser beam path and fully fills the back of the objective, as shown in Figure 3-10a. This creates the smallest excitation volume and the excited florescence is coupled back to the detection pinhole. The near point and far point mirrors, M1 and M2 respectively are shown. The objective itself acts as the near point aperture, whilst the detection pinhole acts as the far point aperture as illustrated in Figure 3-10b and c.

This alignment is complicated as one cannot simply observe the laser beam on these virtual apertures[1]. The only feedback available is the photomultiplier signal of the fluorescence.

---

[1] Following the viva of this work it was noted that the omission of an excitation pinhole was a grave oversight, and the concept of a virtual aperture was erroneous The record of the alignment procedure remains purely as a faithful record of the procedure actually used. Time and availability of equipment did not permit the experiments to be repeated with require improvements.

Furthermore, the separation of the mirrors M1 and M2 is actually less than the separation between M2 and the objective (near point). There is considerable cross talk between the controls of M1 and M2, and consequentially many iterations are required to achieve a good alignment. The mirrors M1 and M2 in Figure 3-10 correspond to the top periscope mirror PS2 in Figure 3-1 and the top IR port turret mirror on the confocal scanner, shown in Figure 3-11.

The large degree of cross-talk between the alignment mirrors requires that the mirrors be quite close to their ideal position at commencement. The turret mirror had very little tilt control. To assist with an initial alignment Leica provided us with an alignment tool, which is temporarily attached to the IR port on the laser scanner as is depicted below in Figure 3-11. The alignment tool consists of two apertures through which the laser beam must pass. This is exactly the same as the alignment depicted in Figure 3-9, and the beam steering is achieved entirely with the upper and lower periscope mirrors. Once the laser beam passes through both the apertures of the alignment tool the IR turret port mirror should be adjusted to its central position. This usually provides a sufficiently good alignment to at least allow light to out of the objective. Once light can be observed from the objective the coarse alignment is complete. Some users may require an IR viewer or indicator card for longer wavelengths.

---

[1] Whilst the detection pinhole is a genuine user controllable aperture it is none the less hidden from view for the purposes of alignment. It is worth noting that the detection pinhole itself can move out of alignment and needs to be corrected from time to time. However, this should only be done by a qualified service engineer.
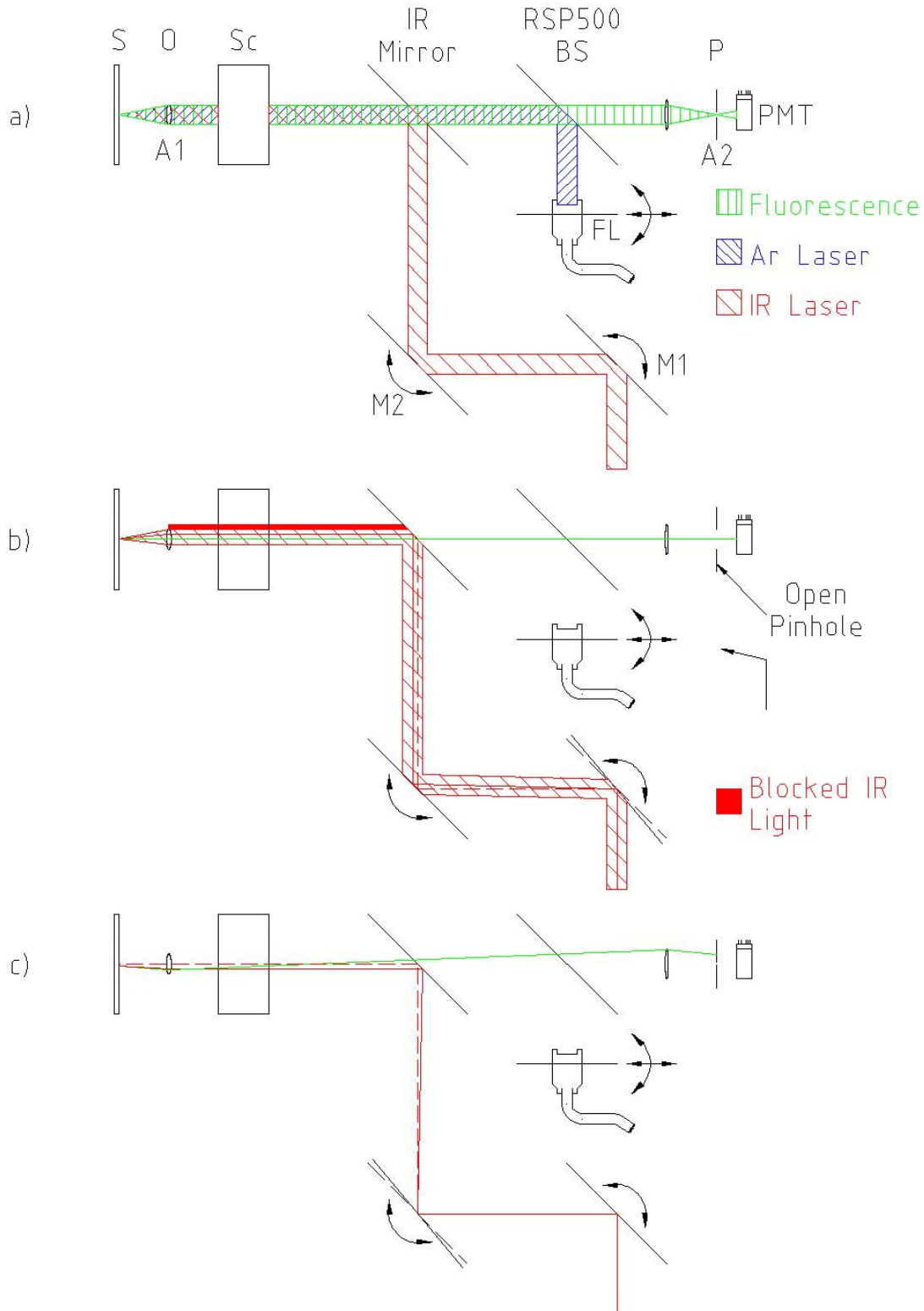
Figure 3-10   Alignment Conditions for the Confocal Microscope
Three alignment conditions are shown for a simplified confocal arrangement, the beam scanner, expander and filters and many of the fixed mirrors have been omitted for clarity. a) Shows ideal alignment illustrating a fully filled objective. b) Shows the effect of near point mirror (M1) alignment with the effective near point being the objective itself. c) Shows the effect of the far point mirror (M2) alignment, with the far point aperture (A2) being the detection pinhole. The Ar Laser was aligned by the engineer using a similar technique, however it is easier because the fibre optic launch coupler (FL) provides independent (ie. No cross talk) tilt and translation controls.
Legend*: S – Sample, O – Objective, Sc – Scanner and Microscope Optics, P – Detection Pinhole, PMT – Photomultiplier Tube, FL – Fibre Optic Launch.*
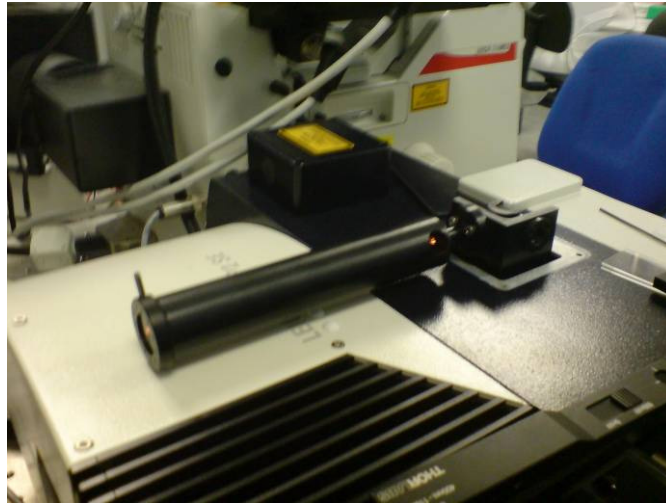
Figure 3-11 **Photo of the Leica Alignment tool.**
The alignment tool assists with the initial coarse alignment..

Fine Alignment

The next stage of alignment requires a fluorescent slide and the IR laser to be producing pulses. Occasionally during the alignment, light is back-reflected from the microscope down the laser path, and into the laser itself. This can destabilise the lasing and cause the laser to come out of mode lock and operate in continuous wave mode. If the signal suddenly disappears during the alignment this should be checked.

A fresh fluorescent slide should be prepared from a solution of fluorescein each time. The slide is prepared by dropping 25-50µl of fluorescein solution onto a slide and covering with a cover slip. Excess solution should be dabbed away with a tissue, taking care not to suck all the solution from under the cover slip by capillary action. The edges of the cover slip may be sealed with nail varnish to prevent evaporation. Fluorescein in solution was used as, once dried, it becomes more susceptible to photobleaching. Whilst in liquid form, the volume subject to excitation is continually replenished by the surrounding fluorescein. The microscope software should be configured for 2-photon imaging (see section "Configuration for Multi-Photon Imaging" in Appendix B.3).

In wide field, it is impossible to assess the z-position of the focal plane when the sample has little or no lateral spatial variation. The focal plane will need to be located in confocal mode. Set the Ar^+ laser at about 25% percent, and the PMT voltage at around 100V. Adjust the z-position until the fluorescein is located. Adjust the focal plane to the approximate centre of the fluorescein.

Deactivate the Ar^+ Laser. Open the detection pinhole to the maximum extent and increase the PMT voltage to about 800V. Open the shutter for the femtosecond pulses. If the coarse alignment was good enough there should be a signal detected. Otherwise, try increasing

the PMT voltage and check the laser is pulsing. When a signal is acquired, maximise it using the periscope mirrors (M1 in Figure 3-10). The Histogram window is a useful tool for assessing this. If the PMT saturates reduce the voltage. Once the signal has been maximised, reduce the pinhole until the signal begins to diminish and then optimise the signal again using the turret mirror on the IR port (Figure 3-12) of the confocal laser scanner. Once this has been optimised, open the pinhole a little and optimise the signal again using the periscope mirrors, iterating until the pinhole size can be reduced to at least 1.5 airy without loss of detected signal.

The analogy to the near-point and far-point aperture is explained, by considering the objective itself as being the near point and the pin hole as being the far point. When the pinhole is open, the signal is dependant on how much light gets through the objective to the fluorescent dye. When the pinhole is closed down, the signal is dependant on how much light gets through the centre of the pinhole. When the pinhole can be closed down to approximately one airy the IR laser is in optimum alignment.
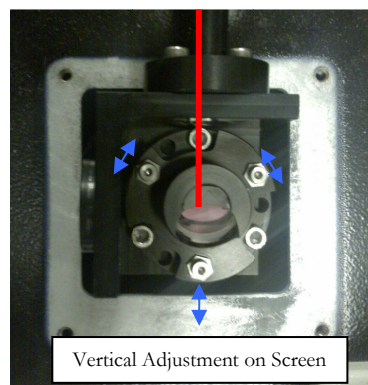
Figure 3-12   IR Input Turret
Photograph of the IR Input Laser turret on the confocal scanner. The three screw controls indicated adjust the angle of the laser. Adjusting each of the controls will displace the acquired image in the direction indicated by the blue arrows.

Regretfully, the Ar^+ laser which is used to image the cells is not always perfectly aligned and whilst the procedure above will, if executed carefully, produce optimum results, unless the IR laser is co-linear with the Ar^+ laser the targeting will be inaccurate.

The final stage of alignment uses 1 micron fluorescent beads, prepared according to the procedure in section 3.4.2. Both lasers, the Ar^+ and the IR laser, are used simultaneously. The microscope is put into continuous image mode and the Ar^+ laser is switched on to 1% power. Adjust the PMT voltage avoiding saturating the image and then open the IR shutter. The alignment should be very close and only a slight adjustment of the IR input port turret should be required to bring the IR and the Ar^+ laser into perfect alignment. If they are not, repeat the power alignment procedure again. If this does not improve the situation then the Ar^+ laser is grossly out of alignment. Under the warranty only a Leica engineer may adjust this.

3.3.2.   MEASUREMENT OF LASER POWER THROUGH THE OBJECTIVE

The confocal scanner does not transmit all the light that arrives at the IR laser input port through the scanner to the objective. The transmittance of the laser scanner depends on the objective used and the beam expander. Following alignment, a measurement of the transmittance was made by measuring the light incident on the IR port of the confocal scanner and the light that emerged from the microscope objective.

Average power measurements were performed using a Thor Labs PM120 optical power meter equipped with a S130 photodiode in a slim housing which allowed it to be easily inserted between the objective and the sample stage when the objective was in the withdrawn position. The results of the measurements for each combination of beam expander and microscope objective are tabulated in Table 3-2.

Average Power Incident on the IR Input Port: 75.4 mW

Objective	Average Power Measured Through Objective using:		
	Beam Expander 1	**Beam Expander 3**	**Beam Expander 6**
40x	7.67 mW	5.56 mW	697μW
63x	6.37mW	4.56mW	551μW

Objective	Transmittance of the objective and BE Combination		
	Beam Expander 1	**Beam Expander 3**	**Beam Expander 6**
40x	10.17%	7.38%	0.93%
63x	8.44%	6.05%	0.73%

Table 3-2   Transmittance of the confocal scanner and microscope objectives

3.3.3.   MEASUREMENT OF POINT SPREAD FUNCTION

Although it is possible to estimate the point spread function (PSF) from the wavelength of the light and the numerical aperture of the lens using equations (2-29) and (2-30), knowledge of the actual performance of a particular instrument can only be achieved by performing a measurement of the PSF. A measurement of the actual PSF is also required to perform deconvolution of the images.

Measurements of the PSF were performed by imaging sub-resolution fluorescent beads. Fluorescent beads are small beads of gel containing high concentrations of fluorescein. They are commercially available in a range of sizes to serve as calibration samples. The measured image from a microscope is the convolution of the object being imaged and the instrument's PSF. If the object is much smaller than the PSF, then wherever an object is, a copy of the PSF will be superimposed. It would seem from this that you would want the smallest possible point sources of fluorescence and even quantum dots have been used for this purpose in other work. However, small sources also produce much smaller signals as they have less fluorescent molecules and require very low noise high sensitivity detectors. If the size and shape of the beads is accurately known, then deconvolution can be used to remove the beads themselves from the image leaving

just the point spread function and allowing larger beads to be used in practical measurements. We had two sizes of beads available, 1μm and 200nm. The 1μm beads were useful for alignment of the IR laser to the confocal microscope's Ar$^+$ laser, but the smaller size of the 200nm beads provided the best balance of small size and sufficient fluorescence for a measurement.

Even with their bright fluorescence, a number of beads had to be averaged to obtain a sufficient signal for a measurement of the PSF. A field of view containing many beads was imaged. Occasionally beads would aggregate together and although the beads were too small to be resolves these aggregations of the fluorescent beads could be distinguished by their intensity.

When acquiring images for the measurement of the 3D PSF, the choice of voxel size is important and depends on what the measured PSF will be used for. If the PSF is to be used for deconvolution, the images for the 3D PSF measurement should be captured at the same resolution and scanner configuration as the images that the measured PSF will be used to deconvolve. If the result of setting these parameters is that the PSF is smaller than 1 voxel then deconvolution will not yield any improvement in the image. If the PSF is to be used to measure the shape and size of the 3D PSF then smaller voxels will produce a more accurate image. However, if the bead is imaged at too high a resolution then photobleaching and thermal damage will occur more rapidly as the laser is spending more time on the bead and it will be difficult to get a large number of beads into the field of view.

The beads were mostly in the same plane and, once imaged, the data was loaded in Matlab. The images were strongly smoothed to facilitate location of the beads. Sites containing a single bead were selected manually, using the mouse, to get approximate positions. The centres of the beads were located in 3D using the function that was developed to locate and track PCNA foci in chapter 4. The smoothed data was only used to locate the centre of the beads. The PSF measurement averaged the original data from all beads. 15x15x15 voxel cubes, each centred on the detected bead centres, were extracted from the image. The extracted regions were averaged to produce a 3D image of the 200nm bead convolved with the point spread function.

To obtain the microscope's PSF, the averaged image of the beads was deconvolved with the calculated object of a 200nm bead of uniform fluorescence. The deconvolution was performed in Matlab using the `deconvlucy()` command which implements the Lucy-Richardson method. This method is less susceptible to degrading the image in the presence of Poisson noise.

Measurement of the 1-Photon PSF at 488nm

The 488nm laser is predominately used for imaging by exciting fluorescent molecules. The fluorescent beads could be imaged at very high zoom, facilitating accurate high resolution

measurement of the confocal microscope's PSF. Measurements were collected using the 40x objective which has a numerical aperture of 1.25.

Figure 3-13 shows the central planes through a 200nm bead and illustrates many of the features of the theoretical PSF function even without deconvolving the bead. The elongation of the PSF in the axial direction and side lobes in the xz and yz planes are clearly shown. However, the PSF exhibits a clear asymmetry, which can be attributed to refractive index mismatch. These images were captured using beam expander 6, which over fills the back pupil of the microscope objective, maximising the effective NA of the microscope objective. This image was deconvolved with calculated 200nm fluorescent beads and radial and axial profiles were measured through the centre of the PSF. These profiles are shown in Figure 3-14. The profiles fit the theoretical shape very well but are significantly larger than theoretically predicted values.
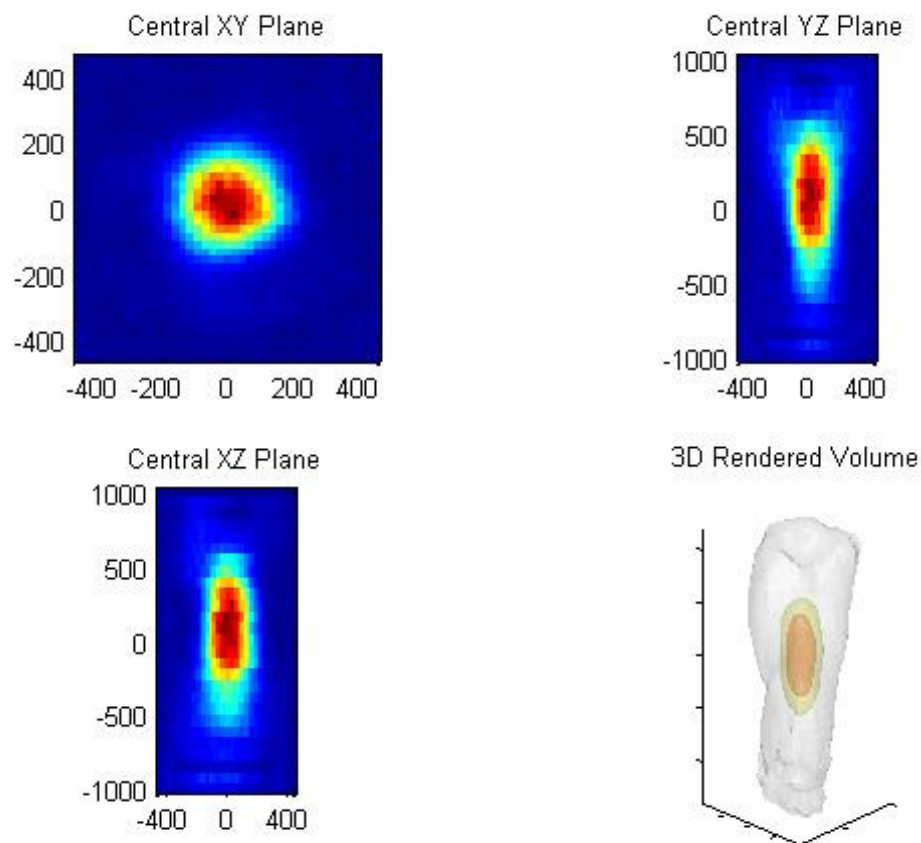
Figure 3-13   1-Photon 488nm confocal PSF with a over-filed objective.
The central planes through the measured PSF following deconvolution are shown, and 3D isosurfaces of intensity illustrate the 3d distribution of the PSF function. The YZ plane and XZ plane images exhibit ringing at the edges of the images which is caused by the discrete Fourier transform used by the Lucy-Richardson deconvolution.
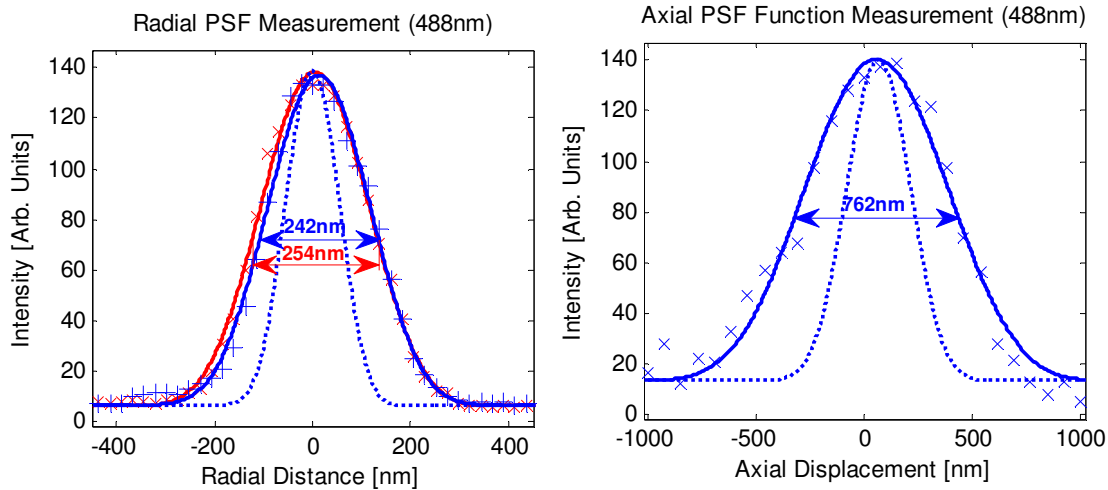
Figure 3-14   Profiles through the deconvolved 3D PSF in Figure 3-14.
The Radial PSF Measurement shows profiles in the x (red) and y (blue) direction through the central point, the axial PSF measurement is a profile in the z-direction through the central point. The dotted line represents the theoretical confocal PSF for this objective excited with 488nm light.

As was explained in section 2.2.2, the theoretical point spread functions are for infinitely small excitation and detection pinholes. The detection pinhole was set to 1 Airy, allowing the light from the 1st Airy disk pass through to the PMT detector. This omits most of the out of focus fluorescence, allowing 70% of the in-focus fluorescence to pass into the PMT. The non-zero size of the pinhole enlarges the actual PSF. A better estimate of the PSF could have been obtained considering a finite sized detector as was done in [28].

The measurements were repeated using beam expander 1 (BE1), which was used for IR laser beam and so is important for alignment measurements. BE1 significantly under fills the objective of the microscope and results in an enlarged PSF both radially and axially. The length and radius, shown in Figure 3-16 of the PSF are both nearly twice that of the PSF measured using BE6 which over fills the objective. The image in Figure 3-15 also shows the PSF is skewing indicating a misalignment of the laser.
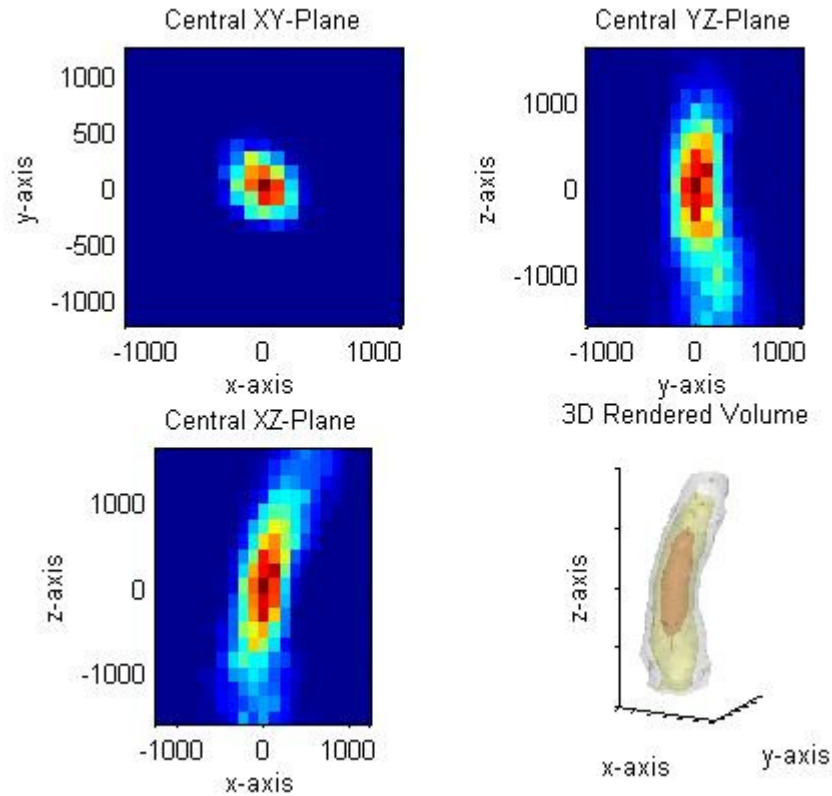
Figure 3-15 1-Photon 488nm confocal PSF with an under-filled objective.
The central planes through the measured PSF following deconvolution are shown, and 3D isosurfaces of intensity illustrate the 3D distribution of the PSF function. The YZ plane and XZ plane images exhibit ringing at the edges of the images which is caused by the discrete Fourier transform used by the Lucy-Richardson deconvolution.
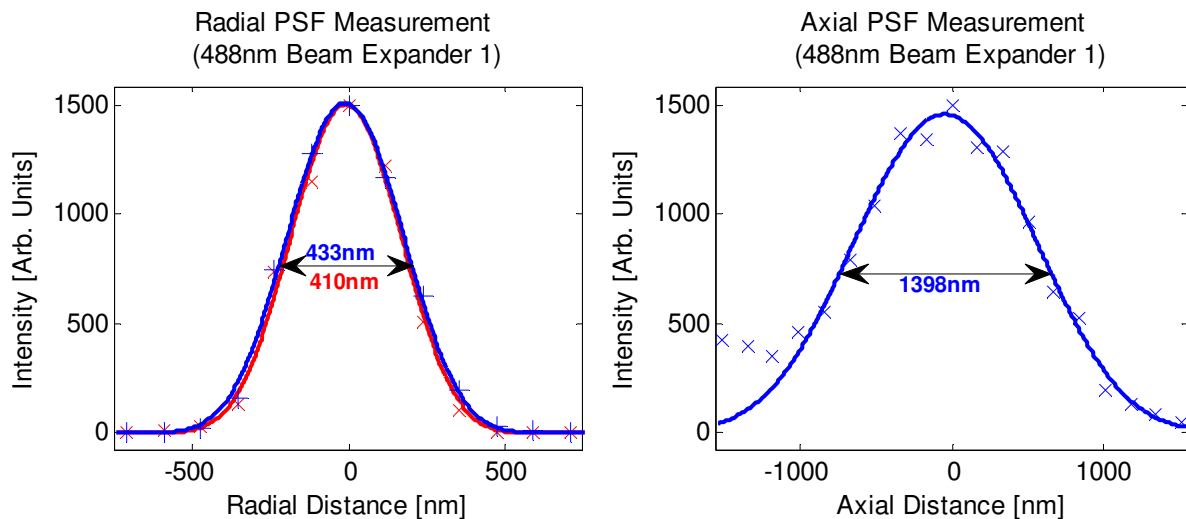
Figure 3-16   Profiles through the deconvolved 3D PSF using the 488nm line through Beam Expander 1 and the 40X Objective.

Measurement of the 2-Photon PSF

The two-photon PSF was measured following alignment of the IR laser to the confocal microscope's Ar$^+$ laser. Figure 3-17 shows the field from which the single 200nm beads were identified. Measurements have to be performed quickly as the 200nm beads are considerably

more susceptible to IR damage than the 1μm bead. Usually only one or two attempts to capture a field could be made before the beads started to explode. Similarly, if too large a zoom was used, the laser scanner would raster the beam more slowly and the beads exploded under the thermal stress induced by the relatively high power of the IR beam.

From Figure 3-17 the single 200nm beads can be seen and have been circled to identify them. The other green spots are much more intense and indicate that the beads at those locations have aggregated. These foci were extracted and averaged together, and the results   shown in Figure 3-18.
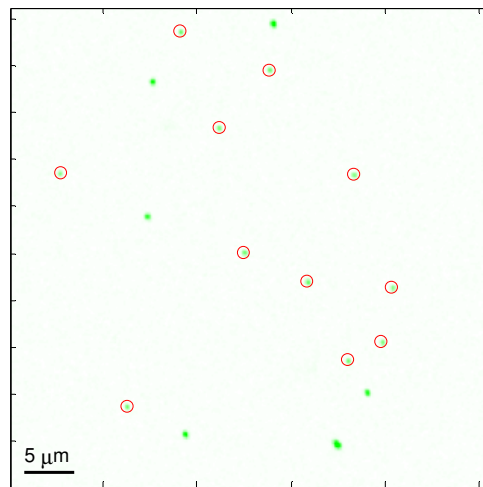
Figure 3-17   Section through the centre of 200nm Fluorescein beads imaged using 2 photon NIR Imaging.
The image shows the central section through the bead used for the measurement of the PSF. The image is the convolution of the beads and the PSF. The single isolated beads have been selected, and are indicated with the red circles. The pixel size is 94.1nm x 94.1nm, sections were taken at 168.7nm intervals in the z-direction.

Z-Series of XY planes

X-Series of YZ planes

Y-Series of XZ planes
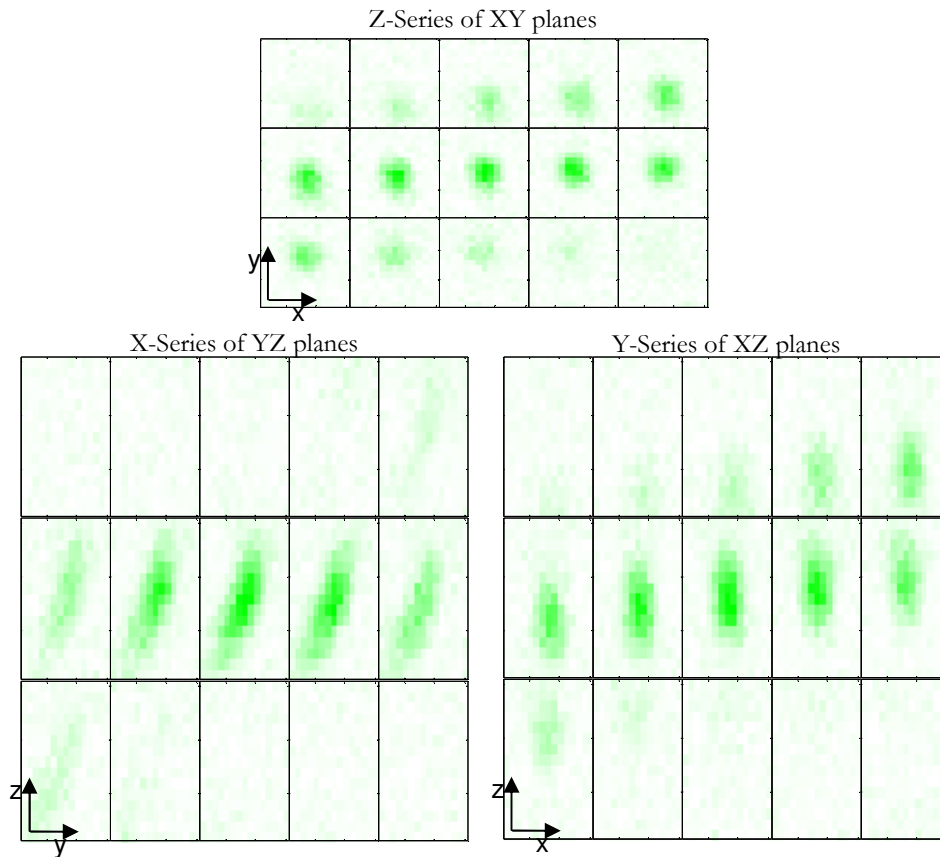
Figure 3-18   *Z, X and Y Sections through the centre of the averaged 200nm Fluorescein bead imaged using 2-photon NIR imaging.*
The Z-Series images show XY-Planes as the z-coordinate increases. The Z-Coordinate increases from left to right and top to bottom. The same system is used in the X and Y series images of the same data. The X-Series images show the presence of a slight skew in the PSF. These images have not yet been deconvolved and are the convolution of the 200nm bead and the microscope's 2 photon PSF.

Figure 3-18 presents volume data for the beads convolved with the PSF as slices in each of the orthogonal directions. It is clear from this X-Series data, even without deconvolving the 200nm bead to the recover the microscope's 2-photon PSF, that there was a serious misalignment similar to the misalignment observed in the 1-photon PSF measured in Figure 3-15.

This volume data was deconvolved with a calculated 200nm sphere, taking into account that the dimensions of the voxel in the z direction was greater than its dimensions in the x and y directions. The deconvolved 3 dimension point spread function is shown in Figure 3-19. The PSF has shrunk as it is no longer convolved with the 200nm beads used to measure it.

Z-Series of XY planes

X-Series of YZ planes

Y-Series of XZ planes
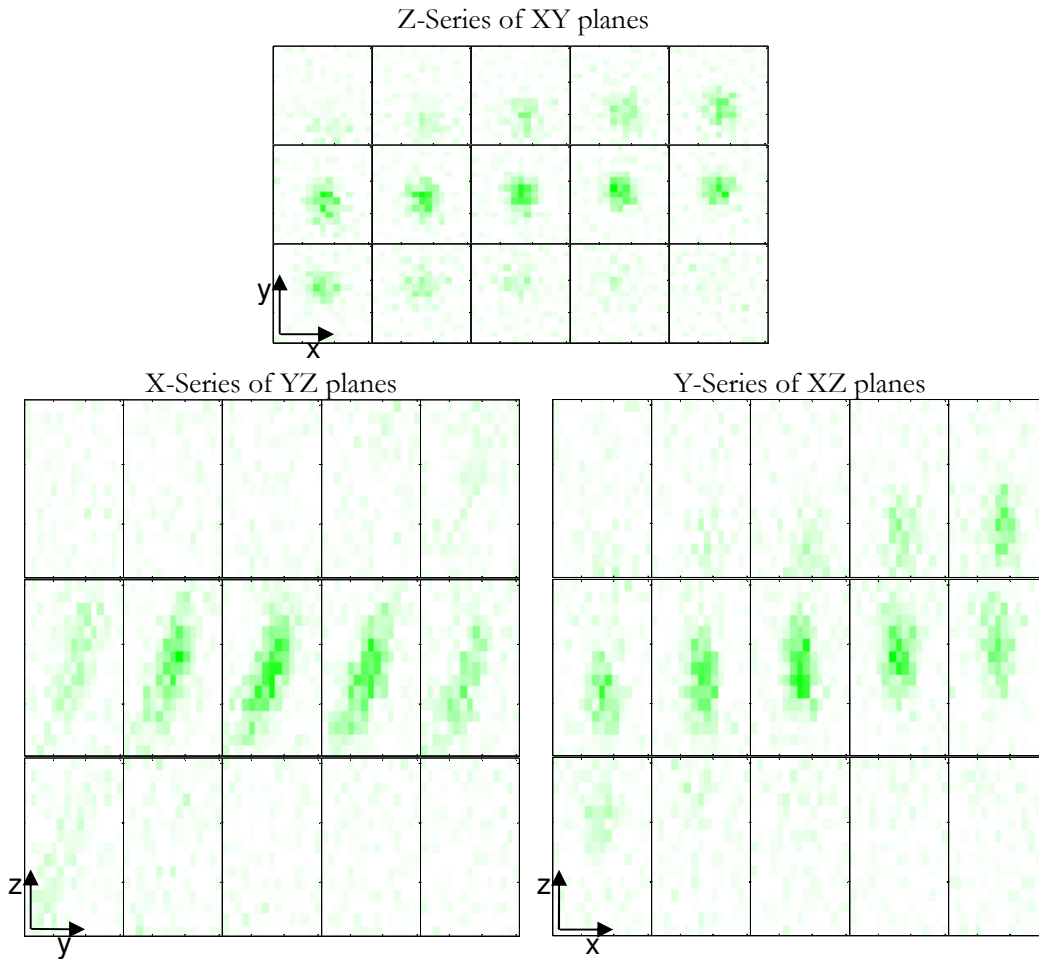
Figure 3-19   *Z, X and Y Sections of the 2-Photon Point Spread Function.*
The point spread is recovered from the averaged image of the 200nm bead by deconvolution with the model 200nm bead.

2 Photon Radial PSF Measurement

2 Photon Axial PSF Measurement
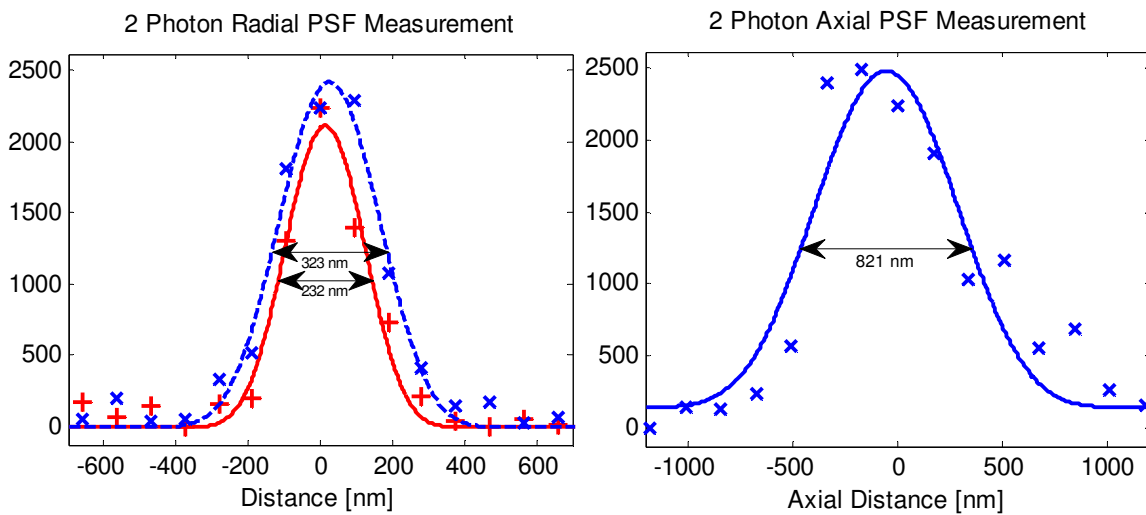
Figure 3-20   *Measured Profiles of the 2-Photon Axial and Radial PSF*
The point spread is recovered from the averaged image of the 200nm bead by deconvolution with the model 200nm bead.

Profiles were extracted through the central voxel in the x, y and z directions. The x and y profiles were fitted to curves with the same form as the square of the radial PSF given by

equation (2-29), and the z-profile was fitted to a curve of the same form as the square of the axial PSF given in equation (2-30).

From the measurement of the radial PSF it can be seen that its full width at half maxima is between 262 and 323nm. The theoretically predicted FWHM of the radial 2-photon PSF is 2.32 optical units, which corresponds to 200nm for an objective with a NA of 1.4 and operating at a wavelength of 758nm.

The axial 2-photon PSF measurement did not fit the form of theoretical function so well, but the "fitted" size of the axial point spread function is actually slightly less than theoretically predicted of 1.02 microns. In addition it exhibited a noticeable skew and the measured FWHM was 822nm.

The slightly larger radial point spread function indicates that back pupil of the object may not have been filled and a correspondingly lower effective numerical aperture was observed. It seems likely that the chromatic aberration caused the components of the light to be dispersed axially, leading to the greatly increased axial PSF which also explains the considerably broadened pulse duration measured at the focus in the following section.

3.3.4. MEASUREMENT OF PULSE DURATION AT THE FOCUS

It is essential to know both the pulse duration entering the confocal microscope's scanner and the pulse duration at the focus of the microscope. In multi-photon microscopy, pulsed lasers are used to increase the instantaneous peak intensity. An accurate measurement of the pulse duration is all the more important when considering that the detected signal is related to the Nth power of the instantaneous intensity, where N is the number of photons involved in the absorption event. If, in 2-photon imaging, the pulse duration is doubled by the microscope the detected signal would be reduced in intensity by a factor of 4 and this effect is heightened in the 3-photon DNA damaging experiments where the amount of damage would be reduced by a factor of 8.

Measurement of pulse duration at the focus is not trivial. It is clearly not possible to install an autocorrelator at the focus so it was decided to use the microscope itself as the autocorrelator. The delay stage that was built for the SPPX-STM experiments was used to split the incoming pulse into two replica pulses prior to the laser input port of the confocal scanner. At the focus, the light is absorbed by two-photon absorption in a fluorophore and the fluorescence is detected by the microscope. The SPPX's Michelson interferometer possesses a motorised delay stage for coarse adjustment and a piezo translation stage to vary the delay to obtain a fringe resolved autocorrelation trace. In this way all the necessary elements are available

to perform a 2nd order fringe resolved autocorrelation. The remaining problems are simply those of implementation in the face of the practical constraints of the microscope.
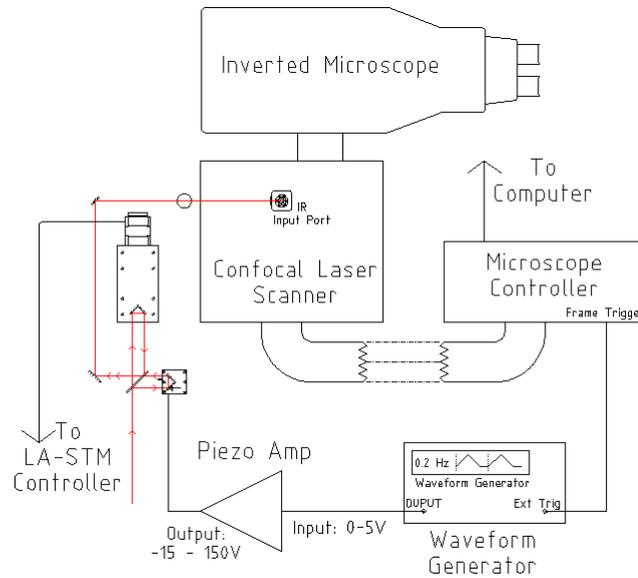
Figure 3-21   Schematic of the Configuration for in-situ Fringe Resolved Autocorrelation.
Schematic showing show the Michelson delay stage operated in conjunction with the laser scanning confocal microscope to perform a fringe resolved auto correlation measurement at the focus of the microscope.

The first of these problems is the limited information available as to the internal design of the both the confocal scanner unit and the microscope. Some of this is due to the manufacturer's (Leica) desire to protect their proprietary design. For instance, little information was made available about the precise design of the beam scanner or the extent to which it limits the beam diameter close to its scan limits. However in many cases the Leica engineers did not have the details required themselves. For example the phase-shifts and reflectivity of the optics in the infra-red region of the spectrum were not available as the microscope was not designed with any regard of the phase shifts for the IR spectrum. This meant that to a great extent the whole confocal microscope system had to be treated as a black box system.

The black box philosophy is perpetuated by Leica's data acquisition system. The simplest implementation of the autocorrelator would be to park the beam and record the signal from the detector PMT as function of time, whilst simultaneously scanning the piezo stage on one arm of the Michelson interferometer. This was not possible as all data acquisition and microscope control was handled by Leica's proprietary control software. The Leica scanner electronics do provide some limited trigger signals, primarily designed to assist engineers with diagnostics. These are delivered through a 15-pin D-connector on the rear of the scanner control electronics. They are undocumented in the user manual and pinouts have been provided below in Table 3-3. The trigger ports provide 4 inputs to control advanced time lapse features in the Leica Control Software (LCS) and 4 outputs, 3 of which have dedicated uses for microscope diagnostics and

one of which is user controlled through the advance time lapse module. To protect the microscope electronics from damage by external signals the trigger signals, in and out, are electrically isolated from scanner electronics by electronic opto-isolators[1]

Signal Name	Description	Pin
+5V	Supply 5V between +5v and 0V pins to power the electronic opto-isolators for	11
0V	the trigger signals.	8
Trigger Out 1	Line Sync – A short TTL pulse at the beginning of every line	7
Trigger Out 2	Frame Begin (blanked) – On for the duration of each frame	14
Trigger Out 3	Frame Begin (un-blanked) – On for the duration of the data acquisition.	6
Trigger Out 4	User Defined – Used for Infrared Laser shutter control in DNA damage experiments.	15
Trigger In 1	User Defined Input	4
Trigger In 2	User Defined Input	12
Trigger In 3	User Defined Input	5
Trigger In 4	User Defined Input	13

Table 3-3   ***Signals of the "Triggers" port of the Leica Scanner Control electronics.***
The function of the trigger outputs appears to vary between different revisions of the Leica TCS SP2 hardware and LCS software. These were the values at the time of these experiments, but they should be checked on a new microscope or after and update of the microscope firmware or software.

Although control of the microscope is entirely through the LCS software, it does provide for a number of modes of data acquisition including xyz for volume imaging, xyt and xyzt for time lapse imaging of 2D sections and 3D volumes and most usefully in this case an xt mode, which allows a signal scan line to be repeatedly sampled at a regular time intervals. Recall that the simplest solution identified was to park the beam. However, as long as the field of view has no spatial variation there is no need to park the beam. Indeed if the beam is being scanned, this may further mitigate the effects of photobleaching. The "Frame Begin" signal allows the data acquisition to be synchronised with the motion of the piezo stage. As delay between the pulses is varied during the scan, the resulting interference between the pulses causes fringes in the confocal image. The piezo is fed a triangle wave from a signal generator which is amplified to provide the high voltages required for the piezo stage. The full period of a triangle wave has a ramp up and a ramp down. The period was chosen to be a little over twice the frame time. Whenever a frame starts the 'frame begin' signal triggers the signal generator to output 1 cycle of a triangle wave. When the frame finishes the LCS software waits a preset period of time to ensure that the piezo stage has returned to its start position before commencing another frame. In early experiments it was shown that the piezo could not simply fly-back to the start as this caused mechanical vibrations in the next cycle. Other than the synchronisation trigger signal, all timings have to specified and set manually. A typical timing scheme is shown below in Figure 3-22.

---

[1] Electronic opto-isolators use light-emitting diodes and photodiodes to transmit and receive signal through a transparent insulating layer to protect the electronics on either side from each other, and should be distinguished from an opto-isolator that only allow light to pass in one direction using a faraday rotator and polarising optics.
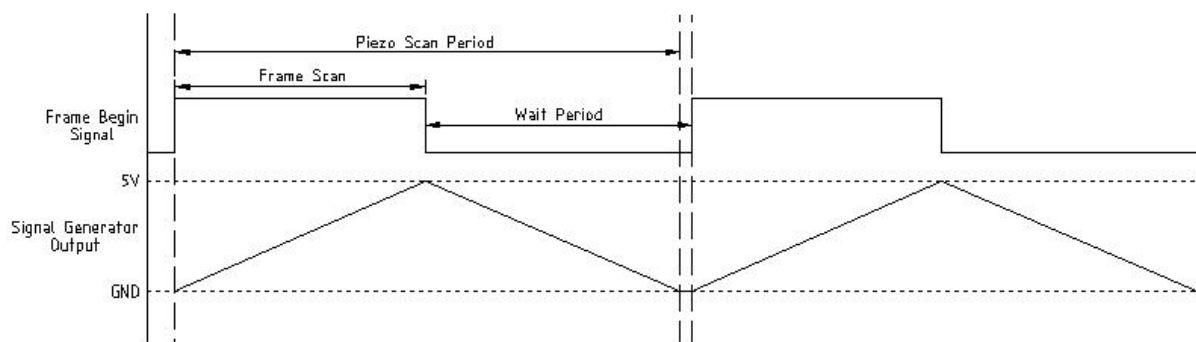
Figure 3-22   Signal Timings for in-situ FRAC measurements
Signal generated for control of the piezo translation stage in relation to the trigger signal from the Leica scanner control electronics. The "Frame Begin" signal starts a triangle wave cycle to be output. Adjustment of the upper and lower voltage limits of the triangle wave adjusts the scan range of the autocorrelation. The period of the piezo-scan must be manually adjusted to more than twice the frame scan.

Although the adjustment of the scan range is possible by changing the peak to peak voltage of the triangle wave, the stage is limited to a maximum movement of 100μm and so a maximum delay variation of 667fs. Coarse adjustment of the delay is achieved with the motorised stage. Experimentally this is most easily achieved by allowing the microscope to continuously free scan and slowly scanning the motorised stage through the 0 delay point. The signal is significantly increased at zero delay due to the 2-photon process.

There is a great deal of flexibility in the definition of the frame data acquisition parameters. There is independent control of the line frequency, the number of samples in a line, the number of lines acquired, the delay between acquiring lines and whether lines are acquired in a bi-directional or uni-directional[1] manner. These factors all affect the time it take to complete a line or frame and consequentially if the frame time changes as a result of changing on of these frame parameters then the piezo scan rate must be manually adjusted.

In choosing appropriate parameters, a number of factors must be taken into account and balanced. Firstly, the total fluorescence signal is quite small and so the dwell per pixel should be long enough to gather enough photons to overcome the background noise. When the data is processed, all the pixels in the x scan line are averaged to obtain a mean intensity. The mean intensity for each line becomes a data point on the autocorrelation trace. The delay between the lines should be minimal so bi-directional scanning is used. The line frequency used was 1400Hz, which was the fastest data acquisition rate the microscope could handle. An example is shown in Figure 3-23. Sufficient lines are required to resolve the fringes in the autocorrelation whilst capturing the entire delay scan range. In this example there are 1200 lines, and each line has 128 samples in it. Using the same techniques described section 0 an autocorrelation trace with a

---

[1] In unidirectional scanning data is acquired left to right and then the beam flies back and repeats the process, in bi-directions scanning the data is acquired first left to right then the next line is acquired in the right to left.

calibrated delay is shown in Figure 3-24. Obviously the signal is a lot noisier than that from the commercial autocorrelator.
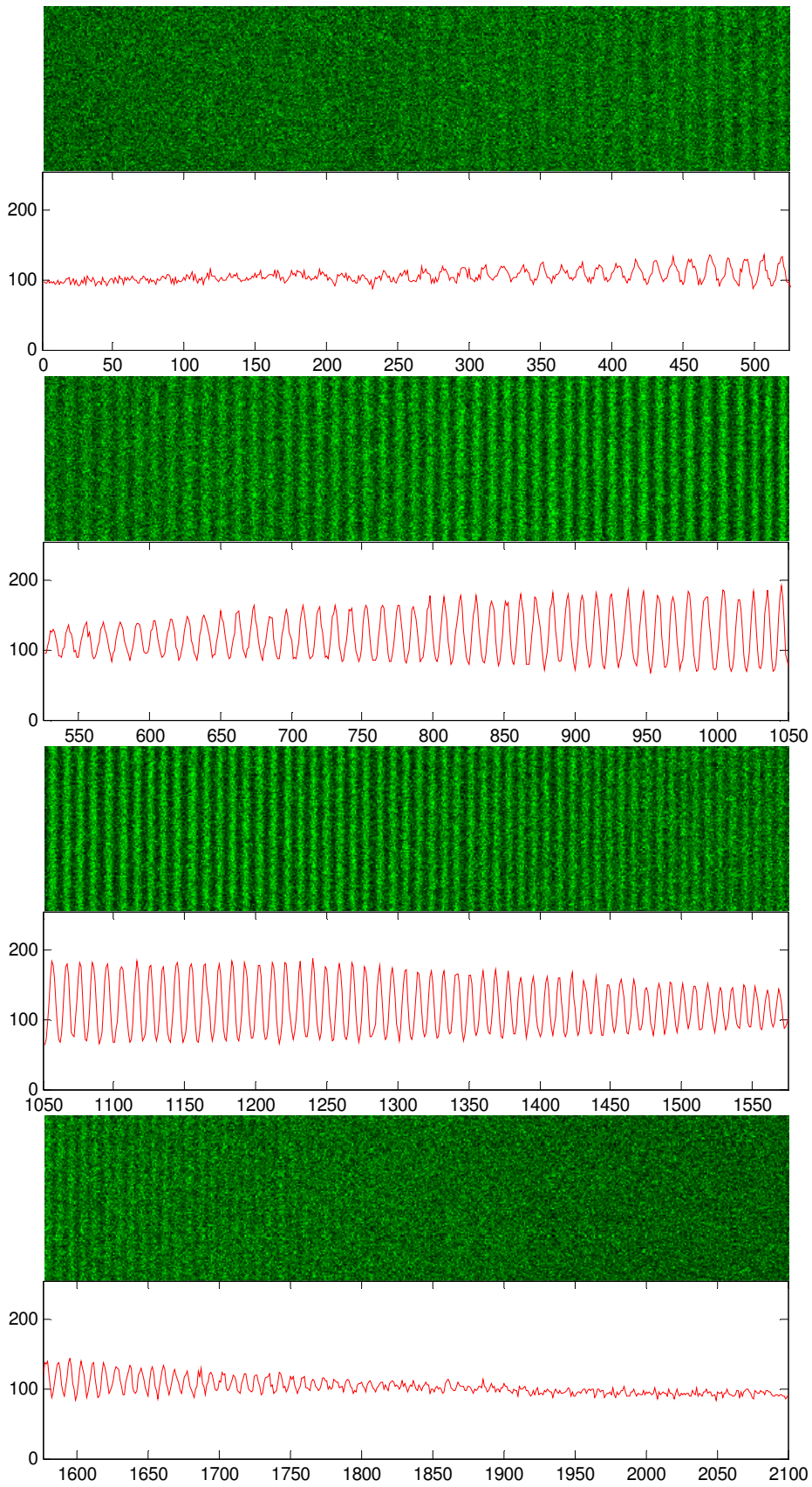
Figure 3-23   In-situ Fringe Resolved Autocorrelation
Raw data from a FRAC measurement, consisting of 2100 lines split into four sections for ease of display. Average intensity for the column is plotted in the graph beneath each section of the image.

Although the DC component does not look like a Gaussian, if it is fitted to one, it shows good fit but reveals that only a narrow section of the centre of the Gaussian has been sampled. By extrapolating the Gaussian fit one can obtain estimate of the FWHM of the autocorrelation and hence the pulse duration.
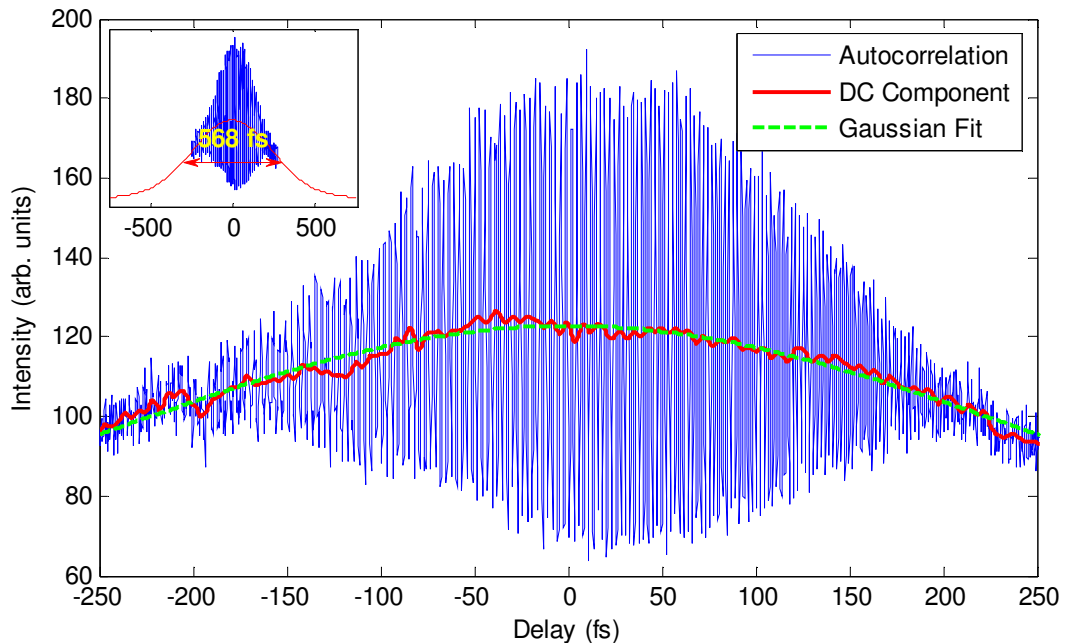
Figure 3-24   FRAC Trace of Pulses at the Focus of the Confocal Microscope
A fringe resolved autocorrelation trace with the DC component shown in red with a Gaussian fit to the DC component shown in green. The inset shows the extrapolation of the Gaussian fit revealing that only small central section of the autocorrelation pulse was captured. The fitted Gaussian has a FWHM of 568±34fs corresponding to a pulse duration of 401±25fs.

The pulse duration is 401±25fs, which represents a hugely broadened pulse. The pulse is also heavily chirped as evidenced by the relatively narrow region of fringe visibility and the knowledge that this pulse has a bandwidth-limited duration of 87fs. This level of broadening was unexpected. The main source of broadening is usually attributed to the microscope objective. Chromatic aberration spreads the pulse energy spatially along the axial direction of the objective. This can manifest as a broad autocorrelation trace. This particular objective is apochromatic, which means that the lenses chromatic aberration is corrected to ensure 3 separate wavelengths all come to a focus in the same place. The main cause of dispersion should be material group velocity dispersion. However these sorts of objectives are generally made of low dispersion glass. The broadening observed corresponds to a group delay dispersion of about 10,000fs^2. This corresponds to about 20cm of low dispersion glass or 6cm of flint glass. There are no known components in the scanner or objective that would contain anything like this much glass. Without further details of the construction of the scanner one can only speculate on the cause of the dispersion. One theory is that the apochromatic correction does not extend to the IR,

another is that the high reflectivity mirrors in the scanner are broadband dielectric mirrors. These are renowned for having a very complex spectral phase response. Indeed, broadband dielectric mirrors for femtosecond application have to be specially designed, and are very expensive often costing >£600 per mirror and possessing strong polarisation dependences and resonances away from their operating region.

3.4. SAMPLE PREPARATION

This section will detail the methods used for the preparation of the samples and specimens used in this work.

3.4.1. STM SAMPLES

Work on the SPPX STM was primarily concerned with the development of the instrument and only simple reference samples were used such as Highly Oriented Pyrolitic Graphite (HOPG) and thermally evaporated gold on mica which when annealed forms atomically flat Au(111) terraces. The samples were mounted on a stainless steel sample plate so that they could be installed in the STM.
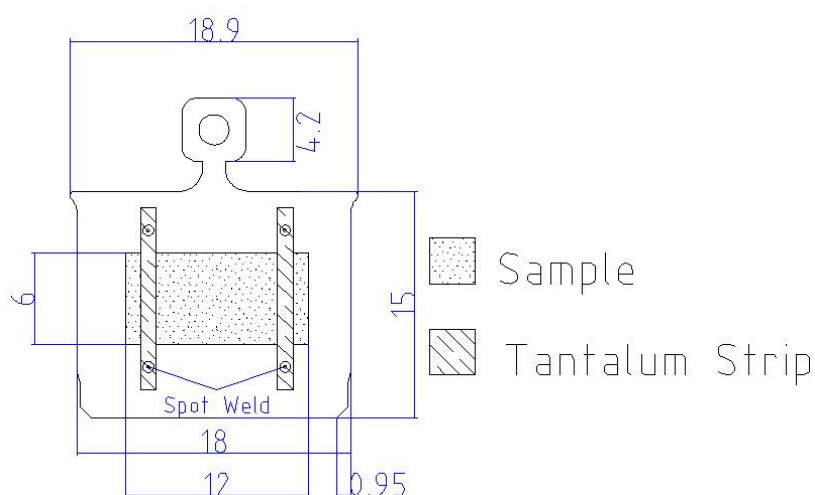
Figure 3-25   Omicron Sample Mounting Plate
All samples for use in the STM must be mounted on the sample plate. The sample is secured to the sample plate by spot welding tantalum strips to the sample plate over the sample. The Sample plate can accommodate samples up to 10mm long by 12 mm wide. HOPG and AU(111):Mica samples were cut to 12x6 mm.

Highly Oriented Pyrolitic Graphite (HOPG)

HOPG consists of layers of carbon atoms. The bonds within a layer are quite strong, however the inter layer bonds are very weak. HOPG used in this work contained very few defects and possessed large atomically flat terraces. It is particularly useful for desktop STM as it does not contaminate in air and can be easily cleaned by cleaving the graphite layers using a simple tape lift method, which will be described. Atomic resolution images of HOPG are also used to calibrate the piezo scanner.

The graphite was purchased from Advanced Ceramics and is available as slab of graphite with dimensions with layer 12x12 mm in length and width and 2 mm thick. This slab is first divided into four 12x12 mm squares of graphite 0.5 mm by separating the slab with a scalpel. Each of these squares is carefully cut in half to yield 8 6x12x0.5 mm graphite samples. The samples are then cleaved by performing a tape lift.

The HOPG sample is placed best side up on a piece of white PVC plastic which provides a better contrast to observe the graphite. The best side is usually the shiniest one with the least visible defects. A length of adhesive tape is placed over the graphite and lightly pressed down and smoothed with the pad of the finger. The tape is then lifted away taking the top few layers of graphite revealing a clean surface. The surface should be inspected for any flakes of graphite that remain partly attached to the surface. Large flakes should be removed with a pair of plastic tweezers talking great care not to touch the clean surface. It can then be attached to the sample plate as described above.

Au(111) on Mica

Au(111) films were evaporated onto mica using a commercial Edwards evaporator.

The mica was purchased from Agar. It is available in three sizes: 25x75 slides, 25x25 mm squares or as 11x11 mm cover slips. They are all 0.15 mm thick. Although the 11x11 mm slides are more convenient they are also considerably more expensive. The mica can be easily cut to size using scissors, but this can cause stress fractures through sample. A better way is to guillotine the mica. This was achieved by sandwiching the mica between two glass microscope slides aligned with each other and allowing the portion of the mica that is to be cut away to protrude from the glass. This portion is cut with very sharp razor blade, whilst moderate pressure is applied to the glass-mica-glass sandwich. This pressure prevented the stress fracture from spreading into the sample.

Once the mica had been cut to the required size, either 5x10 mm or 10x10 mm, it was placed into the evaporator sample heating stage. This stage allowed the mica to be heated whilst the gold was evaporated. Gold wire was placed in a molybdenum evaporation boat. The boat and sample holder containing the mica were placed in the evaporator vacuum chamber. The chamber was pumped down to a pressure not greater than $5x10^{-6}$ mbar, and if it was clean and had been left to pump down for an extended period of time is was possible to obtain pressures as low as $1.0x10^{-6}$ mbar.

The basic process for the evaporation of a gold film is very simple. A high current is passed through the evaporation boat containing the gold. The gold is melted and in vacuum it evaporates following a ballistic path, until it hits the relatively cooler mica surface where it

condenses. The mica sample is heated to allow the gold atoms to remain mobile on the surface so that they organise into a crystalline surface.

There are three main parameters that control the thickness and surface quality of the gold: The current used through the evaporation boat, which determines the rate of gold deposition; the temperature of the sample which determines the mobility of the gold atoms after they condense on the surface and the duration of the evaporation stage. Sufficient current must be used to cause the gold to evaporate and increasing the current will increase the rate of evaporation. Values in the range of 20-24A can be used. Whilst 20A is barely enough current to cause evaporation, 24A can create opaque films of gold in as little as one minute. If too high a current is used, the films produced are of a very low quality and may contain only a few small atomically flat areas. A balance needs to be struck between producing films in a timely manner and films of a sufficient quality.

The temperature of the mica substrate determines how quickly the atoms of gold attach to any pre-existing nucleation sites on the mica. If the mica is too cold, the gold atoms will almost immediately condense on the surface and will not organise into atomically flat terraces. When the temperature is too high, then impurities are driven out of the mica as it decomposes which contaminate the sample. Higher temperatures lead to larger terraces and less overall variation in thickness.

Whilst the evaporation current and the substrate temperature determine the quality of the sample, the evaporation time should be used to determine thickness. If all that is required is a conducting sample then this parameter is not critical. Precise thickness and sub-monolayer deposition are extremely difficult to control. This work only required thick films and these were successfully produced by evaporating gold at 21A for 1 hour onto a mica substrate heated to 350°C. After evaporation the sample substrate was maintained at 350°C for an additional hour before allowing it to cool in vacuum to form surfaces slowly.

3.4.2. CONFOCAL MICROSCOPE SAMPLES

Preparation of Fluorescent Beads

Fluorescent beads were used for alignment of the IR femtosecond laser. The fluorescent beads used were FluoSpheres® manufactured by Invitrogen Inc. Two sizes of bead were used with diameters of 1μm and 200nm. Initially beads were dissolved into a 2% aqueous solution, placed under a cover slip and the edges sealed with nail varnish. However the beads were too mobile and tended to aggregate. Instead 10 μL of bead solution was mixed with 1mL of mounting medium. The mixture was agitated in a sonic bath for 5 minutes which helped to

separate the beads. Then 50 μL of the mixture was placed on a slide with a cover slip over the top. The mixture was allowed to harden in the refrigerator at 5° C for 8 hours before being imaged. Samples were stored in a -20°C freezer thereafter.

Cell Preparation

Two types of cell were studied. In chapter 4, live Chinese hamster ovary (CHO9) cells transfected with a modified DNA sequence to produce GFP tagged PCNA were used to detect DNA damage caused by three photon absorption of the IR laser. The cells were cultured and produced by Rosalind Meldrum of the Biosciences Dept. at the University of Birmingham using the procedure described in [41].

In chapter 5, fibroblast cells dosed with gamma-radiation to induce double strand breaks (DSBs) in the DNA were used. These were produced by Chris Bruce of the Medical School. at the University of Birmingham. Cells were cultured, and placed in an irradiator. They were then exposed to the required doses of radiation. The slides were then kept in an incubator for 30 minutes to allow time for the γ-H2AX to form foci at the DSBs. The cells were then fixed, immunostained with Alexa488 fluorescent marker and covered. The cells were stored in a freezer at -20°C until required for imaging. Cells were prepared on five slides. Four of the slides were irradiated, with 8Gy, 6Gy, 4Gy and 2Gy of radiation, whilst the last was slide reserved as a control. The slides were marked with the dose of radiation they received for identification.

CHAPTER 4.

4. 3-Photon induced DNA Damage

The work reported in this chapter was done in collaboration with Dr Rosalind Meldrum of the Biosciences department of the University of Birmingham. My work centred of the acquisition of the data and its processing, as well the integration and alignment of the femtosecond laser with the confocal microscope, whilst the Rosalind Meldrum provided much of the motivation and the biological interpretation, which lie outside of my area of expertise.

In this chapter, a technique is developed to induce precise damage in DNA using multi-photon interactions and to monitor, in real time, the migration and localisation of the proteins involved in the repair and replication processes at the damage sites in live cells. A Ti:sapphire laser operating at 758nm in the IR region with a nominal pulse duration of 100fs is used to precisely induce UV-type DNA damage by a 3-photon (3P) absorption process[40] in the nuclear DNA of live Chinese hamster ovary cells. Proliferating cell nuclear antigen (PCNA) transfected with green fluorescent protein allows the migration of the PCNA to be visualised in real-time by confocal fluorescence microscopy. A spatiotemporal analysis of the regions targeted with the NIR femtosecond laser allows the measurement of the PCNA kinetics to be undertaken. The half-life of protein localisation to the damage site was measured and found to range from 100-325 seconds.

Further observations also provided evidence for the control of protein kinetics in the replication and repair process by intra-cell signalling pathways[46]. Replication centres that were not targeted but were in the vicinity of the 3P damage site were activated in response to the 3P induced damage. These sites exhibited localisation of PCNA on similar timescales to that of the primary damage site although they were usually smaller and less intense

4.1. INTRODUCTION

Multiphoton microscopy (MPM) is still a specialised technology that has been used successfully by a limited number of groups. The technical complexities introduced by non-linear excitation and absorption currently preclude its use at the level that single-photon confocal microscopy is used. It is commonly perceived that the most important niche for MPM lies in high-resolution imaging of morphology and physiology in intact tissues, but the high resolution that it can provide for non-imaging uses may overtake the applications for imaging. However, most non-imaging applications are used in conjunction with imaging, either single-photon or multiphoton. This makes multiphoton technology a very powerful and versatile scientific tool. Non-imaging applications include initiation of photochemistry and photobiology in very small volumes 'in vivo' or 'in vitro'. Amongst these applications are photolysis of caged compounds[47-49], localised photobleaching [47, 50], fluorescence excitation for the purpose of diffusion measurements [51, 52] and the introduction of localised DNA damage in cells[40, 53-55]. Ablation of sub-cellular structures by multiphoton beam targeting has been used to porate cell membranes[56] and for precise cutting of chromosomes[57].

The ability to produce localised specific ultra-violet type damage in DNA by three-photon absorption from a pulsed near infra-red laser beam [40] is a significant improvement on single-photon methods[58]. DNA damage can be targeted at specific sub-cellular structures that can be visualised under white light or fluorescence if tagged with an appropriate fluorescent dye. The near infra-red light that transmits efficiently through the common glass optics used in commercial microscopes excludes the need for expensive specialised UV optics that give poorer images. Time-resolved data of GFP-tagged proteins diffusing to sites of DNA damage can be collected more rapidly and efficiently as the induction of the DNA damage and the subsequent imaging can be carried out on the same instrument. The limiting factor on the highest data collecting efficiency possible is the dead time introduced by the inertia of the optical components when changed from those optimised for infra-red transmission to the components optimised for imaging at shorter wavelengths.

The level of the DNA damage inflicted is determined by the properties of the ultrashort pulses that caused it. The wavelength and energy of the pulse are obvious determinants but the pulse length also has a significant influence. It has been observed that, for the same pulse energy, destructive effects from scanning over a cell were more pronounced with shorter pulses[59].

Laser beams focused internally in living cells have substantially boosted research on DNA damage and repair. The importance of this biological process is underscored as inefficient repair of DNA damage can impair the essential functions of replication and transcription in a cell. For

biological organisms, including humans, this can manifest in premature aging and death or severe pathological conditions related to genetic inheritance of deficient repair processes.

Coupled with the application of GFP (green fluorescent protein) tagged to specific cellular proteins, the localized laser-induced DNA damage in biological cells enables measurement of the molecular diffusion of proteins involved in DNA repair. Many of these proteins are involved in replication and transcription as well, so the technical advances facilitate the spatiotemporal analysis of molecular exchange between these cellular functions.

Laser beam properties required to induced ultra-violet type DNA damage in cellular DNA by 3-photon absorption from near-infra red (NIR) wavelengths have been defined previously[40]. The imaging system available for those experiments was of a greatly inferior quality to the commercial confocal microscopes that have been produced in subsequent years. With modern imaging facilities, we have detected that the 3-photon NIR absorption that creates DNA damage takes place at shorter beam dwell times and lower average powers than calculated previously. In the work reported by Meldrum et al[40], the pulse length from the laser was given as 120fs although no accurate measurement was systematically made. This was true also for the estimation of a 200fs pulse after broadening through beam deflection mirrors and the microscope optics. Measurements performed with the system used in the current work show that the previous estimates of pulse broadening may have been greatly underestimated.

The increased sensitivity of the imaging system now used has revealed that the 3-photon NIR induced DNA damage occurs at lower powers and peak intensity than estimated before. Accurate measurements and calculations of the point spread function and the pulse broadening have been reported in sections 3.3.2 and 3.3.4 respectively. These yielded more comprehensive information on the optimum instrument settings at which DNA damage may be induced in cells.

4.2.   VISUALISING DNA DAMAGE IN LIVE CELLS

The first attempts to integrate the Ti:sapphire NIR laser with the Leica confocal microscope to cause targeted DNA damage proved extremely difficult. The cells were not marked with any fluorescent dye and imaging could only be achieved in transmission mode. This is not a confocal imaging method, has relatively poor axial resolution and it was difficult to know when the site to be damaged was in the focal plane. Furthermore, once the laser had been fired there was no way to immediately visualise the damage. The 3P damage leads to the formation of cyclobutane pyrimidine dimers (CPDs). To visualise this damage the cells had to be removed, fixed and antibody-stained with a florescent marker to identify the damage[40]. When the cells were returned to the microscope, some days later, the damage sites could not be located. Whether this was because the focal plane was not correctly estimated prior to damaging the cells,

or the laser did not cause damage in these cells or the cells that were damaged could not be located is not known. However, it was clear that a method of visualising the cells prior to irradiation with the NIR laser was required.

Proliferating cell nuclear antigen (PCNA) is a protein that is involved with the repair and replication of DNA. Essers et al [60] also describes the process by which GFP can be fused with PCNA, to allow it to be visualised by fluorescence microscopy. Early experiments were performed using the GFP-PCNA transfected Chinese hamster ovary (CHO9) cells kindly provided to Rosalind Meldrum by Jeroen Essers. The data presented in this chapter was obtained from cells prepared by Rosalind Meldrum following the procedure described in [60].

Although the focus of this work is on the analysis of DNA damage and its repair, PCNA is also involved in DNA replication that occurs during the cell cycle which was covered in section 2.3.2. To enable easy identification of the PCNA localisation foci marking the damage sites cells in the G1 or G2 phases were targeted rather than the cells many with DNA replication sites found in the S-phase cells.

4.2.1.   DNA DAMAGE INDUCED AT POINT SITES

The procedure for inducing 3P DNA damage at point site within a cell is described in Appendix B3. Figure 4-1 shows an example of field of view before and after irradiation with the IR laser set to 75mW and dwell period at each site of 5ms. All laser powers quote the measured intensity at the input to scanner.

At the target locations, following irradiation, PCNA localises to the damage sites. However, within the same cells other regions that were not irradiated also show increased concentrations of PCNA. It is suggested that remote replication centres have been activated in response to the damage at these damage sites, which is supported by the work of Solomon et al [46].

The images presented in Figure 4-2 show the whole of a 512x512 pixel field of view. A 3D rendering of the cell that is circled (blue-dotted line in Figure 4-1) is shown in Figure 4-2.

A 3D rendering is naturally limited in the level of detail that it can show. It must be very strongly smoothed to so that the intensity varies slowly over the volume to permit iso-surfaces of intensity to be rendered. It shows three iso-surfaces, the lowest intensity level is shown in green and identifies the nucleus of the cell, the foci have significantly higher intensities than the background and iso-surfaces have been drawn to represent the foci at two intensity levels.

It can be seen from these images that, over time, the size of the foci increase as more PCNA migrates to the damage sites. Figure 4-3 shows a section through the centre of the foci in

the plane that the damage was induced. It illustrates the appearance of the foci (foci 5 & 6) in sympathy to the DNA damage that occurred at the irradiated sites (foci 1-4).

Preliminary measurements also analysed the response to dwell time at 75mW. Dwell times of 100ms to down to 5ms were tested. 5ms was the shortest dwell time the time-lapse macro could accurately handle. In these measurements, damage was observed at each dwell time tested. Single point foci sizes (and intensity) appeared to remain constant but at the high powers the localisation was almost instantaneous. In the patterned DNA damage experiments thermal damage was observed at long dwell time and cells were heated to the point that the nucleus of the cell collapsed (see Figure 4-4f).
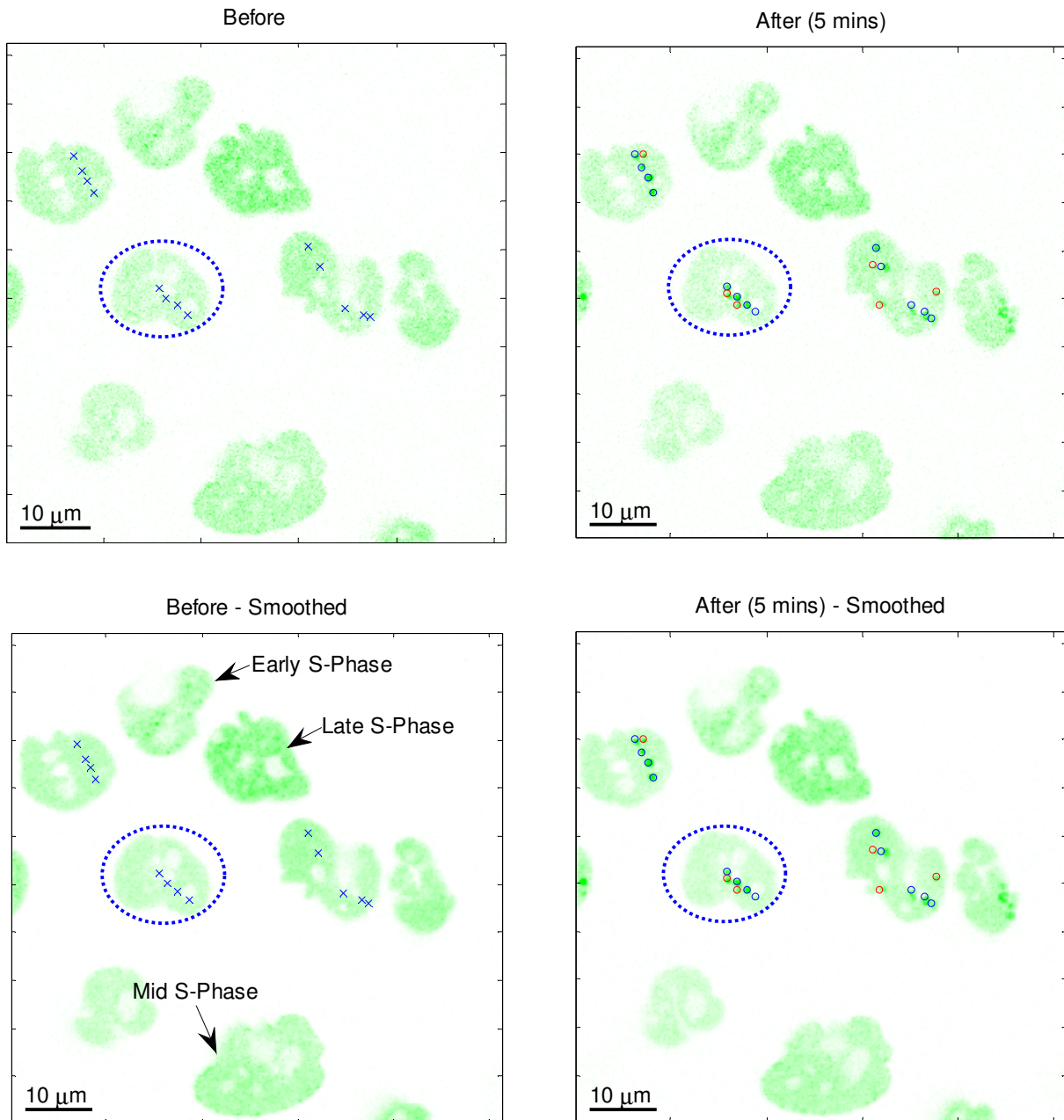
Figure 4-1   ***Images of Cells Before and After Irradiation by the NIR laser.***
Images of cells before (left) and after (right) the target locations (blue crosses and circles) are irradiated with the NIR laser, causing 3 photon damage and the localisation of PCNA to facilitate repair of the photo damage. The red circles highlight regions that were not targeted but following irradiation by NIR exhibit a sympathetic localisation of PCNA. Smoothed images (bottom) highlight localised area of high concentration better than the original data, which exhibits noise from the PMT. Targeted sites were irradiated with an average laser power of 75mW at a wavelength of 758nm, the dwell time at each site was 5ms.
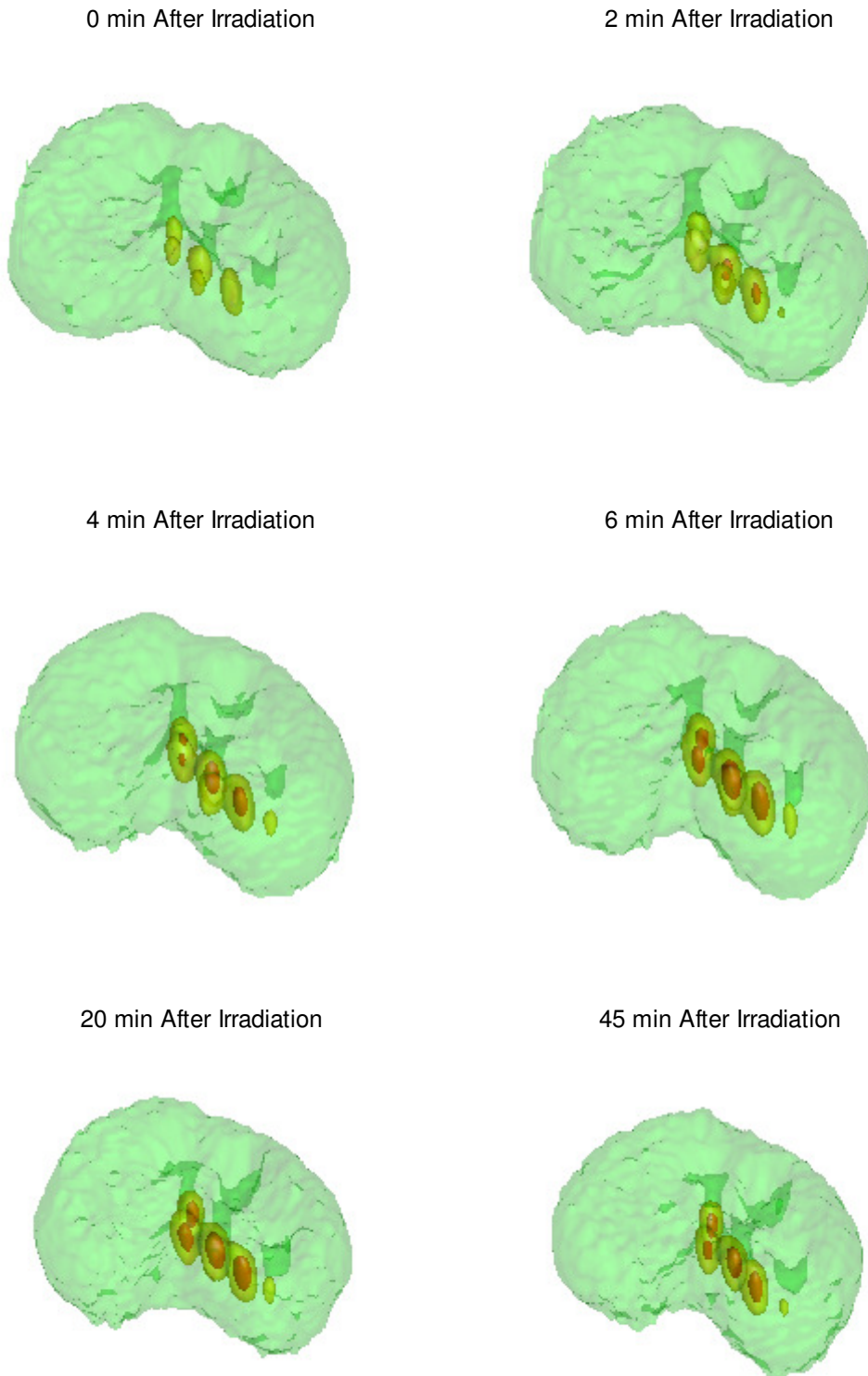
0 min After Irradiation   2 min After Irradiation

4 min After Irradiation   6 min After Irradiation

20 min After Irradiation   45 min After Irradiation

Figure 4-2   ***3D visualisation showing localisation of PCNA following 3p induced DNA damage***

These visualisations show 3D renderings of intensity iso-surfaces at three levels. The lowest level identifies the edge of the nucleus, and is shown in green, and has a low opacity, to reveal the PCNA foci formed inside the nucleus. The yellow and red shells are also intensity iso-surfaces, with the red marking high concentrations of PCNA. The PCNA gradually localised in the first 6 minutes, and then remain at approximately the same intensity for the rest of the time. The images shown here are frames from a movie, which can be found on the cover disk. The movie shows images at 1 minute intervals.

Note: Due to dead time between the irradiation phase and the after imaging phase the first slice of the "0 min" series was taken 7.2 seconds after the irradiation phase completed The acquisition of each z-series took 28.5 seconds.
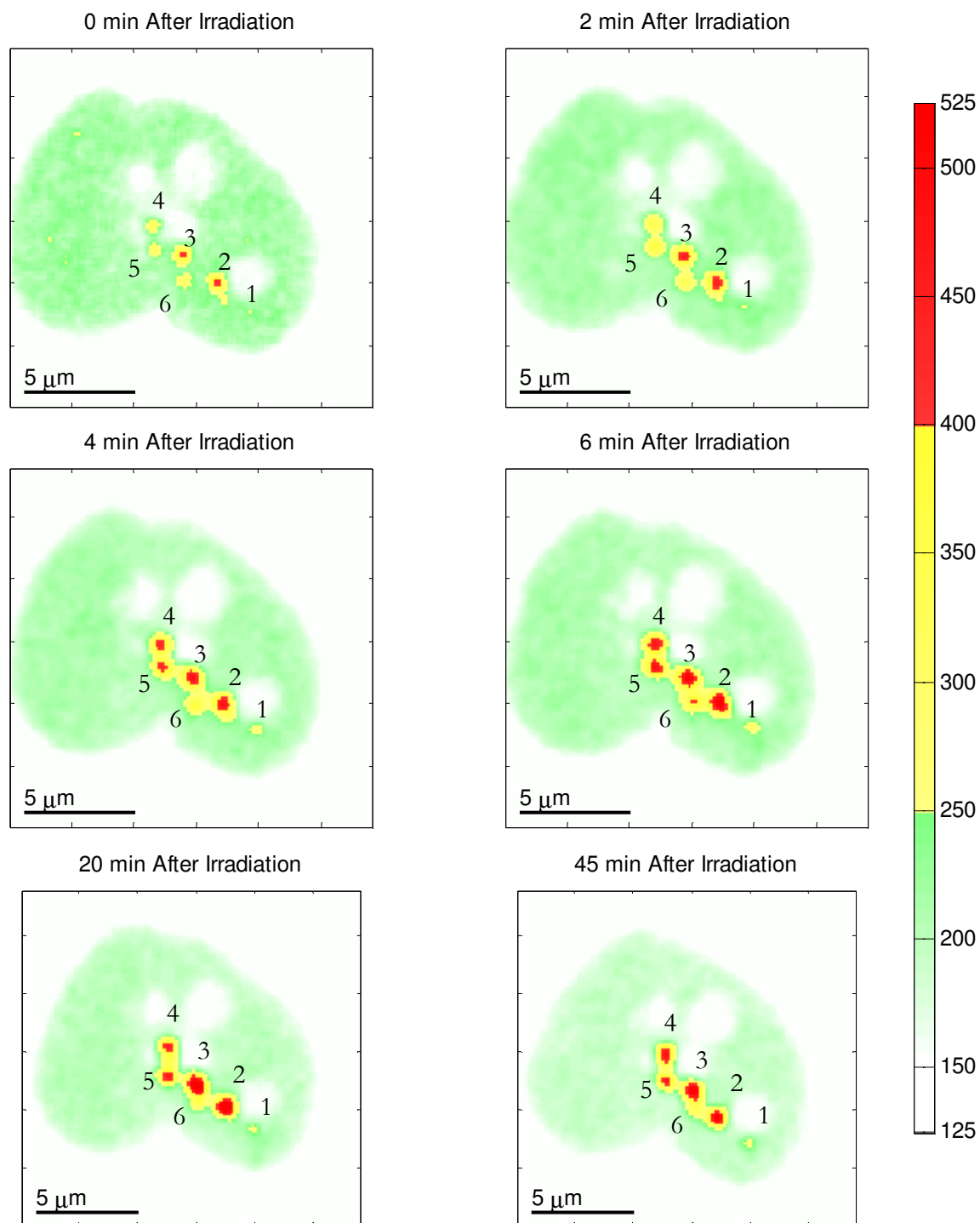
Figure 4-3 **Sections showing the localisation of PCNA following 3P induced DNA damage**

This time sequence of images show a section through the nucleus of a cell following 3P induced DNA damage. The colour scheme is can be related to the one used for the 3D visualisation in Figure 4-2.

4.2.2.   PATTERNED DNA DAMAGE

The Leica bleaching macro only permits points to be bleached and has no facility to inscribe lines or patterns in the samples. A pattern of points can be defined but only up to a maximum of 19. Patterned damage can be achieved by setting a single bleach point within the image and then moving the sample, using the motorised sample stage, to create the desired

pattern. The dwell at the bleach point must be long enough for the movement to complete. The motorised stage was controlled by the WinPOS application which could be scripted to perform a particular sequence of movements. A short C++ program was written to create scripts that defined a meandering path. The resulting movement inscribes a series of parallel lines in the sample, the velocity, the line length, inter-line spacing and number of lines can be independently adjusted.

The speed of movement determines the effective dwell time. If the IR spot in the focal plane has a Gaussian profile then the effective dwell time is defined as the time taken to move two standard deviations.

The technique was developed to perform damage over large fields of cells, enabling the identification of samples removed from the microscope for immunostaining to be located again. This method was not necessary once the GFP-PCNA transfected cells were adopted but it does illustrate how much the sensitivity varies in different cells, even within the same batch.
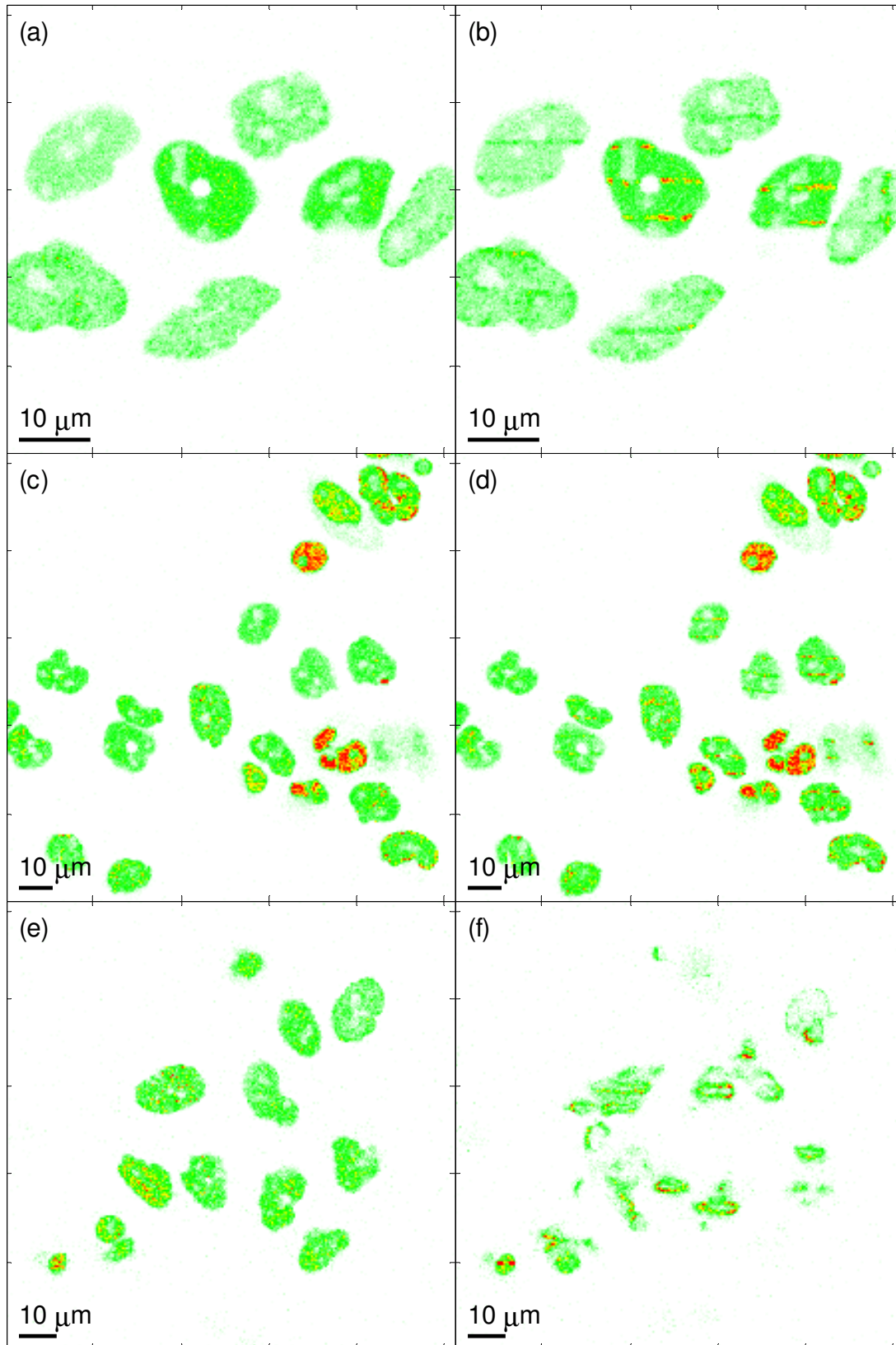
Figure 4-4 **Patterned 3-photon induced DNA damage.**
Stripes of 3P DNA damage were induced in the cells by rastering the sample stage using remote controlled step motors. The images on the left show the cells before irradiation, the images on the right show the migration of PCNA to lines of 3-photon induced damage. The laser had an average power 75mW and b and d were both exposed to an equivalent of a dwell time of 25ms, whilst f, was exposed to a dwell time of 100ms, and the resulting damage appears to have immediately destroyed the cells. The lines of DNA damage are visible, but the nuclei of the cells have been destroyed and PCNA can be seen to have dispersed.

4.3. DOSE MEASUREMENTS

Measurements were performed to identify the lowest level at which 3-Photon DNA damage could be induced in order to determine the sensitivity of the living cells to damage by this process. We determined a threshold level of peak intensity of IR laser light that would induce DNA damage in a cell and analysed the dynamics of the PCNA protein involved in the repair process.

4.3.1. DETERMINING PEAK INTENSITY AT THE FOCUS

The four measurable factors that determine the peak intensity of the laser pulses at the damage site are:

- the PSF of the microscope, measured in section 3.3.3;
- the pulse duration at focus of the microscope, measured in section 3.3.4;
- the average laser power;
- the laser repetition rate, specified as 80MHz;

The average laser power and repetition rate determines how much energy is in each pulse. In section 3.3.2 the transmittance of the scanner and objective was measured. All laser powers quoted in this chapter are for the laser power measured at the laser input of the confocal scanner unless stated otherwise. The power at the objective is obtained by multiplying the laser power by the transmittance measured in Table 3-2. The DNA damage experiments were performed using the 40x objective and the Beam Expander 1, and so the transmittance is 10.17% for all measurements in this chapter.

Using the measurement of the 2 photon PSF from section 3.3.3 it is possible to determine what the 1 photon infrared PSF is likely to be by taking the square root of the 2P PSF. This shown in Figure 4-5 and the FWHM of the 1P radial PSF is 349nm. By the same method, the 1P axial PSF can be determined and can be shown to be 1097nm.
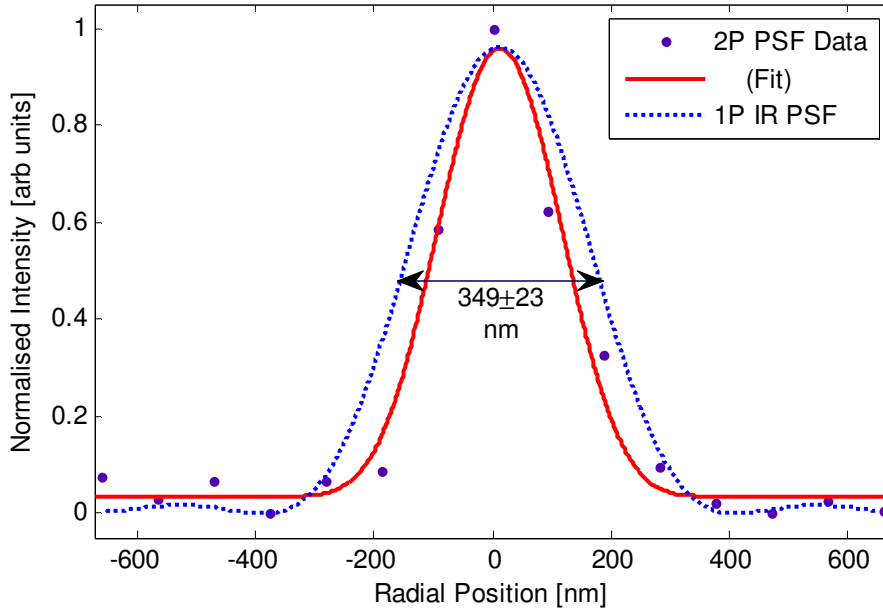
Figure 4-5   ***1-Photon IR PSF***

The first step in determining the peak intensity is to calculate the energy in a single pulse which is obtained by dividing the average laser power by the repetition rate. The peak power is obtained by dividing the pulse energy by the pulse duration. To get the peak intensity, the size of the focused area needs to be considered.

If a Gaussian beam is assumed, the beam waist of the beam is circular with a radius, r_0, defined as the point at which the intensity has fallen to e^{-2} of the axial intensity, and the radial intensity profile of the beam is given by (4-1), where I_0 is the axial peak intensity.

$$I(r) = I_0 \exp\left[-\frac{2r^2}{r_0^2}\right] \tag{4-1}$$

The power in the whole beam can be obtained by integrating the intensity (4-1) over all space as shown in (4-2).

$$P_0 = 2\pi \int_0^\infty I(r) \cdot r \cdot dr$$

$$= \pi I_0 \left[-\frac{r_0^2}{2} \exp\left[-\frac{2r^2}{r_0^2}\right]\right]_{r=0}^{r=\infty} = \tfrac{1}{2} I_0 \pi \cdot r_0^2 \tag{4-2}$$

Equation (4-2) can be rearranged to give the peak intensity I_0 in terms of the power in the beam, P_0, and the waist of the beam, r_0. The radius of the beam waist and the FWHM of the PSF are related by equation (4-3).

$$r_0 = \frac{FWHM}{\sqrt{2 \cdot \ln 2}} \qquad (4\text{-}3)$$

The equations are built into the worksheet shown in Table 4-2. It calculates the peak intensity, I_0, and also performs the error analysis. It provides two values for I_0, one uses the theoretical expression for the point spread function based on the wavelength of the light and the Numerical Aperture (NA) of the objective to estimate the beam waist. The other method calculates the beam waist using equation (4-3) and the FWHM of the PSF measurement. The PSF measurement revealed that the focus was not as small as the theoretically calculated PSF, probably because the back-pupil of the objective was not over filled reducing the effective numerical aperture.

In the experiments in this chapter only the laser power was varied, the pulse duration and point spread function of the microscope remained constant. A table of the peak intensities for each of the average laser powers used in these experiments is provided in Table 4-1.

Average Laser Power [mW]	Peak Intensity [GW/cm^2]		
75	172	±	19
50	115	±	13
25	57	±	7
20	46	±	5
10	23	±	3

Table 4-1 **Table of Peak Intensities calculated from average laser powers.**
The Peak intensity at the focus was calculated for each of the average laser powers at which experiments were performed.

Laser Pulse Properties	Value	Error
Laser Power	75	0.5
Transmittance	0.1017	0.001
Average Power at Sample [mW]	7.63	0.09
Repetition Rate [MHz]	80	0
Energy Per Pulse [pJ]	95.34	1.1
Pulse Duration [fs]	401	25

Cross-Sectional Area (Calculated)	Value	Error	Area cm^2	Error	Peak Intensity GJ/cm^2	Error
Wavelength [nm]	758	5				
Objective NA	1.2	0.05				
R_0 (Airy Radius) [nm]	385	16				
FWHM	325	14				
r_0 (Gaussian Beam Waist)	276	12	2.39E-09	1.4E-10	199	17

Measured PSF Radius	Value	Error	Area cm^2	Error	Peak Intensity GJ/cm^2	Error
FWHM (Radial PSF)	349	23				
r0 (Gaussian Beam Waist)	296	20	2.76E-09	2.6E-10	172	19

Table 4-2 **Worksheet for calculating Peak Intensity at the focus**
This worksheet is used to calculate the peak intensity at the focus of the microscope. The green shaded boxes on the left are where the values and errors on those values are entered. The peak intensity is calculated on the right. The peak intensity is calculated for both the theoretical PSF and the measured PSF to allow for comparison. The measured PSF is larger than the theoretical PSF and so the calculated peak intensity is lower.

4.3.2. THRESHOLD 3P DAMAGE RESULTS

A series of damage sites were defined in a number of cells using a range of average laser powers. The average laser powers and corresponding peak intensities are listed in Table 4-1. At each intensity level a number of damage sites were specified. They were irradiated using the NIR laser and then imaged immediately afterwards and at 1.635 second intervals. The frame rate was limited by the scanner as 1.635 seconds was the fastest achievable scan time that would produce good quality images. Images of the cells before and 70 seconds after irradiation at each power level are shown in Figure 4-6 and Figure 4-7.

At 75mW strong foci of PCNA had migrated to each of the targeted damage sites. In the cells that were irradiated with 50mW a number of behaviours were observed. Not all the cells responded in the same way. Cell 1, labelled in Figure 4-6c&d appears to in a G0 (resting) phase state except for two pre-existing PCNA foci which may be replication centres. Five damage sites were targeted within the cell but only one site had PCNA localised to it following irradiation. In addition, there was noticeable reduction in intensity of the pre-existing PCNA foci.

Average Laser Power: 75mW

Average Laser Power: 50mW

Average Laser Power: 25mW

Intensity Scale
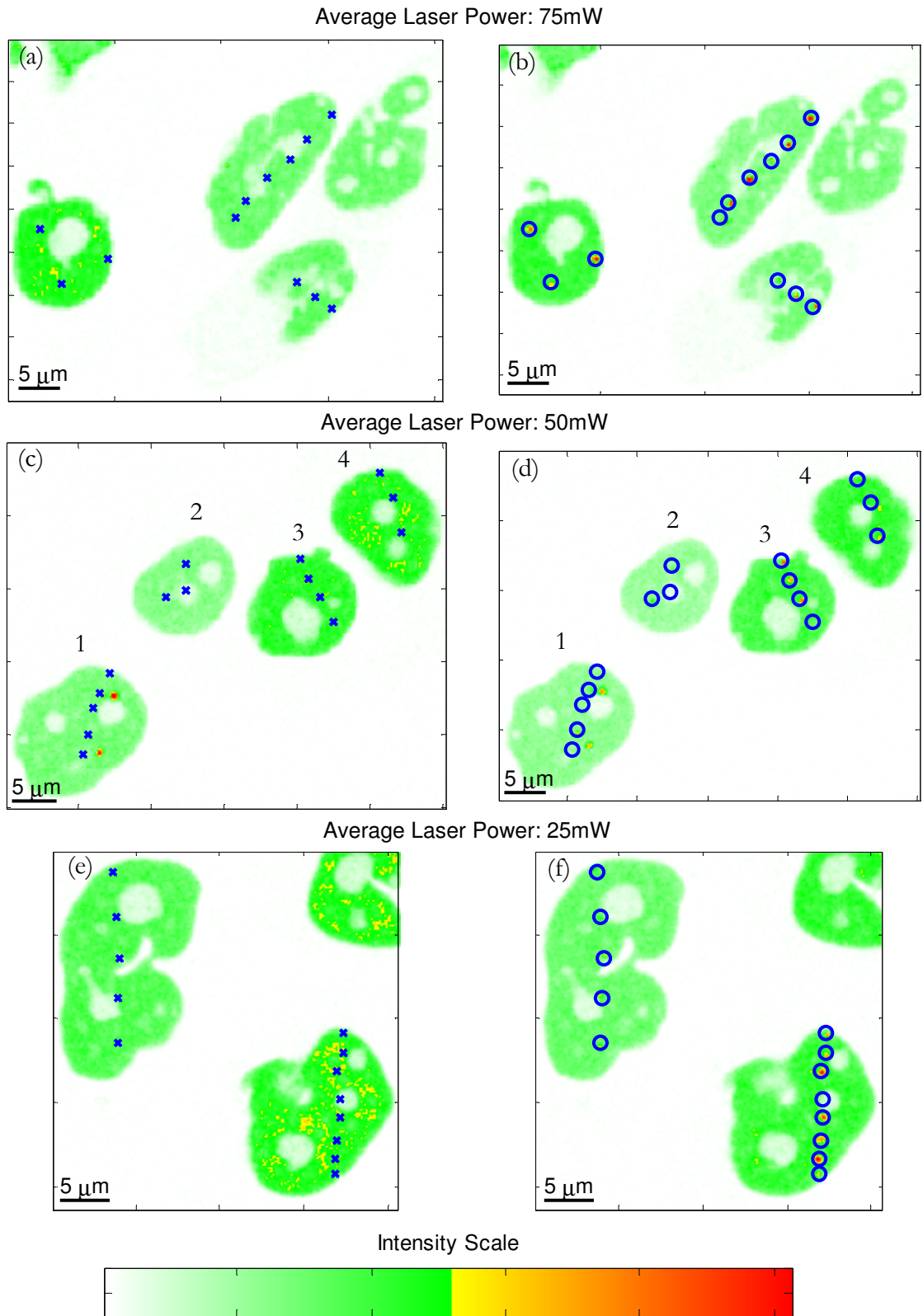
Figure 4-6   NIR 3-photon induced DNA damage at 75mW, 50mW & 25mW
This figure shows images before (left) and after (right) the induction of 3-photon DNA damage. The after images were taken 70 seconds after damage targets were irradiated. Damage targets are marked with 'x' in the before images and with a 'o' in the after image.

Average Laser Power: 20mW

Average Laser Power: 10mW

Intensity Scale
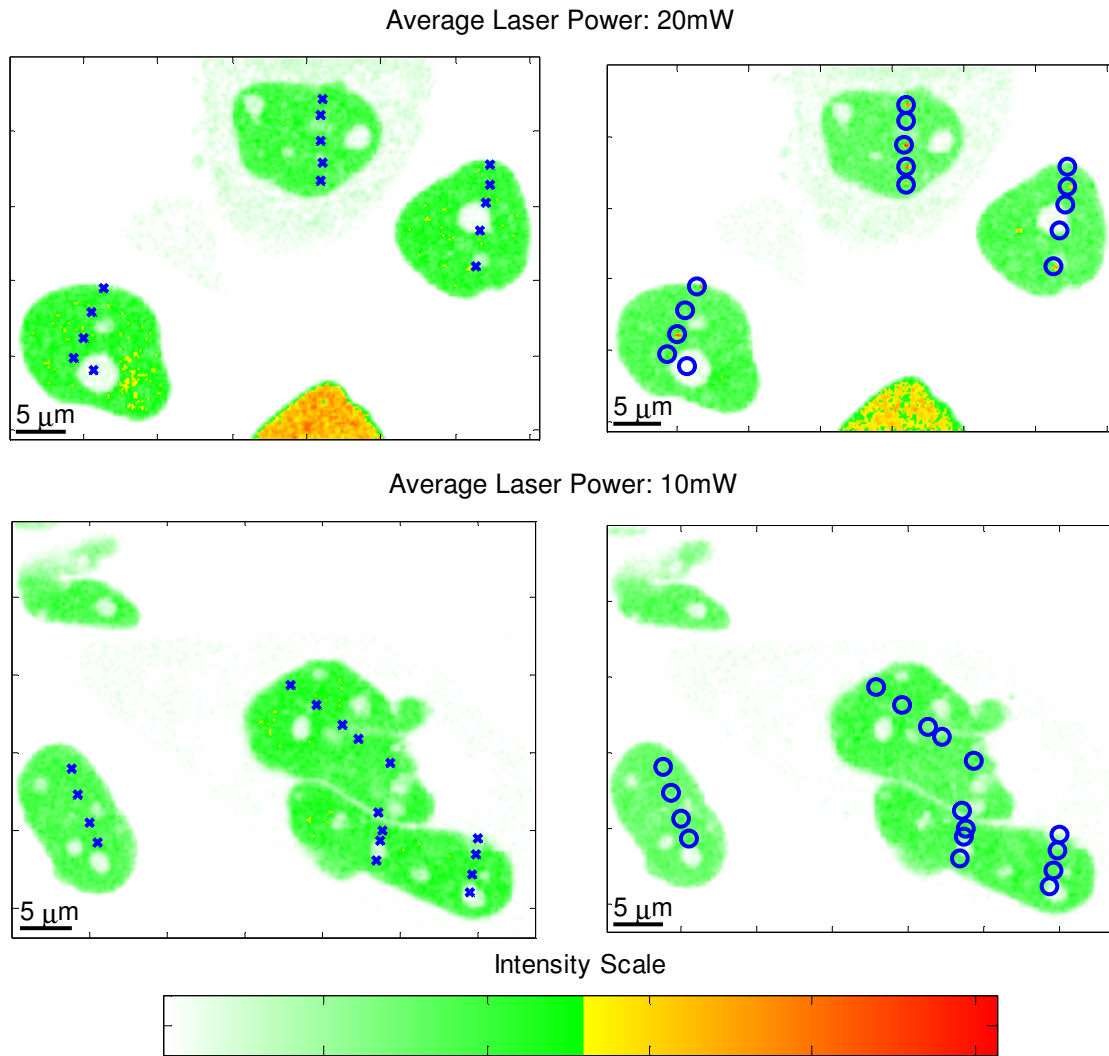
Figure 4-7   *NIR 3-photon induced DNA damage at 20mW & 10mW*
This figure shows images before (left) and after (right) the induction of 3-photon DNA damage. The after images were taken 70 seconds after damage targets were irradiated. Damage targets are marked with 'x' in the before images and with a 'o' in the after image.
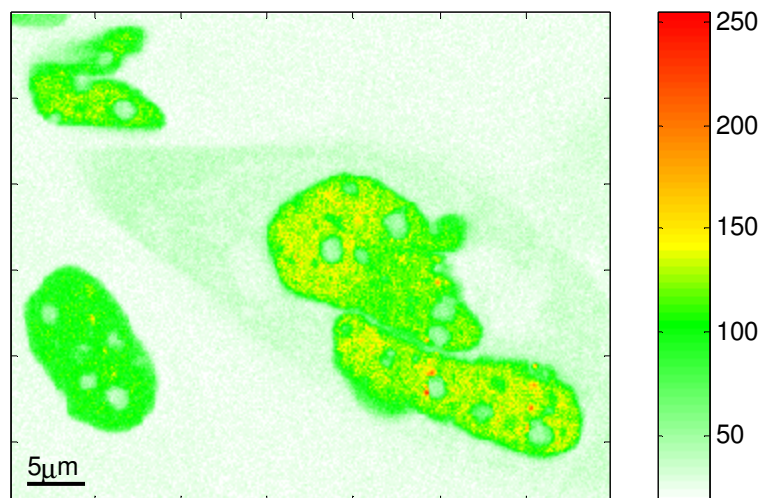
Figure 4-8   *PCNA localisation 120 seconds after irradiation at 10mW*
Damage is detected following irradiation at 10mW. Foci formation took longer and they are much fainter. This figure is the result of time averaging five frames (8.2 seconds) starting at 120 seconds and a careful selection of the colour scale to highlight the damage sites.

The distribution of DNA in a cell nucleus is inhomogeneous. Different levels of coiling and super-coiling of the DNA-protein structures that form chromatin exist throughout the nucleus and dynamic changes in these DNA structures take place when the cell divides. Thus the density of DNA may be greater in certain areas of the nucleus[61]. The probability of 3 photon absorption will be greater where the packing of the DNA is denser and these areas are more likely to sustain damage than areas where the chromatin is less densely packed. This explains why some targeted sites express damage while others do not.

Cells one and two are noticeably less intense than cells three and four as they are not expressing as much GPF tagged PCNA protein. Cell 2 only yields low intensity localisations of PCNA at the sites targeted that were within the GFP-PCNA containing regions of the cell. It is possible that cells one and two divided from the same original cell, and same could be true for cells three and four. Cells three and four responded as might be expected to the NIR 3P damage, with the formation of high intensity PCNA foci.

At 25mW localisation of PCNA following irradiation with NIR pulses was still observed. In Figure 4-6e&f two cells are shown; the cell to the left has less GFP-PCNA present prior to irradiation than the rightmost cell that was targeted. Although the localisation occurs in both cells, it is much more pronounced in the right hand cell. It is not clear from the data but the cell may be about to enter very early S-phase of the cell cycle. The sensitivity (or the repair response involving the PCNA) of the cells to radiation damage is known to be dependent on the phase of the cell cycle and cells are especially sensitive to radiation damage in the S-Phase[62].

At 20mW localisation of PCNA is still just visible and at 10mW there appears to be no damage detected. It would appear that a threshold level for the damage lies between 10mW and 20mW. By time-averaging a number of frames from the acquisition, it is possible to detect the damage that was caused. The foci of PCNA are slower to appear after irradiation than at the higher powers and are not much more intense than the background. Figure 4-8 shows the time averaged measurement 120s after irradiation and reveals the presence of GFP-PCNA foci. A different colour scale to that used in Figure 4-7 is used to highlight the feature of the foci.

The measurement at 10mW corresponds to a peak intensity of only 23 ± 3 GJ/cm^2 which is less than $1/8^{th}$ of the power previously thought to be the threshold for such a process, making this the most sensitive detection of 3P induced IR damage that has been performed.

A number of target sites were either in or on the boundary of nucleoli (the white coloured organelles in the nucleus devoid of GFP-PCNA). When irradiated, these sites did not form GFP-PCNA foci. Whatever barrier that kept the background GFP-PCNA from entering the nucleoli did not permit PCNA to migrate into the structure following irradiation. This behaviour was

consistently observed whenever nucleoli were targeted and GFP-PCNA was never seen to migrate into the nucleoli in response to the damage.

4.3.3. PCNA KINETICS FOLLOWING DAMAGE

During the initial measurement it was noticed that the PCNA took some time to localise to the damage sites. Regions of interest were defined around the foci and the average fluorescence was measured as function of time. However, over the extended data acquisition period the foci would move out of the defined ROI. Movement was observed in the x and y direction and it seemed probable that there may also be movement in and out of the focal plane. A method of tracking the foci in 3D and 2D was needed.

Foci Tracking

The images were loaded into Matlab, and were strongly smoothed in the spatial dimensions. Smoothing allow the foci tracking algorithm to locate the maximum more reliably.

Smoothing was achieved by performing two consecutive filtering operations with 3x3x3 (or 3x3 for 2D datasets) Gaussian kernels with a standard deviation of 0.65 pixels. This is roughly equivalent to performing the smoothing with a 5x5x5 (or 5x5 for 2D datasets) kernel and a standard deviation of 0.9 pixels. The amount of memory on the machine was limited and insufficient to perform the latter operation with the 3D datasets, so although the processing time for running the former operation twice took as long, it could be completed on the computer available.

Once the images had been smoothed, the user could select the damage sites manually by clicking on the centres on them in the image. This only had to be done for one plane in one frame. For each foci marked, the foci tracking algorithm would inspect the neighbouring pixels (including the z-direction if the image was a 3D dataset) and if there was a more intense neighbouring pixel it would move the position of the foci to that pixel and repeat the process until the marked foci position corresponded to the brightest pixel in the vicinity.

Once this had been completed for all the points marked as foci in a frame, it would be repeated in the adjacent frames using the position in the previous frame as a starting point. In this way, so long as the foci never disappeared and moved gradually, the foci tracking algorithm could move the ROI within the foci, allowing the average intensity of the foci to be measured as a function of time.

Using the 3D time lapse dataset shown in Figure 4-2 and Figure 4-3 the PCNA foci were selected and the movement tracked throughout the 45 minute duration of the measurement. The movement of the foci is shown in Figure 4-9. Using the 3D data set meant that even if the focus

drifted then it was possible to capture and analyse the whole of the foci throughout the experiment.
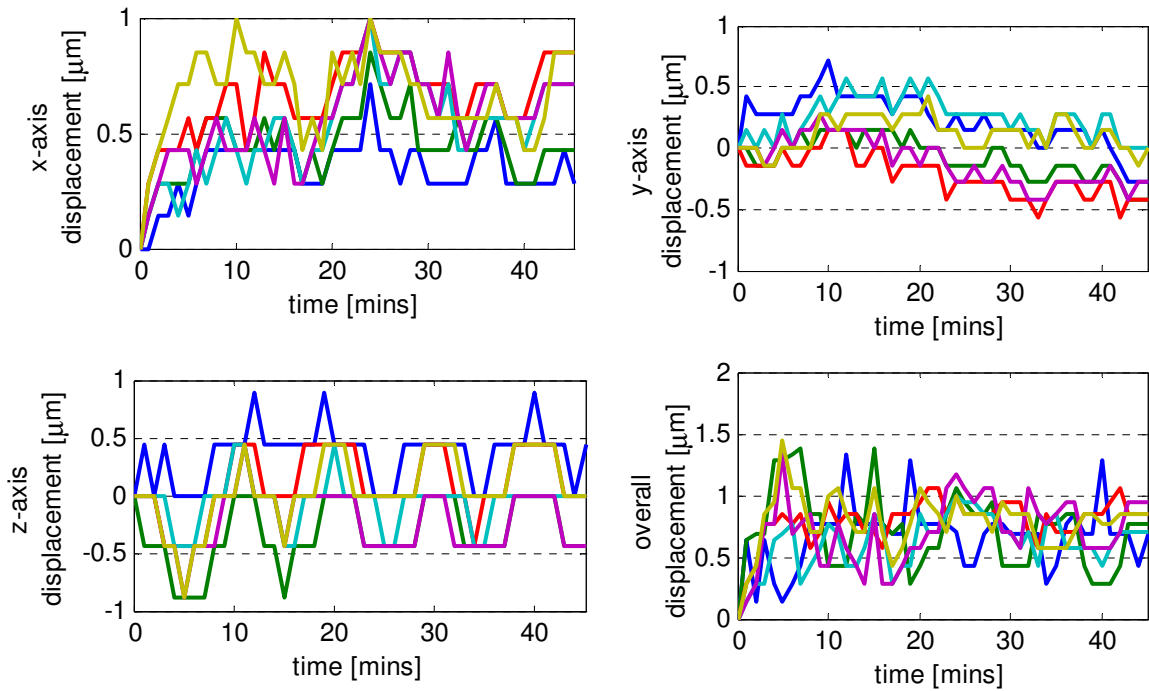
Figure 4-9   **Movement of PCNA foci tracked in 3D over a 45min period.**
The foci moved with the cell and also with respect to each other. The distance moved by the foci over the duration of the measurement was between 0.5μm and 1μm.

PCNA Localisation in 3D

A 3D rectangular ROI of 5x5x5 voxels was cantered on the tracked foci position. The maximum, mean and standard deviation of the voxel intensity within the ROI was measured for each frame in the time series. The results are plotted in Figure 4-10. The volume containing the cell was scanned almost continuously with the 488nm Ar^+ laser for 45 minutes. This caused photobleaching of the GFP. To compensate for the photo bleaching, another ROI was defined within the nucleus of the cell at the beginning of the time series. The average of the intensity in the background ROI was measured and all subsequent frames had the intensity multiplied by a constant factor such that the equivalent region in the following frames had the same average intensity.

From the results in Figure 4-10, the foci rapidly increase in intensity and then reached peak levels. The foci very slowly begin to dissipate as the repaired process continues. However, after 4 minutes of continual imaging the photobleaching had destroyed most of the fluorescence in the sample. The foci reached their maximum intensity after 8 to 10 minutes.
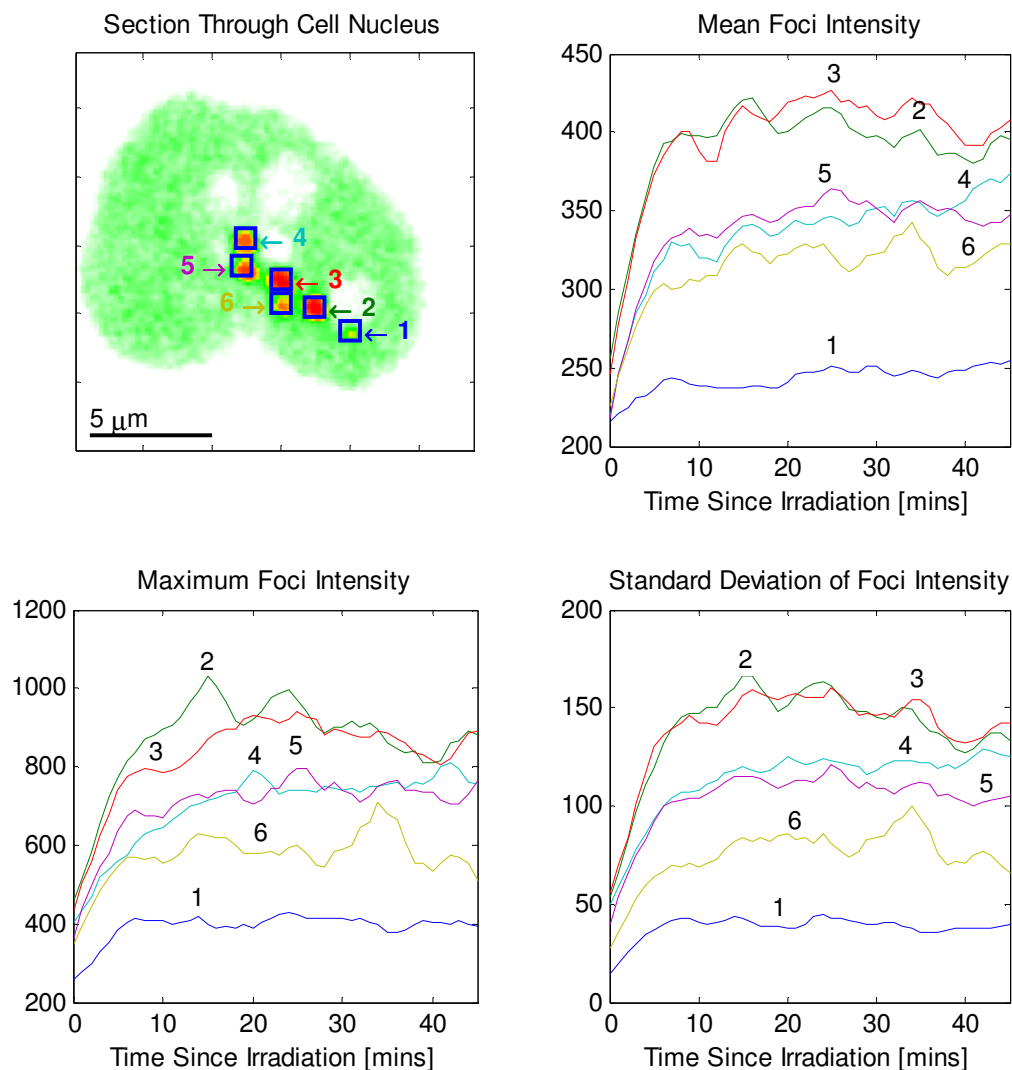
Figure 4-10   Dynamics of PCNA Localisation following 3P induced DNA damage.
This time sequence of images shows a section through the nucleus of a cell following 3P induced DNA damage, with 50mW of laser power and dwell time of 5ms. The colour map is related to the one used for the 3D visualisation in Figure 4-2. Foci 1-4 at sites that were targeted for damage, foci 5 and 6 formed sympathetically.

The first part of the mean intensity time profile was fitted to an exponential localisation using the equation (4-4). By fitting the data to this equation, it was possible to measure a localisation half life. The fitted data is shown in Figure 4-11 and the table of parameters for fitting the data from the ROIs to equation (4-4) is provided in Table 4-3. The mean localisation half-time for foci that form at damage site is 2.17±0.26 minutes or 130±15 seconds.

$$I = a \cdot \left(1 - e^{-\frac{\ln(2)}{t_{1/2}} \cdot t} \right) + b \qquad (4\text{-}4)$$
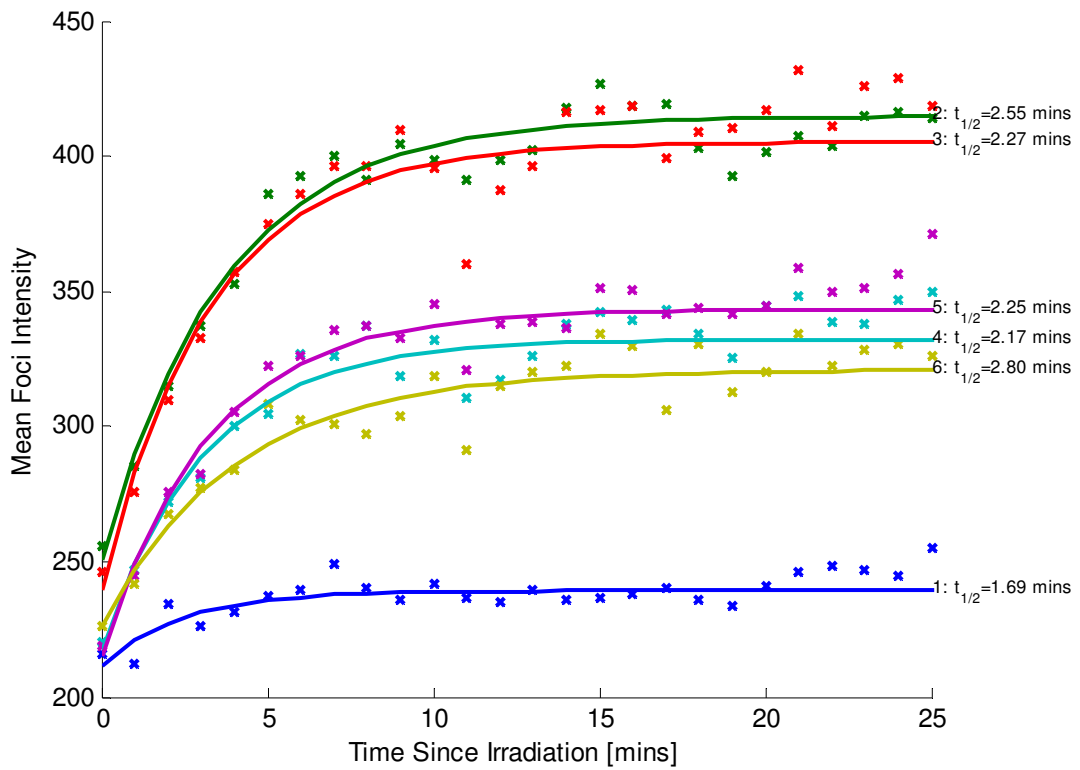
Figure 4-11 **Fitting of PCNA Localisation half-times.**
This time

ROI	a	$t_{1/2}$ [mins]	B
1	27±05	1.69±0.73	211±05
2	164±09	2.55±0.37	251±09
3	166±14	2.27±0.46	239±14
4	114±09	2.17±0.41	217±09
5	128±07	2.25±0.31	215±07
6	94±09	2.80±0.75	226±09

Table 4-3 **Results from fitting PCNA localisation dynamics**
ROIs 1 to 4 were located on targeted damage sites. ROIs 5 and 6 formed in sympathetically. The mean half life for foci formed at damage sites is 2.17±0.26 minutes.

The formation of sympathetic PCNA foci is evidence that intra cell signalling may be occurring. Replications forks may be stalled by cell signalling molecules activated by the proximity of damage. Single and double strand breaks occur as a result of this stalling and form DNA damage to which PCNA localises. In this case, two PCNA foci appeared sympathetically in response to the damage and were labelled as ROI 5 and 6. They have localisation half-times that are consistent with the localisation of foci at damage sites.

PCNA Localisation in 2D

Performing the PCNA localisation measurements in 3D provides a higher immunity to focal drift and movement of the cells out of the focal plane but each frame of volume data takes

a little under a minute to capture. In order to measure the localisation half-time with high resolution, the PCNA measurement was attempted in 2D which although restricted to only capturing one plane would allow that image to be captured at a high frequency. In contrast to the 3D imaging, which could only capture images every minute, the 2D measurements capture images every 1.635 seconds.

Using the data from the threshold measurements in section 4.3.1 for laser powers at 75mW, 50mW and 25mW ROIs for PCNA foci were selected and tracked through the time series in a similar manner to that used in the 3D dataset analysed previously. Square ROIs of 7x7 pixels, centred on the tracked positions of the foci, were used to evaluate the mean, maximum and standard deviation of intensity of the foci. Images identifying the ROIs for the foci, the time profile of the mean, maximum and standard deviation of intensity within the ROIs for laser powers of 75mW, 50mW and 25 mW are plotted in Figure 4-12, Figure 4-13 and Figure 4-15 respectively.

When the measurement at 75mW was performed, due to a problem with switching the optics to imaging mode, the after time series did not start until 65 seconds following the irradiation. In this time the foci had almost completely localised to the damage sites. Over the duration of the measurement, the PCNA foci at the damage site either remained constant or continued to slowly increase. In addition to the 6 PCNA foci that were created in direct response to the IR DNA damage there was a small pre-existing focus. An ROI was placed on this focus to monitor its behaviour in response to the damage. This would suggest that the localisation half time was considerably less than 60 seconds, which is quicker than was observed in the 3D measurement.
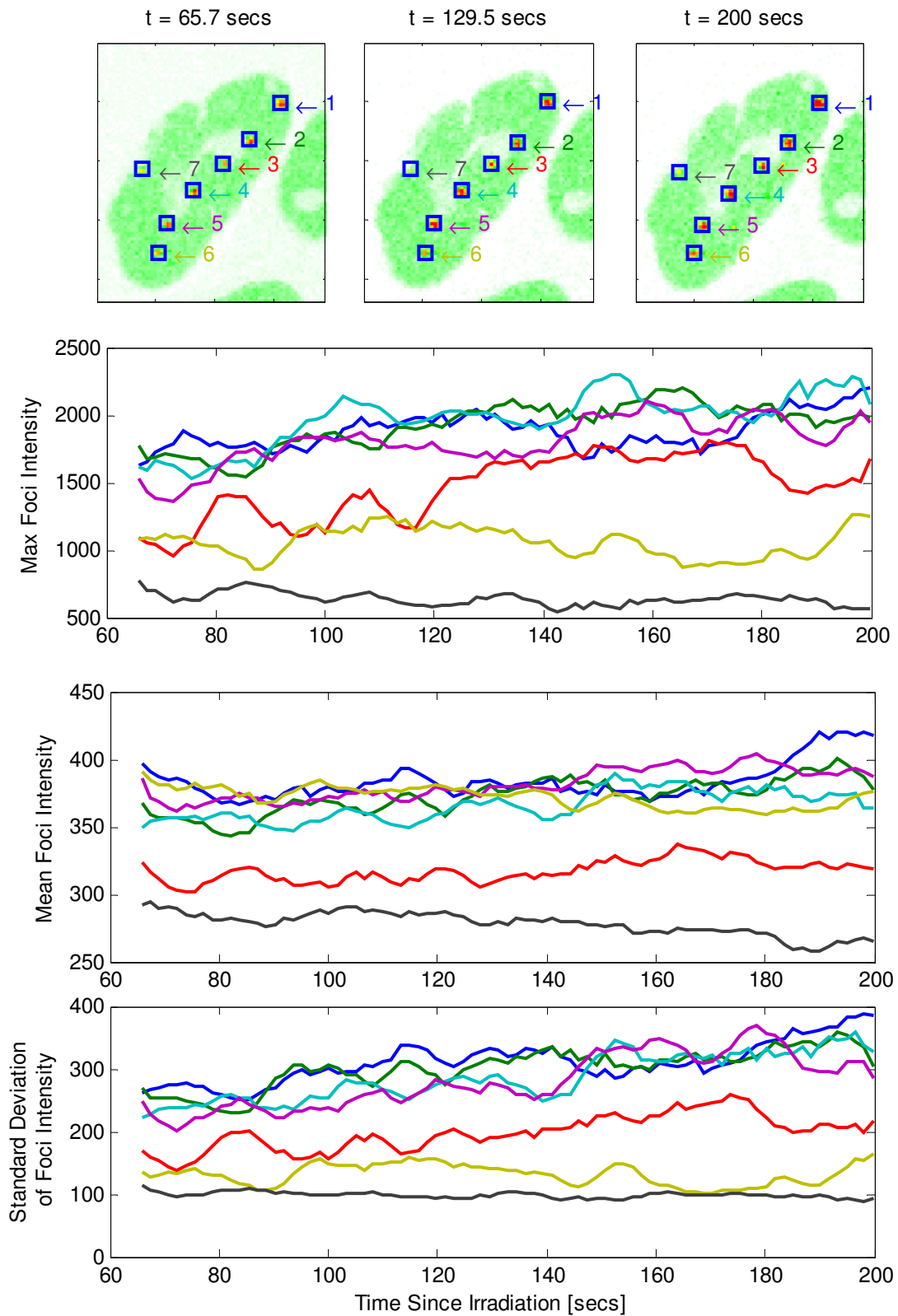
Figure 4-12   *Localisation of PCNA in 2D following irradiation at 75mW*
Images show the original data at different times after irradiation. The blue boxes indicate the ROI for the foci created by the laser irradiation. The data plotted on the axes below the images have been smoothed using a moving average with a window span of 5 samples. The ROIs 1-6 are damage sites created by the 3P induced NIR damage. ROI7 marks a site where PCNA had localised prior to damage being induced by the NIR Laser. The colour of the lines in the time profiles correspond the colour of the ROI labels in the images above.

Over the course of the 200 second measurement, the remote PCNA foci reduced in intensity by a small but detectable amount. This reduction probably reflects repair of DNA lesions and release and diffusion of PCNA from the repaired damage.

In measurements performed with an average laser power of 50mW, the first image was captured just 7.4 seconds after the NIR damage. Even in this short period foci 1, 2 and 3 are clearly and distinctly visible in the first image in Figure 4-13., although the mean intensity is quite small. Over the duration of the measurement the intensity of the foci increases to a maximum level. There are some long time scale fluctuations in the intensity of the PCNA. These could be due to either focal drift or more complicated processes relating PCNA's role in the repair process. One argument against focal drift is that the fluctuations in the intensity of the foci are not correlated across foci as a function of time.

Localisation of PCNA at damage sites in the upper cell, where ROI 4&5 were located, was much slower than in the lower cell. The mean intensity localisation profile was fitted to equation (4-4) as had been done in the 3D measurement and the results are shown in Figure 4-14 and Table 4-4 shows the fitted parameters for equation (4-4). The foci labelled A and B, which formed sympathetically, did not fit the exponential localisation equation and proved very difficult to analyse. The phenomenon of intra-cellular signalling is analysed in more detail in section 4.4.

At 25 mW the localisation occurred more quickly. The measurement was performed for longer after the initial localisation and the mean intensity began to fall off but some minutes later increased in intensity again. This illustrates how complicated the role of PCNA is in the DNA repair process. The same analysis and fitting was performed on this data and the results are presented in Figure 4-15, Figure 4-16 and Table 4-5. The fitting of PCNA localisation times to equation (4-4) was only done using the first 300 seconds of data as after that the complicated repair process could not easily be modelled.

This sort of analysis was not possible with the 20 and 10 mW datasets as these were captured at only 8-bit intensity resolution and only exploited a relatively small range of that. Although the quality was sufficient to present an image, more detailed analysis was frustrated by a low signal to noise ratio.
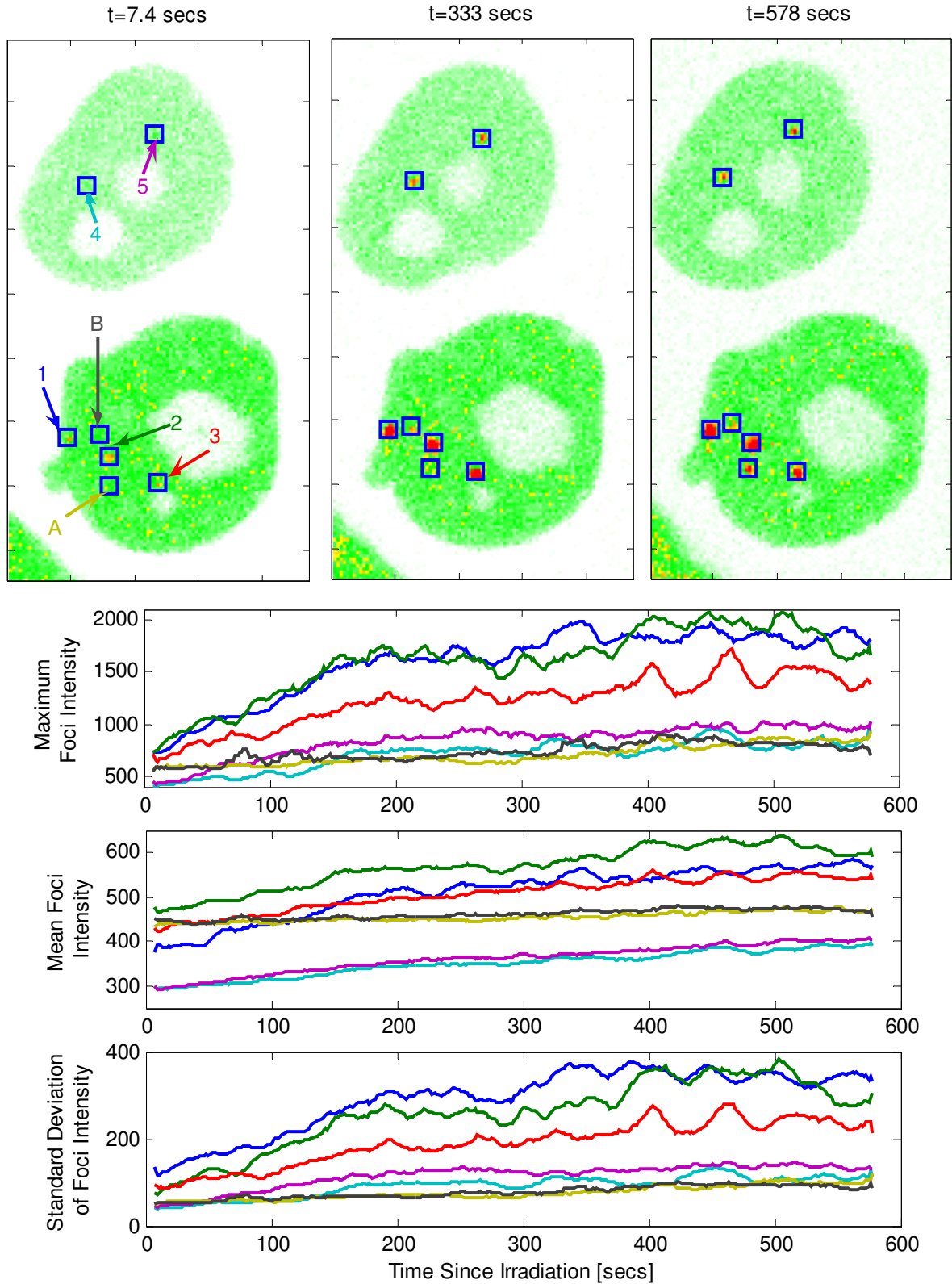
Figure 4-13   *Localisation of PCNA in 2D following irradiation at 50mW*
Images show the original data at different times after irradiations. The blue boxes indicate the ROI for the foci created by the laser irradiation. The maximum, mean and standard deviation of intensity are calculated for each ROI and at 1.6 second intervals. The data plotted in the figures below the images have been smoothed using a moving average with a window span of 11 samples. ROIs 1-3 and 4-5 are at the damage site whilst the ROIs marked A&B
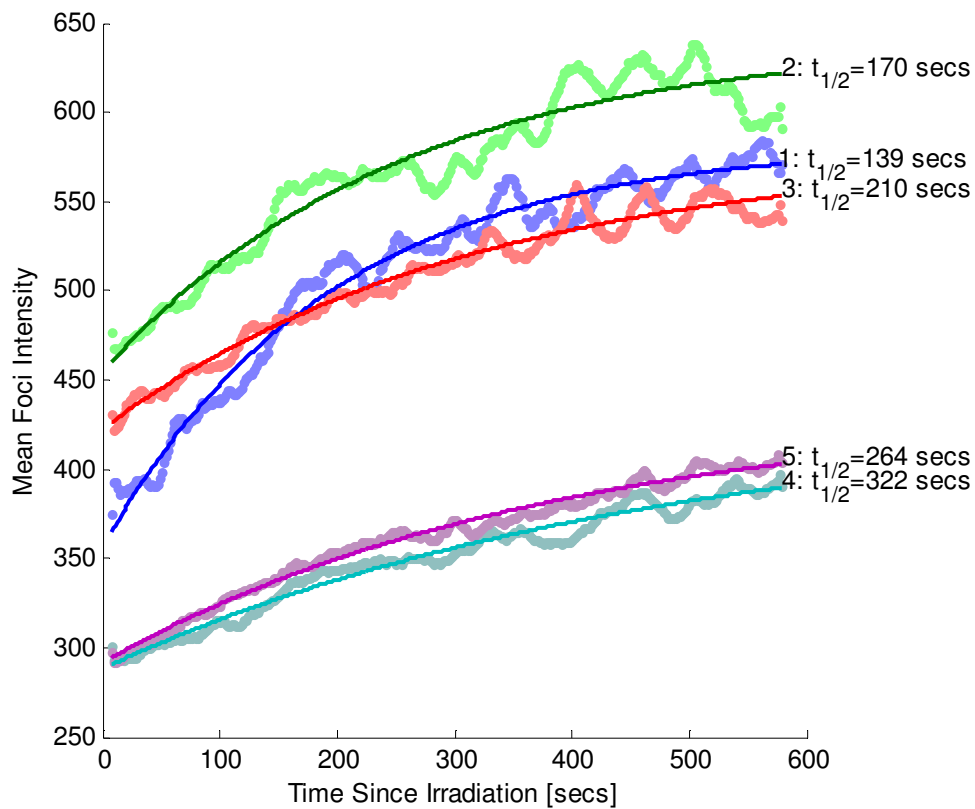
Figure 4-14 **Fitting of PCNA localisation following irradiation (Laser at 50mW)**
Images show the original data at different times after irradiation. The blue boxes indicate the ROI for the foci created by the laser irradiation. The maximum, mean and standard deviation of intensity are calculated for each ROI and at 1.6 second intervals. The data plotted in the figures below the images have been smoothed using a moving average with a window span of 11 samples.

ROI	a	$t_{1/2}$ [secs]	b
1	223±2	139±4	361±2
2	183±3	170±10	455±3
3	153±3	211±11	422±2
4	142±5	322±21	288±1
5	143±2	264±11	291±1

Table 4-4 **Results from fitting PCNA localisation dynamics (Laser at 50mW)**
ROIs 1-3 and ROIs 4 and 5 are from the lower and upper cells respectively shown in Figure 4-13
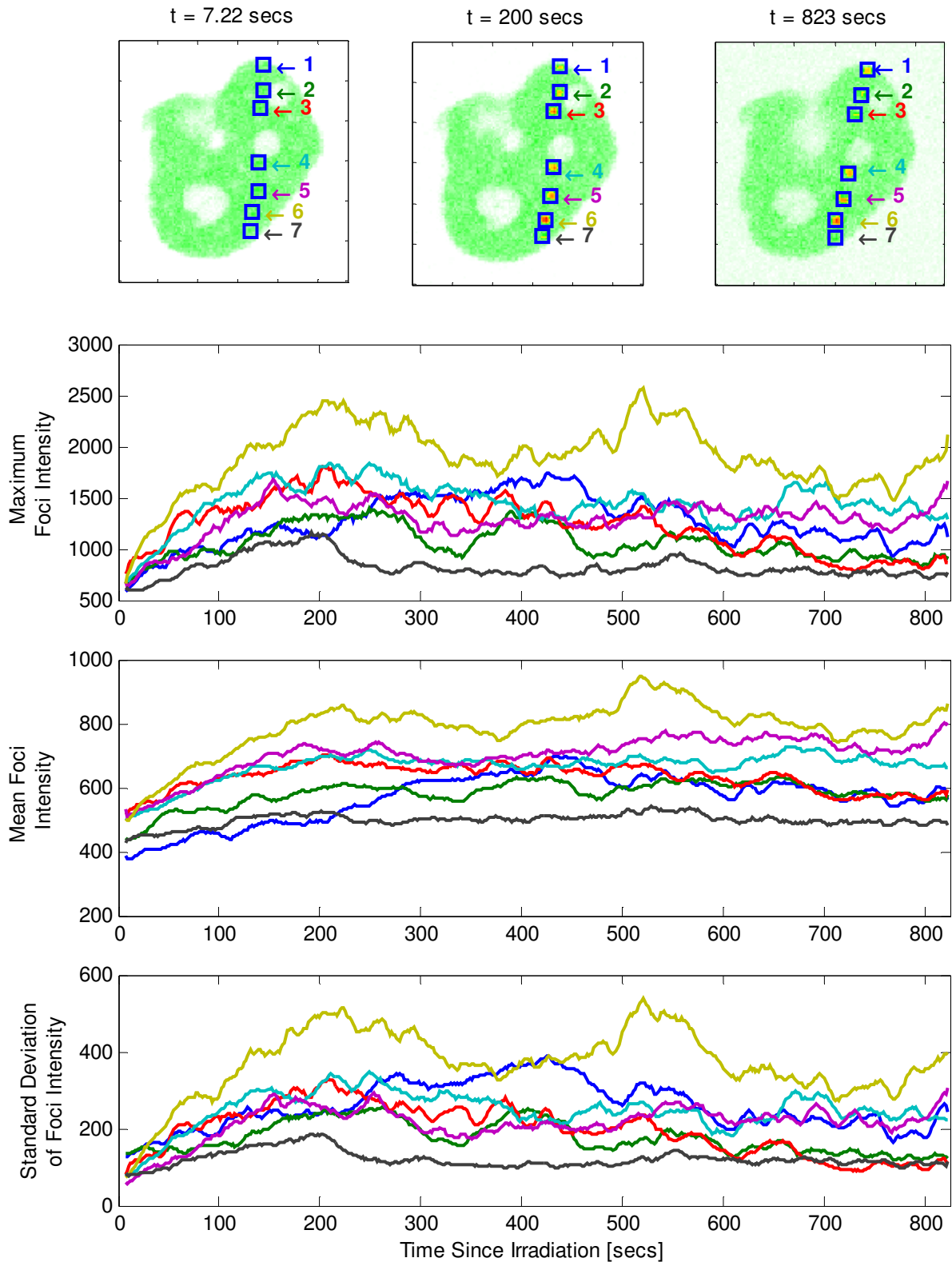
Figure 4-15 **Localisation of PCNA in 2D following irradiation at 25mW**

Images show the original data at different times after irradiations. The blue boxes indicate the ROI for the foci created by the laser irradiation. The maximum, mean and standard deviation of intensity are calculated for each ROI and at 1.6 second intervals. The data plotted in the figures below the images have been smoothed using a moving average with a window span of 11 samples.
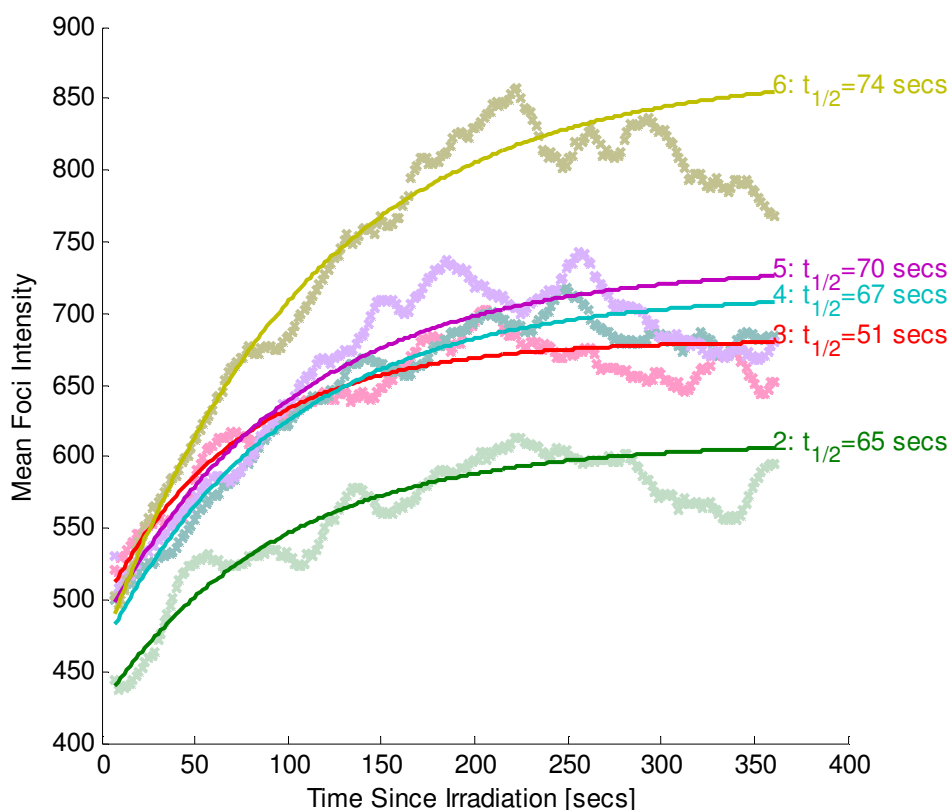
Figure 4-16   Localisation of PCNA in 2D following irradiation at 25mW

Images show the original data at different times after irradiations. The blue boxes indicate the ROI for the foci created by the laser irradiation. The maximum, mean and standard deviation of intensity are calculated for each ROI and at 1.6 second intervals. The data plotted in the figures below the images have been smoothed using a moving average with a window span of 11 samples.

ROI	a	$t_{1/2}$ [secs]	b
2	184±4	65±4	426±5
3	187±5	51±3	494±5
4	249±3	67±3	465±4
5	252±7	70±3	481±7
6	406±5	74±3	464±6

Table 4-5   Results from fitting PCNA localisation dynamics (Laser at 25mW)

PCNA Kinetics Conclusions

The modelled used to analyse the localisation of PCNA to DNA damage sites was possibly over-simplistic. It was primarily intended to measure how quickly foci of PCNA formed in response to 3P induced DNA damage. Considerable variation was observed in the half-lives of the localisation of PCNA with values ranging for 50-260 seconds. Whilst it was hoped that this could be related to laser intensity, insufficient data was analysed to be able to draw any conclusions. In the same field of view where two cells were irradiated with the same average laser power different values of the half life were measured and it appeared that cells that expressing

less GFP-PCNA had lower response times than those that produced a lot of GFP-PCNA. There are many other parameters that were not within experimental control that could have affected the results. In addition to the level of GFP-PCNA present in the cell, the phase within the cell cycle may well have impact on PCNA kinetics. The actual position of the damage site relative to important sub-nuclear structures almost certainly plays a role. These structures may only be visible under specific staining.

4.4. INTRA-CELL SIGNALLING

The appearance of the PCNA foci in response to, but not at, the targeted sites of damage was noticed in a number of instances during the experiments to determine threshold intensity levels required to induce 3P DNA damage and to observe the PCNA kinetics. These foci appear to have formed in sympathy to nearby DNA damage providing evidence for the existence of intra-cell signalling pathways.

In the final experiment with 3P induced DNA damage, a site was targeted with the IR laser at 50mW. The targeted damage site was chosen to be close to a pre-existing replication centre (see Figure 4-17) that was active, as indicated by the higher local concentration of PCNA. The target was irradiated for 25ms with 50mW average laser power, measured at the input to the laser scanner.

As has been seen in previous experiments, PCNA rapidly migrated to the damage site, and after about 120s the PMT was saturated. In this case, the gain on the PMT was deliberately set to be more sensitive so that small changes in the relatively less intense nearby replication centre could be more accurately measured. This will skew the intensity reading of the primary damage site.

The montage of images shown in Figure 4-18 shows how the PCNA distribution in the cell develops over the course of the measurement. The nearby replication centre (RC) brightens almost immediately after the damage has been caused. However, in addition to the RC that was identified prior to irradiation becoming brighter, a more remote RC also becomes significantly more intense albeit at a later time. This remote RC is also identified in Figure 4-18.
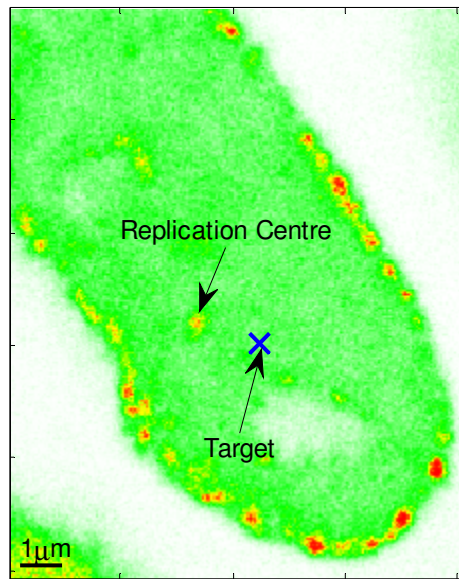
Figure 4-17   Mid S-Phase cell prior to irradiation with NIR Laser.

The area to be targeted is about 1.25μm from the replication centre identified. The bright red and yellow foci surrounding the edge of the cell are replication centres. The location and number of replication centres indicates that this cell is in the mid S-phase of the cell cycle.
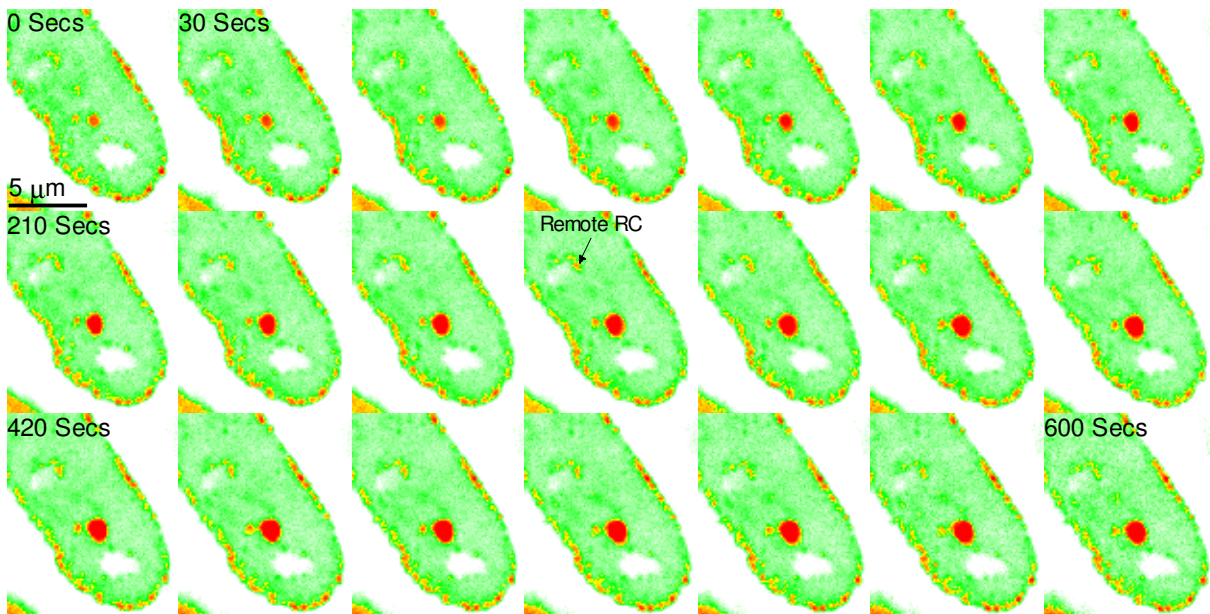
Figure 4-18   Montage showing development of sympathetic foci following DNA damage.

The first frame at 0 seconds was actually taken at 7.5 seconds after irradiation, due to the time required to switch the optics. Each subsequent frame is taken at 30 second intervals, and shows the initial growth of the targeted damage site, and increase intensity of the adjacent and remote replication centre (RC). After 120 seconds the foci at the primary target site saturated the PMT detector. After approximately 300s the remote RC reaches its peak intensity.

Using the foci tracking algorithm developed for the PCNA kinetics measurement that was discussed previously, ROIs 1 and 2 were designates at the near-by and remote replication centres (RCs) respectively. It was necessary to use the tracking algorithm as the whole cell moved considerably during the measurement. The ROIs were square and measured 7x7 pixels. The ROIs defined for the damage site and the background position were larger square ROIs measuring 12x12 pixels. The cell's movement was also tracked. Obviously the tracking algorithm which locates local maxima would not track a random background location. Similarly, as the damage site was saturated it would not be able to track the centre of the damage site.

Instead the movement of the whole cell was tracked by identifying the RC around the edge of the cell. The average displacement of these peripheral foci was applied to the manually selected damage site ROI and the background ROI so that these ROIs would move with the cell as a whole. The background ROI was used to compensate the photo-bleaching.
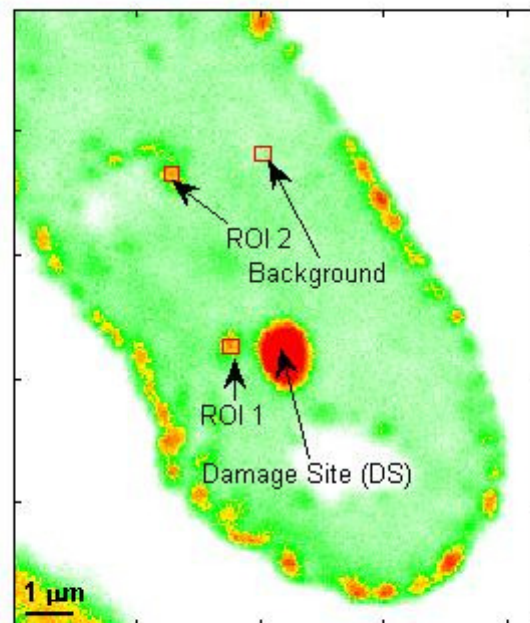
Figure 4-19   ***ROIs specified for the intra-cell signalling measurements.***

As in the measurement of protein kinetics, the mean intensity of pixels within the ROIs was measured. The mean intensity time profiles of the ROIs are shown in Figure 4-20. The saturation of the PMT at the damage site caused a marked kink in the intensity profile for that ROI in Figure 4-20. The nearby RC (ROI1) reacts almost immediately to the damage site, and begins to increase in intensity, reaching a maximum after about 400s, whereupon it rapidly decreases in intensity, returning to its initial level, presumably because its task has been completed.

There is a further remote RC that activates during the measurement. Arguably this could be in response to the DNA damage at the primary damage site. No change was observed in the mean intensity of the remote RC until 120s after the damage had occurred. After which there was brief rise in intensity, followed by a slower reduction in intensity. By the end of the 600s measurement the remote RC has returned to its initial level.
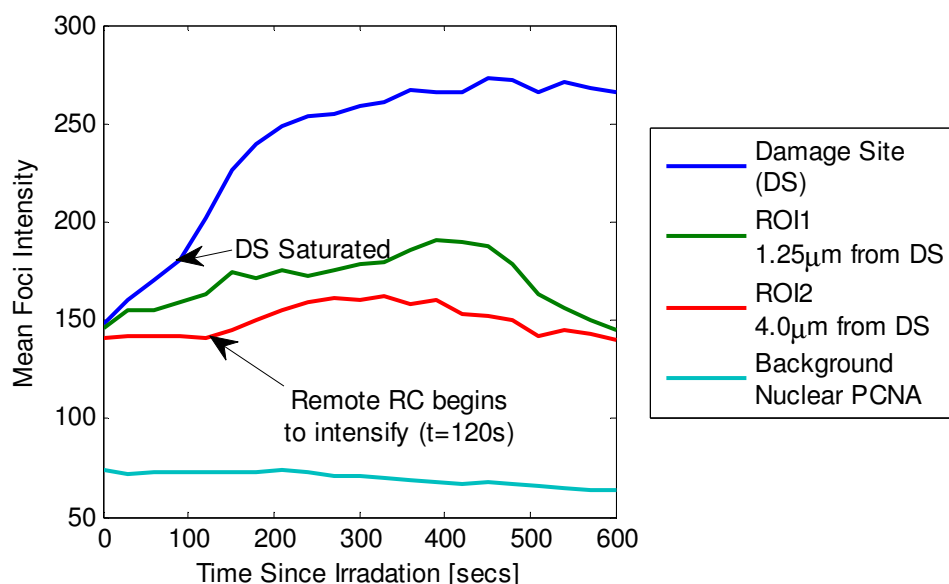
Figure 4-20   *Mean intensity of replication centres following damage at a nearby site.*
The Damage Site begins to increase intensity immediately and soon saturates the detector. The nearby replication centre in ROI 1 begins to increase in intensity immediately, whilst the remote replication centre remains at the same intensity for about 120s, before beginning to increase in intensity.

This is only a single measurement but if it can be shown to be repeatable then the lag time measured between damage being inflicted and the distant RCs being affected by cellular signalling molecules activated by the localised damage could provide valuable insight into the intra cellular signalling pathways.

4.5.   CONCLUSIONS

This system was successfully used to precisely induce UV type damage by a three photon process. By analysing the deposition of energy throughout the focal volume, it was established that previous papers have overestimated the peak intensity at the focus of the microscope as a consequence of underestimating the pulse broadening that occurs as the pulse transits the scanner and microscope objective and underestimating the focal volume of the objective lens. In these experiments it shown that there is a significant chromatic aberration and that great care must be exercised when selecting a microscope objective for multi-photon work to ensure that the chromatic aberration correction is employed over the IR portion of the spectrum that composes the short pulse. This work also illustrates the importance of measurements of the pulse

duration at the focus of the laser. The pulse duration measured in section 3.3.4 showed how an 86fs bandwidth limited pulse was broadened to 153fs before it had even reached the microscope. The microscope itself then broadened the pulse to 401fs. This level of broadening was totally unexpected although it seems that the chromatic aberration of the objective contributed significantly to this broadening.

The main result of these measurements is that 3P damage has been observed with intensities as low as 23±3 GJ/cm2. The live imaging techniques developed for this work have also revealed more information about protein kinetics of PCNA and showed that localisation occurs on a time scale of minutes. Significant variation in PCNA localisation was observed and further work is required in this area to identify all the parameters that determine the mobility of the PCNA in a cell.

The techniques developed here will allow a quantitative analysis to be performed in future work that seeks to address what factors influence protein mobility and the extent of the influence they have. They have been applied here to measure localisation of PCNA foci, not just at damage sites, but also at remote replication centres, providing evidence of intra-cell signalling pathways.

4.6. FURTHER WORK

The system developed here has already been successfully used again to carry out further work[63] on the analysis of oxidative damage using different cells and proteins. However the system could be greatly improved by the following additions, which have been place in order priority of implementation:

- Relocation of the laser, so that it is on the same table as the microscope;
- Selection of Objective for multi-photon work;
- Addition of a Pulse Compressor to control pulse duration at the focus;
- Implementation of Microscope incubator.

Having the laser in two separate rooms, on different tables, was necessary at the time of the experiments as the laser needed to be shared between many experiments. However, this is detrimental to the long-term stability of the system. It required hours of daily alignment for experiments, and considerably more alignment if the wavelength was changed. This was quite common as the other experiment used the laser at 800nm.

Although the objective that was used for IR multi-photon experiments in this work was supposed to be corrected for IR, the measurements clearly show that it was not. In a recently published paper Keatings et al [64] demonstrated a simple technique for characterising microscope objectives at long wavelengths for multi-photon(MP) work. Although the wavelength

range that they cover is for 1,400 nm to 1,650 nm, the techniques could be readily applied to the shorter wavelength required for the Ti:sapphire laser operating at 750nm. Before any new objective is purchased, for use in multi-photon work, it should be evaluated using this technique.

The addition of a pulse compressor, in combination with the techniques for measurement of pulse duration at the focus, would allow DNA damaging to be accomplished with considerably less average power to the laser. The same would be true of any MP process that may be used with the microscope. However, the addition of a pulse compressor is secondary to resolving the chromatic aberration issues with the objective lens.

A microscope incubator would allow long term imaging of live cells. Cells could have damage inflicted on them at different points to investigate the variation in sensitivity to DNA damage throughout the cell cycle and also the genomic viability of the damaged cells.

CHAPTER 5.

5. Automated counting of γ-H2AX Foci in radiation dosed cells

This chapter presents the implementation and performance analysis of three foci counting algorithms in 2D and 3D. The foci counting algorithms implemented were a simple intensity threshold algorithm, the Compact Hough Transform and Radial Mapping Algorithm (CHRAM) [65] and an algorithm developed in this chapter based on the Meyer watershed algorithm [66]. The effects and sensitivity to the detection parameters for each algorithm were investigated and a systematic method of determining these parameters was developed.

In 2D the CHARM algorithm dominated in performance, whilst in 3D the water shed algorithm was just as accurate, but executed in less time, and provided details about the foci, such as size and intensity distributions. This algorithm was applied to a study of radiation dosed fibroblast cells. Induced double strand breaks were induced and γ-H2AX foci formed at these lesions. The γ-H2AX was fluorescently marked by immunostaining and the number, average size and intensity of foci was studied as a function of the radiation dose received by the cells.

5.1. INTRODUCTION

Phosphorylation of chromatin histone protein H2AX occurs at double strand breaks (DSB) in cellular DNA. The phosphorylated protein is known as γ-H2AX and foci of this protein form in response to the geno-toxic stress formed at double strand breaks and stalled replication forks. γ-H2AX appears also to mark stalled transcription sites on chromosomal DNA where it promotes the binding of NDH II, the nuclear DNA helicase II [67].

DSBs in cellular DNA have serious implications for the stability of its genome, and the survival of the cell. H2AX that has been fluorescently tagged allows sites of DSBs to be visualised as foci of fluorescent material in the nucleus. By counting the number foci an estimate of the damage to the DNA can be made. Although this method is used extensively, the counting is most commonly carried out manually by eye using wide field microscopy. This has two main limitations. The first is that manual counting is open to bias on the part of the operator in terms of what the operator will consider to be a countable focus, the numbers of foci involved can be considerable and counting them time consuming, causing the task to become monotonous, increasing the likelihood of human error. The second limitation is that a wide field microscope cannot distinguish between two foci which might be on top of each other. Here the superior axial resolution of the confocal microscope allows the differentiation between foci that are in different focal planes, but in the same position in the XY plane.

An application was written in Matlab to read and analyse the data files produced by the Leica microscope. Section 5.2 covers the development of a robust algorithm to detect the foci and extract information regarding their dimensional distribution within the nucleus. Section 5.3 utilises the tool to measure the damage and repair to cellular DNA irradiated by different doses of the gamma radiation. The development of the application itself is not discussed, although its use is referred to in the text, and the source code is available on the enclosed cover DVD.

5.2. DEVELOPMENT OF A FOCI COUNTING ALGORITHM

The detection and characterisation objects in the 2D field is a general problem that has many applications in the conventional wide field light microscopy as well as topographical scanning probe microscopes such as STM, AFM and other derivative variants. There are already a number of programs that have been written to process this type of data including both commercial applications such as the Scanning Probe Image Processor (SPIP) and open source applications like Gwyddion. Both of these programs provide grain analysis tools that permit the user to detect & mark grains and obtain the properties about them. There was no openly available tool that would perform a similar function to identify 3D blobs in a volumetric data set.

After brief investigation it was apparent that within the available time constraints modification of Gwyddion to handle 3D datasets was too great a task. The Leica control software is also capable of recording time series and measurements of detector wavelengths. These represent an additional two dimensions of data. Selection of the appropriate dataset would also need to be integrated into the Gwyddion codebase.

Instead Matlab was used to develop a specific application to process and present the native data files produced by Leica Microscope control files. Matlab's image processing libraries and tools to manipulate multi-dimensional data made it particularly suitable to this application. The application that was developed provided a framework to experiment with different detection algorithms and their application to multi-dimensional datasets.

5.2.1.   CHOOSING A FOCI DETECTION ALGORITHM

Beyond the specific foci-counting application detailed here the detection of 3D blobs has further applications in medical imaging for MRI and CT Data. The approach adopted was to review 2D algorithms that could be adapted to 3D data. There are number of algorithms that have been applied to 2D analysis these include:

- Threshold Detection;
- Compact Hough And Radial Mapping (CHARM) method;
- Watershed detection.

Threshold Detection

Threshold detection simply marks regions that have intensity greater than a specified level. It is simple to implement, uses very little processing power but it is only really suitable for detecting relatively high contrast areas of high intensity on uniform background.

Figure 5-1 show a 2D example, using one section through a cell that has been exposed to radiation as the data source. It is clear from the image that if the threshold is set too high then foci are missed and if too low, the foci merge together and are counted as one. Simultaneously the detection algorithm becomes susceptible to background noise causing an artificial increase in the number of foci detected.

The image showing detection with a medium threshold exhibits all the problems of the both a high and a low detection threshold, having false positive detection, foci merging and missed foci.

Detection Threshold	Number of Foci Detected
High (1500)	95
Medium (900)	778
Low (500)	3138

Table 5-1   ***Foci Detection using different thresholds***

Table 5-1 lists the numbers of foci detected using each detection threshold. It is clear that the Low and Medium threshold situation the number of detected foci is dominated by the false positive detection rate.
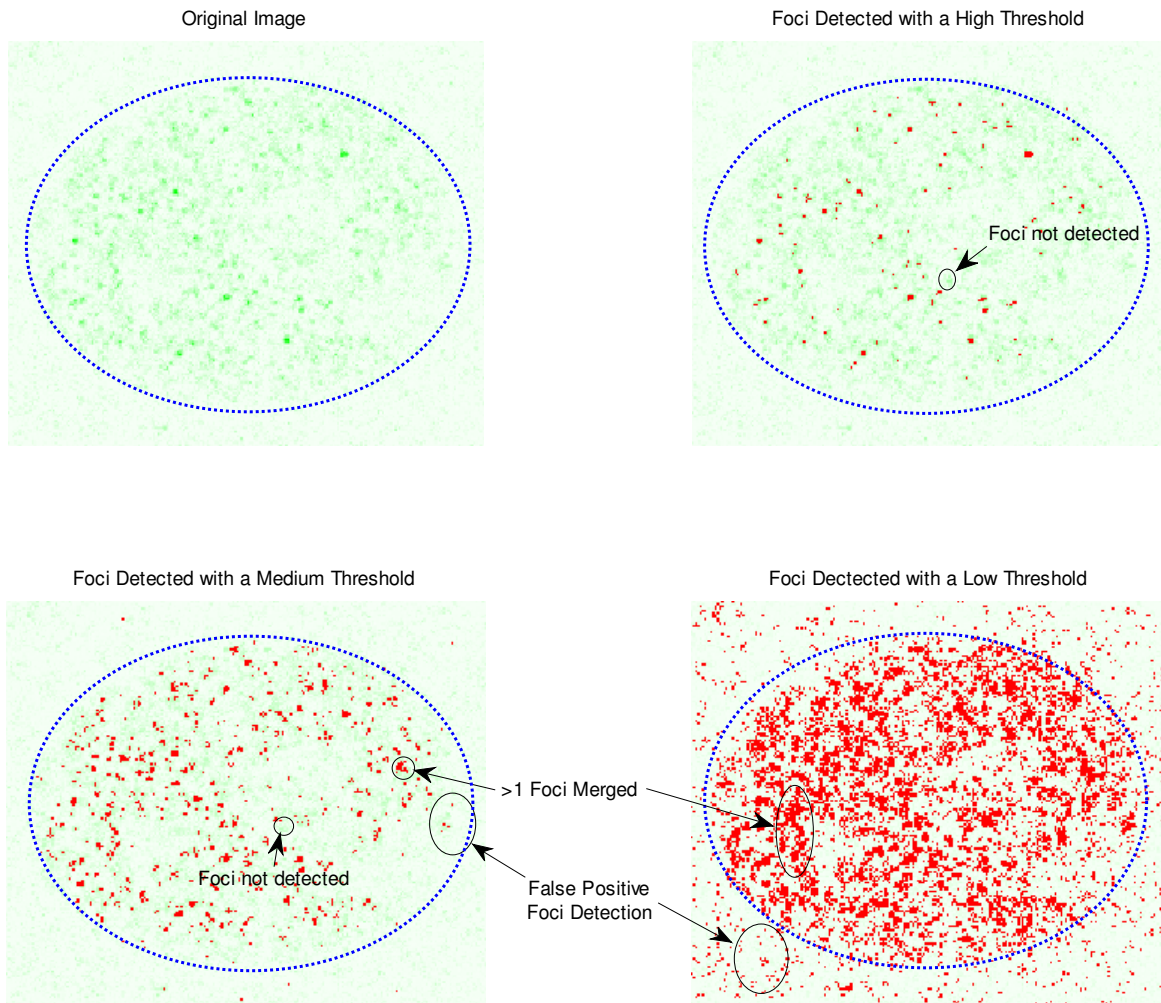
Figure 5-1   ***Threshold Detection of Foci***
A section through the nucleus of a cell exposed 2Gy of radiation. The cell was fixed shortly after exposure to the radiation with no time allowed for repair. The intensity was recorded with 12-bit resolution, allowing a maximum value of 4096 intensity levels. The high medium and low thresholds were 1500, 900, and 500 respectively. Areas coloured red exceed to threshold, and the blue dotted line indicates the edge of the nucleus.

The CHARM Method

The Compact Hough Transformation and Radial Mapping (CHARM) method was proposed and developed by Barber et al [65, 68]. That work sought to develop a fast method for

automatically counting γ-H2AX foci for high content screening in wide field microscopes. The algorithm developed only worked in 2D.

The vertical distribution of foci through a cell was compensated for by two approaches. The first employed an extended focus method in which the z-focus of the microscope was varied during the image acquisition period. The second was a more traditional technique, whereby images of sequential focal planes were acquired and a maximum intensity projection was created.

The algorithm described in Barber et al's work is designed to detect faint and indistinct circular objects. The algorithm has a number of steps, detailed below and depicted in Figure 5-2:

Two perpendicular Sobel operators are used to assess gradient magnitude and edge direction from the image.

Pixels with a gradient magnitude greater than a predetermined threshold are designated as "edgels".

At each edgel the direction information from the Sobel operation is used to draw a line perpendicular to the edge in an accumulator field. The line is drawn between the minimum and maximum expected radius. This causes the centre of the circular objects to become accentuated as the central pixel receives contributions from all the detected edgels around it.

The accumulator field is smoothed using a Gaussian low pass filter.

Peaks in the accumulator field are extracted using an H-Maxima transform. This is implemented in MathCAD using the `imextendedmax()` function in the image processing toolbox.
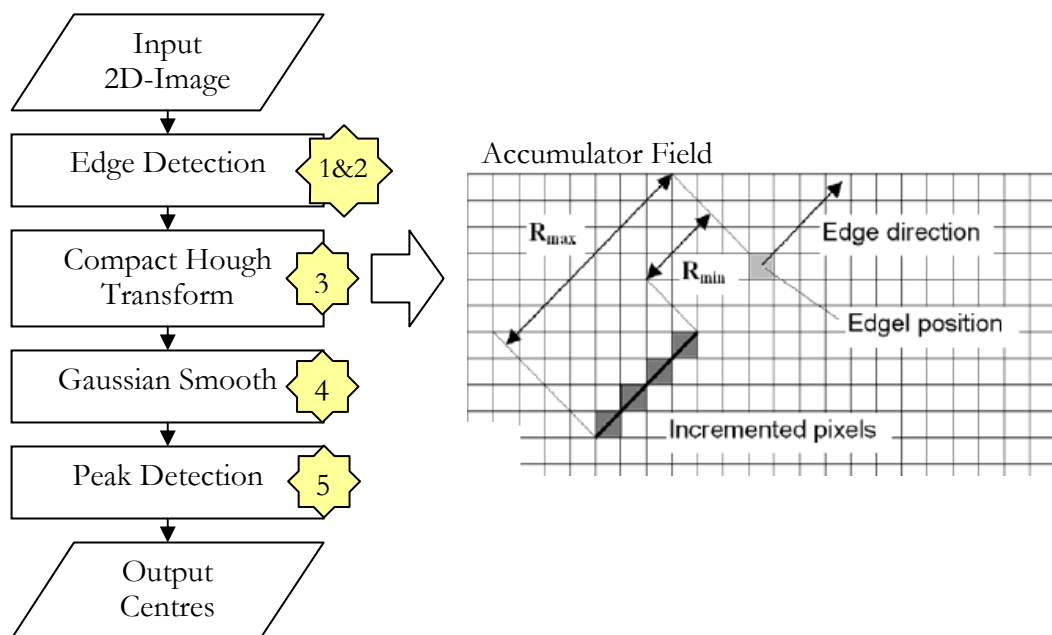
Figure 5-2   The CHARM Algorithm
This figure shows a flow chart of the main processes in the CHARM algorithm. The accumulator field is populated using the radial lines drawn between R_{min} and R_{max} in the direction of the edge gradient. (Figure adapted from [65])

Maximum Intensity Projection

Detected Edgels

CHARM Accumulator Field

Detected Foci Centres
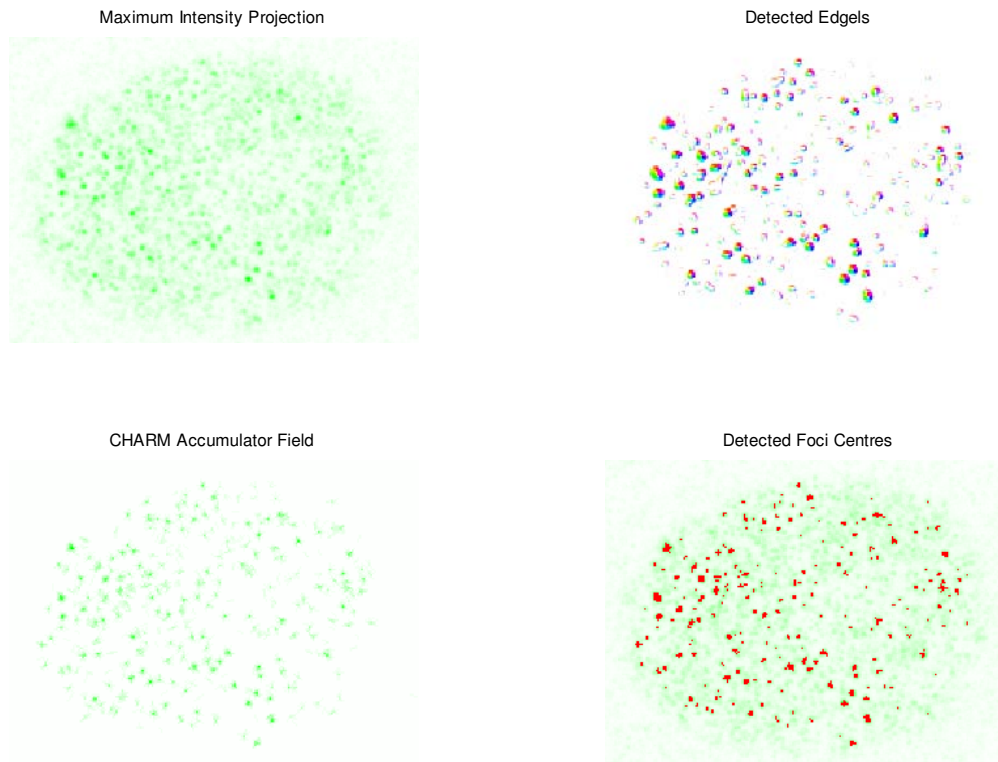
Figure 5-3   2D CHARM Detection Algorithm - High Edgel Threshold
(Top Left) shows the original 2d image. (Top Right) shows the output from the sober operates. The gradient magnitude and direction are encoded in the colour using saturation and hew respectively. (Bottom Left) Shows the content of the CHARM accumulator after Compact Hough Transform. (Bottom Right) Shows the original image overlaid with the detected foci centres, shown in red. The edge detection threshold was set to 1500, and 193 foci were detected.

Figure 5-3 above and Figure 5-4 below show a cell processed with the CHARM algorithm. It is the same cell that used in the threshold example, except that the starting data for this cell is a maximum intensity projection of all the focal planes (xy-planes) in the stack of images.

Both figures use the same source data, and only vary in the choice of the edgel detection threshold. The CHARM Algorithm first operates on the intensity field, with orthogonal Sobel operators. Sobel operators are frequently used in image processing for edge detection. They produce a field that is proportional to the gradient in the horizontal or vertical directions. These horizontal and vertical components of gradient are then transformed into a two scalar fields, representing the magnitude and angle of the edge. Sobel operations can be implemented entirely with integer operations, which greatly reduce the processing requirements.

The Edgel detection threshold determines the minimum magnitude of the gradient a pixel must have, to be used in the Compact Hough Transformation (CHT). The detected edgels image in Figure 5-3 and Figure 5-4 show the edgels that were selected in each case. The pixel colours in the image depend on the magnitude and angle of the gradient. A Hue, Saturation and

Value (HSV) colour scheme was used. The hue varies the colour in cycle from red-blue-green-yellow-red, and represents the direction of the slope, whilst the magnitude of the slope is encoded using the saturation. Whiter pixels have lower magnitudes, whilst pixels with a large magnitude appear to have a more intense colour. The edges of a focus appear as a rainbow coloured circle.
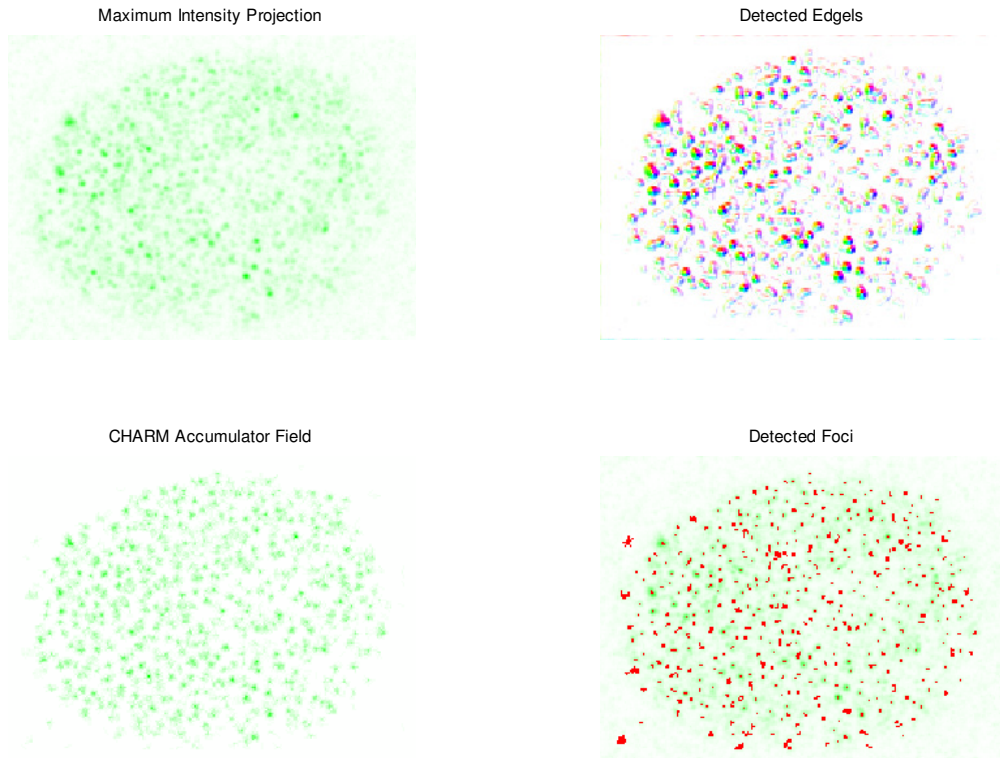
Figure 5-4   *2D CHARM Detection Algorithm – Low Edgel Threshold*
(Top Left) shows the original 2d image. (Top Right) shows the output from the Sobel operators. The gradient magnitude and direction are encoded in the colour using saturation and hue respectively. (Bottom Left) Shows the content of the CHARM accumulator after Compact Hough Transform. (Bottom Right) Shows the original image overlaid with the detected foci centres, shown in red. The edge detection threshold was set to 750, and 403 foci were detected.

Once the edgels that will be used in the CHT have been selected, pixels in the accumulator field are incremented along the line calculated in the CHT, as discussed previously and illustrated in Figure 5-2. The results are shown in the "CHARM Accumulator Field" images. The star patterns can be seen plainly in the images where the lines drawn from each edgel during the CHT cross over at the centre of the detected foci.

These peaks are much more distinct that those in the original intensity image, and can be automatically detected using H-Maxima transform. The resulting Foci centres are displayed as red dots on top of the original data in Detected Foci Image.

Edgel Detection Threshold	Number of Foci Detected
High (1500)	193
Low (750)	403

Table 5-2   ***Foci Detection using different thresholds***

These results show that the CHARM algorithm works well with 2D data. This algorithm has a number of parameters to optimise its operation. These include:

- The edgel detection threshold.

- The R_{min} and R_{max} parameters which are the upper and low bounds for the radii of the objects to be detected.

Configuration of these parameters requires some prior knowledge of the objects under analysis. The figures above used R_{min} and R_{max} of 1 and 4 pixels respectively, which were determined to provide sensible results for our data. These values would need to be reconsidered under any of the following conditions:

The physical size of pixels is changed (by either adjusting the optical zoom or adjusting the sampling digestion process).

The size of the objects under analysis was found to be significantly different.

It is interesting to note when the edge detection threshold was increased, although number of foci increased markedly, a careful inspection of the detected foci output by the algorithm, showed that the false positive rate remained very low. This indicates the edge detection threshold need only be set above that of the background noise.

The next stage in the CHARM algorithm as described by Barber et al involved a boundary search and radial mapping to determine the extent of the foci. However, this was not reported with sufficient detail in those papers to allow the functionality to be recreated here. The Gradient map was too noisy to be used for boundary detection in our dataset.

The algorithms were able to identify the foci, but in this form it requires the image to be flattened to 2D. This has two effects. If two foci are on top of each other or even very close to each other they are effectively merged and counted as one, also any information about the vertical distribution of the foci is lost.

In spite of the lack of effective boundary detection the algorithms ability to accurately determine the centres of the foci, and relatively low sensitivity to the edge detection threshold parameter made it a strong candidate for extension to 3D.

The Watershed Algorithm

The watershed algorithm in two dimensions is conceptually very simple. Consider a topographical image in the XY plane. The intensity at each point is then manifesting as a height

projection such that islands of high intensity present as mounds on the landscape. The landscape can then be turned upside down and the mounds become bowls. Water (or rain) that is sprinkled on the surface collects in the bottom of the bowls. As the bowls fill, water from two bowls will meet. This marks a watershed boundary. In this way all the foci can be detected, not just their centres but also their extent.

The Fernand Meyer [66] watershed algorithm was used. It is implemented in the image processing toolbox of Matlab. However this algorithm requires some pre-processing to optimise its performance and reduce over-segmentation which otherwise leads to a high false positive detection rate. The steps in the process are as follows and sample images of the 2D watershed algorithm are shown in Figure 5-5:

1. **Acquire Image** (Figure 5-5a)

2. **Smooth (3x3 Gaussian Kernel)** – Smoothing helps create more gently varying intensity fields and reduces over segmentation in the watershed algorithm.

3. **H-Maxima suppression** – Helps suppress small background maxima.

4. **Initial Threshold Detection** (Figure 5-5b) – Cell is selected; by applying low level threshold, to automatically define a region of interest (ROI).

5. **Dilate the mask** region (Figure 5-5c) – The ROI mask is dilated by 1 pixel in every direction.

Perform Fernand Meyer **Watershed Algorithm** (Figure 5-5d) – The watershed algorithm is executed on the smoothed data in the region defined by the threshold.

Reduce labelled regions to their full width at half maxima (Figure 5-5e)

Original Image   Initial Threshold Detection   Mask Dilation

Watershed Detection   Foci Shrinking

Interstitial region
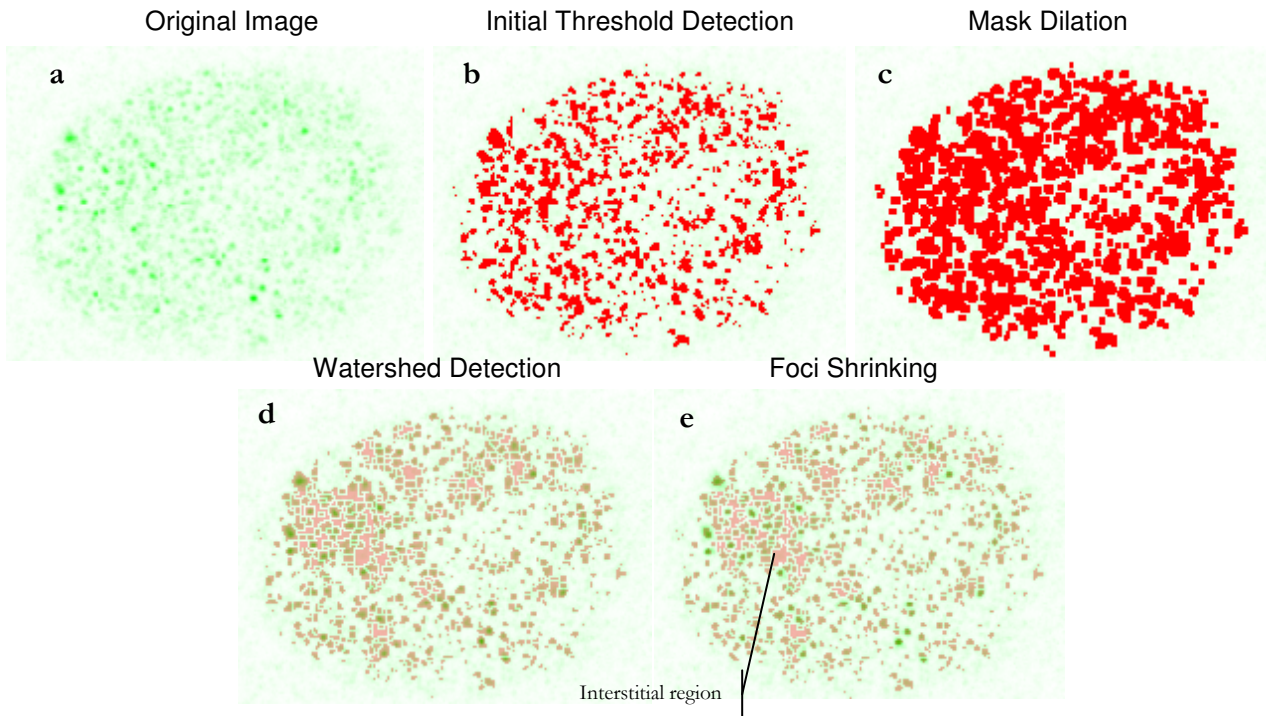
Figure 5-5   ***Watershed Detection in 2D***
a) Shows the original data, which is a maximum intensity projection through the z-series of XY Planes. b) An intensity threshold operation identifies the parts of the cell that might be foci, providing a rough ROI, which is expanded by a morphological dilation (c). The watershed algorithm is executed on the original data, in the regions defined by the mask (c) and the resulting detected foci are shown in (d). The regions identified by the watershed algorithm are analysed and reduced in size so that only the upper portion of their full width at half maxima (FWHM) are high-lighted, allowing more consistent automatic assessment of their size. 680 foci were detected.

It can be seen from the figure that the foci have been detected and marked, however there are a significant number of regions that have been detected by the watershed algorithm that do not contain foci. These regions have been marked only by virtue of the fact that they are entirely surrounded by other foci, and by analogy with the watershed concept, the water simply has nowhere to go. This would be a very shallow pool. There are number of parameters that need to be adjusted to optimise the foci detection. These are:

- The size, shape and strength of the smoothing kernel.
- The threshold for maxima suppression, which is used by the h-maxima transform.
- The threshold value for initial threshold detection.

Overview of 2D Grain Marking Algorithms

In two dimensions, the CHARM algorithm was the most robust and accurate marking algorithm, however, it was only capable of marking the centres of the foci, and in its current form is limited to 2D applications. The simple threshold detection mechanism was shown to be inadequate for the data sets we are working with. A foci detection algorithm that utilised the Fernand Meyer watershed algorithm was also developed. This algorithm was capable of detecting

and marking the entire foci, rather than just the centre, allowing size and shape information to be extracted. Unfortunately in 2D this algorithm suffered, from an over-segmentation problem, causing the foci-number to be artificially increased.

Discussion of these algorithms in 2D provides grounding for their extension into the 3D and multi-dimensions data space which will be further discussed in section 5.2.4.

5.2.2.   VISUALISING 3D DATA

One of the biggest problems with working with volumetric data is visualisation, presentation and exploration of the data. There is an enormous amount of data in even a single XY-Plane and a confocal z-series typically contains 30-40 slices. A typical method for presenting this data is to show a series of focal Planes at different z-positions through the stack of images, as has been shown in Figure 5-6. Even here, there are more sections than can feasibly be shown on the page. Although the dataset has 40 slices, only 20 images are shown. For the most part adjacent slices are very similar, and so adjacent slices are averaged to show contributions from all the slices.

Presentation in the manner of Figure 5-6 is acceptable for creating an idea of how the cell changes in the z direction but an alternative presentation (Figure 5-7) displays data as a sequence of verticals (YZ plane) from left to right across the cell. This reveals two things about the data which are not apparent from the XY planes in the series. Figure 5-7 shows the extent of the "on top" foci problem, where two distinct foci are vertically above each other. When a maximum intensity projection is used (as was the case previously in section 5.2.1 on 2D foci detection algorithms) to flatten the image these foci are merged. Even if foci are not directly on top each other, they may still overlap making them inseparable in the maximum intensity projection.
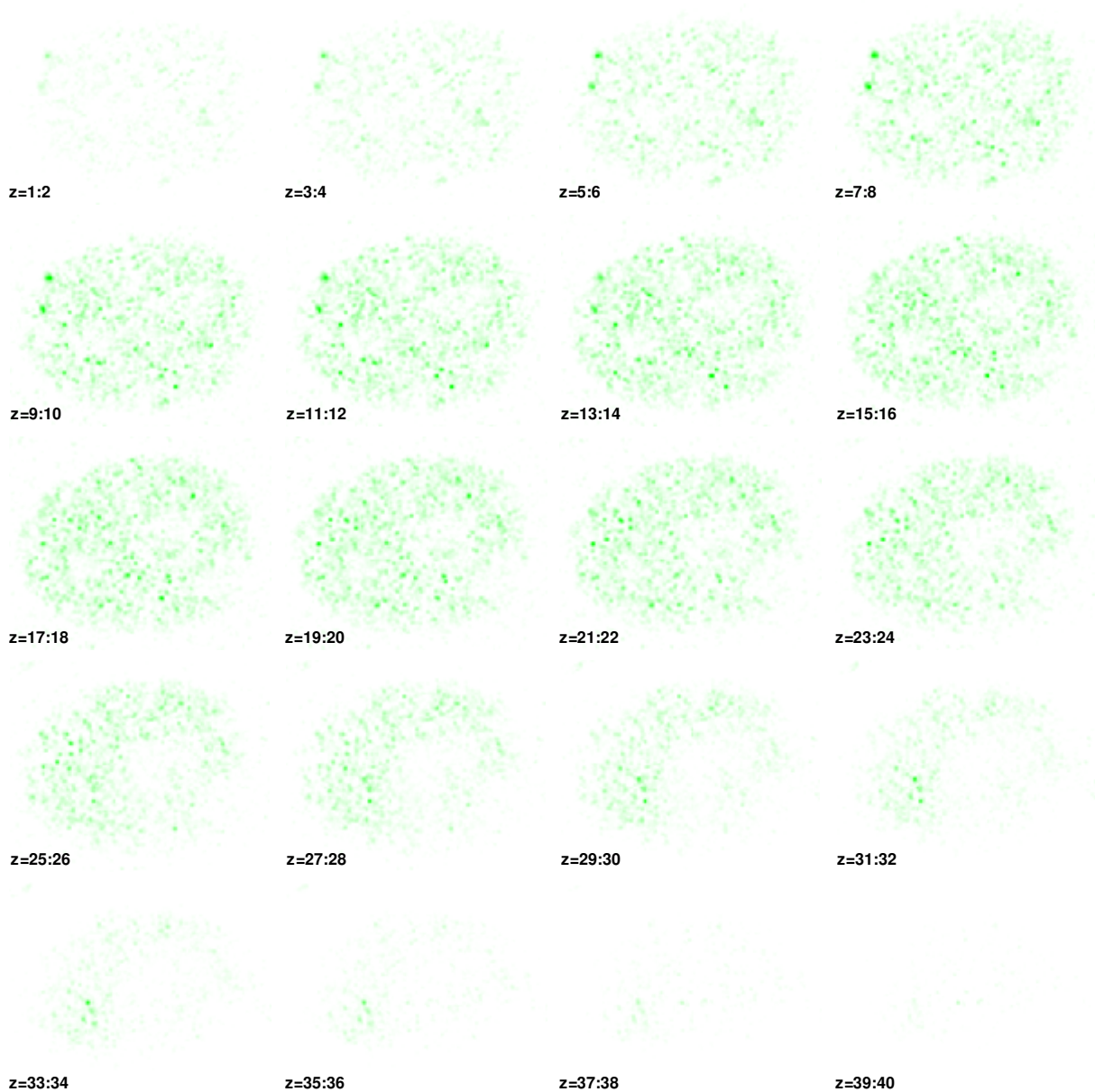
Figure 5-6   Z-Series of Sections Through a Nucleus
Each individual image is a pixel-wise average of two z-slices from the original dataset. The label in the bottom left corner of each image indicates the range of slices that contributed to that image. The printed intensity is consistent between images to facilitate comparison of the images in this figure.
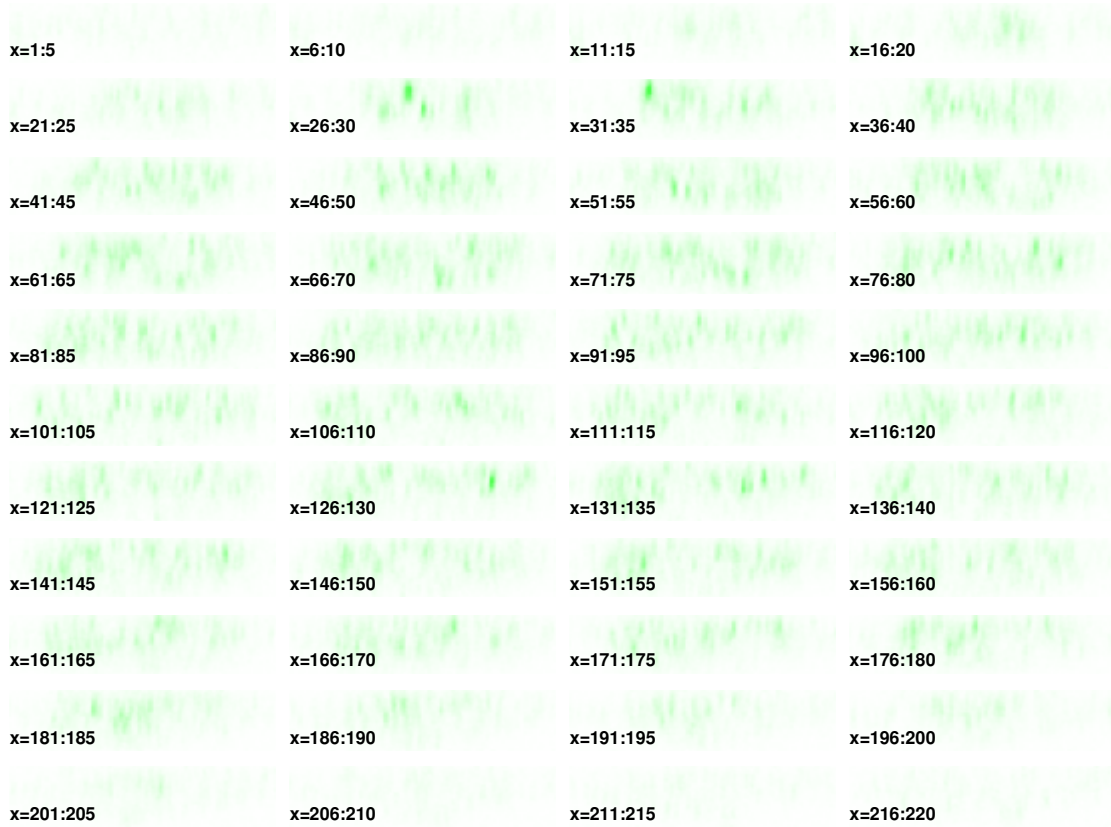
Figure 5-7   X-Series of YZ Sections Through a Nucleus
Each individual image is a pixel-wise average of five x-slices from the original dataset. The label in the bottom left corner of each image indicates the range of slices that contributed to that image. The printed intensity is consistent between images to facilitate comparison of the images in this figure.

Another solution to the problem of presenting 3D data is to utilise 3D rendering technology. The data can be plotted in a virtual 3D space called a "scene". The lighting and viewing angle is specified and realistic view of a 3D object can be rendered. There are two main problems with this approach; the first is that the confocal volumetric dataset contains data throughout its volume and data in the foreground obscures the data behind it. This can be partially resolved by making the whole structure transparent as has been done in Figure 5-8. The second problem is that in a static printed image it is difficult to get an accurate idea of the perspective especially with such an ephemeral subject with its poorly defined low contrast boundaries. Applying different colour-maps to different parts of the intensity spectrum can help identify high intensity features, but this is in essence thresholding and as such it has all of the problems associated with it.

Despite the difficulty that 3D rendering presents for static images, it is fast enough to be performed in real time. This gives the user the ability to view the object from a range of different angles and so develop a good idea of the perspective whilst exploring the data.
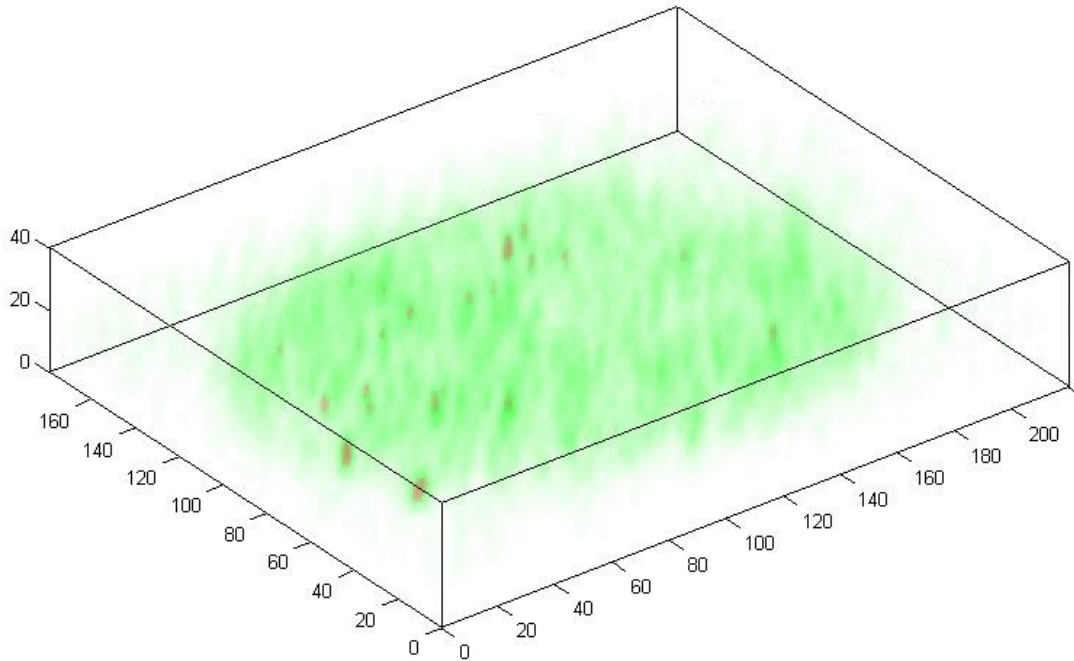
Figure 5-8   **3D Cloud Volume Visualisation**
This visualisation was created using vol3d[69] command, high intensity voxels appear as a brighter green, and have a lower transparency. Very high intensity pixels are shown in red.

The common theme in these 3D visualisation techniques is that visualising 3D data without sacrificing detail is impossible. Whilst viewing individual sections can reveal subtle differences on small scales, this comes at the expense of seeing the bigger picture. The 3D presentation in an interactive live environment allows the user a broader feel for the data. However effective quantitative analysis is very difficult.

One final variation of the presentation of 3D data through the use of sections is shown in Figure 5-9. It only shows a limited amount of data; three orthogonal sections through the data space intersecting a single point are displayed adjacent to each other. The lines drawn on top of the images indicate the positions the adjacent sections have been taken through. The colour scale has been selected to provide good contrast over the complete intensity scale. The red colour at the top of the scale is reserved to mark regions of interest.
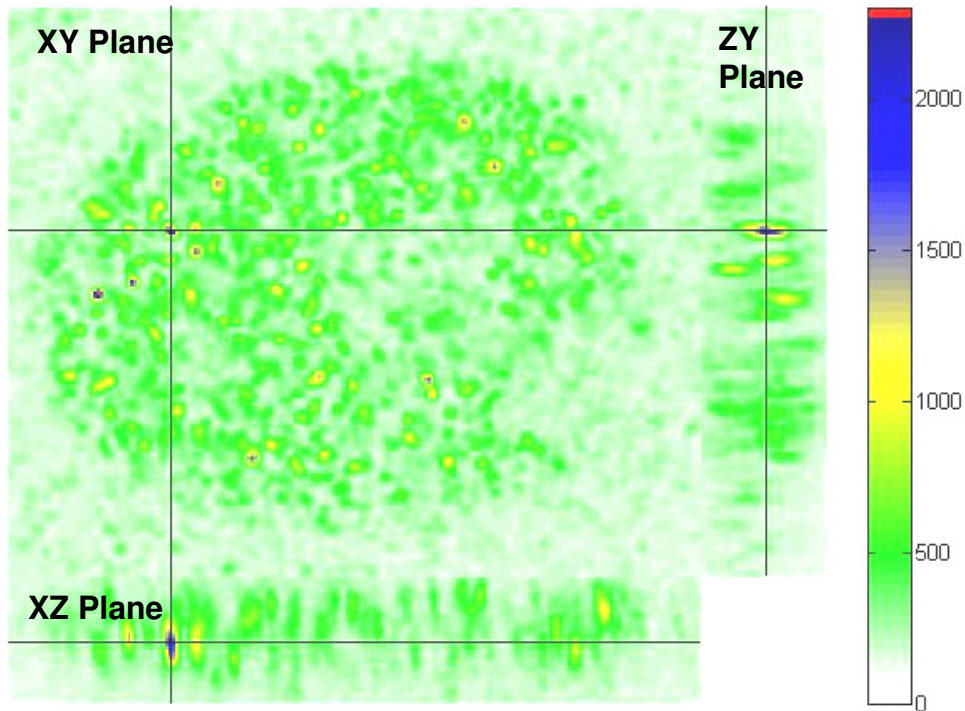
Figure 5-9   ***XY-XZ-ZY Sections through a Nucleus***
The figure shows three sections. The main image is a single XY Section from the z-Series. The adjacent images are vertical sections through the stack of XY Sections at the positions indicated by the crossed-hairs.

5.2.3. THE DATA EXPLORER

The Data Explorer is an application that has been written in MATLAB for the purpose of displaying, navigating and analysing confocal data containing foci. It provides a GUI environment to develop foci detection algorithms in 3D. It can read the native Leica data file format and has support for time, detector wavelength and channel selection. It also supports a range of 3D filtering tools which include Gaussian Smoothing, Median Smoothing and H-Maxima filtering.

The presentation shown in Figure 5-9 is especially useful for looking at an individual object as the cursor can be placed in the middle of the object. This presentation is used as the interface in the data explorer (Figure 5-10) that was developed to test and demonstrate the 3D foci detection algorithms. The user is able to navigate the data-space by dragging the mouse over any of the sections, repositioning the cross-hair as it moves. Positioning the cross-hair in XY-Plane image automatically adjusts the section displayed in the adjacent images. Similarly, positioning the cross-hair in the XZ or ZY plane permits selection of the XY-Plane that is shown in the XY-Plane image.
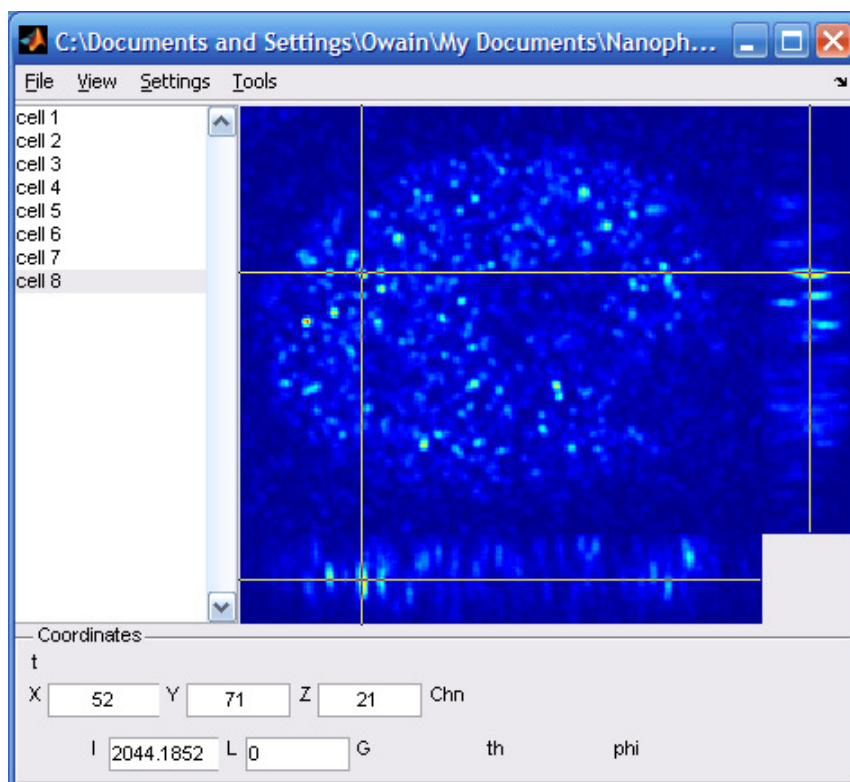
Figure 5-10   Data Explorer for Foci Detection
A Screenshot from the data explorer.

5.2.4.   FOCI DETECTION ALGORITHMS IN 3D

Section 5.2.1 reviewed a number of algorithms that have been used to detect foci in 2D images. This section discusses the modifications needed to extend the functionality of these algorithms to 3D. All the algorithms covered in Section 5.2.1 were implemented in the Data Explore application. For all the algorithms, the detection process is similar and is briefly explained in Figure 5-11. To facilitate comparison of detection techniques, all the algorithms assessed will be executed on the same data set.

Original data was acquired using the confocal microscope described in chapter 3. The cell was dosed with 2Gy of radiation and the γ-H2AX was stained with Alexa 488, a fluorescent die. The objective was a 63x Oil Objective with a numerical aperture 1.4. The confocal scanner was configured to give a voxel size of 115x115x112nm, and to record intensity with a bit-depth of 12bits per voxel. This was as close to cubic pixels as could be achieved. Other parameters were configured to optimise the image quality.

Using voxels with the same dimension in each direction simplifies the analysis. Prior to detection, the data was smoothed using a 3x3x3 Gaussian kernel, with a standard deviation of .65, followed by an h-maxima suppression filter. Regional maxima with a height of less than 200 intensity units were suppressed.

```
┌─────────────────┐
│      Start      │
└─────────────────┘
         │
         ▼
┌─────────────────┐      Smoothing reduces the effect of noise from the
│     Smooth      │──┐   imaging detectors used in the acquisition of the
└─────────────────┘  │   data. Smoothing can be achieved used either a
                         Gaussian or box shaped kernel.
```

Smoothing reduces the effect of noise from the imaging detectors used in the acquisition of the data. Smoothing can be achieved used either a Gaussian or box shaped kernel.

Mark Foci
(Creates the mask layer)

The detection algorithm identifies the voxels that form foci in the data volume. These voxels are marked in a mask layer. The mask layer has the same dimensions as the volume data, but contains the mask data instead of the intensity data.

Label Foci
(Creates the label layer)

Once the foci have been marked a labeling algorithm identifies groups of connected voxels. Each group of pixels is given a unique identifying number. The MatLAB function `bwlabeln()` is used. This label data, similarly to the mask data, is stored in a label layer.

Calculate Statistics

The label layer is used to extract region properties, which are returned as an array of structures containing a range of information about each of the detected foci. This is achieved using the `regionprops()` MatLAB function.
Further processing allows measurement of the maximum, minimum, mean and modal intensity values, as well and weight equivalent diameters.

Figure 5-11   ***Flow chart showing the general Foci Detection process.***

5.2.5.   ANALYSIS OF FOCI PROPERTIES
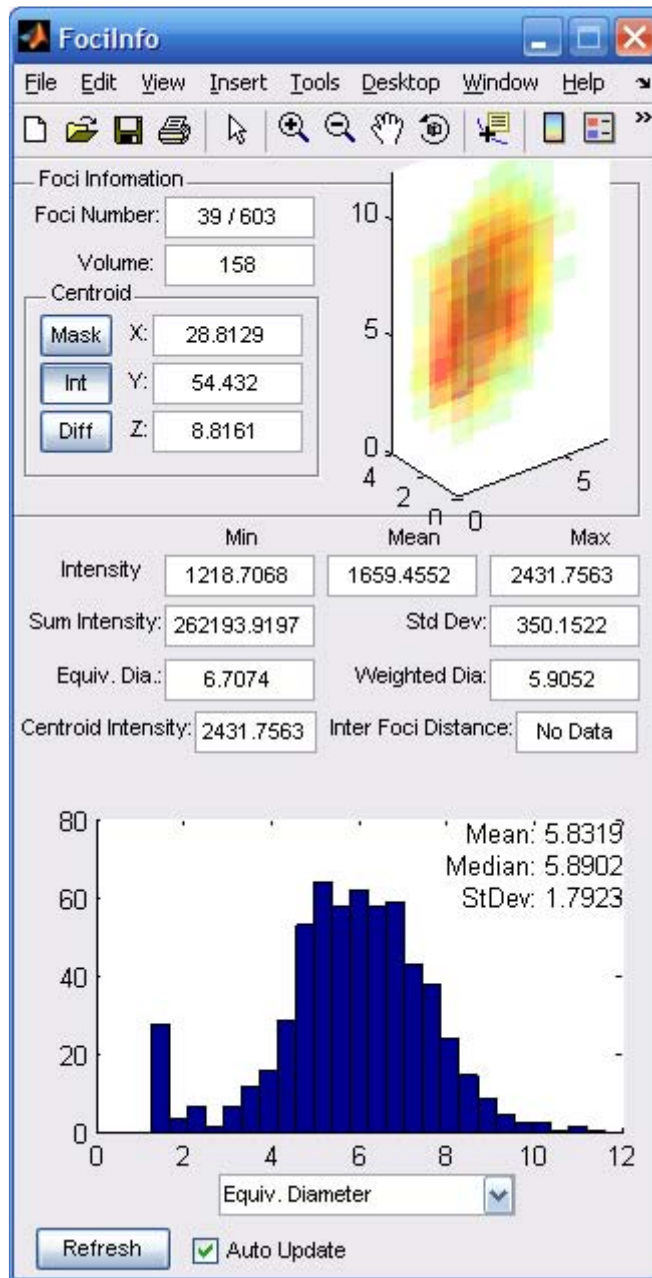
Figure 5-12   Foci Information Display
This window displays information about the detect foci.

The Foci Information dialog, shown in Figure 5-12, presents a wide range of statisical properties of the detected foci to be analysed. Histograms of the size, intensity and spatial distribtuion characteristc of the detected foci population may be plotted. Individual foci can also be selected allowing a 3D rendering of the foci to be visualised in the Foci Information dialog. The size, volume of the selected focus as well as maximum, minimum and mean intesities of the voxels that makeup the focus are displayed on the Foci Information dialog.

Threshold Detection in 3D

The extension of the threshold algorithm from 2D to 3D is trivial. The mask layer simply indicates whether the value in the data space is above or below a predetermined threshold. The threshold detection algorithm was executed on test data for a range of threshold values. In Figure 5-13 the number of foci detected was plotted as a function of the detection threshold.
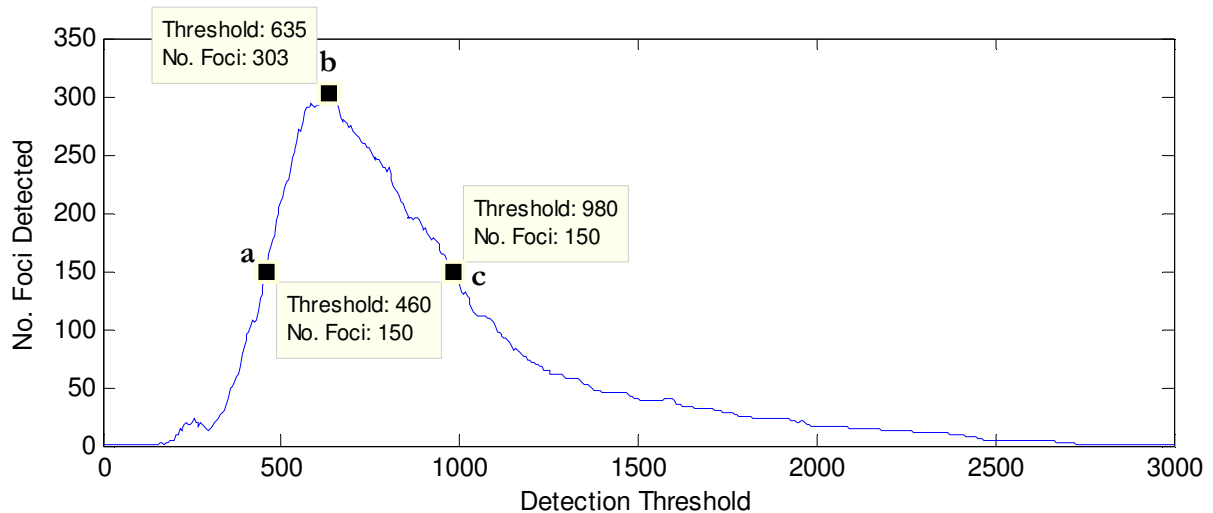
Figure 5-13 **Dependence of Foci Detection sensitivity as a function threshold value**
Figure shows the variation in the number of Foci detected as a function of the detection threshold used. At the points a, b, c snapshots of the data and marked regions were recorded. These are shown in Figure 5-14 a-c respectively.

At very low thresholds, all the voxels are marked and consequently they are all in contact with each other so only 1 connected region is detected. As the threshold is increased, fewer pixels are marked and the region is broken up into smaller regions. However, these smaller regions are still significantly larger than a single foci, Figure 5-14e illustrates this well. The 3D image of the detect "foci" shows the connected network of marked voxels actually contains anything from 8 to 14 foci. It also illustrates the 3D visualisation problem again, as at first glance, from the section that is presented in Figure 5-14a, this might not be apparent.

Figure 5-14b displays the marked regions when the detection threshold is set to yield the largest number of foci, corresponding to point b in Figure 5-13. At this threshold there are still multiple foci being detected as one focus, as shown by Figure 5-14e. At the same time, the threshold is already too high to detect many of the foci. As the threshold is further increased, fewer and fewer foci have a large enough absolute intensity to be detected. Figure 5-14c&f clearly show that the threshold is set too high, and the number of foci is underestimated.

The threshold detection method consistently underestimated the number of foci. Even when the threshold value was chosen to maximise the number of foci detected it was clear that large numbers were not being included. If the threshold was reduced, the marked region became contiguous resulting in an artificially low number of detected foci.
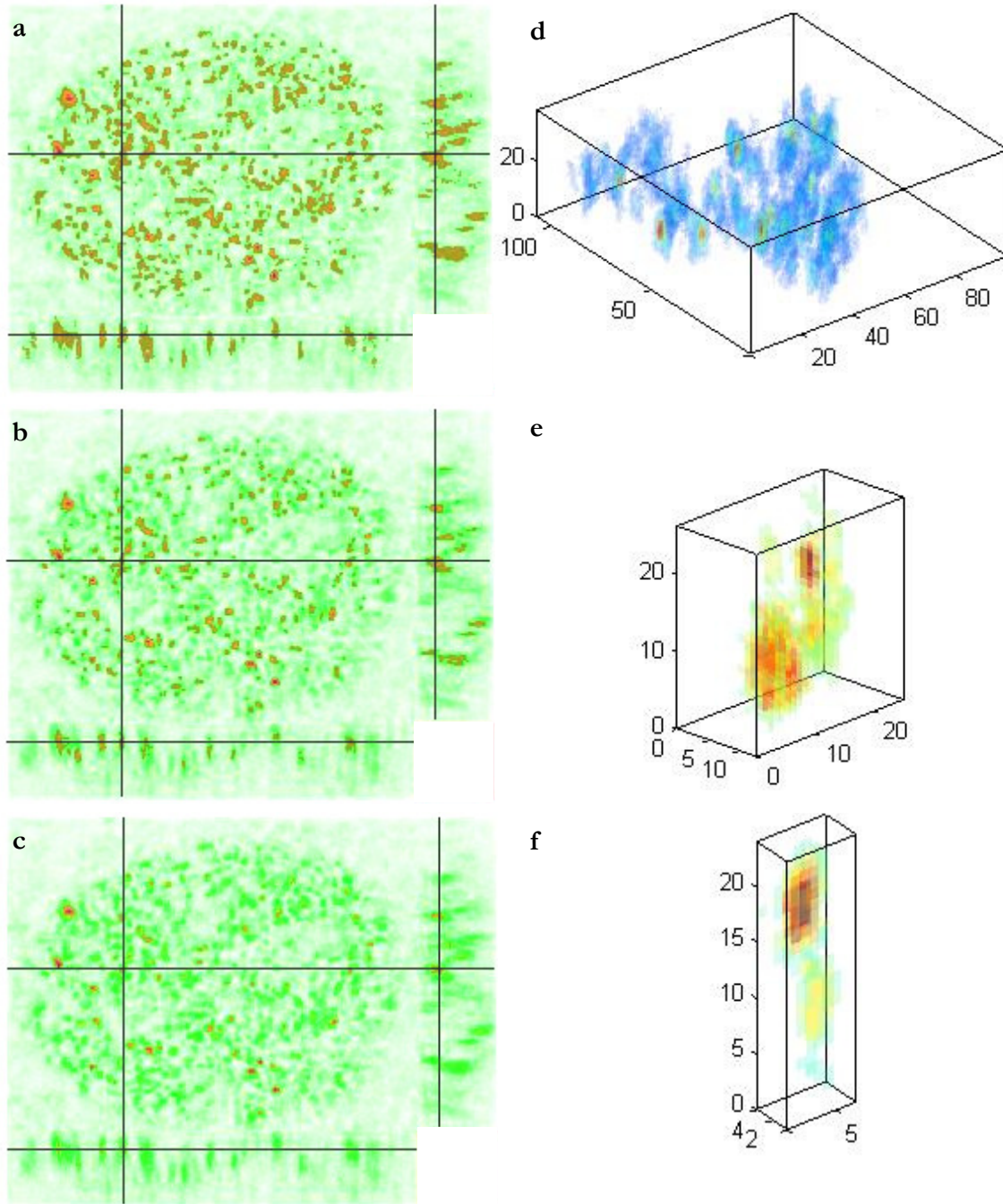
Figure 5-14   3D Threshold Detection Example
Figures a, b and c show the same dataset with threshold values of 460,635 and 980, corresponding to the point labels in Figure 5-13. The cross-hairs (data cursor) are in the same location on each of the panels, and figures d - f represents a 3D rendered visualisation of the detected Foci under the data cursor.

CHARM Detection in 3D

The extension of the CHARM algorithm to 3D has two prerequisites, an efficient 3D gradient algorithm, as the Sobel operator is a 2D operation, and an efficient method for incrementing the accumulator. A 3D-Sobel gradient filter and a 3D Bresenham Line algorithm were implemented for this purpose.

Equation (5-1) shows the gradient estimation using the 2D Sobel kernel Horizontal (Sx), and vertical (Sy). The filter is applied by moving the kernel over the image. An estimate of the gradient at a particular point is achieved by centring the kernel at that point and multiplying the elements of the Sobel kernel with corresponding elements of the 3x3 sub-matrix of the data centred on the point. These products are then summed and the result provides an estimate of the gradient in a particular direction (depending on which operator is used).

Consider the Sobel operator, Sx. Column 2 contains all zero elements, and column 1 is a negative of column 3, if the intensity field is increasing to the right then the result is positive and conversely a field that is decreasing to the right (increasing to the left) will yield a negative result. The central row has a larger magnitude than the adjacent rows, which emphasises the gradient for the nearest neighbours.

Once the filter kernel is applied over the whole image, the resulting field provides an estimate of gradient in the x-direction across the entire field. The process is repeated on the original data using the Sy kernel to yield a field that represents the gradient in the y direction. Notice that the Sobel Kernels are orthogonal to each other.

$$Sx = \begin{bmatrix} -1 & 0 & 1 \\ -2 & 0 & 2 \\ -1 & 0 & 1 \end{bmatrix} \quad Sy = \begin{bmatrix} -1 & -2 & -1 \\ 0 & 0 & 0 \\ 1 & 2 & 1 \end{bmatrix} \tag{5-1}$$

If the concept is extended to 3D then a 3x3x3 kernel will be required, and three orthogonal kernels will be required. The 3D filtering kernels Sx, Sy, Sz that were used are shown in Equations (5-2) to (5-4). The subscripts indicate which plane in the z direction the matrix represents.

All of the features of the 2D Sobel operators can be seen in these [3x3x3] kernels. Specifically, they possess similar anti-symmetry of the elements about the plane of operation and the weighting of the elements depending of their distance from the centre. This is most clearly illustrated in Sz_1 and Sz_2 in equation (5-4).

$$Sx_1 = \begin{bmatrix} -2 & 0 & 2 \\ -4 & 0 & 4 \\ -2 & 0 & 2 \end{bmatrix} \quad Sx_2 = \begin{bmatrix} -4 & 0 & 4 \\ -8 & 0 & 8 \\ -4 & 0 & 4 \end{bmatrix} \quad Sx_3 = \begin{bmatrix} -2 & 0 & 2 \\ -4 & 0 & 4 \\ -2 & 0 & 2 \end{bmatrix} \qquad (5\text{-}2)$$

$$Sy_1 = \begin{bmatrix} -2 & -4 & -2 \\ 0 & 0 & 0 \\ 2 & 4 & 2 \end{bmatrix} \quad Sy_2 = \begin{bmatrix} -4 & -8 & -4 \\ 0 & 0 & 0 \\ 4 & 8 & 4 \end{bmatrix} \quad Sy_3 = \begin{bmatrix} -2 & -4 & -2 \\ 0 & 0 & 0 \\ 2 & 4 & 2 \end{bmatrix} \qquad (5\text{-}3)$$

$$Sz_1 = \begin{bmatrix} -2 & -4 & -2 \\ -4 & -8 & -4 \\ -2 & -4 & -2 \end{bmatrix} \quad Sz_2 = \begin{bmatrix} 0 & 0 & 0 \\ 0 & 0 & 0 \\ 0 & 0 & 0 \end{bmatrix} \quad Sz_3 = \begin{bmatrix} 2 & 4 & 2 \\ 4 & 8 & 4 \\ 2 & 4 & 2 \end{bmatrix} \qquad (5\text{-}4)$$

Note also that Sx, Sy, and Sz are the same kernel simply rotated to measure the gradient in orthogonal directions. This 3D extension to the Sobel operator was derived by logical extension of the 2D Sobel operator. It should be stressed that this is only yields an estimate of the gradient. The elements of the kernels are all integers to facilitate efficient computation. If real values were used in the elements, the values 8, 4 and 2 would become 1, $1/\sqrt{2}$ and $1/\sqrt{3}$ respectively. Even though the values used are not in proportion to the real values they have been empirically assessed to provide good results and a degree of immunity from noise and artefacts. Using these particular values also greatly increases the speed of execution of the filter as multiplication by bases of two can be implemented very efficiently.

Once the 3 components of gradient have been calculated they can be transformed into a magnitude and direction components, where the direction is provided in the spherical polar coordinates, theta and phi.

The output from the Sobel filter can be seen in Figure 5-15c. The same ring patterns can be seen around the edges of the foci in XY, XZ and ZY planes as can be seen in the output of the 2D Sobel operation, shown in Figure 5-3. Note that, in Figure 5-15c, the direction of the edge is not encoded as it is composed of two components and it is not possible to effectively visualise that information. Figure 5-15a&b show the original (unsmoothed) data and the smoothed data respectively.

The next stage in the CHARM algorithm thresholds the magnitude of the gradient to detect voxels that will be used as edgels in the Compact Hough Transform.

To perform the Compact Hough Transform a method was needed to increment the pixels that lay along the radial line between the maximum and minimum feature sizes. With the theta and phi components from the Sobel filter output, the Cartesian beginning and endpoints of the radial lines can be determined. A line is then drawn between them and all the voxels along

that line in the accumulator are incremented by 1. A 3d version of the Bresenham line algorithm [70] was implemented in MatLAB, to determine which indices of the voxels in the accumulator were to be incremented.

The accumulator field that was produced when the 3D Compact Hough Transform was applied to gradient data is shown in Figure 5-15d. The star patterns are less pronounced than those in Figure 5-3 as the lines cut though the planes displayed in Figure 5-15d. Careful inspection shows that foci have a spiked appearance. This field is filtered using a Gaussian kernel and results shown in Figure 5-15e.

The resulting field is a relatively clean volume of data with foci marked in it although some of the foci are touching, the centres of the foci can be detected using the same extended maxima peak detection command as was used in the 2d case. The Matlab command `imextendedmax()`, operates on an N-Dimensional dataset.

The detected peaks, with their centres marked in red, have been indicated in Figure5-15f which shows the accumulator field. Although many foci appearing in Figure 5-15f do not seem to be marked, this is usually because the section that has been displayed does not intersect the centre of those particular foci. As with the 2D version, this algorithm proved very successful with the detection of centres of foci but was unable to extract useful information about their extent.

Figure 5-16 shows the smoothed dataset, overlaid with the marked foci, detected in Figure 5-15e. It shows a good detection rate although the same caveats apply as those for Figure 5-15f. A focus that has apparently been disregarded may simply have its actual centre out of the plane currently displayed. Also the execution in 3D is very time consuming. Processing the dataset shown here took 15 minutes. The majority of the time was actually in incrementing the accumulator. Matlab code runs fastest when the options can be put in terms of general matrix operation. It is not particularly efficient at cycling through every individual element in a large matrix. If the code had been written in C, or if this particular procedure had been written in C the execution speed could probably be greatly increased.

One other problem that is noticeable with the application of the CHARM algorithm in 3D is that it is optimised for spherical objects and, due to the point spread function of the microscope, the foci are actually ellipsoidal. This resulted in two main artefacts in the CHARM accumulator; larger γ-H2AX foci would present as a line of high value pixels in the CHARM accumulator from one foci of the ellipsoid to the other. An example is the artefact labelled A in Figure 5-16. Alternatively the algorithm would detect two foci, each one centred at each focus of the ellipsoid, an example is shown in Figure 5-16, labelled B.
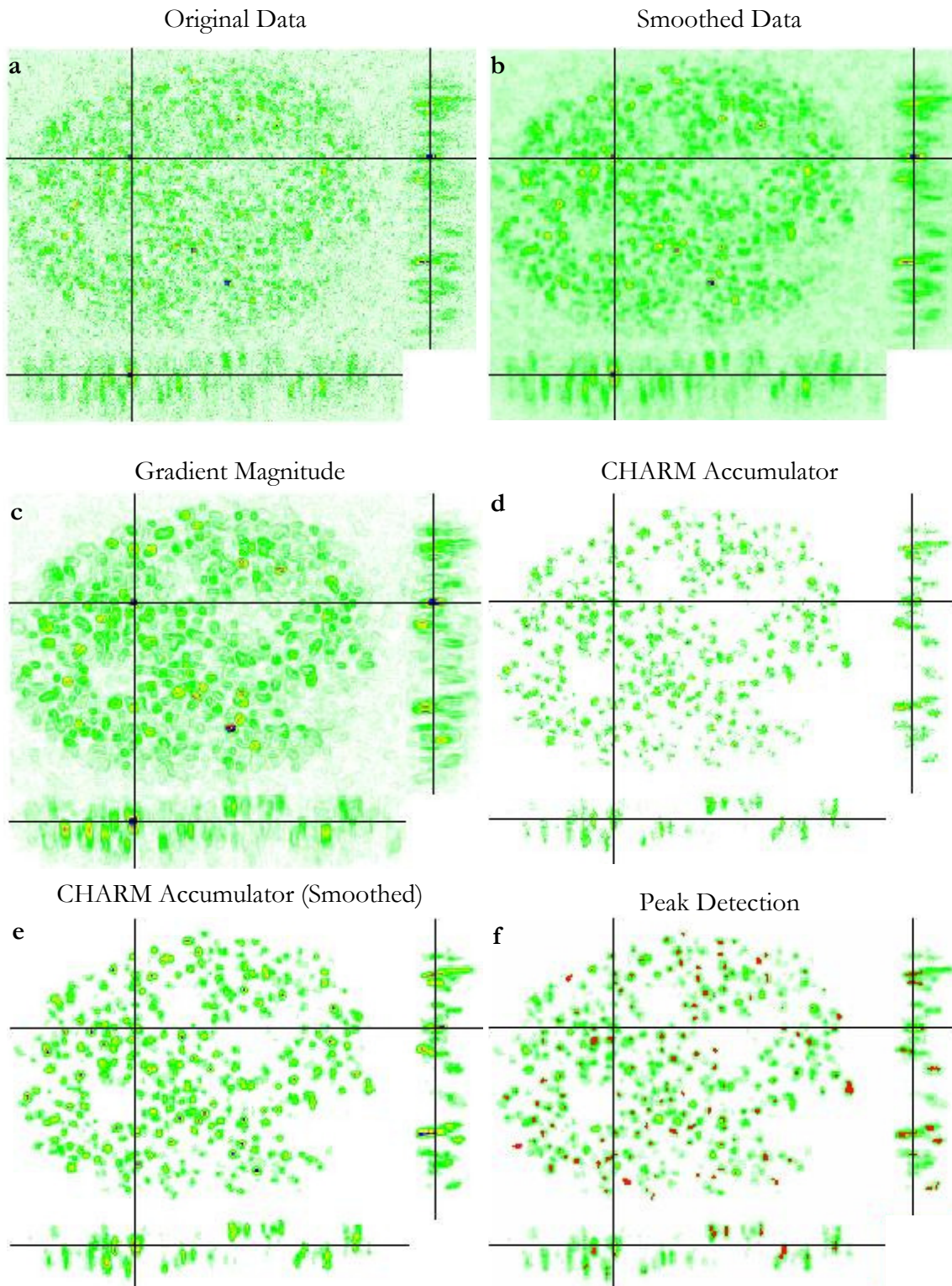
Figure 5-15   **3D-CHARM Foci Detection Algorithm**
Figure showing the output from each step of the CHARM detection process. a) Shows the Original Data b) Shows the smoothed data. Smoothed with a 3x3x3 Gaussian kernel and small maxima suppressed. c) Shows magnitude of the gradient calculated using the 3D Sobel operations. d) Shows the output of the 3D-CHARM accumulator field, after the Compact Hough Transform. e) Show the smoothed output of the 3D-CHARM accumulator. f) Shows the peaks identified in the CHARM accumulator field that indicate the centres of the foci in the data field.
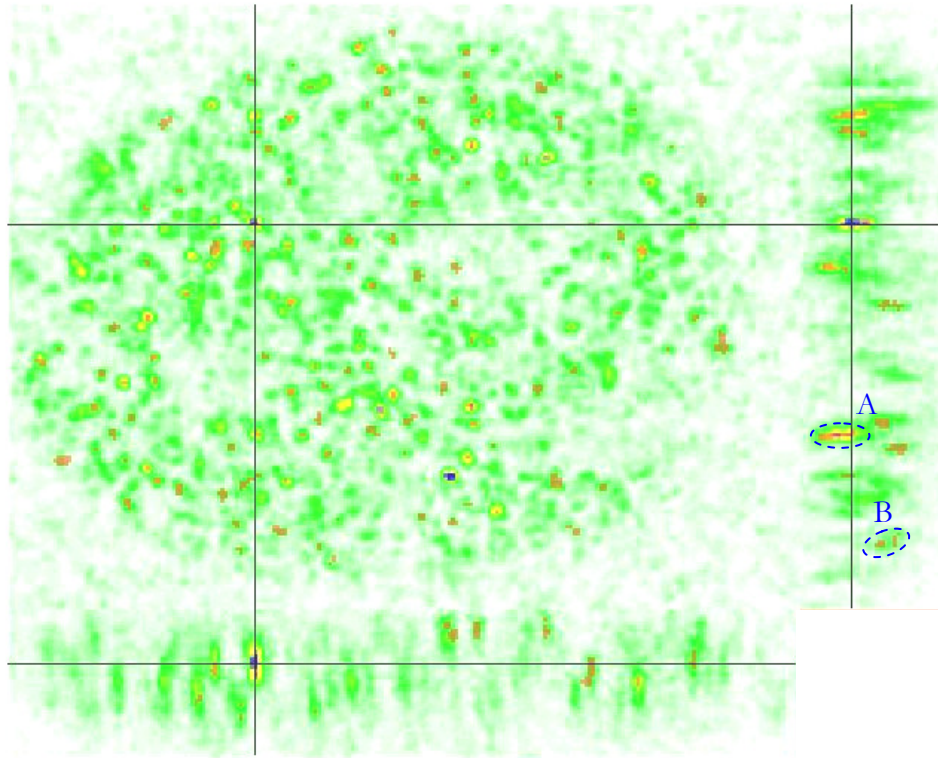
Figure 5-16   Foci Detected with the 3D-CHARM algorithm
Figure shows the section through a nucleus of a cell that has been dosed with 2Gy of radiation. γ-H2AX foci were detected using a 3D variant of the CHARM algorithm. The foci that have been labelled A and B show two artefacts that occur when using the CHARM algorithm in 3D. A shows that a line between the (geometrical) foci of the ellipsoid that represents the γ-H2AX foci.

Watershed in 3D

The watershed algorithm in 2D was covered in some detail on page 2 and conceptually the extension to 3D does not hold any particular challenges. Figure 5-17 shows the output of each of the stages for the 3D algorithm using the orthogonal-planes presentation. The original data and smoothed data images are the same as those in Figure 5-15. Thresholding was performed on the smoothed data. All voxels with intensity greater than 610 were marked in the mask field. Refer to Figure 5-13, which was calculated using the same data set. It can be seen that the number of regions that would be created is around 290. However we know that some of the foci are merged into a single region. The marked voxels in the mask layer are dilated by one pixel in each direction. The dilation causes many of the regions to merge and following the dilation there are around 80 distinct regions, ranging in size from single foci to large segments of the nucleus. Some examples are shown in Figure 5-18.
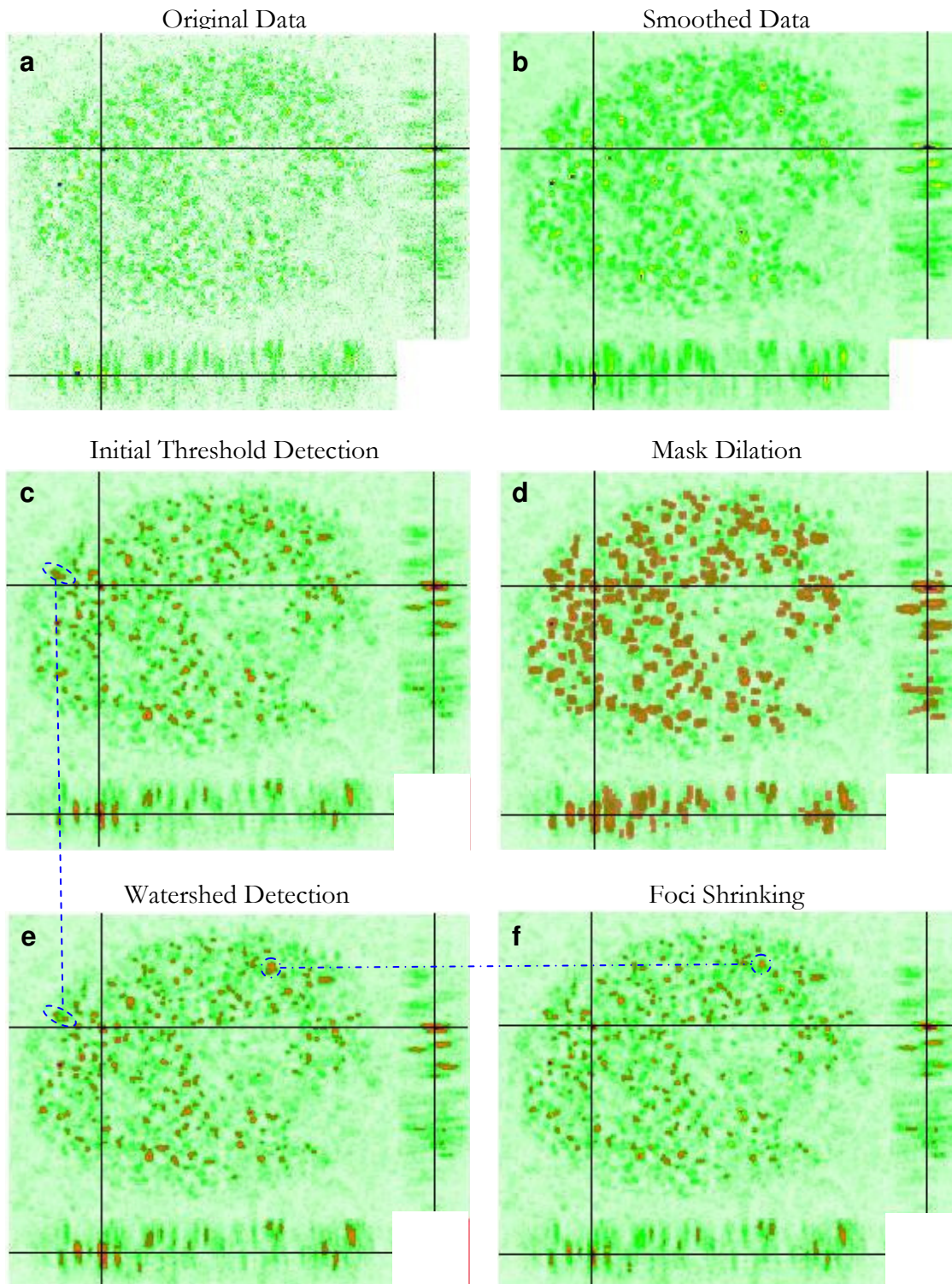
Figure 5-17   3D Watershed Foci Detection Algorithm
This figure shows the output from each stage of the watershed foci detection algorithm. a) shows the section through the original data. b) Shows the smoothed output after a Gaussian smoothing, using a 3x3x3 kernel with standard deviation of 0.65, and the suppression of maxima with height of less than 200 intensity units. c) Shows the region selected following an initial threshold of voxels with an intensity value greater than 610. d) The mask selected in the threshold phase is dilated by 1 pixel in each direction and the resulting mask is shown in d. e) Shows the output following the watershed detection. In f the foci have been shrunk so that for each focus only the voxels with an intensity greater than half the maximum of that focus are marked. This enables a fair and quantitative estimate of the foci size.
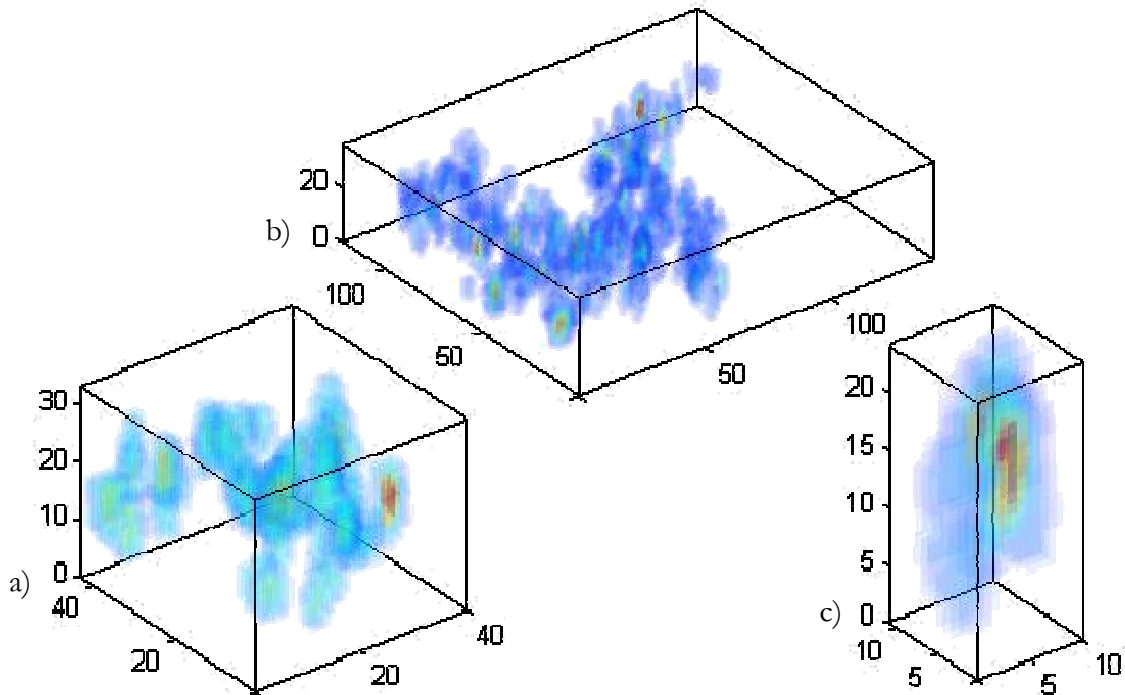
Figure 5-18   Selected connected regions from the Mask Layer.
a) Shows an agglomeration of foci. b) Dilation of the mask has caused a region with high foci density to merge into a single connected region. c) Shows a single focus that has been selected by the initial threshold operation.

The use of the mask layer allows the watershed algorithm to exclude the vast majority of the background. The dilation is necessary to accommodate the gap that is always placed around the foci at the watershed boundary to separate two foci. Without the dilation step small but intense foci are not detected by the watershed algorithm as it sees them with no context of the background.

The merging of the foci in the dilation step is not problematic as the watershed algorithm will segment these regions into the constituent foci. The output from the watershed algorithm is shown in Figure 5-17e. Initially this figure appears very similar to threshold image Figure 5-17d prior to dilation. Closer inspection will show that a number of the regions in the figure 5-17d have been segmented to reveal two distinct foci. A comparison is highlighted by the blue dashed marker. It should also be noticed that the over-segmentation that was present in 2D is not present in 3D. It is much more difficult to totally enclose a region that does not contain a foci in 3D and this was reason for the over segmentation in 2D.

The final step is to reduce the size of the foci so that the marked diameters of the foci represent the full width at half maxima. This allows a more consistent measurement of the foci size. In Figure 5-17, the blue dash-dotted marker links the same foci before and after the foci shrinking process. It can be seen here that the foci has shrunk in size. Figure 5-19, shows the

same foci in 3D. Notice how following the reduction in size the foci is a much better defined ellipsoid.

Before Shrinking   After Shrinking
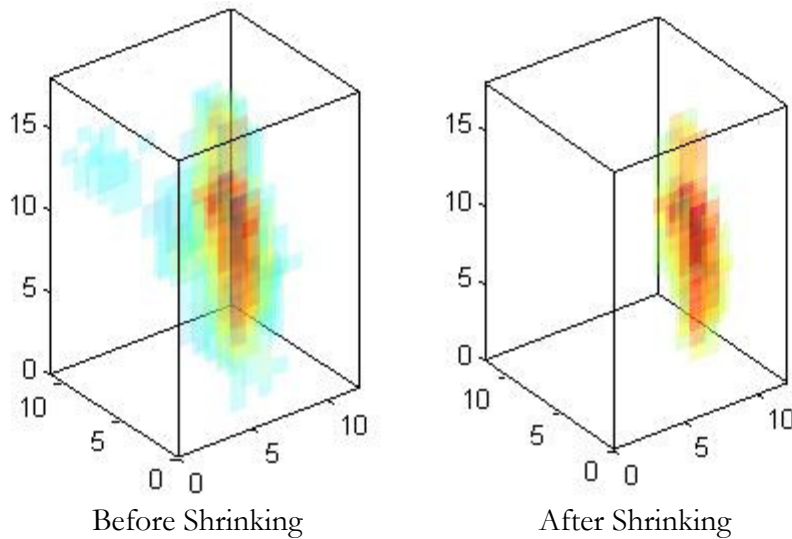
Figure 5-19   3D Rendering of a foci before and after shrinking to its FWHM.

5.2.6.   SUMMARY OF FOCI DETECTION ALGORITHMS

Three different algorithms for the detection of foci have been implemented and reviewed here. The numbers of foci detected seems to depend heavily on the algorithm and parameters used. Table 5-3 summarises the findings of the number of foci detected here, and lists the configurable parameters of each algorithm.

Foci Detection	Number of Foci Detected		Configurable Parameters
	2 Dimensions	**3 Dimensions**	
Threshold Detection	778	303	• Threshold Level
CHARM Detection	403	413	• Gradient Threshold • Minimum Radius • Max Radius • Accumulator Peak Detection Threshold
Watershed Algorithm	680	438	• Initial Threshold Detection Level

Table 5-3   Foci Detection Results on the same cell with different algorithms

Beyond simply counting the number of regions that are detected, more intelligent forms of analysis can be implemented. With marked and labelled regions it is possible to extract certain statistics regarding the properties of the foci. This information is conveniently presented through the foci information screen in the data explorer tool which was discussed in section 5.2.5.

There are many properties that can be extracted but Figure 5-20 shows a particularly useful one, the "Equivalent Diameter". This can be thought of as a measurement of volume but

with the units of length. When the equivalent diameter is calculated, the number of voxels that contribute to the focus is counted to establish the volume. The equivalent diameter is then the diameter of a sphere of that volume.
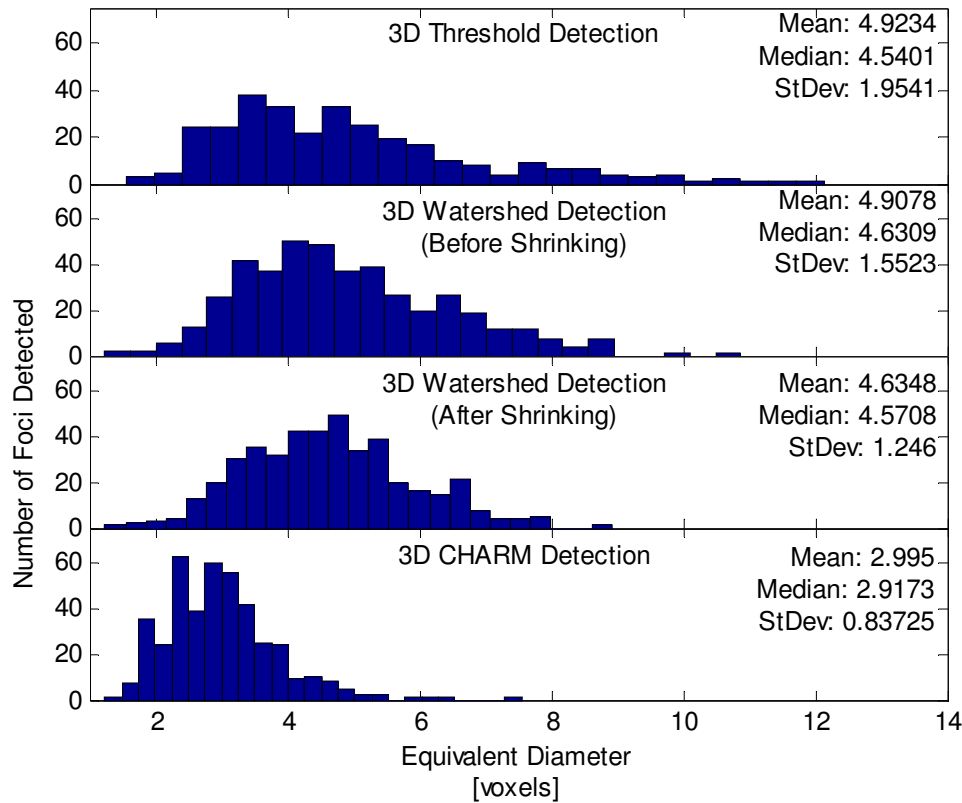
Figure 5-20   Distribution of foci sizes as detected by different algorithms

Figure 5-20 shows a series of histograms, one for each of the detection algorithms; it shows a distribution of the size of the regions that the algorithms detected as foci. The threshold detection algorithm detected fewer regions but there were significant numbers of much larger regions. The modal equivalent diameter was 4.5 voxels, but significant numbers of foci were detected with equivalent diameters of 10-12 voxels, representing regions with volumes in excess of 14 times that the modal volume. This is consistent with observations in Figure 5-14 where it is evident that foci have merged to form larger detected regions. The histogram for the watershed algorithm shares the same form as that of the threshold detection histogram at small sizes but overall there are more foci and none as large as those detected by the threshold algorithm alone. The tail toward large foci is greatly reduced and the distribution in foci sizes is generally much tighter.

The histogram for the CHARM algorithm indicated much smaller foci but great care should be taken in interpreting this data. The CHARM algorithm was only able to identify centres

of foci and it is clear, even in the static diagrams, that the size of the regions detected did not cover the full extent of the foci.
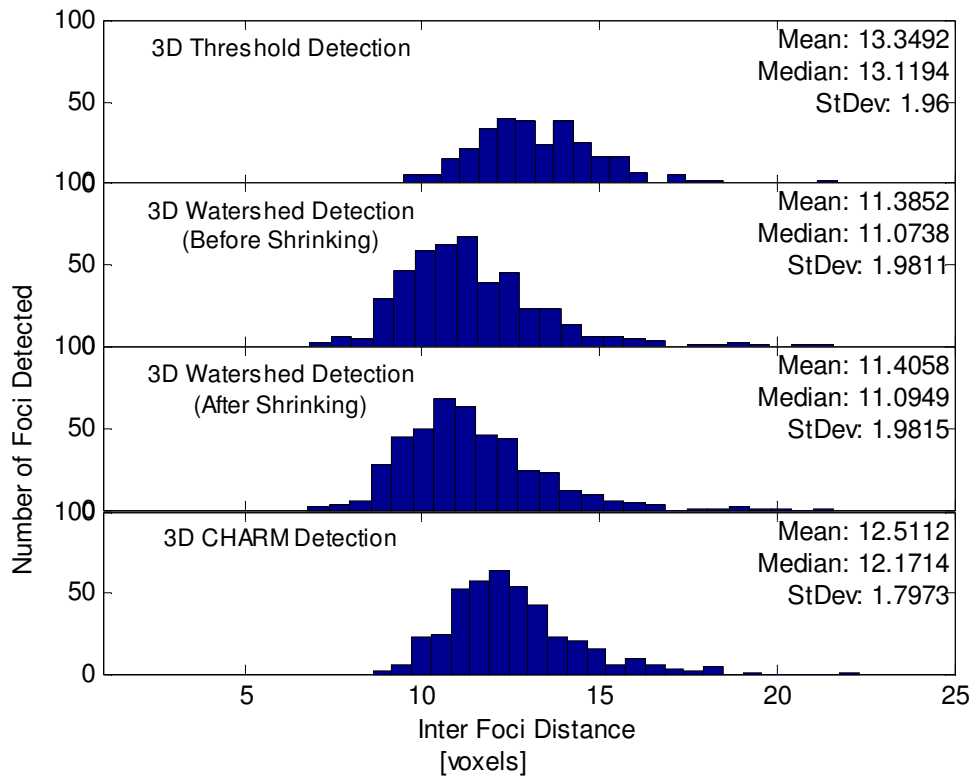
Figure 5-21 **Comparison Spatial distribution of Foci as detected by different algorithms**

Another interesting measurement is the inter-foci distance. The inter-foci distance is the average distance from the centroid of the foci to the centroid of the nearest 10 foci. It can be used as a measure of the foci density. Figure 5-21 shows the inter-foci distances for each of the algorithms. The shape and spread of the distribution is very similar for all the algorithms. Their means all fall within a standard deviation of each other indicating that this method is quite insensitive to the detection algorithm. As this method only uses centroid information it can be reliably used with the data collected using the CHARM algorithm. Here, a good agreement between the CHARM and watershed algorithms is exhibited. As the watershed algorithm ran approximately 24 times faster than the CHARM algorithm, this will be used in the work in the following sections.

Before moving on to the application of this technique to a biological problem, it is worth noting that these algorithms are quite sensitive to the choice of parameters. Up to this point only 1 dataset has been used and the "number of detected foci" has ranged from a few hundred to several thousand, depending on the choice of algorithm or parameters. Whilst, at the extremes,

rudimentary inspection of the data immediately reveals that there is a problem, determining the optimum parameters can be a difficult task. Table 5-3 lists the algorithm specific parameters for the different algorithms but in addition to the algorithm specific parameters all the algorithms were executed on smoothed data. The method of smoothing and parameters used were stated at the beginning of section 5.2.4, and were consistently maintained in these tests. The additional smoothing parameters include the size and shape of the filtering kernel and the strength of the maxima suppression filter. Considering the range of parameters it seems to be impossible to compare numbers of foci from one study to the next unless all parameters are controlled. However, it is not always possible to maintain the same values from one sample to the next. Environmental conditions and sample quality vary significantly from slide to slide. Different parameters are required to optimise detection efficiency for each measurement. What is required is a systematic method to determine the optimum parameters. This will be covered in a more detail in the following sections.

5.3. CELL DAMAGE MEASUREMENTS

In this section the results of an experiment are reported where cells were exposed to varying amounts of radiation causing the formation of γ-H2AX foci. The 3D watershed algorithm developed previously was used to analyse the number and properties of the foci that were detected following irradiation.

5.3.1. DATA ACQUISITION

The γ-H2AX foci were stained with Alexa 488 fluorescent marker to enable their visualisation with the confocal microscope using the 488nm line of the confocal microscope's Ar^+ laser in the confocal scanner. The slide exposed to 8Gy of radiation was expected to have the highest fluorescent intensity. The laser intensity and PMT detector voltages were set to maximise the detected signal without causing saturation in the PMT. The measurement of subsequent slides used these values for the laser intensity and PMT detector voltages to permit comparison between slides. The voxel size was maintained at constant size and shape throughout the whole series of measurements. The voxel dimensions were 115x115x114nm which was as close to cubic as could be achieved using the Leica microscope control software.

At least six fields of view were captured from each slide to obtain a reasonable number of cells for analysis at each dose. Maximum intensity projections through the z-axis for each of field are provided in Appendix A and a representative selection is presented in Figure 5-22. The volume data was analysed and the cells that were entirely within the acquired data field and separate from each other were labelled. Data from a total of 81 cells was collected with the number of cells at each radiation dose varying from 12 to 19 cells.
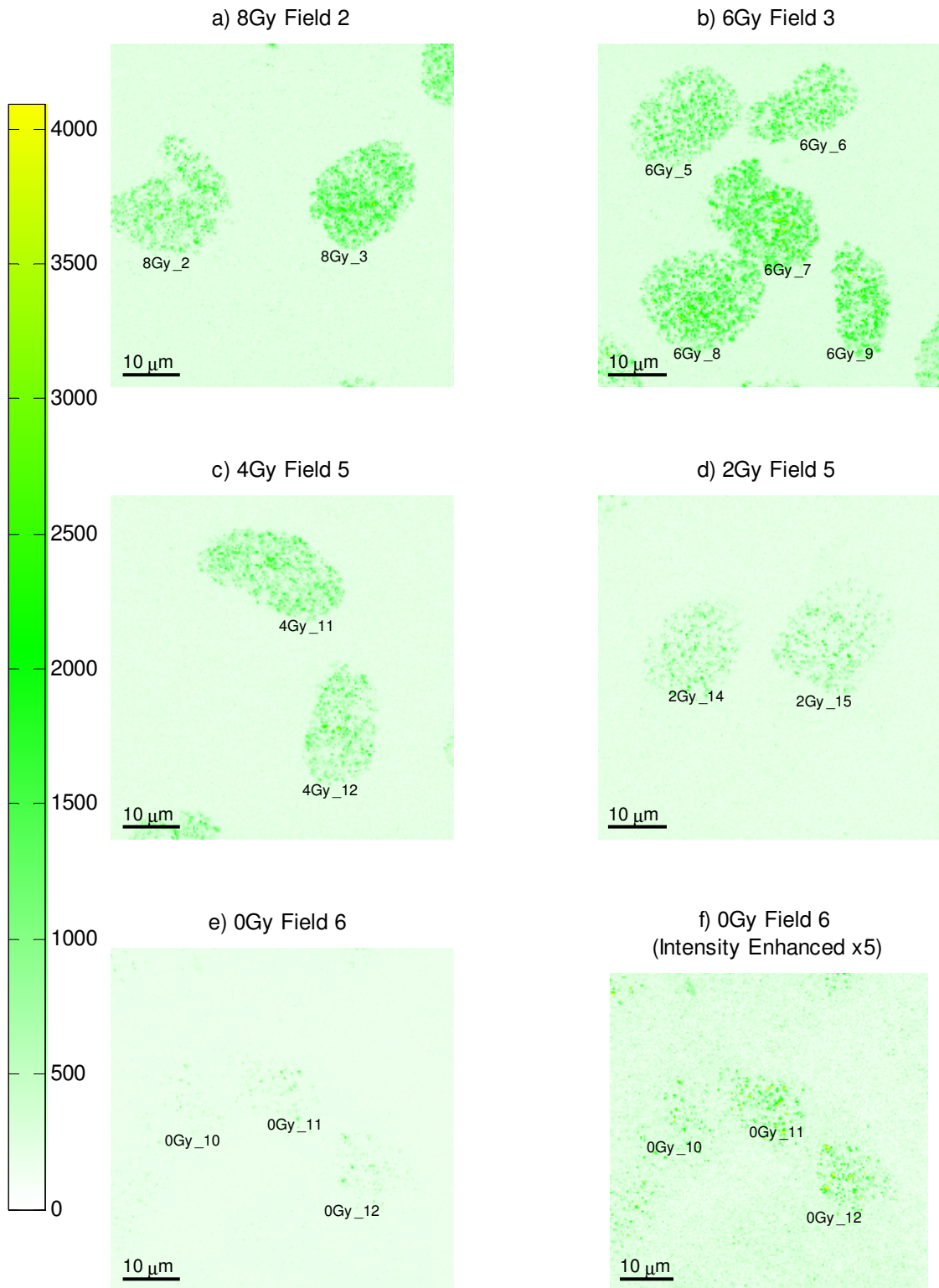
Figure 5-22 *γ-H2AX foci in the nuclei of cells exposed to varying levels of radiation.*
Images a-e are examples of cells from the complete data set (Appendix A). They are presented as maximum intensity projections. Image f, shows the same data as image e, but colour scale in the image has been adjusted to enhance the low intensity foci. The cells have been labelled using their unique identifiers in the experiment.

5.3.2. OBSERVATIONS

In spite of efforts to maintain the constant parameters there was a wide ranging variation in the level and fluctuations of the background as well as in the number and intensity of foci in nuclei that had received the same dosage of radiation.

By visual inspection of Figure 5-22, it can be seen that as the radiation dose is reduced the intensity and number of foci in the cells also appears to reduce. In the control sample, which was not irradiated, it was difficult to locate the focal plane that the cells were in by looking for the fluorescence. By visual inspection, through the eye-piece of the microscope in wide-field mode, the cells could be visualised using transmitted white light. It was verified that the cell density was as great in the control as in the radiation treated cells but they had not taken up as much of the γ-H2AX staining. Figure 5-22f shows an intensity enhanced image, where the cells can more easily be identified but, even under enhancement, identifying the cells and nuclei from the fluorescence image is a difficult task. At the other end of the scale the cells receiving high doses of radiation, of 8Gy and 6Gy, appear to have similar numbers and intensity of γ-H2AX foci, possibly indicating that beyond a certain point of irradiation no more foci are generated.

5.3.3. APPLICATION OF THE WATERSHED ALGORITHM

Determining data processing and detection parameters

The watershed algorithm was used to detect and extract properties of the foci in these images. In the first attempts, the parameters for the algorithm were optimised using the cells from the 8Gy data series. The algorithm was applied to the other cells exposed to lower levels of radiation using the same parameters but visual inspection of the marked regions showed foci were either being missed in the initial threshold phase or the maxima suppression filtering was flattening out genuine foci. However, if the parameters were adjusted for these cells then over-segmentation was observed when the foci detection algorithm was re-executed on the 8Gy cells using the new data.

It was clear that the algorithm parameters needed to be optimised, not just between radiation doses but from one field to the next. The early investigation in section 5.2 revealed that varying the detection parameters can cause a significant variation in the number of foci detected. Varying the parameters between the measurements, if done without care, could invalidate any meaningful comparison.

The amount of data, combined with difficulties of visualising the complete 3D data set, makes thorough visual assessment of the marked regions impractical. Instead it was decided to develop a systematic method of determining optimum detection parameters. Some of these could

be kept constant throughout the measurement, others would vary, but in a consistent and reproducible manner.

The parameters for determination in the foci detection problem are:

- the size and shape of the smoothing filtering kernel;
- the initial threshold detection level;
- the strength of the maxima suppression.

These will be considered in turn. The first of these to be considered is the smoothing kernel. The smoothing step of the algorithm serves to reduce noise in the image. The spatial sampling in these images results in voxels that are smaller than the PSF of the imaging system. Random fluctuations that are smaller than the PSF of the microscope can usually be attributed to noise on the PMT. Using a smoothing function that is roughly commensurate with the PSF of the microscope can help reduce this problem. For this reason a Gaussian shaped kernel is used. The size of the kernel is 3x3x3 voxels and the standard deviation of the kernel is 0.65 voxels wide. As the image voxel size and the point spread function remain constant throughout the measurement, the size and shape of the smoothing kernel also can remain constant.

The next parameter for consideration is the initial detection threshold value. This is used in the first step of the detection process. It is used to identify the parts of the image that exceed the background where no foci are found. When set at the correct level it should select most of the nucleus in a moderately irradiated cell. To determine the correct level, a 3D-rectangular box shaped region of the field is selected that contains no foci or nuclei. This region is smoothed (see Figure 5-23) using the same method and parameters as the data.
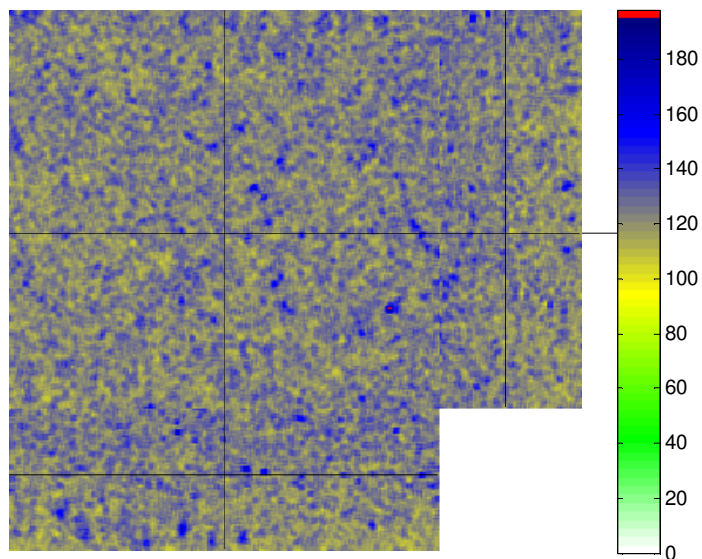
Figure 5-23   Background noise from a region within 8Gy Field 1
This figure displays an orthogonal plane presentation of the region containing no nuclei or foci, after smoothing with Gaussian kernel. Note the colour axis is only scaled over 0 to 200, whereas the intensity in the whole image varies from 0 to 4096. This scale serves to emphasise the noise.
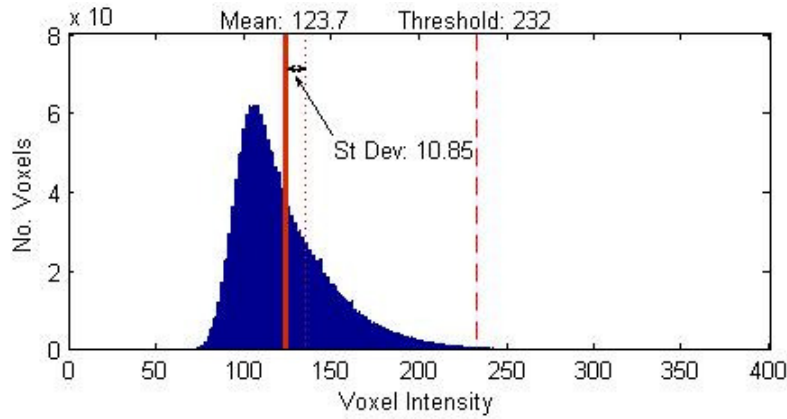
Figure 5-24   Histogram of background intensity values.
This histogram is of intensity values from the background region, represented in Figure 5-23. The superimposed vertical lines denote the Mean, Mean + Standard Deviation, and the calculated threshold value (mean + 10.StDev).
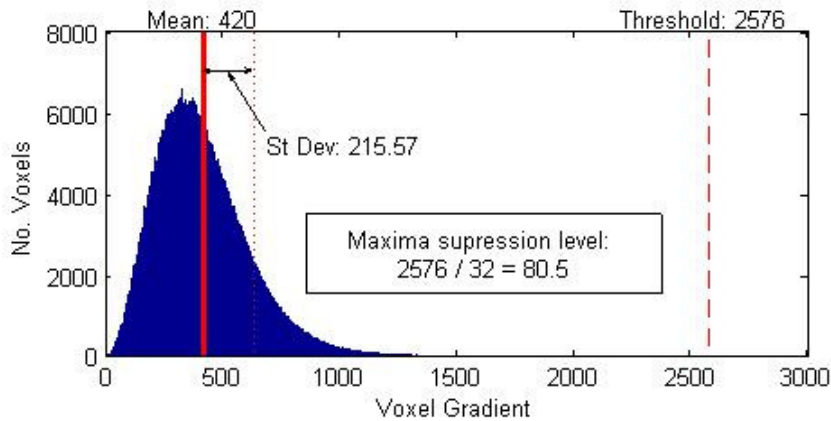
Figure 5-25   Histogram of the gradient of background intensity values.
This histogram is of the gradient magnitude of the background intensity values from the background region, represented in Figure 5-23. The superimposed vertical lines denote the Mean, Mean + Standard Deviation, and the calculated threshold value (mean + 10.StDev). The Maxima Suppression threshold is obtained by dividing this number by 32, which is a multiplying factor created by the Sobel filtering process.

The mean and standard deviation on voxel intensity values are calculated. The objective is to automatically choose a level that will exclude the vast majority of the background without excluding values that might actually be foci. The threshold is determined by taking the average intensity of the background and adding a number of standard deviations to it. This approach permits the system to automatically compensate for noisier data sets. Empirically, a standard deviation multiplier of 10 was found to give good results. Figure 5-24 shows a histogram of voxel intensities in the background region. The mean, standard deviation and automatically detected threshold are marked on the figure.

The last parameter that must be determined is the strength of the maxima suppression. The purpose of this is to suppress the maxima that occur through natural fluctuations in the detectors. Whereas the threshold accounts for an offset, the maxima suppression is supposed to suppress small local maxima on a larger trend. The choice of this parameter is quite significant. If it is set too high genuine foci get flattened out of the image, if set too low over-segmentation

occurs and foci are detected at every random fluctuation in intensity. The approach taken to resolving this problem was to use the 3D Sobel operator that was developed for the CHARM algorithm to obtain a gradient magnitude field for the background region and then, in a similar manner as for the threshold value, the mean and standard deviation were calculated. For the reasons explained in section 5.2.4 the Sobel operator uses integer elements in its filtering kernel. The sum of the positive (negative) elements is 32 (-32). One effect of this is that the magnitude of the gradient is multiplied by a factor of 32. This must be compensated for, and the parameter that is used by the maxima suppression filter, $hmax_{threshold}$, is calculated from the magnitude of the gradient filed, **G**, using equation (5-5). Once again the standard deviation multiplier was established empirically. A histogram of the gradient of the background region is shown in Figure 5-25 and is marked with the mean, standard deviation and automatically detected threshold.

$$hmax_{threshold} = \frac{\text{mean}(\mathbf{G}) + 10 \cdot StDev(\mathbf{G})}{32} \qquad (5\text{-}5)$$

For every field, at every dose, an area devoid of features was selected and this detection parameter determination procedure was carried out. A table of results is provided in Table A-1 in Appendix A. Average values for detection parameters are listed in Table 5-4. Even within the same slide the background level varied somewhat. This can be seen by either examining Table A-1 or noting the standard deviations in Table 5-4.
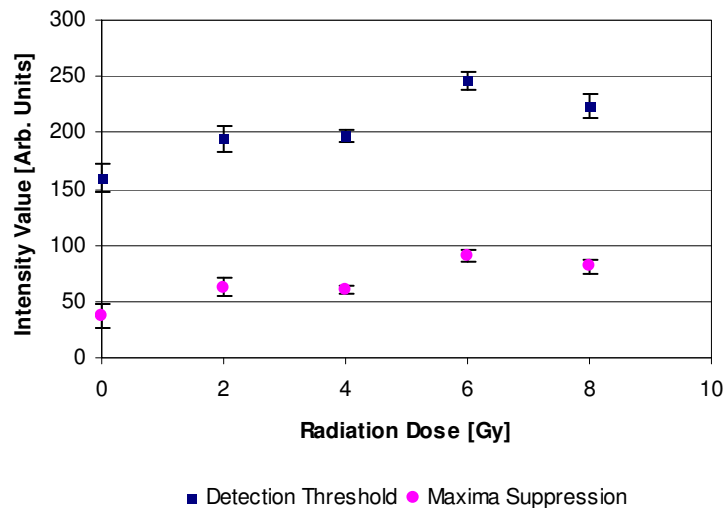
Figure 5-26   ***Variation of detection parameters with radiation dose***
The values plotted here are those shown in Table 5-4. It should be noted that the error bars indicate the standard deviation and not a standard error. Their presence is intended to illustrate the spread values determined in the different fields that were measured.

Radiation Dose [Gy]	Detection Threshold	Standard Deviation	Maxima Suppression	Standard Deviation
8	223	11	81	6
6	246	8	91	5
4	197	5	61	3
2	195	11	63	8
0	160	12	37	10

Table 5-4   Summary of detection parameters and their standard deviations

From Figure 5-26 it can be seen that both the automatically determined initial detection threshold and maxima suppression threshold are higher for the higher radiation doses. These values have been determined in a systematic and repeatable manner and provide optimum detection parameters across a range of samples.
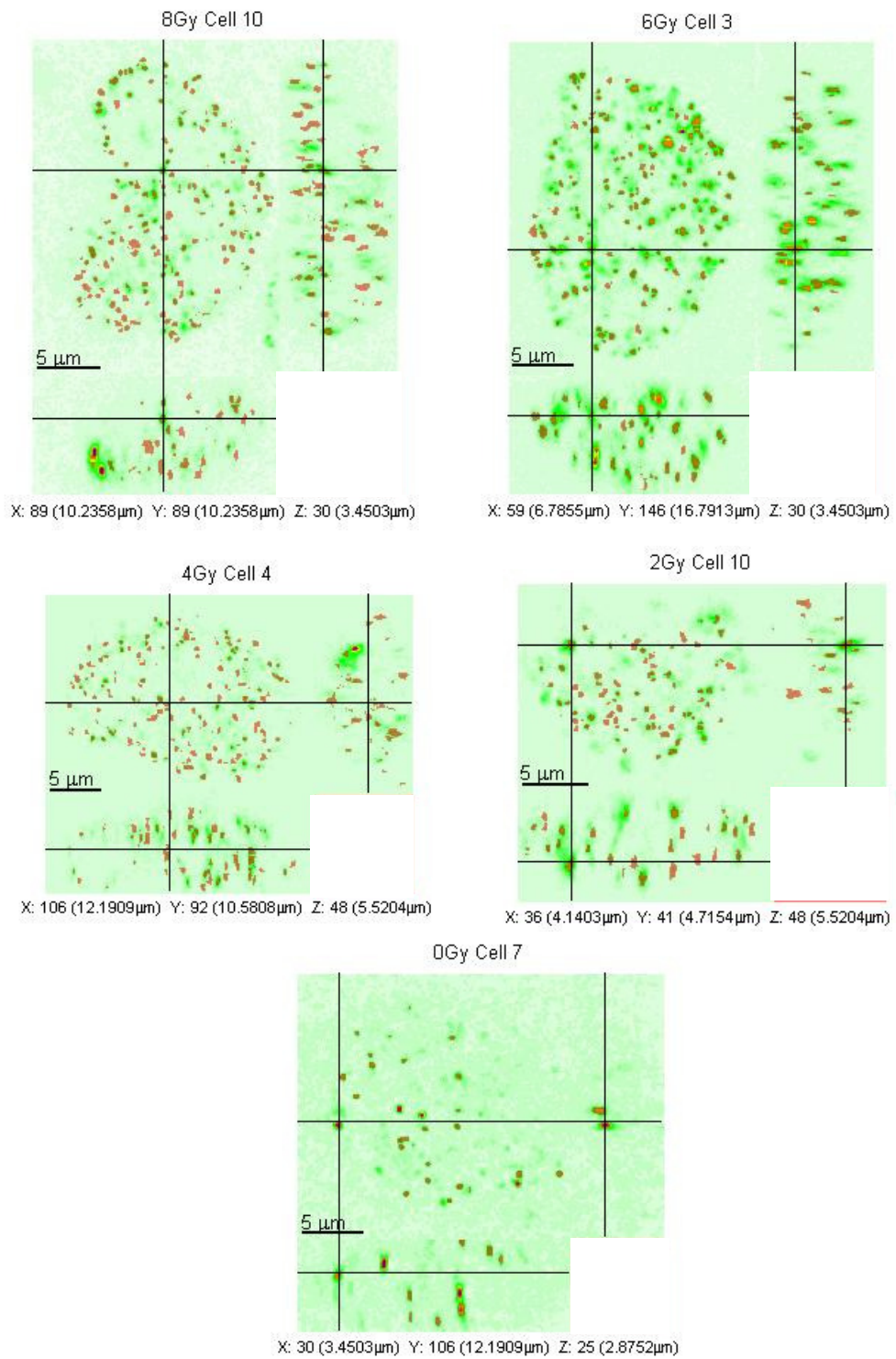
Figure 5-27   Marked Foci in Cells irradiated with varying levels of radiation.
This figure shows an orthogonal section presentation of the irradiated cells. The foci are marked in red, the radiation dose and the cell identifier are given in the title above each image. The coordinates at the bottom of each image indicate the position of the cross-hair within the cell from the top left.

5.3.4.   DATA ANALYSIS

Number of Foci

Using the automatically determined detection parameters each cell was processed and one cell from each dose is shown in Figure 5-27 as an example. The number of foci detected in each cell is listed in Table 5-5, and the averages are plotted in Figure 5-28.

	Radiation Dose				
Cell No.	8Gy	6Gy	4Gy	2Gy	0Gy
1	1433	647	531	655	**372**
2	840	**439**	613	538	91
3	1158	**1102**	507	701	313
4	1059	837	1102	335	42
5	505	748	870	675	**24**
6	773	587	519	290	313
7	505	1081	663	618	139
8	**488**	934	1098	376	84
9	752	526	627	360	88
10	1115	902	1109	572	142
11	854	1026	**1300**	458	111
12	1022	880	789	511	187
13	**1480**	495	485	**764**	
14	1095	1101	751	577	
15		807	1076	662	
16		547	**415**	**249**	
17		544	491	315	
18		1027	583	738	
19		581			
Mean	*934*	*780*	*752*	*522*	*159*
Max	*1480*	*1102*	*1300*	*764*	*372*
Min	*488*	*439*	*415*	*249*	*24*
St Deviation	319	228	274	166	114
Error on Mean	*85*	*52*	*65*	*39*	*33*

Table 5-5   Number of Foci Detected in irradiated cells
The table shows the number of foci that were detected in each cell. For each radiation dose the mean, maximum, minimum, and standard deviation of the number of detected foci has been calculated. Maximum and minimum foci values have been highlighted in red and green respectively. The error on the mean is calculated as a standard error, on the set of results collected at the radiation dose.

Figure 5-28 shows the number of foci increasing with the increasing radiation. In spite of having a relatively large population of cells there was still a significant spread in the number foci detected. It should also be noted that the size of the nuclei, themselves, also varies considerably and it was noticed that the smaller nuclei showed less foci. The cells that had the most detected foci for each radiation dose are highlighted in red in Table 5-5, they are also visibly more intense in the maximum intensity projections in Appendix A.
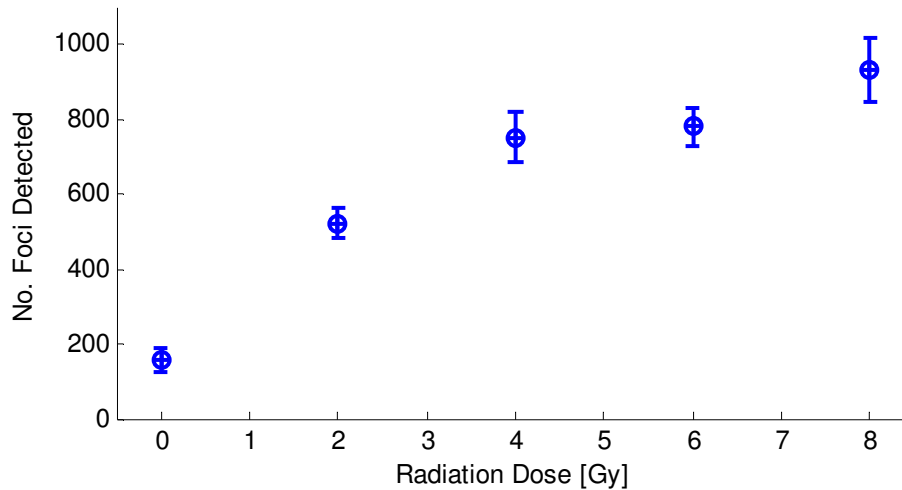
Figure 5-28   Average number of γ-H2AX foci against the radiation dose
The source data for this figure is in Table 5-5

Foci Intensity

The Foci detection and analysis tools that have been developed in this work permit the extraction of properties of foci and cells beyond the simple numbers of foci detected.

Information can be extracted at various levels of granularity. The properties can be considered at the foci level, at the cell level, or at the batch level. In this case cells were batched into groups depending on the radiation dose they were exposed to. Consider the specific example of maximum foci intensity; when applied to an individual focus of gamma-H2AX, it is represented by a scalar value corresponding to the most intense voxel in the foci. A cell has many foci and so it must either be represented as a distribution of values or these values must be aggregated, for example by averaging, into a single value. Using the intensity example, the mean of the maximum foci intensities was used and the standard deviation provides an estimate of the spread of the values. These values have been calculated in Table 5-6 and aggregate values have been plotted for the set of radiation doses the cells have been exposed to in Figure 5-29. It shows that, as the radiation dose is increased, the intensity of the foci increases. One explanation for this is that, as the radiation dose is increased, multiple DSB occur in close proximity which the individual sites can not be resolve and they appear as more intense single foci.

These intense foci could also be the result of blocked replication forks at replication centres. Hundreds of replication forks can be active at one replication centre. Damage in the actively replicating DNA causes stalling of the replication forks and cell signalling causes the replication to stop when damage occurs in the DNA remote from them. The repair systems become heavily occupied and the blocked replication forks that cannot be protected quickly become converted to double strand breaks adding to those already formed by the radiation absorption.

The maximum intensity was observed in cells dosed with 6Gy. At 8Gy the intensity fell off. One explanation is that at very high radiation doses any cells actively replicating will be so highly damaged that they will die and disappear from the population being examined before the cells are fixed. The remaining cells will be non-replicating cells that have sustained radiation damage but little or no damage through stalled replication forks.

Cell No.	Radiation Dose									
	8Gy		6Gy		4Gy		2Gy		0Gy	
	I	SD	I	SD	I	SD	I	SD	I	SD
1	947	498	974	501	534	306	616	373	390	224
2	741	398	876	464	539	357	505	374	307	124
3	870	462	1116	615	934	548	536	294	443	225
4	626	453	1028	520	505	287	565	338	204	57
5	664	481	772	382	799	522	619	393	207	56
6	659	350	803	445	630	389	600	354	296	162
7	598	515	1034	582	497	290	580	327	255	114
8	601	503	1022	520	583	338	608	378	241	135
9	648	440	956	544	669	372	591	367	222	84
10	662	406	883	503	508	277	688	407	222	76
11	664	386	1136	615	573	347	841	419	281	187
12	701	436	837	494	555	367	855	559	252	150
13	634	383	890	503	620	356	552	337		
14	577	322	768	523	505	291	461	258		
15			824	445	453	263	470	284		
16			967	518	773	503	384	160		
17			1135	618	638	418	361	183		
18			697	406	648	399	436	254		
19			724	395						
Mean	685	431	918	505	609	368	570	337	277	133
Max	947	515	1136	618	934	548	855	559	443	225
Min	577	322	697	382	453	263	361	160	204	56
Standard Deviation	104	59	137	71	124	85	133	92	74	59
Error on Mean	28	16	32	16	29	20	31	22	21	17

Table 5-6   Intensity of foci in radiation dosed cells
Table shows the average measured maximum intensity (I) for foci in each cell, and the standard deviation (SD) in the set of foci maximum intensities.
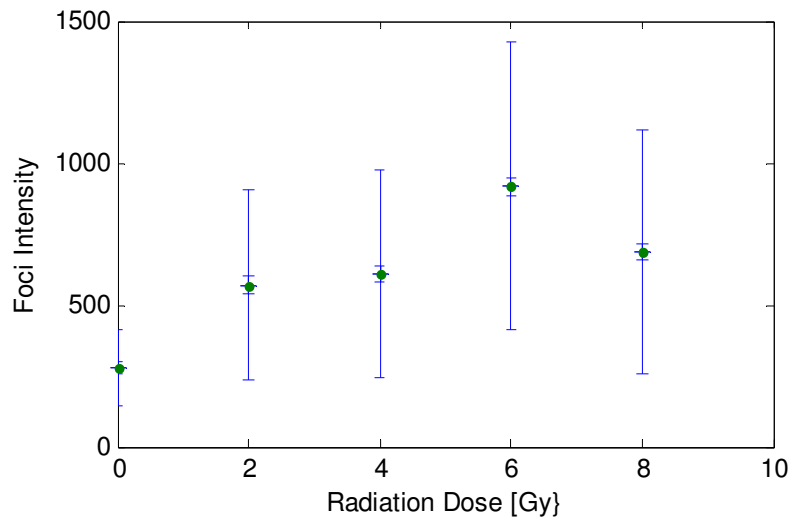
Figure 5-29   Average maximum intensity in foci in irradiated cells
The source data for this figure is in Table 5-6. Each data point has two vertical error bars. The small error bars denote the standard error on the mean, whilst the larger error bars indicate the standard deviation either side of the mean value, to visualise the spread in foci intensity.

Foci Size

It was noticed from observations of the data that there appeared to be a significant variation in the size of foci. Once the foci were detected by the watershed algorithm their regions were shrunk. This was achieved by taking each focus in turn, working out the maximum intensity and then excluding all voxels in the foci that were not at least half of the maximum intensity. This is analogous to measuring the full width at half of the maximum of the height a peak in a curve. The remaining voxel in the foci were counted to establish volume. The equivalent diameter is the diameter of a sphere that would have the same volume as the foci.

An equivalent diameter was calculated for every foci, and the results aggregated together to provide mean foci diameters and standard deviations for cells and batches of cells in the same way as was done in the previous section with the intensity.

The results are shown in Table 5-7 and Figure 5-30 shows the average foci diameter as a function of radiation dose. This shows that the average foci size and the spread in sizes do not have a significant dependence on the radiation dose. The control sample that was not exposed to radiation shows slightly large foci. This might be expected, as the foci in the control cells were not the result of double strand breaks in the DNA caused by radiation and there were considerably fewer of them. The foci in the un-irradiated cells can mostly be attributed to stalled replication sites, which are expected to be larger than DSB lesions. Whilst it is reasonable to expect to see these sorts of foci in the irradiated cells, the statistics would be overwhelmed with the foci created due to the DSBs.

The size of the foci is as expected. The DSB lesions that are marked by γ-H2AX are smaller than the PSF of the microscope, so it is expected that a large number of features with the approximate size of the PSF will be seen and that is what is shown in Figure 5-30.

Cell No.	Radiation Dose									
	8Gy		6Gy		4Gy		2Gy		0Gy	
	d	SD	d	SD	d	SD	d	SD	d	SD
1	561	131	586	125	596	140	589	128	691	140
2	560	114	571	118	586	142	576	116	639	110
3	573	138	583	133	632	149	589	118	659	88.6
4	561	122	577	123	590	139	572	122	601	121
5	593	130	590	134	604	151	573	120	595	81.7
6	608	169	574	124	615	139	572	124	659	123
7	578	139	602	133	605	136	575	111	641	113
8	620	153	586	128	585	127	586	127	630	123
9	586	131	588	135	588	124	582	118	634	116
10	589	149	594	131	588	129	583	114	626	116
11	599	136	585	138	594	156	743	196	658	125
12	615	144	591	128	592	133	548	128	683	116
13	590	139	582	134	602	122	570	118		
14	610	156	562	118	611	160	583	119		
15			558	104	595	139	567	115		
16			600	129	620	138	583	129		
17			603	142	611	143	579	139		
18			576	126	590	126	602	160		
19			586	118						
Mean	589	139	584	127	600	139	587	128	643	115
Max	620	169	603	142	632	160	743	196	691	140
Min	560	114	558	104	585	122	548	111	595	82
StDev	20	14	12	9	13	11	40	20	29	16
Err of Mean	5	4	3	2	3	3	10	5	8	5

Table 5-7   Equivalent Diameter of Foci in Irradiated Cells
Table shows the average foci diameter intensity (d) for foci in each cell, and the standard deviation (SD) in the set of foci equivalent diameters.
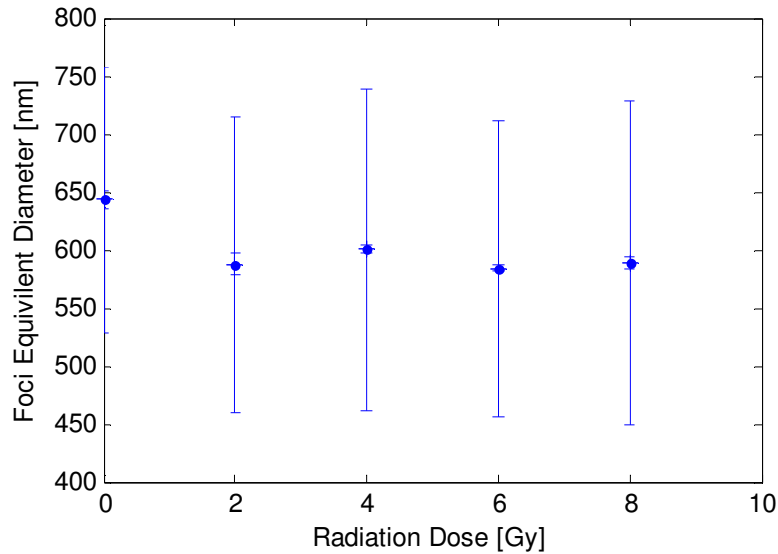
Figure 5-30   *Average Foci Equivalent Diameter of Foci in Irradiated Cells*
The source data for this figure is in Table 5-7. Each data point has two vertical error bars. The small error bars denote the standard error on the mean, whilst the larger error bars indicate the standard deviation either side of the mean value, to visualise the spread in foci diameter.

5.3.5.   SUMMARY OF RADIATION DAMAGE RESULTS

The application of the 3D watershed detection algorithm to the irradiated cells has confirmed that the number foci increases with increasing doses of radiation but that the spread in the number of detected foci is very large. The automatic detection parameter determination procedure developed helped to ensure that the detection parameters were chosen in a systematic manner. The number of foci detected is greater than previous literature has reported which also has shown large variations in the number of reported foci from one publication to another. It is clear that unless a method for determining what constitutes countable foci is developed these sorts of foci counting studies cannot be compared with each other.

The tools developed provide researchers with more information than the number of foci. Potentially, biologists can take the foci information data that is yielded by this program and apply selection rules, identifying foci that satisfy certain criteria. In this work, full use of that capability was not demonstrated but it was used to study average foci intensity and size statistics. This study showed the average size of γ-H2AX foci was independent of the radiation dose and that cells dosed with radiation showed γ-H2AX foci with higher intensities corresponding to greater numbers of aggregated γ-H2AX proteins. However, in the particular data set studied at the highest radiation dose the intensity of the γ-H2AX foci was lower although there were still more foci detected.

CHAPTER 6.

6. Development of an SPPX-STM

In this chapter work is undertaken towards the goal of atomic spatial resolution with femtosecond temporal resolution. By combining the high temporal resolution provided by pump-probe femtosecond laser pulses with the ultimate resolution yielded by the scanning tunnelling microscope it should be possible to observe electron dynamics on the atomic scale.

The chapter starts with a review of previous efforts to combine femtosecond lasers and scanning tunnelling microscopy to develop a microscopy technique that attempts to achieve the ultimate spatial and temporal resolution, a femtosecond time resolved scanning tunnelling microscope.

It goes on to describe the challenges of implementing a SPPX arrangement, including how we attempted to resolve the problems of delivering light to the STM and how pump probe experiments could be performed. Customised step motor and piezo controllers were constructed and the development of the associated firmware and software is also described.

So far environmental noise proved to be too great and the sensitivity of the equipment has been insufficient to detect the small signals above the environmental noise. Recommendations made at the end of this chapter highlight the way forward for this work that build on the successful development of a delay stage and mirror shaker arrangement that are crucial to the SPPX method. The shaker arrangement allows lock-in to be performed at higher frequencies, without destabilising the STM junction.

6.1. INTRODUCTION TO TIME RESOLVED STM

6.1.1. OVERVIEW

A number of previous attempts have been made to improve the time resolution of the STM with the aim of providing information on the ultrafast dynamics of electrons whilst maintaining the resolution that can only be obtained in STM. The applications for such technology would extensive as long as the requirements of the sample and the operating environment were not too restrictive. Areas where such a tool could be used include the investigation of photo carrier excitation and recombination in novel semiconductors, the study of electron transfer in organic photosensitive dyes and studying the processes of photosynthesis in a single chlorophyll molecule.

Two reviews of the field were published in 2002. Steeves and Freeman [71] focused exclusively on the combination of pulsed lasers and STM to improve the temporal resolution of the STM whilst Grafstrom [72] covered the wider field of photoassisted STM, reviewing all areas relating to the use of optical excitation in conjunction with STM including nano-structuring, site selective desorption and a section on combining scanning near field optical microscopy with STM. In addition, a relatively short section was included on using ultrafast femtosecond pulses to obtain high temporal resolution measurements from the STM. The most recent review on the subject is published in the book edited by Yamashita et al [73] in 2005, which is broadly divided into two parts, one on the generation of ultrashort pulses and the other on reviewing previous work in ultrafast time resolved STM.

6.1.2. LASER-STM COUPLING CONFIGURATIONS

Although many attempts have been made to integrate STM and femtosecond laser technology they can all be divided into three basic arrangements, which are illustrated in Figure 6-1.

a)   Photo Gated STM   b)   Evanescent Coupling   c)   Direct Coupling
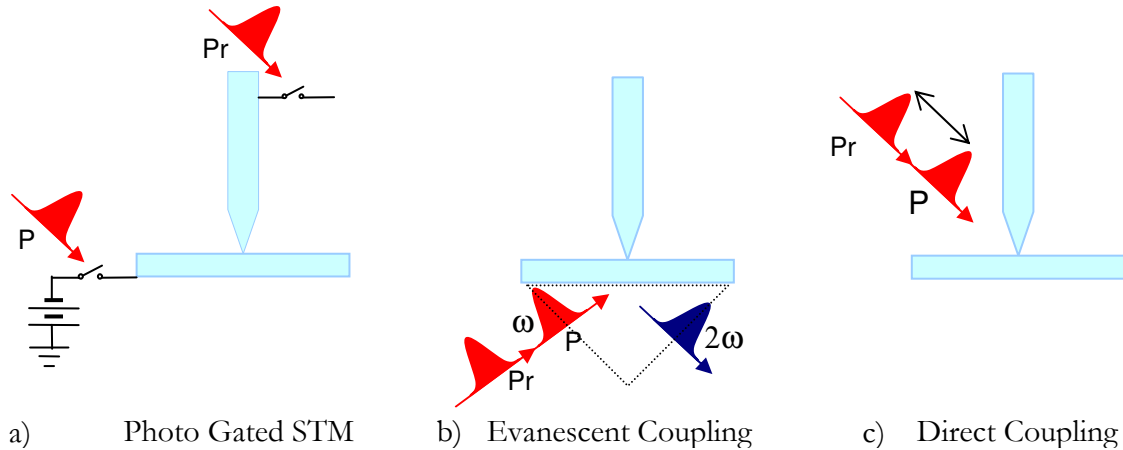
Figure 6-1   Three Laser-STM coupling schemes

Three arrangements for ultrafast optically coupled STM reported in the literature. The pump pulse (P) creates some transient alteration to the STM junction, which is sampled by the Probe Pulse (Pr).

a) first reported by Weiss et al [74], b) first used by Feldstein et al [75] b) first used by Hamers and Cahill [76]

Photo Gated STM

The Photo-Gated STM (PG-STM), shown in Figure 6-1a, was first suggested by Weiss et al [74]. The pump pulse is incident on a photoconductive switch connected to the sample. The switch is briefly turned on for the duration of the laser pulse which creates a voltage pulse in the sample. The probe pulse arrives some short time later and is incident on another photoconductive switch in line with the STM tip. The tip is only connected to the STM electronics for a short while and the delay between the pump and probe pulses can be varied. In this way, the pump pulse initiates some process, in this case a voltage pulse is created, and the probe pulse allows the signal to be sampled some time later. The dark resistance of the photo switch on the STM tip was about 30MΩ, which is small compared to the resistance of a tunnel junction which typically operates in the range of 100MΩ to 1GΩ. This meant that when the probe pulse was off the STM could still operate normally but the increase voltage from the sample would not generate much additional current. Weiss et al used this arrangement to study the propagation of a voltage pulse down a transmission line and detected signals with a picosecond timescale. They attempted to show that the signal originated from the tunnel current by withdrawing the tip by 50Å whereupon they observed the signal to disappear. Interestingly, the peak in the time resolved signal width became narrower as the tip was withdrawn. This indicates a capacitance was involved and although Weiss et al attributed this behaviour to a quantum capacitance based on a coulomb blockage process. It was finally proved by Groeneveld and van Kempen [77] that the signal was dominated by the geometrical capacitance and that the spatial resolution was on a scale of microns. This proved that the signal was simply the result of the charging time for the stray capacitance caused by the tip-sample gap.

Evanescent Coupling

The arrangement shown in Figure 6-1b, was first proposed by Feldstein et al [74] for the study of ultrafast reactions at surfaces. A thin 550Å Ag film was evaporated onto the hypotenuse face of a right prism. The STM tip was positioned above the Ag film. The prism was used to couple the excitation light to the surface plasmon, enabling the frequency and the wavelength to be matched to the plasmon frequency and wavelength. When the tip-sample separation was modulated by 1-10nm at 2kHz, the intensity of the probe beam and the second harmonic were also found have a component modulated at 2Khz, which could be used to identify the component of the spectroscopic signal in the vicinity of the STM probe. This shows that the optical probe signal depended on the tip-sample separation but does not provide any information as to whether the tunnelling current modified the signal. Currents were detected at a distance of 1μm from the surface and were attributed to plasmon scattering [78]. Therefore it was deduced that this method would not be able to retain the nanometer resolution of STM. The glass prism also limits the minimum duration of the pulses as the prism will cause pulse broadening although this could probably be compensated for pulse durations down to 25fs, at which point the higher-order dispersion effects become significant[9].

Direct Coupling

The last of the coupling mechanisms to be dealt with here, shown in Figure 6-1c, was also the first reported in the literature. Its invention is widely attributed to Hammes and Cahill [76], although Steeves and Freeman[71] report that the first publication of this method was made as an anonymous research discloser[79].

In the direct coupling arrangement, the ultrashort pulses are focused directly onto the STM junction. Like the other methods discussed, it is a pump probe technique and the delay between the pump and probe pulse is varied whilst a signal is sought in the measured tunnelling current. There have been many attempts to successfully realise this scheme [7, 76, 80-82]. All of these reported attempts have struggled to detect the relatively small signal from the few electrons that represent the ultrafast dynamics of the system against the background of all the other processes that swamp the detected signal. However, of the schemes considered, this is the only one which has any real prospect of being able to simultaneously achieve the atomic resolution the STM is capable of whilst being able to take full advantage of the ultrafast laser technology available today. The time dependant signal must originate from the tunnelling process and the pulse duration must not be broadened unnecessarily if the goal of angstrom-femtosecond spatiotemporal resolution is to be attained. None the less there many processes occurring at the tunnel junction and these must be understood in order to avoid them.

6.1.3.   ORIGINS OF THE TIME DEPENDANT SIGNAL

A number of contributions to the time dependant signal measured by the STM have been identified in the literature [71-73] in addition to the ultrafast tunnelling signal that is subject of these measurements. They are:

- Thermal effects from the laser;

- Transient surface photo-voltage (SPV);

- Multiphoton photoemission.

These effects do not produce tunnelling currents but contribute to the signal measured by the STM. A brief description of these effects, with examples and recommendations for avoiding those signals follows.

Thermal Expansion

When the laser is incident on the tip and sample, both are subject to thermal expansion. In steady state illumination this is not a problem, as they will reach thermal equilibrium and the STM servo circuit will adjust the height of the STM to maintain the current set point. However, under pulsed illumination or varying intensity the expansion of the STM tip can be considerable and appreciable thermal expansion is observed experimentally with repetition rates up to 100KHz [83]. A theoretical finite element analysis by Gerstner et al [84] showed that these effects can be significant up to repetition rates of 200MHz. Gerstner's theoretical analysis also showed that for a 1 picosecond pulse the tip expansion occurs on a nanosecond time scale.

The inherent sensitivity of STM to the tip-sample separation can cause even very small variations in tip-sample separation to lead to large variations in the tunnelling current. This is a problem as many experiments attempt to be more sensitive to the small laser assisted signal by modulating the amplitude of the laser and detecting the signal phase sensitive lock-in detection. The thermal expansion effect has been used to perform laser-assisted STM, where the thermal expansion was used to perform displacement modulation STM. The light that causes the temperature dependant phenomenon also causes an expansion of the tip and therefore auto-gates the tunnel current.

In the experimental LA-STM paper by Gerstner et al [82] on development of a LA-STM, they employed direct tunnel illumination and expressed the need to use low excitation intensities and high frequencies to avoid modulating the tip-sample distance. This was especially important in their work as they used amplitude modulation and phase sensitive lock-in detection of the time resolved signal.

Surface Photo-Voltage (SPV)

Many semiconductors have charged surface states and the fields created by these surface states lead to a bending of the energy bands, creating a depletion layer at the surface (see Figure 6-2). If a photon with greater energy than the band-gap is absorbed then a pair of photo-excited carriers will be created. The carriers will be separated by the local electric field. One of them will be accelerated towards the surface state, where the carriers will accumulate thus reducing the band bending.
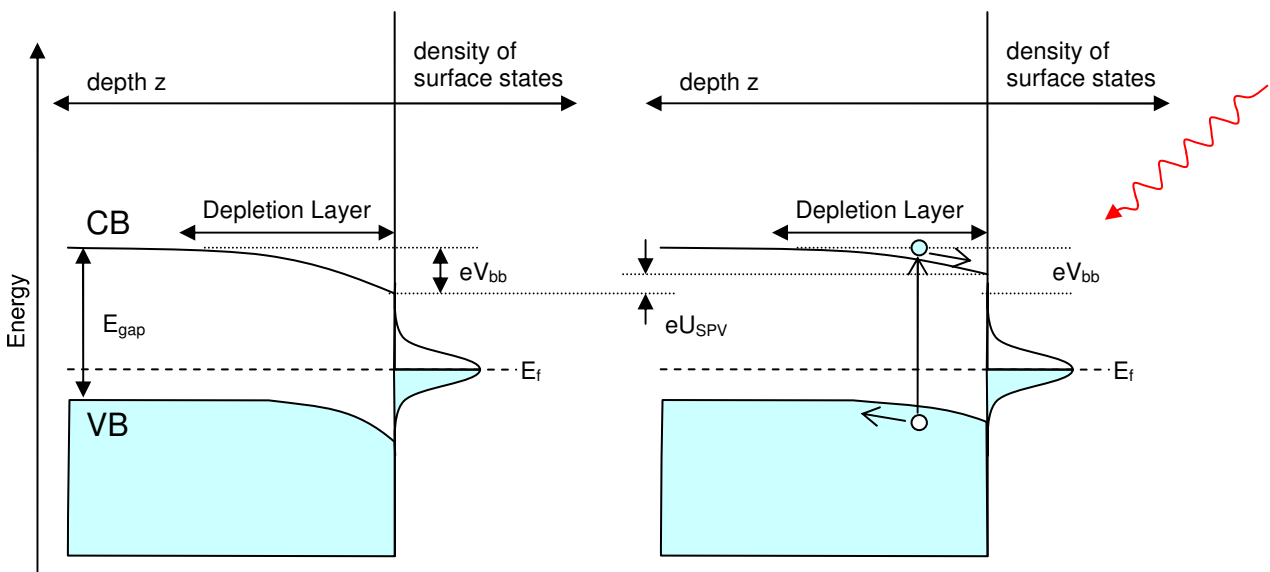
Figure 6-2   ***Energy Diagram to show development of a Surface Photo-Voltage***

These photo-excited carriers will recombine by thermionic emission on a nanosecond to microsecond time scale, depending on the carrier concentration, temperature and barrier height [82]. The magnitude of surface photo-voltage is dependant on the number of photo-carriers.

The nature of this transient potential variation leads to a displacement current in the STM tip similar to that experienced in the PG-STM configuration. As the signal has a capacitive origin, rather than a tunnelling origin, it can be distinguish from a true time resolve tunnelling signal by its continued presence when the tip is withdrawn. This signal can be avoided by selecting samples that have no surface states.

Multiphoton Photoemission

Multiphoton photo emission (or Multiphoton photoelectron emmission) is the process by which two photons can be simultaneously absorbed by an electron, promoting it to the vacuum level. The process of multiphoton emission in the presence of an STM tip is not well understood but it is believed to be influenced by the field enhancement caused by the STM tip. It was studied

by Feldstein et al [75], using the evanescent coupling, by exciting the surface plasmon resonantly in the silver and using the STM tip to provide field enhancement of the evanescent wave.

Multiphoton photoemission is often detected from amplified laser outputs but has also been detected from the frequency doubled output of a femtosecond oscillator at the relatively modest fluencies of 5mJ cm^{-2} [82]. However, these experiments were performed in vacuum and it is not expected to be such a serious problem in air, on a bench top STM.

Ultrafast Tunnelling

The last contribution to the time dependant signal is the ultrafast tunnelling current that we seek to measure. However, it is the smallest of the signals and, in all the reviewed literature, only one group has managed to prove that they have measured an ultrafast time dependant signal with its origins in the tunnelling current. Takeuchi et al [7] first proposed an alternative method of detecting the time dependent signal in a direct couple arrangement that did not modulate the intensity. Instead, the delay between the pulses was modulated by shaking the retro reflector of one arm of the interferometer. This modulation was achieved with a "shaker stage" and the signal driving it was used as the reference for phase sensitive lock-in detection of the time dependent tunnelling signal.

They used this arrangement to measure the photo carrier recombination time of non-doped n-GaAs(001) with a carrier density of about 1×10^{15}cm^{-3}. It was used again in 2004 and in an initial publication [5, 6] of the results of measuring a transient signal on a novel low temperature grown sample of GaN$_x$As$_{1-x}$ (x=0.36), two exponentially decaying transient signal were detected with time scales of 653±25fs and 55.1±5.0ps. The slower signal was attributed to dissipative photon scatter by hot electrons excited by the pump pulse which occurs on the sub-picosecond to picosecond time scale. However, the source of the faster transient signal could not be explained. Details of the signal analysis [85] were not published until almost a year later. It focused of the effects of the interference between the pump and probe pulse at short delays, finite pulse width, the amplitude of the delay time modulation and time constant of the lock-in detection but provided no new or further interpretation for the physical origin of the signal.

The signal was proved to originate from the tunnelling current by measuring the detected lock-in signal as a function of tip-sample separation and an exponential decay in the magnitude of the signal was observed, proving that the signal was related to the tunnelling current and not a displacement or photoemission current.

6.1.4.   THE SHAKEN PULSE PAIR EXCITATION (SPPX) METHOD

In the previous section, the novel lock-in detection mechanism that sets SPPX-STM apart from other laser assisted STM was mentioned. In this final section some of the details of the SPPX system will be looked at in preparation for the design and development of an SPPX that is the subject of Chapter 6.

A simplified schematic of the key components of the SPPX apparatus is shown in Figure 6-3. As with the Hamers and Cahill and the Gerstner arrangements it is a pump-probe experiment with the laser light directly coupled to the STM junction. The main difference is that rather than modulating the laser amplitude the delay time between the pulses is modulated and lock-in detection is used to identify the signal at the frequency corresponding to that of the delay modulation. As the delay stage is swept across the delay range it is also modulated. The delay stage may sweep a few hundred picoseconds in a few hundred seconds. The oscillating delay stage, referred to as the shaker stage, uses delay amplitude ranging from a 20fs to 100fs, with modulation frequencies in the few tens of hertz range.

When the pump pulse impinges on the system, electrons at the tunnel junction are promoted to excited states, and begin to relax back to their ground states. Whilst the electrons are in the excited state, the instantaneous tunnelling current is higher as more of the higher energy states are occupied. These electrons quickly relax to their ground state on a timescale much too fast for the STM amplifier to be able to measure. If the pumping is repetitive then a small increase may be observed in the time averaged current.

The arrival of the probe pulse some time (femtoseconds to picoseconds) after the pump pulse must now be considered. This pulse will excite electrons to the excited state again causing another momentary increase in current. Assuming that the pump and probe pulse are identical replicas of each other and that when the pump pulse arrives locally it elevates the whole population to an excited state, if it arrives within the relaxation time of the transient, then there will be less electrons that can be promoted to an excited state. As a result the ability of the probe pulse to raise the tunnelling current is reduced, see Figure 6-4. Therefore, at low pump-probe separation the laser induced tunnelling current would be reduced.
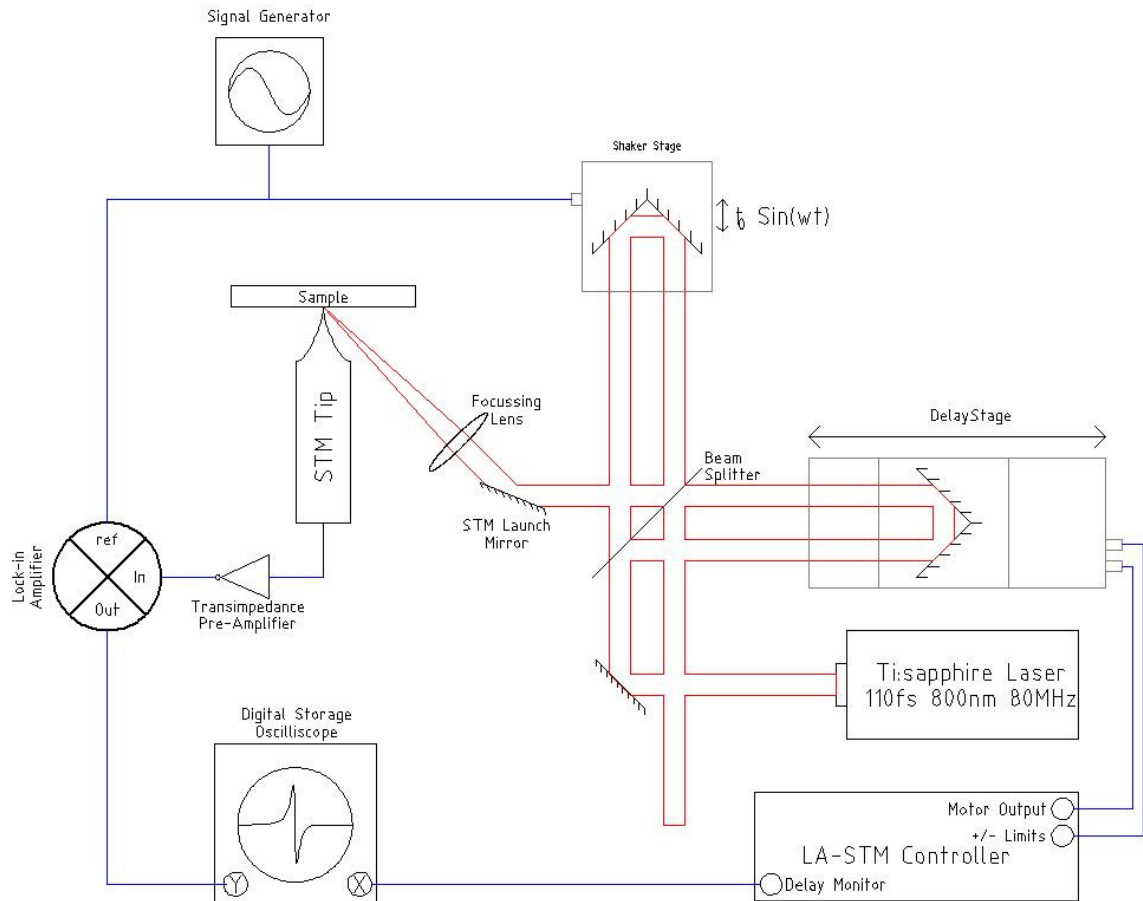
Figure 6-3   Schematic of SPPX-STM arrangement

The pulsed laser beam is split by the beam splitter, which together with the retro reflectors on the delay and shaker stages form a Michelson interferometer. The main output from the Michelson is directed to the STM tip by a mirror and a lens. N.B:. This is a simplified laser coupling arrangement. The lengths of each arm of the Michelson can be varied independently. The delay stage allows the separation of the two pulses output from the Michelson interferometer to be varied whilst the shaker stage creates a small periodic variation in the signal which the lock-in amplifier uses to detect the time resolved component of the signal.
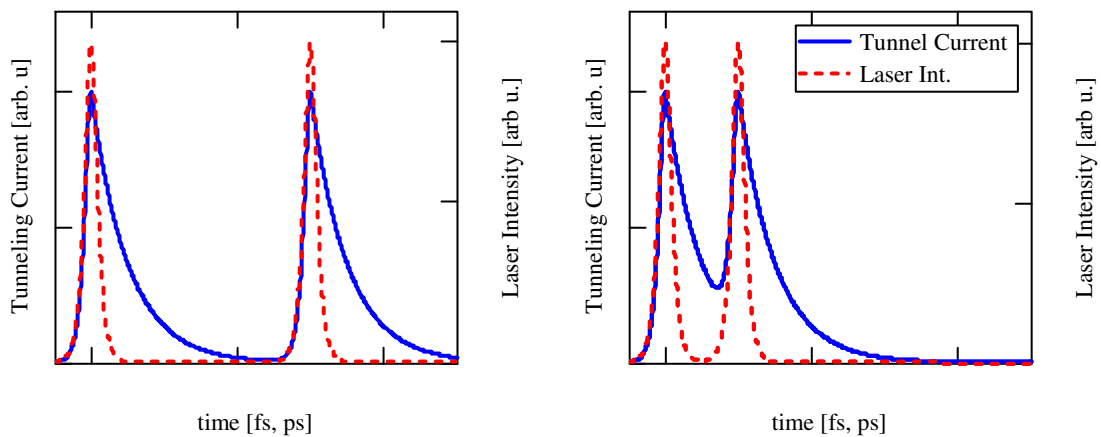
Figure 6-4   Effect of the ultrafast pulse pair on the instantaneous tunnel current

The tunnel current measured by the STM is the time averaged instantaneous tunnel current (blue solid line). At long delay times compared with the relaxation time of the transient studied the average tunnel current is higher, at lower delay time there are less electrons in the lower energy state, and so the effect of the probe pulse is reduced.

It can be considered that the time resolved component of the tunnelling current, I_t, is similar to the forms shown in Figure 6-5a. It is dependant of the pump-probe pulse temporal separation, t_d, which is swept and modulated, by the delay stage and the shaker stage respectively. If the STM electronics were sensitive enough and the signal was large enough compared to the background then the tunnelling current that would be observed is shown in Figure 6-5b, and current measured is given by:

$$I_t(t_d^0 + \Delta t_d \sin(\omega t)) = I_t(t_d^0) + \Delta t_d \sin(\omega t) \cdot \frac{dI_t}{dt_d} + O(\Delta t_d^2).$$

(6-1)

Where t_d^0 is the delay set by the delay stage, $\Delta t_d \sin(\omega t)$ is the modulated delay and the RHS is given by a first order expansion of the generalised tunnelling current, $I_t(t_d)$, and the higher order terms are represented by $O(\Delta t_d^2)$. The sine term on the right hand side is obtained by lock-in detection. The signal shown in Figure 6-5b is filtered to obtain the signal at the modulation frequency, shown in Figure 6-5c, and this is multiplied by the reference signal from the modulation source to show the phase of the detected signal relative to the modulated signal. This is low pass filtered to obtain a signal that is proportional to the 1st differential of the time dependant signal which is shown in as the thick blue line Figure 6-5d.
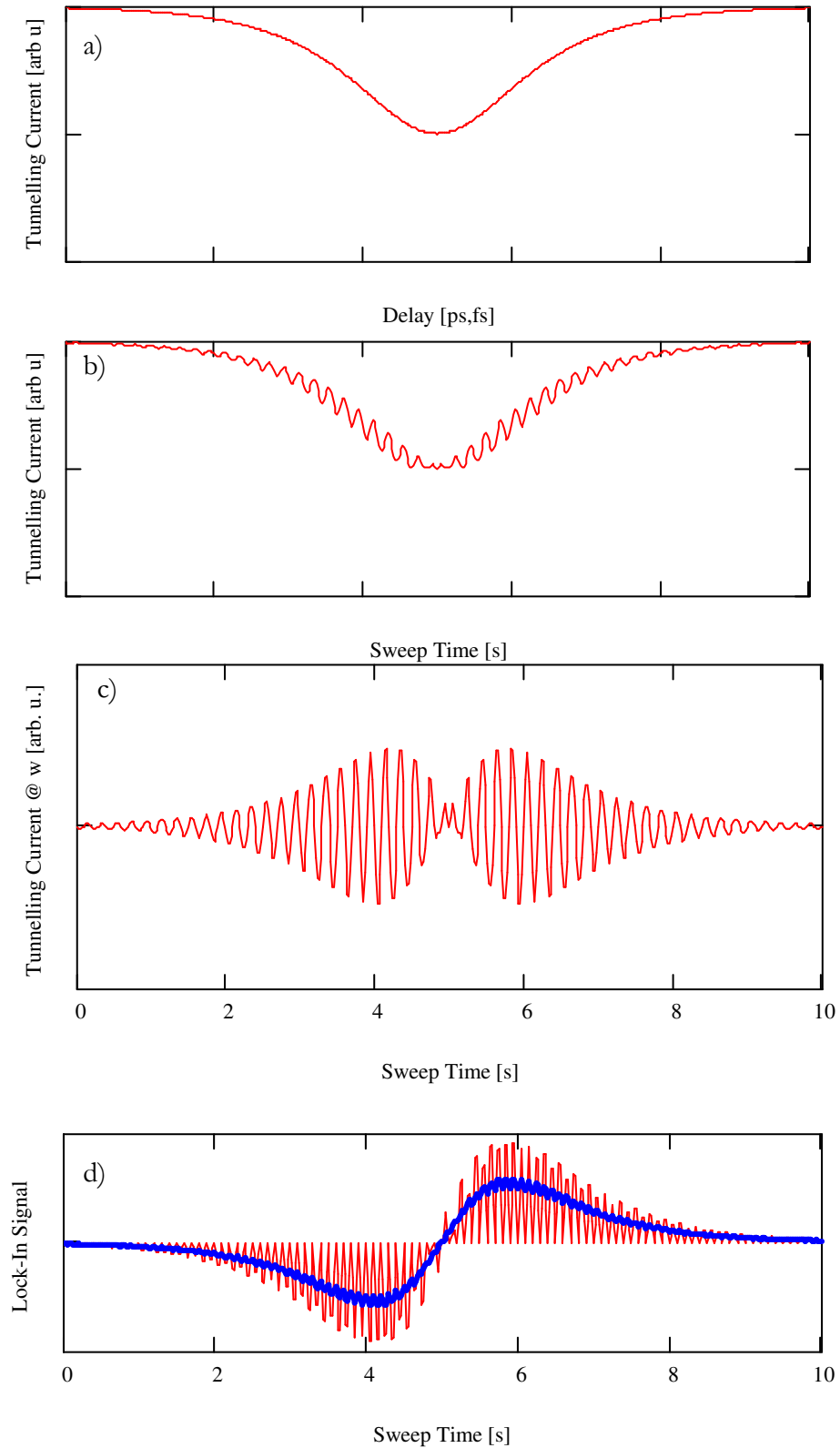
Figure 6-5   Lock-in Detection of the time resolved tunnelling signal
a) *Hypothetical time averaged tunnelling signal. b) The measured tunnelling signal measured in a modulated sweep.*
c) The signal at the frequency corresponding to the modulation. d) The signal multiplied by the modulation reference
signal (red) and low pass filtered (blue) produces a signal proportional to the first differential of the actual signal
shown in a).

6.2. DESIGN OF AN SPPX-STM

The origin of the time resolved signal in SPPX is from the quantum tunnelling phenomenon which is the only phenomenon capable of attaining atomic resolution. Finally, the SPPX technique is a pump-probe technique where the pulse separation is periodically dithered and the time resolved tunnelling signal extracted by performing lock-in detection at the frequency of the dither. This means that the average intensity is constant, minimising the thermal load on the system. Other methods that employ intensity modulation have observed thermal fluctuations in the sample and at the STM Tip.

A schematic of the SPPX was shown in Figure 6-3. The main sub-systems are the:

1. STM and Controller – Depicted as the STM Tip and Sample in the schematic.
2. Laser to STM Coupling Arrangement – Depicted as the STM Launch Mirror and Focussing mirror
3. Delay Stage and LA-STM Controller
4. Shaker Stage
5. Lock-in Signal Detection
6. Data Acquisition System

Figure 6-3 is only a schematic representation of the arrangement, and it does not take into account the practicalities of the design. The following sections describe the equipment used and steps taken to integrate the sub-systems into a SPPX-STM system. The focus of this chapter is on the engineering tasks that were undertaken.

6.3. THE SCANNING TUNNELLING MICRSCOPE

For the SPPX arrangement, the STM should offer good optical access to allow the laser to couple to the Tip-Sample junction. The SPPX measurements are time consuming and closed-loop stabilisation of the Tip-Sample separation is not possible so the open-loop stability of the STM junction must also be good. If a good lateral spatial resolution is also required, the XY drift must also be minimised. Good open loop stability is often achieved by a very compact design but this conflicts with the open optical access requirement allowing the laser to be coupled to the tip.

Thermal expansion of the sample and the instrument itself, as well as piezo creep in the scanning mechanism, are the leading causes of the open-loop tip drift and tunnel gap variation in the STM. It is well know that at near 0K temperatures piezo creep and thermal drift are minimised. Low temperature systems have their own practical problems and are considerably more expensive. An Ultra High Vacuum (UHV) is required which complicates sample transfer and other routine operations. However, many samples require UHV environments as they contaminate quickly in the air.

Initially a UHV STM and system was going to be used for this project and the STM and UHV chamber that were designed for it are provided in Appendix B. Ultimately that system was reassigned and an Omicron LH micro-STM was used instead. Its operation has been explained in section 3.2.

The Omicron controller for the LH STM has limited scope for expansion. Whilst it has an auxiliary input for one of the Analogue to Digital Converter (ADCs), there was no programmable output to control additional equipment. This necessitated the data acquisition for SPPX measurements being carried out by an independent measurement system which is discussed in the section 6.6.

6.4. COUPLING THE LASER TO THE STM

Whilst it may seem that targeting the laser at the STM tip is a simple matter, it is more complicated than the single mirror and lens that was shown schamtically in Figure 6-3. The laser must be focused to a spot centred on the STM tip-sample junction. If it is focused on the shank of the STM tip then thermal expansion of the STM tip is increased [72] and fluctuation in laser intensity causes a variation in the tunnelling current due to the thermal expansion. Laser coupling and focusing was achieved by means of a simple microscope design.

6.4.1. LAUNCH MICROSCOPE

A microscope arrangement was constructed using Comar's tube mounting system. In addition to focussing the laser to a small spot at the STM junction, which was the launch microscopes primary purpose, a camera was integrated into the arrangement to assist with the initial approach of the STM tip to the sample surface. A drawing of the microscope that was built is shown in Figure 6-6.
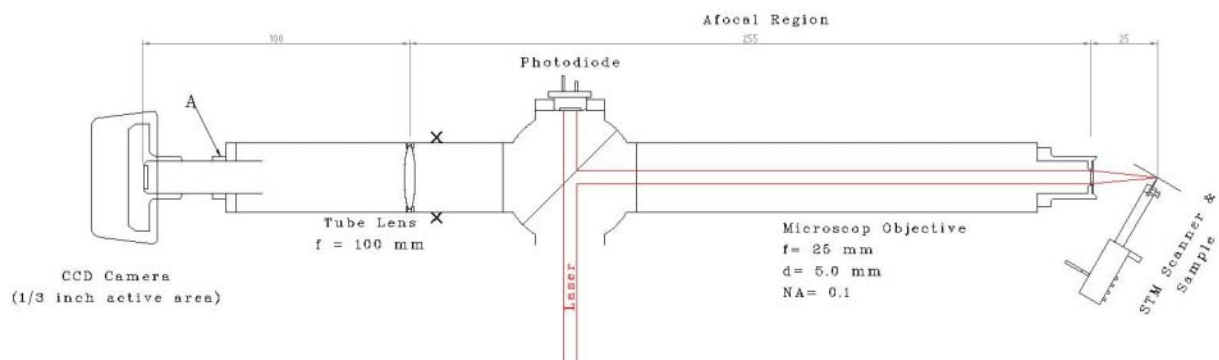
Figure 6-6   Laser Coupling Microscope
This arrangement can be used to assist with approach of the STM tip to the sample surface and also to align and target the laser spot onto the STM junction. The diagram is a scale drawing of the microscope arrangement. Given the parallel laser beam the objective is a simple design optimised for focussing lasers rather than for imaging. The laser power is measured using a photo diode placed at the position indicated. The dimensions marked are measured in mm.

The microscope is estimated to focus the laser to a 7μm spot on the tip of the STM. The CCD was only used as an alignment aid and was not used for quantitative measurements. Table 6-1 lists dimensions an paramters of the microscope arrangement shown in Figure 6-6.

Objective			CCD Dimensions			
Focal Length	[mm]	25	Diagonal		[mm]	8.47
Diameter	[mm]	5	Aspect Ratio			1.33
Numerical Aperture (NA)		0.07	Lines per Frame			400
Laser Wavelength	[nm]	800	Height		[mm]	5.08
Laser Spot Size	[um]	6.97	Width		[mm]	6.77
Imaging Wavelength	[nm]	550	Line Height	(Image)	[um]	12.7
Imaging Resolution	[um]	4.79		(Object)	[um]	3.175

Tube Lens						
Tube Length	[mm]	255	Max Angle		[°]	2.58
Focal Length	[mm]	100	Max Field Of View		[mm]	2.25
Clear Aperture (Diameter)	[mm]	23	System Magnification			4
			Image Diameter		[mm]	9.01

Table 6-1   *Microscope Design Worksheet*

This worksheet is used assist in selection of the objective, Tube lens and tube positioning. The entries are in put into the green fields, and the calculated results are output in the yellow fields.

6.4.2. ALIGNMENT

The microscope built in the previous section, does not in itself have any ability to adjust its focus. However, the whole assembly is small enough and light enough that it can be focused by moving it in its entirety. The tube mounted on a v-block clamp with coarse elevation control. The v-block clamp itself is has fine adjustment for elevation and yaw. The stage is mounted on a translation stage which permits translation in the direction of the microscope optic axis. This allows the microscope to be positioned and then the focus can be fine tuned.

When being used to assist with tip approach of the STM tip to the sample, the user must observe the tip and the reflection of the tip in the sample surface. As the tip approaches the sample the tip and the reflection will appear to come together. Coarse approach of the STM is achieved by approaching the tip to the surface using the STM coarse approach motor. Once the tips are as close together as can be achieved without them touching the STMs auto-approach can be used to find the surface.
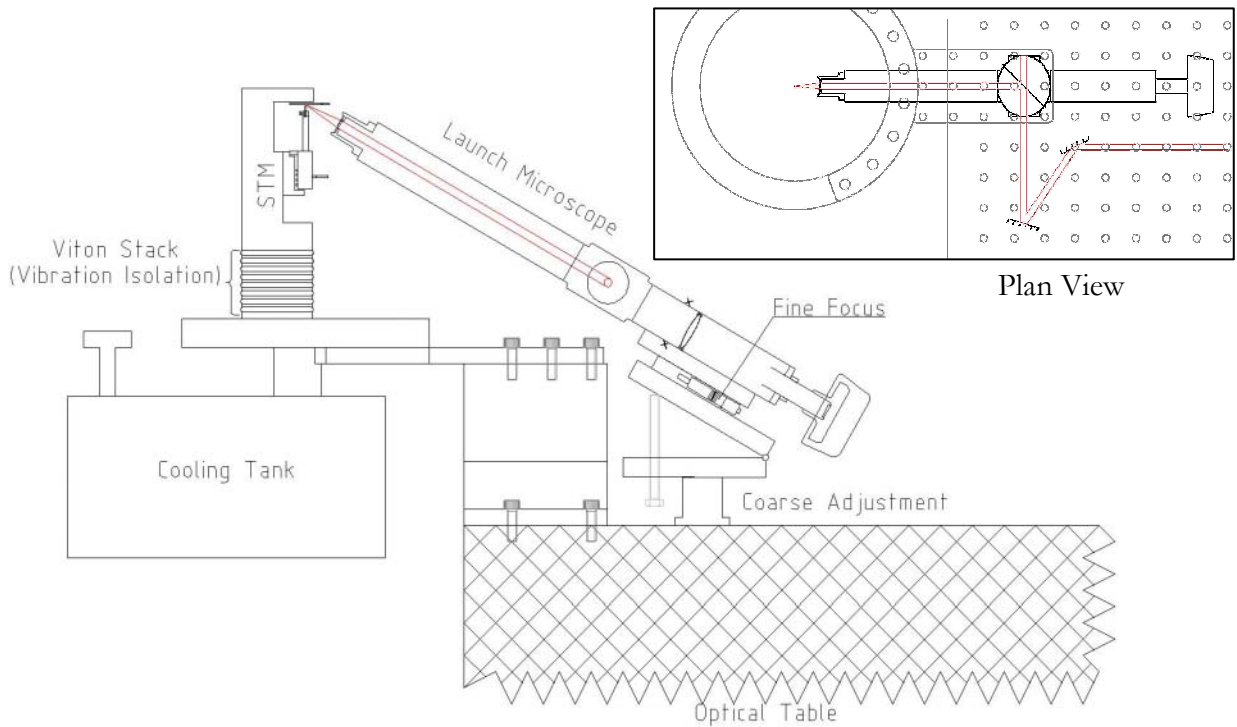
Figure 6-7   *Positioning of the Launch Microscope on the Optical Table.*
The optical microscope viewed from the side provides an aperture through which the laser may be targeted at the STM tip. The microscope is attached to a tilt table and the translation stage allows for fine focus control. The cooling tank is a vestigial appendage of its former use in vacuum. The inset shows a plane view of the laser launch and steering mirrors.

Once the tip has been approached, the laser can be aligned to the STM junction. Unfortunately, the camera was only used to produce an image on a monitor and there was no data acquisition system. The sample used for testing was graphite as it remains clean in air. Having been cleaved, it produces a mirrored surface and scatters very little. This can make locating the laser on the surface difficult. The most effective method that was discovered was to use the mirrors to adjust the light into the microscope to steer the laser spot onto the shank of the STM tip. Then it can be walked down the shank of the tip using the steering mirrors until it reaches the STM junction.

6.5.   DELAY STAGE AND LA-STM CONTROLLER

Shaken Pulse Pair eXcitation (SPPX) is a pump probe methodology. The delay stage determines the separation of the pump and probe pulses. The pulse is divided into two pulses by a Michelson interferometer with different arm lengths. Both of the arms are variable, one makes small high-frequency variations to the delay, to modulate the tunnelling current, so that it may be detected by lock-in detection. This is controlled by the shaker stage discussed in section 6.6. The other arm allows for the larger changes of pulse separation. The mirror is mounted on a step-motor controlled translation stage. This translation stage is referred to as the delay stage because it varies the delay between the two pulses.

The delay stage was a commercial "Neat RM400 Compact Ball Way Table", which has 4in travel. A step-motor drives a worm screw (called a 'lead screw') to move the delay stage. The lead screw has a 2mm pitch, ie. the stage will move 2mm for every revolution. The motor that drives the lead screw is used as a bi-polar step motor, with 400 whole steps per revolution. Using whole steps, the stage may be driven in 5μm steps. Micro-stepping provides a mechanism to sub divide whole steps and achieve better stepping resolution at low speed and improved smoothness of movement at higher speeds, avoiding resonance and reducing vibration coupled into the table.

An excellent online tutorial for step motor basics and control systems and circuitry has been written by D. W. Jones [86] and draws significantly on sections of [87]. A limited discussion of step motors and controllers is provided in section 6.5.1 in order to explain the operation of the controller that was built.

A controller was necessary to operate the delay stage and one was designed that could be customised for the purpose of acquiring SPPX spectra automatically. It was envisaged that the whole process of acquiring SPPX spectra could have been completed by a single box of electronics and that it would control the delay stage, the shaker stage and the data acquisition. However, eventually only the step-motor controller elements were actually implemented.

6.5.1.   STEP-MOTORS

Step-motors move in well defined and discrete steps whereas normal power motors tend to focus only on converting electrical energy into mechanical power. There several types of step-motor, uni-polar, bi-polar, multi-filament, and multi-phase motors. The type of motor that the delay stage used was a bi-polar motor. A diagram of a bi-polar motor is show in Figure 6-8. At the centre is a permanent magnet, with an odd number of pairs of poles. The one in the figure has 3 pairs of poles. This is called the rotator, while about the edges there are two coils at 90° to each other. These coils remain stationary and so it is called the stator. The number of poles in the rotator determines the angle moved in a single whole step and the motor performs a step that alternately energises the coils in a sequence, so the rotator moves one step.

In a bi-polar motor there are two windings, each with two terminals. The polarity of the voltage applied to each of the four terminals is independently controlled. If both terminals of a winding are the same polarity then no current will pass as there is no potential difference across the winding. Assuming each of the two terminals in a winding can either have a positive or a negative voltage applied to it, the current in the winding may be either forward, backward or nil. If the windings are energised in the sequence indicated in Figure 6-8, then the rotator will rotate clockwise. Each of the steps in the sequence corresponds to a whole step, each step corresponds to 30°.
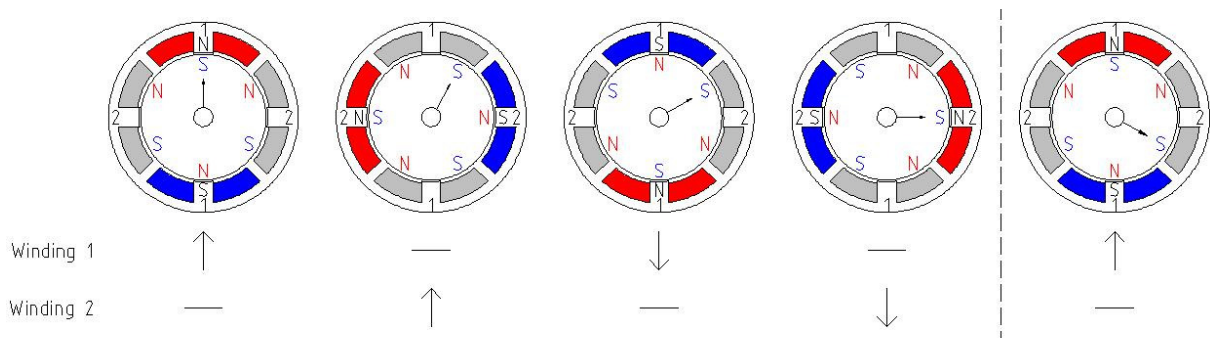
Figure 6-8   Bi-Polar Step Motor
A bipolar motor with a 6-pole rotator. By cyclically energising the windings in the stator in turn with the correct sequence of polarity the rotator moves around. The north and south poles of energised windings are coloured red and blue respectively. Coils that have no current running through them are coloured grey.

The sequence of the energising of winding 1 is the same as winding 2 but out phase by 90°. Considering only the state of being on or off and the polarity, it is very easy to understand how the rotator moves around. In Figure 6-8 only one winding at a time is energised. If both windings are energised the rotator will come to an equilibrium position (approximately halfway) between the two positions the rotator would have were only one or the other energised. This is called half stepping and with care can double the precision of the step motor and the delay stage that it is attached to.

In half-stepping the magnitude of the current in the windings is still constant. If the magnitude as well as the polarity of the current in the windings can be controlled then finer positioning can be obtained. This is called micro-stepping, and theoretically the angle of motor can be predicted by equation (6-2), where α_{step} is the angle of a whole step and I_2 and I_1 are the currents in the windings 2 and 1 respectively.

$$\theta = \frac{\alpha_{step}}{\pi/2} \arctan\left(\frac{I_2}{I_1}\right) \tag{6-2}$$

I_2/I_1 is simply a ratio of currents, but the total torque exerted on the axel of the motor is proportional to the square root of the sum of the square of the currents in the windings. In order to maintain a constant torque, the familiar relationship of equation (6-3) is used; the equation for a circle.

$$I_{max}{}^2 = I_1^2 + I_2^2 \tag{6-3}$$

If I_1 and I_2 are chosen to move around the circle, then they will of course cause the motor to rotate in the same direction, and I_1 and I_2 will be sinusoidal and co-sinusoidal with respect to each other. These two wave forms, just as the discrete sequences in Figure 6-8 were, are 90° out of phase with each other.

This would seem to offer an unlimited precision, or at least a precession limited only by the accuracy with which the current to the winding can be controlled. Indeed this is a limiting factor, but only in low friction motors. A certain amount of torque is required to overcome the static friction of the motor. If the micro steps are made too small, that the torque will not be enough overcome this friction and the motor will stall.

6.5.2. ELECTRONICS HARDWARE

The following requirements for the controller were established:

- It would support micro-stepping.

- It would support limit detection. ie. It would not stall on its end stops.

- It would be remotely controlled over a RS232 serial connection.

- The controller would keep track of its position.

- The controller would support variable speeds.

- The controller would support smooth acceleration to the specified speed at the specified acceleration.

- The controller would still accept commands and respond to status requests whilst executing movements.

Although commercial step motor controllers exist that do provide these capabilities they were too expensive and although step motor controllers are expensive, most of the complicated power distribution electronics are available as inexpensive integrated circuits.

Circuit Design

A simple microcontroller based design was developed. It consisted of just 4ICs, one power regulator and a handful of passive components. The simplicity of the design was possible due to the relatively powerful microprocessor selected allowing much of the control logic to be offloaded to the processor, rather than requiring complex timer and logic circuitry. The full schematics for the controller and firmware sorce code are provided in Appendix B.4.

A Renesas R521134FP microcontroller was used. It is an 8-bit microcontroller, with 1K ram and 16K of program memory. It has an extensive range of features, and those that were used and contributed to its selection include:

- 20MHz Clock Speed,

- High precision Timers (2x 8 bit with 8 bit pre-scaler and 1x16bit)

- 3 Digital IO ports (8bits each)

- 10-bit Analogue to Digital Converter.

- 2x UART (Serial Controllers)

- On-Chip debugger

- Free C-Compiler and Integrated Development Environment

- Real-time debugging suite

The UART allowed communication by RS232 serial connection with the remote computer. A MAX232 IC was used to achieve the RS-232 line voltages.
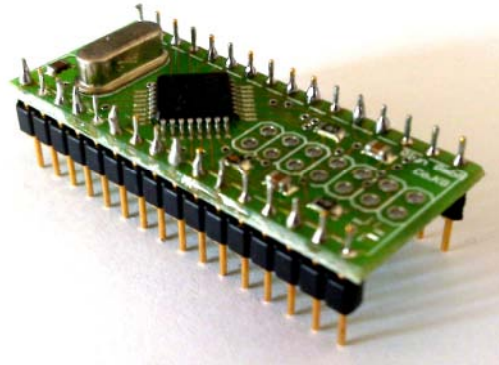
Figure 6-9 ***Renesas R521134FP Microcontroller and Development Board***
The microcontroller is the small square black surface mounted chip in the picture. The development board provides access to the terminals of the surface mounted microprocessor through a standard DIL32 package that is easier for prototyping. It also includes a 20MHz crystal to drive the microprocessor at high speed. The holes in the centre of the development board can be connected to an UART interface to allow code to be debugged and the processor to be programmed without removing it from the circuit.

The step-motor control circuitry was handled by a pair ICs that are designed to work together. These were a micro-step controller IC (NJU39610) and a current limited full H-Bridge IC (NJM3772). The Full H-bridge had two high impedance low voltage analogue inputs that could be used to specify the magnitude of the current through each of the windings and two logic inputs that specified the phase. Based on the inputs, the H-bridge was provided with the power for the motors which it distributed to the windings. The current in the windings was controlled by switching the output current to the windings in response the current sensing circuitry. According to the NJM3772 datasheet, the peak current in the windings is given by equation (6-4) where V_R is the analogue signal voltage provided to specify the current in through the windings, and R_S is the value of the sensing resistor. The maximum voltage supplied by the analogue outputs NJU39610 micro-step controller is 2.5V. So using a Sensing resistor of 0.5 Ohms provides a maximum current through the windings of 900mAw which is well within the power dissipation specifications on the H-Bridge.

$$I_{peak} = 0.18 \frac{V_R}{R_S} \tag{6-4}$$

Although the H-Bridge does produce a significant amount of heat it does not require a heat sink to be attached to it. As long as the central ground pins are soldered directly to a large ground plane, it can dissipate its heat through the ground plane.

The micro-step controller was essentially a pair of Digital to Analogue converters. There was 2-bit address bus which was used to specify which of the DACs was being addressed and an 8-bit data bus which specified the magnitude of the current through the winding on bits 0 to 6. The direction was specified by bit 7.

These data and address busses were connected to the microcontroller. By writing out values to the data bus it was possible for the Renesas microcontroller to control the current in the windings of the motor. The Microcontroller firmware would be responsible for calculating the currents and times when steps should be made to provide high precision positioning.

Construction

The circuit was implemented on a double sided PCB which was produced in house. Artwork for the PCB and an inexpensive method for producing it are provided in Appendix B.

The Board had a PCB mounted 9-pin DSUB connector so that it could be connected to the serial port of a computer. The other main connector on the board was a 6 terminal PCB screw terminal adaptor. The terminal is labelled X2 in the schematic and on the PCB layout. This provides connections for the 24V power (X2-3), ground (X2-6) and the connectors for the two motor windings. Also adjacent to the microcontroller were two 16-way SIL connectors, which allowed direct bread-board style connections to be made to the connectors of the micro-controller. These connectors were included in the original design to facilitate future expansion. They were used to connect the limit switch signals to pins on the microprocessor that provided additional digital IO lines.

The step motor was connected through a 9-pin D-Sub connector on the front of the LA-STM unit, wiring details are summarised in Table 6-2.

The LA-STM unit was installed in a metal box, and powered using a switched 25V 1.6A switched mode power supply which provided the voltage required by the motors and a 5 V power regulator provided the 5 V supply necessary for the digital logic components on the board. A diagram of the LA-STM controller front panel is shown in Figure 6-10. The RS232 connection to the computer is accessible from the side of the box and the 9-pin D-Sub connector on the front of the unit provides the connection to the step motor on the delay stage.

Pin No.	LA-STM Wire Colour	Connection on LA-STM PCB	Description	RM400 Wire Colour	
1	Red	X2-1	Winding 1a	Red	Motor Windings
2	Blue	X2-2	Winding 1b	Blue	
3	Green	X2-4	Winding 2a	Green	
4	Yellow	X2-5	Winding 2b	Brown	
5	Not Connected				
6	Purple	μcontroller Pin 7	+5V Power	Red	Limit Switches
7	Brown	μcontroller Pin 17	+ Limit Detector	Blue (black tag)	
8	Black	μcontroller Pin 16	- Limit Detector	Blue	
9	White	X2-6	Ground	Black	

Table 6-2   LA-STM Motor Output and Limit Switch connector wiring

The BNC connectors are provided for future connections. The BNC connectors labelled ADC1 and ADC2 are connected to the pins 13 and 12 respectively of the microcontroller which can be used as 10bit analogue to digital convertors. The original intention was to acquire the output of the lock-in detection through these ADCs but they proved to be too noisy and this feature was re-factored out of the firmware code when support for the limit switches was added.
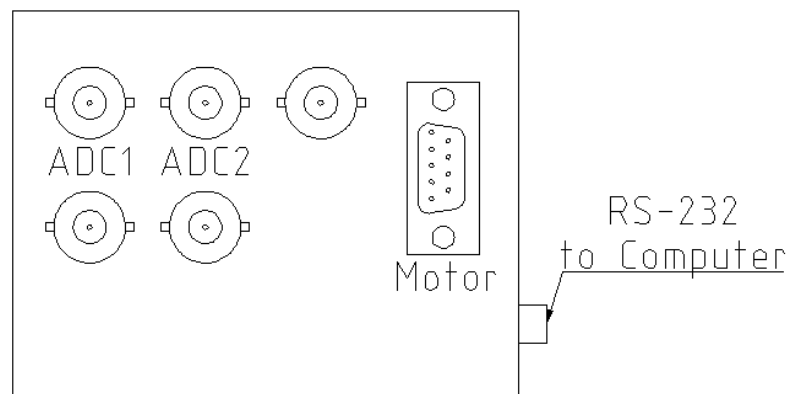
Figure 6-10   LA-STM Controller Front Panel

6.5.3.   MICROCONTROLLER FIRMWARE

The microcontroller provides all the logic that enables the step motor to be controlled. A single whole step is only 0.9° and is further reduced with micro-stepping. The microcontroller provided 8 micro-steps per whole step. On a 2mm pitch lead screw this means a whole step corresponds to 5μm of travel and a micro-step corresponds to only 0.625μm. With a full travel of in excess of 100mm, moving a significant distance in a timely fashion is going to require a high step frequency.

The microcontroller not only needs to keep track of the stage's current position and set the current in the motor windings; it must also calculate the timing between steps during acceleration, deceleration and whilst moving at constant velocity. The code documented here performs these calculations on the fly, allowing the controllers to receive new positioning

commands in the middle of a movement. Many commercial controllers will accept a command to move to a location and pre-calculate all the timings to reach that destination. It cannot be interrupted and will not respond to new commands until the one given is completed, however long that may take.

In addition to the core functionality of controlling the step motor, the microcontroller must also maintain communications with the controlling system over the serial communications system. The LA-STM firmware makes extensive use of the interrupts which are listed in Table 6-3. Indeed, the core step motor control functionality operates in a timer interrupt routine. Two more interrupts are required for low level serial communications whilst the main program loop simply handles the command interface.

Interrupt Name	Trigger	Action
Timer X	Timer X countdown expired.	Perform Step and calculate time until next step.
Serial Transmit Interrupt	Transmission of a byte over the serial interface has completed.	Transmit the next byte (if applicable) from the transmission buffer.
Serial Receive Interrupt	A byte was received on the serial interface.	Store the byte in the receive buffer.

Table 6-3   Interrupts used by the LA-STM Controller Firmware

Step Motor Control Logic

Step by Step

In section 6.5.1, on the step-motors and micro-stepping it was explained that the energising sequence for the two windings was 90 degrees out of phase with each other and that when micro stepping, the current in one winding was sinusoidal whilst in the other it was co-sinusoidal. The micro-step controller has an 8 bit digital to analogue convert. The first 7 bits define the magnitude of the current, whilst the 8th bit defines the sine. There would be 8 microsteps per full step. A table of sin() was calculated for the 9 equally angles from 0-90° inclusive. It was calculated to use the full resolution obtainable with 7-bits, and is shown in equation (6-5).

$$DACBuf[] = [0,25,49,71,90,106,117,125,127] \qquad (6-5)$$

Two counters and direction bits are defined for each of the motor windings. One of the counters starts at 0 and counts up whilst the other starts at 8 and counts down. The counters are used as an index to the DACBuf table that contains the first 90° of the sin() function, which can be written to the micro-step controller DACs to control the current in the windings.

When the microcontroller needs to move on a single micro-step, each of the counters is incremented or decremented depending on the direction bit for that winding. When either counter reaches 8 or 0 the direction bit is flipped. In this way a sinusoidal current is created in each winding with phase separation of 90°. To change the direction of movement you simply need to flip the direction bits for each phase. This low level control step control is of course written into a function, step(dir,N), which simply take the number of micro-steps, N, and the direction, dir, to move in. It should be noted that for each call of the step() function only one movement is made. The number of steps simply allows you to move multiple micro-steps at once. In this version all movements are performed one micro-step at a time. However the use of multiple micro-steps at a time could be used to achieve higher velocities or overcome greater static friction.

Moving from A to B

The step function provides us with a way of moving from one place to another. If a movement of 1000 steps is required, then it is simply required to call the step function 1000 times. The time between each step determines the velocity of the movement. It is not an efficient use of the processor's main loop to spend its whole time waiting to make the next step. The microcontroller has three timers, called Timer X, Timer Y and Timer C. These timers can be used to interrupt the normal execution of commands. Timer X is used to control the period between steps. The timers obtain their clock from the CPU clock (which runs at 20MHz). The number of clock cycles is programmed into the timer and from moment the timer is started this number begins to count down. When it reaches zero the timer interrupt is raised and its handler is executed. Figure 6-11 shows the flow of commands that happen in the interrupt handler. There are number of tasks that must be performed. Obviously the step needs to be made but it also needs to calculate how long to the next step. Moving at constant speed, calculation of the time until the next step is not complicated but when the motor is accelerating, doing this calculation on the fly is not trivial. The method of calculating these intervals will be discussed shortly but for now it may be assumed that this is a function that will take a finite time to calculate.

Initially, the interrupt handler disables any further interrupts. It does not want to be interrupted during this time critical operation. The time is put into a countdown mode, and restarted. The step is made, and the time until the next step is calculated, then the timer is stopped. By comparing the value of the timer with the initial value it can be determined how long the calculation until the next step took. This is discounted from the calculated value as time already served and assuming that there is still any time to wait, this value is programmed into the timer which is restarted and the interrupts are re-enabled. The micro-controller is then able to go

back to executing its main program loop until the interrupt is triggered again when the next step is due. This interrupt will be called for at every step between its starting point and its target destination and one of the jobs of the interrupt handler is to keep a track of the position and stop when it gets there, and start to slow down in time for the destination.
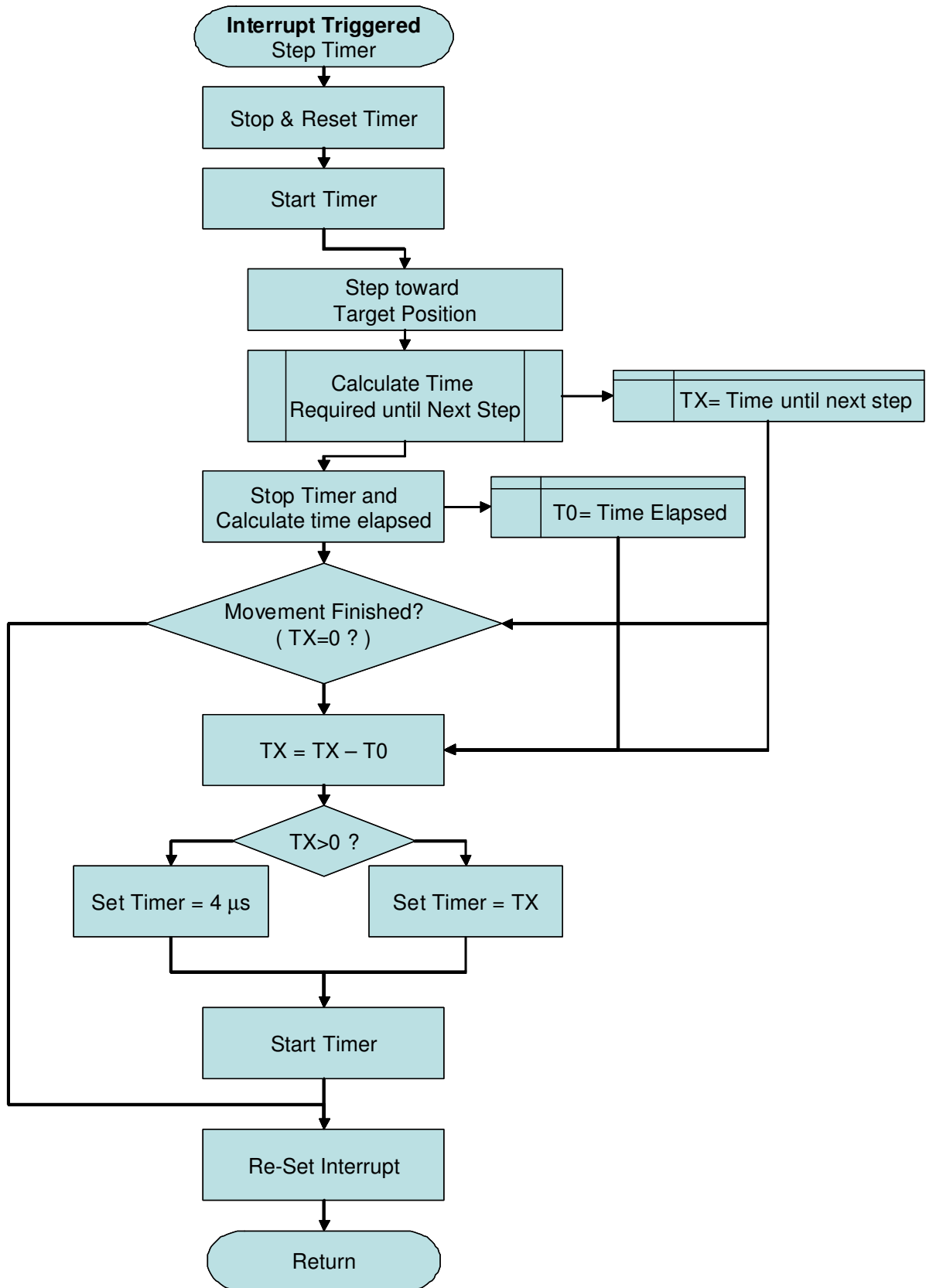
Figure 6-11   Step Timer Interrupt Flow Diagram

Setting the pace (velocity, acceleration, breaking and control)

The concept of operation of this step motor controller is somewhat different to other commercial step motor controllers, where an instruction is usually given and then executed. No more instructions can be processed until that instruction is completed. This means that the timings between steps can be pre-calculated, stored in a table and then executed in sequence.

The LA-STM step motor controller is able to accept new instructions in mid movement and adjust the velocity, acceleration and end point accordingly. This is possible because the inter step timings are calculated on the fly. The step_loop() function which is called by the step-timer's interrupt handler to calculate the time until the next step, not only keeps track of the position of the stage but also its current velocity and is continually adjusting the inter-step timing to attaining the target velocity and position.

Consider movement from one position at rest to another position at rest, with a specified top speed and acceleration. There are three phases to the movement. These are the acceleration phase, the constant velocity phase, and deceleration or breaking phase, and they are depicted in Figure 6-12.
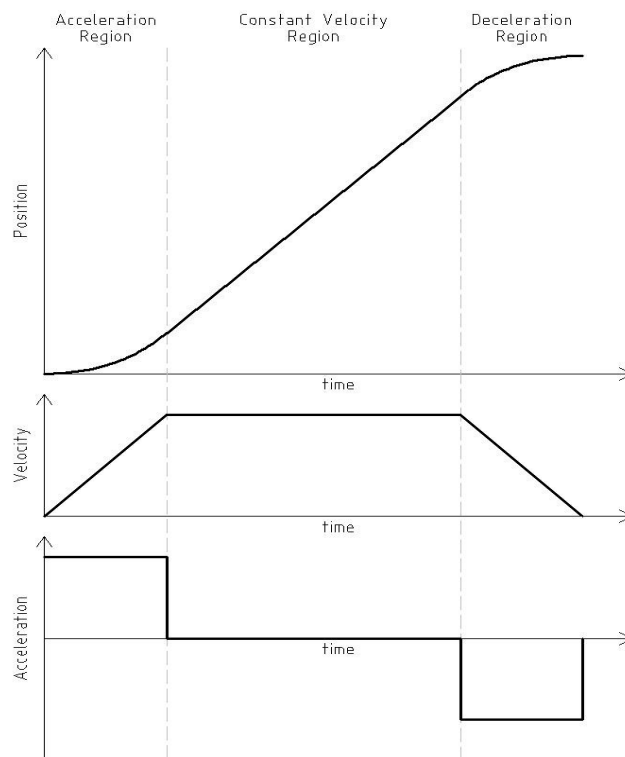
Figure 6-12 **Phases of movement.**

Figure 6-12 shows that there are no discontinuities in the position or the velocity. In the accelerating region, the velocity increases at a constant rate and the position increases quadratically. In the constant velocity region the position increases linearly. Finally, in the

deceleration region the velocity is reducing linearly. By controlling the acceleration the jerkiness of movement can be greatly reduced.

The continuity of the position and velocity are maintained by two state variables; the current velocity, curVel, and the current position, curPos. Similarly there are two target variables for velocity, tarVel, and position, tarPos. By controlling the inter-step timings the current velocity can be gradually changed as specified by the acceleration.

Positions must be stored, as long integers in the microcontroller, in order to have the precision and range to represent the whole travel range of the delay stage in micro-steps. The velocity and acceleration are stored as integers which greatly increases the speed of the code on the microcontroller. All the commands that are received through the serial port use long integers to represent the positions, velocities and accelerations in units of μsteps, μsteps.s^{-1} and μsteps.s^{-2}. Internally velocity, curVel, and the acceleration, a, are represented at in units of (and with the precision to the nearest) 50μsteps.s^{-1} and 2500μsteps.s^{-2} respectively. The time until the next step is calculated using integer mathematics. The following equations return the time until the next step in microseconds.

$$t = \frac{20000}{curVel}\ \mu s, \qquad\qquad \text{at constant velocity} \qquad\qquad (6\text{-}6)$$

$$t = 200\frac{\sqrt{curVel^2 + 2a} - curVel}{a/100}\ \mu s, \qquad \text{whilst accelerating or breaking} \qquad (6\text{-}7)$$

At first glance equation (6-7), look like it might be further simplified, however great care has to be taken ensure that the 16-bit integer does not over flow or that an integer division does not cause unacceptable loss of precision. By distributing the constant multiplicative factor throughout the expression this situation can be avoided. The square root is implemented as a fast integer square root algorithm. An initial estimate of the square root is obtained by using binary logarithms, and a more accurate solution is rapidly converged by successive approximation using the Babylonian method. Obviously, given that this is taking and returning integers as parameters this is more accurate for larger integers.

Initial versions of this program were implemented using floating point mathematics. The RC8 microcontroller series only has an eight bit microprocessor and although the compiler can produce code that will handle floating point calculations this is not natively supported by the processor in the microcontroller and therefore does not execute quickly. The square root and division operations took so long that calculating the time until the next step in the acceleration phase took over 1.5 seconds which is orders of magnitude large than the actual time that needs to

be waited. The code was re-factored to perform the calculation using long integer mathematics. The resultant assembly code was half the size but still executed too slowly. Only when the code was re-written to use integer mathematics, sacrificing precision in the acceleration and velocity, was it possible to perform these measurements on the fly.

The step-loop() function is also responsible for starting deceleration in time to ensure that the velocity is 0 when the delay stage reaches its destination. It will only decelerate at the speed specified for the acceleration. If the user changes the target location and does not allow sufficient time to stop, the stage will begin to decelerate immediately but will come to an abrupt stop at the specified position. If there is a great deal of inertia this can cause the stage to jump and create an error in actual position. The user should ensure this situation is avoided. There are two other circumstances when the stage will come to an abrupt stop. When the "HALT" is issued to the controller and if the limit switches are activated.

Communication and the Control Interface

In the previous sections, the method of determining how steps are made and how the position and velocity can be controlled by varying the time between steps has been examined. However, a method of telling the controller the desired position has not been provided.

Communication with the LA-STM controller is provided through a RS-232 serial interface, using the settings in Table 6-4. This uses two very simple interrupts. The microcontroller can only receive or send one character at a time. When a character is received on the serial line it raises an interrupt. The handler takes the character and stores it in a cyclic buffer. A counter keeps track of the position of the most recently received character and whilst another keeps track of the most recently processed character. If the processed character counter does not equal the received character counter, then some action is required with the received data.

A similar process takes place for transmission of characters which also can only send one character at a time. A procedure wanting to send characters writes them to a cyclic buffer and initiates transmission. When the first character has finished transmitting an interrupt is raised. If there are any more characters in the buffer to be sent, then the next one is transmitted and so on.

Baud Rate:	9600
Data bits:	8
Parity:	None
Stop Bits:	1

Table 6-4 **LA-STM Controller Serial Communication Settings**

These interrupts only handle filling and emptying receive and send buffers. The main program loop continuously polls the buffers waiting for a new command. Of course, if any action

needs to be taken the timer interrupt will take control on the processor execution, but otherwise the main loop just waits for the next command.

Figure 6-13 shows a flow diagram describing the initial operation from power on to entering the main execution loop. First the microcontroller initialises itself, setting its clock speed, and configuring its IO pins. The serial communications are then initialised and the serial interrupt handlers enabled. The step motor control routines are initialised, and the greetings banner and command prompt is transmitted across the serial connection and the main execution loop is entered where it waits for input.

The main loop continually checks to see if any new data has arrived in the receive buffer. If it has and it is a carriage return, then it launches the command parser. A generic command parser was written that took commands of the form:

cmd [*<param>*]

Where "**cmd**" was the command string and "*param*" is an optional command parameter with the data type of a long integer. Originally, it was written to accept a range of parameter types but this was factored out of the code to save space.
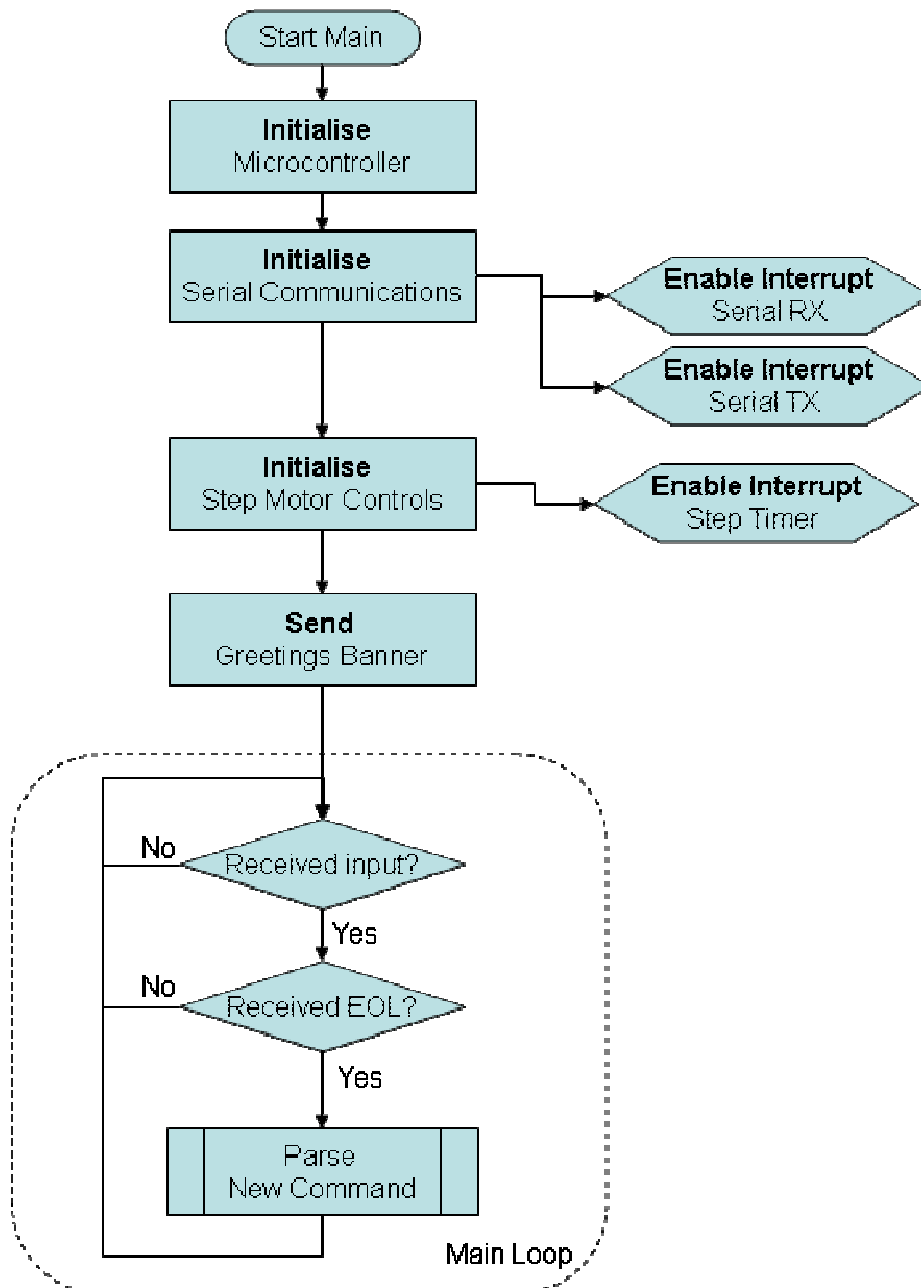
Figure 6-13   **The LA-STM Controller main execution loop**

The commands language is defined in a static constant array of command registration structures. The command registration structure has the following definition:

```
1:  const struct CMD_REG    /* Struct Definition for the command table */
2:  {
3:      char name[CMD_LEN]; /* The string used to call the command from the serial interface
4:                             The string is null terminated and CMD_LEN chars long inc. \0 */
5:      char type;          /* Paramter Type, 0: None, 1: Int */
6:      CMD_FUNC cmd;       /* Function pointer to the interface command */
7:  };
```
Listing 6-1   **Command Registration Structure**

The command parser tokenises the received command and identifies the parameter and the command name. It searches the command table for the command name, and then calls the

function pointed to be the function pointer, *cmd*. Table 6-5 defines the command language to the LA-STM.

Command	Units	Description
gp	steps	Get Position -Returns the Current Position of the step motor
ma *<position>*	steps	Move Absolute – Move to the specified <position>.
mr *<No. Steps>*	steps	Move Relative – Moves <No. Steps> from the current position. If <No. Steps> is –ve it will move backwards.
sv *<Velocity>*	steps·s^{-1}	Set Velocity – Set the target velocity for positioning movement.
gv	steps·s^{-1}	Get Velocity – Returns the current maximum velocity.
sa *<Acceleration>*	steps·s^{-2}	Set Acceleration – Sets the acceleration used when changing velocity.
ga	steps·s^{-2}	Get Acceleration – Returns the current acceleration
sul *<position>*	steps	Set upper limit.
gul	steps	Get upper limit.
sll *<position>*	steps	Set lower limit.
gll *<position>*	steps	Get lower limit
rng	N/A	Range - Locates the upper and lower limits using the limit switches.
demo	N/A	Moves continuously between upper and lower limits, until a new position is specified.
halt	N/A	Stops the motor immediately without a controlled deceleration.
home	N/A	Makes the current position, the home position. All absolute movements are relative to the new home position. If the motor is moving it is halted.

Table 6-5   LA-STM Motor Control Language

When the controller receives a movement command it sets the target position and starts the step timer. As the step calculations are performed on the fly inside the interrupt handler, the LA-STM is able to continue to receive and respond to commands. This can be used to poll the position of the stage during a movement, or update the target position.

6.6. SHAKER STAGE

The key distinguishing feature of the SPPX method is the periodically varied inter-pulse separation against which lock-in detection is performed. The retro-reflector on one of the arms of the interferometer is mounted on a piezo stage, whose position varies periodically, creating a periodic delay variation. The signal detected using a lock-in amplifier is proportional to the frequency at which lock-in detection is performed. Supporting a high frequency modulation signal can be beneficial but it should of course not exceed the bandwidth of the STM pre-amplifier. However, the STM pre-amplifier can handle signals up to at least 50kHz and special

STM pre-amplifiers have been designed with bandwidths in the MHz [88, 89]. These high bandwidth amplifiers were developed to study fast transient tunnelling current on the microsecond time scale.

Unfortunately, the retroreflector has a significant mass, about 200 grams including the mountings. To achieve a delay modulation in the interferometer with an amplitude of 100fs, the peak to peak displacement amplitude must be about 15μm. Even at moderately low frequencies, in region of 150Hz, this vibration exerts a periodic force with amplitude 1.2N. This creates enough of a vibration that it is detectable in the STM junction. Initial experiments where the piezo was attached directly to the optical table detected a 100pA signal in the tunnel current caused by the vibration. For this measurement, the STM was tunnelling with an applied tip bias of 1V, and a current of 1nA. The gain loop was set low and the Piezo was vibrated at 95Hz, and a current at a frequency of approximately 100pA peak to peak was detected. It is not mentioned in the papers by Takeuchi et al, whether this was a problem that they experienced. Perhaps their STM's vibration isolation was able to accommodate it but it might explain why, in their 2004 paper, they used a lock-in frequency of only 20Hz whilst in the 2002 paper, when they first published the technique, they had used 400Hz.

A method was needed to vibrationally isolate the shaker stage from the table without compromising the optical stability of the Michelson interferometer.

6.6.1.   THE MECHANICAL SHAKER ASSEMBLY

A mechanical assembly was designed that would allow high frequency large displacements of the retro-reflector, whilst preventing the mechanical vibration being coupled into the optical table. The assembly is illustrated in Figure 6-14. It employs an auxiliary mass on a spring. It is the same technique that is used in sky scrapers to stabilise them in the event of an earthquake or high winds that may excite the resonant frequency of the building.
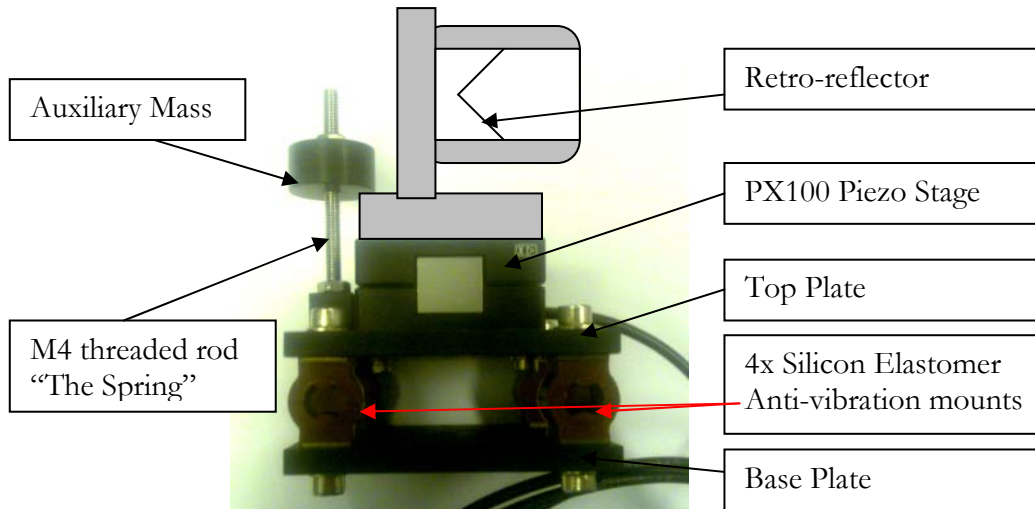
Figure 6-14   Piezo Shaker Stage
A photo of the piezo shaker stage with the retro-reflector drawn in. The auxiliary mass and M4 threaded rod form a tuneable resonance. When the piezo stage is vibrated at the same frequency as the resonance of the auxiliary mass, no vibrations are detected in the top plate. The Silicon Elastomeric mounts damp a small vibration that may be experienced slightly off resonance.

The resonant frequency, ω_1, of a mass, m_1, on a massless cantilever of length, l_1, and a moment of inertia I is given by equation (6-8). The resonant frequency, ω_2, of an unloaded cantilever with a mass per unit length, m_2, evenly distributed along its length and a moment of inertia I is given by equation (6-9) [90, 91].

$$\omega_1 = \sqrt{\frac{3 \cdot E \cdot I}{l_1^3 m_1}} \qquad (6\text{-}8)$$

$$\omega_2 = 3.515 \sqrt{\frac{E \cdot I}{m_2 \cdot l_2^4}} \qquad (6\text{-}9)$$

Where E is the Young's modulus of the material the cantilever is made of and I is the second moment of inertia of the cantilever, which for a cylindrical rod of diameter, d, is given by,

$$I = \frac{\pi d^4}{64}. \qquad (6\text{-}10)$$

The mass per unit length of a cylindrical rod, m_2, made from a material with density ρ is given by,

$$m_2 = \rho \cdot \pi \frac{d^2}{4}. \qquad (6\text{-}11)$$

The resonant frequency for the combined system is given by,

$$\omega_{tot} = \sqrt{\frac{\omega_1^2 \omega_2^2}{\omega_1^2 + \omega_2^2}}. \qquad (6\text{-}12)$$

The threaded rod in Figure 6-14, was made of stainless steel (E=210GPa, r=7780kg.m⁻³). It was an M4 threaded rod, with a core of diameter of 3.3mm, and length of 5cm. The mass was made from brass, and its position could be adjusted on the rod to tune the resonance of the system. It was locked in place with a nut. The nut and weight had a mass of 50g. Adjusting the position of the auxiliary mass allows the resonance to be tuned over several hundred hertz, as shown in Figure 6-15.
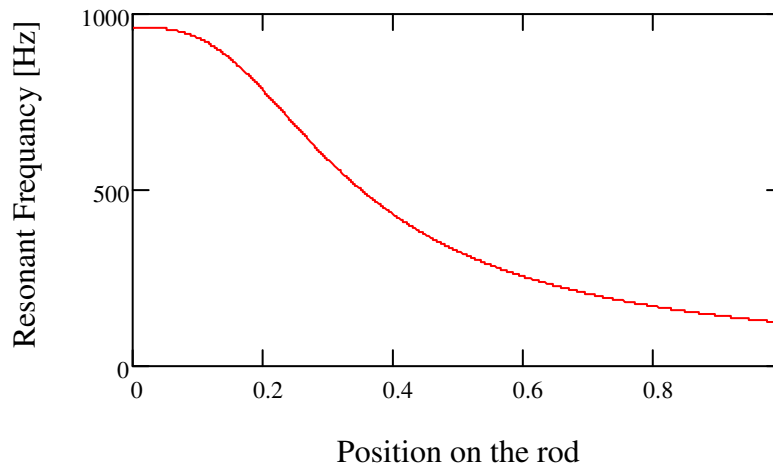
Figure 6-15   **Theoretical Frequency Response of tuneable auxiliary mass**
The frequency response for an auxiliary mass of a 5 cm piece of M4 threaded stainless steal rod as function of the position of the mass on the rod. A position of 0 corresponds to the auxiliary mass at the bottom on the rod whilst 1 corresponds to it being at the top of the rod.

When the shaker was used in STM experiments the frequency of the oscillator was adjusted to minimise the motion in the top plate. The resonance of the tuned mass damper was adjusted to be as close as possible to the natural resonance of the piezo stack. This minimised the power requirements for the piezo, whilst still being able to achieve large displacements at low voltages and without disrupting the STM junction. The periodic displacement of the top plate was measured using a loudspeaker. A cardboard cone was attached to the paper cone of the speaker and the cone was mounted with its apex touching the edge of the top plate, as shown in Figure 6-16. When the piezo was operated away from the resonance of the tune mass damper, the top plate would experience a periodic displacement. The corresponding movement of the speaker cone would induce a current the loudspeaker coil which was amplified and monitored on an oscilloscope.

With the new vibrationally isolated shaker assembly in place, the STM tunnel junction stability test was run again and no noise signal was detected at the STM junction corresponding to the vibration of the shaker stage.
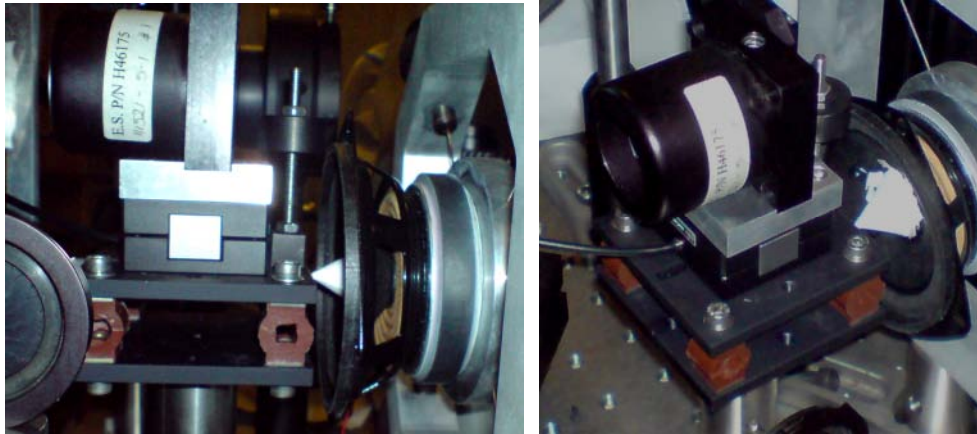
Figure 6-16   Photo of shaker stage in position

6.6.2.   CHARACTERISING THE FREQUENCY RESPONSE

The shaker mirror forms part of the Michelson interferometer that splits the pulses. To characterise the displacement versus frequency response, the Michelson interferometer was aligned to a HeNe continuous wave laser beam. The output of the interferometer was detected by a photodiode, the signal from which was amplified by a trans-impedance amplifier and the output monitored on an oscilloscope. The stage was driven from a signal generator which was buffered by a piezo amplifier. A sine wave was fed to the piezo stage and as the stage moved the fringes were counted on the photodiode. After the piezo amplifier, the voltage applied to the piezo ranged from 0 to 25V. The piezo stack would not accept negative voltages. The peak to peak voltage was kept constant whilst the frequency was increased. At each frequency tested, the numbers of fringes were counted using the oscilloscope's cycle counter function.

The results of the measurement are shown in Figure 6-17, the piezo stack's own mechanical resonance was detected at 91.5±0.2Hz. The PX100 piezo stack has a maximum nominal displacement of 100μm which was slightly exceeded on resonance even though the applied voltage was only 21% of the nominal full voltage.

Further tests showed that, on resonance, significant displacements could be achieved with quite small voltages. The signal generator was tuned to the piezo resonance and the voltage output from the amplifier varied. The fringes were counted in the same way and the displacement against voltage response was found to be linear over the values tested. Off resonance, the displacement per volt was closer to the nominal values. The results are shown in Figure 6-18.
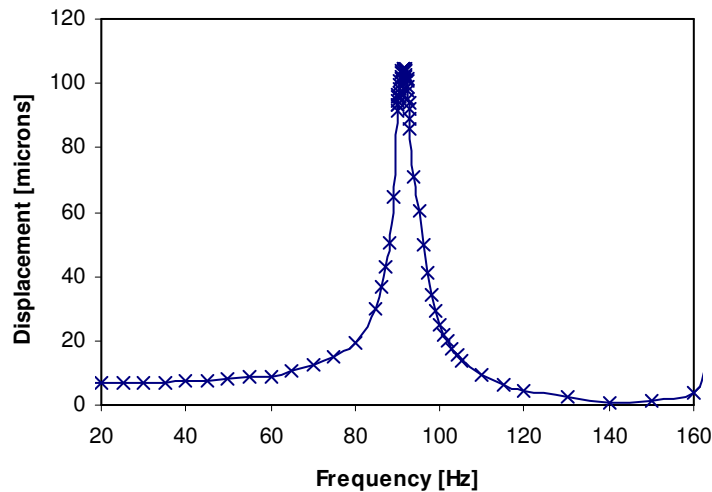
Figure 6-17   Piezo Resonant Frequency Response

Displacement measured by counting fringes from a HeNe laser operating at 633nm. The resonance is centred on 91.5±0.2 Hz. At resonance 661 fringes were detected, corresponding to a displacement of 104μm, which is slightly in excess of the normal maximum displacement.

Off Resonance (55.0 Hz)   **On Resonance (91.5Hz)**

$y = 1.829x - 0.1696$
$R^2 = 0.9952$

$y = 17.51x - 0.7726$
$R^2 = 0.9989$
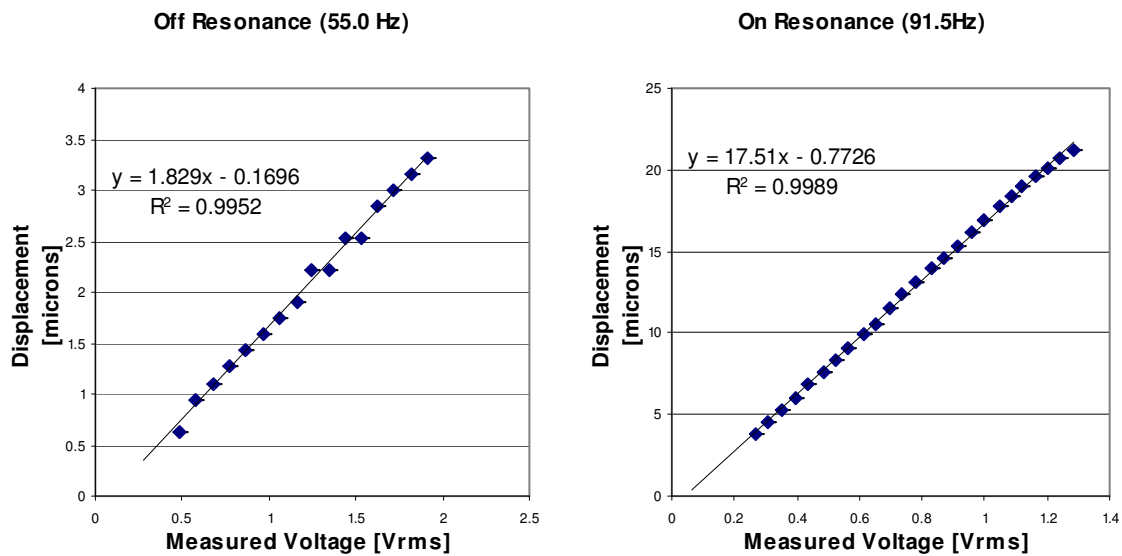
Figure 6-18   Piezo Displacement as a Function of the RMS Voltage

6.7. LOCK-IN DETECTION

The ultrafast tunnelling signal is detected by lock in detection. The principle of lock-in detection and its application to the SPPX tunnelling signal was explained in section 6.1.4. In these experiments, an AMETEK Model 5109 single phase Lock-In Amplifier was used. The lock-in amplifier consists of an internal oscillator generator, a mains notch filter to reduce interference from main frequencies and harmonics thereof, a band pass filter tuned to the frequency of the internal oscillator, a phase sensitive device (PSD) which effectively multiplies the filtered input signal by the phase shifted reference signal, and a low pass filter with a variable time constant. A

block diagram is shown in Figure 6-19. The phase shift prior to the PSD allows the phase reference input to the PSD to be varied. This needs to be adjusted to maximise the signal.
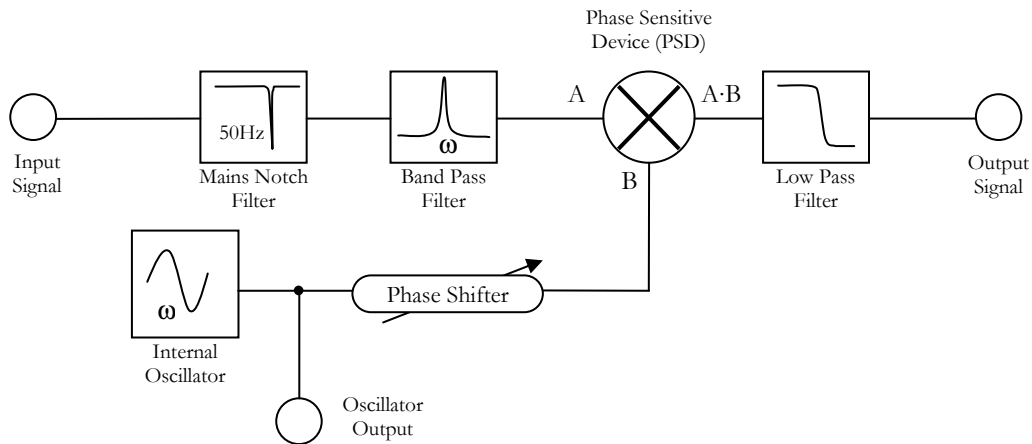
Figure 6-19   ***Simplified Block Diagram of the Lock-in amplifier***

The STM controller provides a buffered amplified signal proportional to the tunnel current which is connected to the input of the lock-in amplifier. All the controls of the lock-in amplifier can be remotely controlled over either GPIB interface or an RS-232 interface. The RS-232 interface was used to control the lock-in amplifier from the data-acquisition system, discussed in the following section.

The output from the internal oscillator is amplified and used to power the piezo, providing the piezo shaker stage and allowing the frequency and displacement of the delay variation to be remotely controlled by the data acquisition software. A diagram showing the electrical connections is shown in Figure 6-20. A digital storage oscilloscope (not shown) was also used for diagnostic purposes. Signals from the oscillator, tunnelling current and the lock-in output were intercepted with BNC T-pieces and could be observed on the oscilloscope.
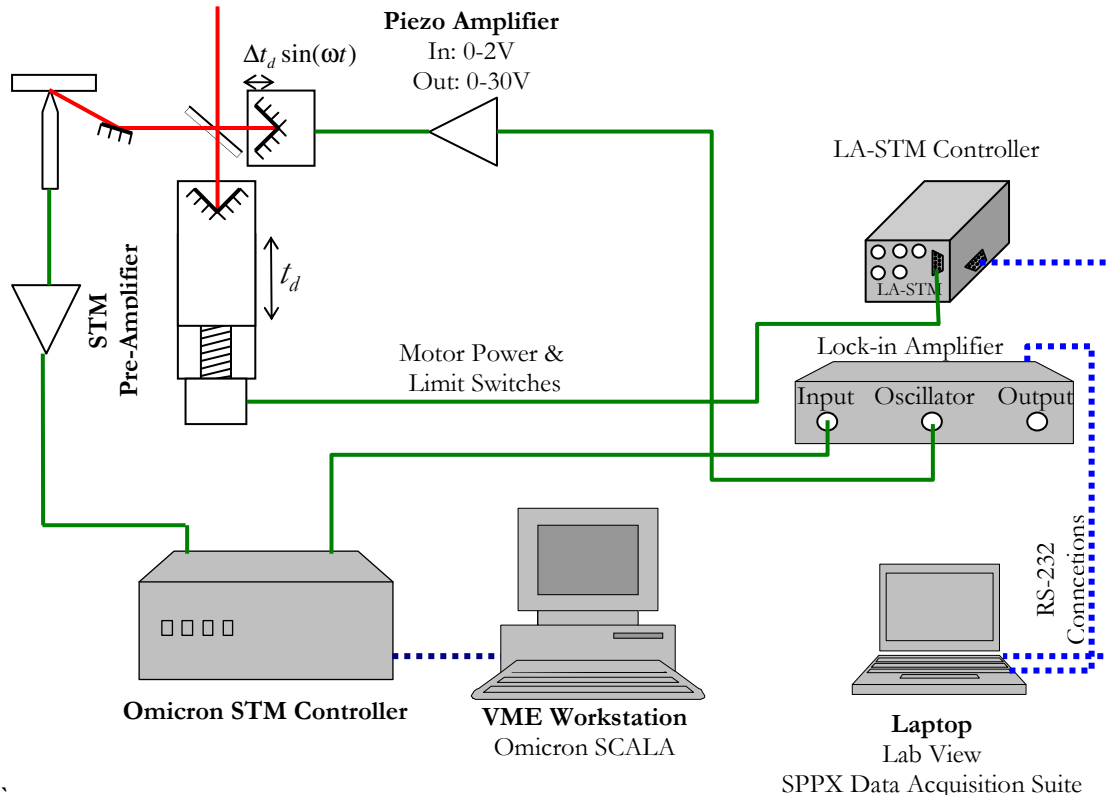
Figure 6-20   ***Diagram Showing SPPX Electrical Connections***

6.8. DATA ACQUISITION SYSTEM

The Lock-in amplifier and the LA-STM delay stage controller can both be remotely controlled over the RS-232 port. Labview 7.1 was used to develop an application to control these devices to collect the SPPX spectra. AMETEK provide a library of Labview components which simplifies the development of applications with the 51XX series of lock-in amplifiers. A similar suite of components was written to handle initialisation and communication with the LA-STM controller using the command language developed in section 6.5.3. The documentation for the application developed in Labview to control the SPPX apparatus is provided in Appendix B.5.

The application has the following features:

- Tools to locate and define the zero delay.

- Presents the displacement of the delay stage as either step calibrated delay time or position.

- Provides complete front panel interface for the Lock-in amplifier.

- Provides manual control for the delay stage.

- Automatically saves spectra.

- Supports averaging of multiple sweeps over the delay range to be investigated.

6.9.   SAMPLE SELECTION

One of the greatest difficulties in this work was the identification a sample that could be assured of providing an ultrafast time dependant signal. Ideally, the system would be verified by measuring the signal from the same sample made by Takeuchi et al in 2002 [7]. However that measurement was made in UHV. Having previously shelved development in UHV, a sample that could be prepared easily and would remain clean in air was required. Furthermore it must exhibit ultrafast dynamics on the sub-picosecond time scale yet be slower than the pulse duration of the laser. The excitation must be repeatable and must not change the surface topography. One final requirement that may be relaxed for an initial measurement is that photo excitation should lead to a highly localised modification of the Local Density of States. This would allow the lateral resolution of the method to be established.

Two samples were considered, the first being highly defected graphite. This could have been produced by bombardment with Argon or Helium ions using one of the departments UHV systems. From femtosecond time resolved pump-probe reflection and photoemission measurements, defected HOPG is known to exhibit ultrafast photocarrier dynamics [92-95]. Photons are excited by the ultrashort pulses leading to the creation of hot-electrons which thermalise by electron-electron and electron-phonon scattering and electron-hole recombination. Each of these processes happens on a femtosecond to a few picosecond timescale. The defects in the graphite affect time constants for electron-phonon scattering and lead to short decay time [92]. Undefected graphite has an electron-phonon scattering time constant of ~2ps. When HOPG is bombarded by with 5keV He^+ ions at a fluence of 5.6×10^{13} He^+/cm^2 this time is reduced to ~100fs. This would seem to make it or even undefected HOPG ideal samples, as they are simple to prepare and will remain clean in air.

The other sample considered was metallo-porphyrin. Porphyrins are a family of conjugated aromatic organic compounds that form a macrocycle consisting of 4 pyrrole subunits and substituted aldehydes. Metallo-porphyrins have a metal atom at the centre of the pyrrole macrocycle, Figure 6-21 shows the structure of a Cobalt(II)-porphyrin, showing the ring of 4 pyrrole subunits, the central metal atom and substituted MethoxyPhenyl at the 5,10,15 and 20 locations on the porphyrin macrocycle.

Porphyrins have 26π, associated with the Soret band [96], electrons that are delocalised over the macrocycle and have short lived photo-excited states[97]. Optical absorption spectra show that the peak of this absorption band is at a wavelength of around 400nm which is accessible using the frequency doubled output of the Ti:Sapphire laser. In addition, with an appropriate substitution porphyrins can form highly ordered self-assembled monolayers on

gold[98, 99] and on graphite[100] using long alkyl chains which have previously been investigate by STM.
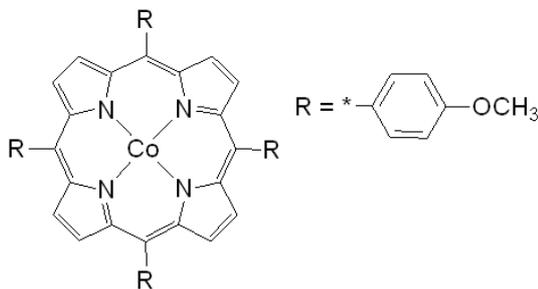
Figure 6-21   Structure Diagram of Cobalt(II)-TetraMethoxyPhenyal Porphyrin (CoTMPP)

Structure diagram from Sigma Aldrich catalogue for 5,10,15,20-Tetrakis(4-methoxyphenyl)-21H,23H-porphine Cobalt(II). It possesses absorbencies with peaks centred on at 417nm and 530nm, measured by UV-VIS spectroscopy.

The fast relaxation localised to the molecule itself and the ability to distinguish individual molecules on a self assembled monolayer would make this an extremely interesting and challenging sample on which to perform SPPX measurements, allowing the lateral resolution of the technique to be established.

Ultimately, a clean cleaved HOPG sample was used. It was selected for its simplicity and ease of preparation. The few-picosecond timescale relaxations in undefected graphite should provide a signal that was within temporal resolution of the laser.

6.10.   INITIAL MEASURMENTS

The laser was tuned to 800nm and produced 110fs pulses measured using the autocorrelator. An etched PtIr tip was used in the STM. The tip was brought to a tunnelling distance from the freshly cleaved HOPG using a tip bias of 1V and current of 0.75nA. A clear atomically flat area of the graphite was found. The STM tip was retracted by several coarse micro-steps and the laser was focused onto the tip of the junction of the STM. The junction was given several minutes to reach thermal equilibrium and then, with a low loop gain, it was re-approached to the surface under the same tunnelling conditions.

The oscillator was set to a frequency of 91Hz and was configured to output at a signal with an RMS amplitude of 0.1V which when amplified produces 1Vrms at piezo corresponding to an oscillation in the delay of ~100fs at that frequency.

The delay stage was scanned from -10ps to 20ps, and the output from the lock-in amplifier was sampled at 100fs intervals. The large scan range was used to compensate for the relatively poorly known 0 delay point. The results of 4 scans were averaged, and are presented in Figure 6-22. The signal is clearly very noisy, but a large peak in the signal can be observed at about 11.9 ps.
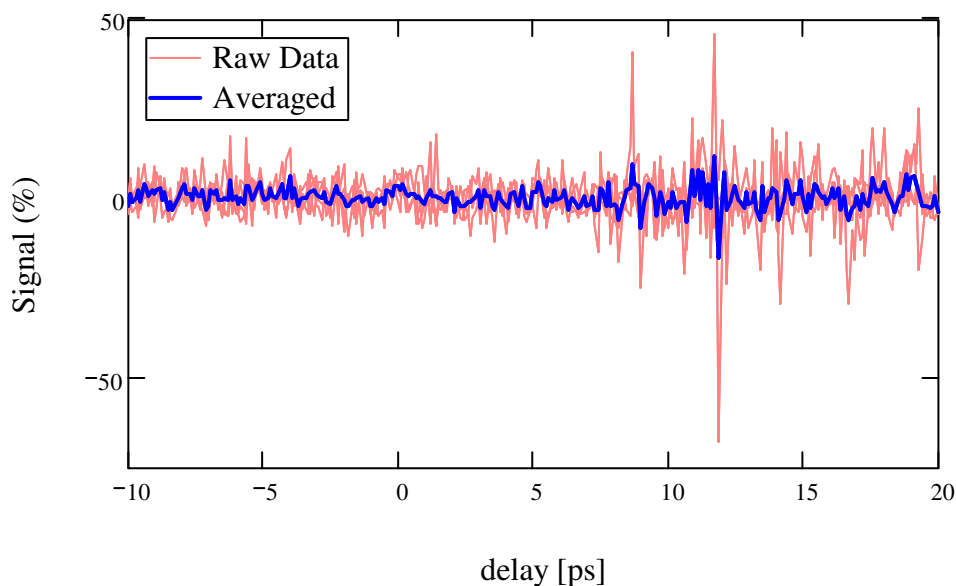
Figure 6-22 **SPPX Spectra Measured on Graphite**

However measurement of this signal could not be reproduced. Subsequent scans between 8ps and 14ps, obtained with the same parameters in the same session, did not show the peak again. Other scans that were taken showed large transient spikes but these results were not reproducible and primarily attributed to noise.

Although significant effort and progress had been made towards the development of an SPPX apparatus, insufficient consideration was given to the requirements of the STM. The STM exhibited high levels of noise which got worse through the life of the project. It was hoped that the SPPX signal, at the frequency the experiment was performed, would be able to overcome the noise at that frequency and that the lock-in amplifier would still be able to detect the signal. In the end this proved not to be the case.

It was surprising that absolutely no significant signal was detected. Given that no special effort was made to suppress the periodic variation of the intensity caused by the interference of the two pulses at delays less than the pulse duration, thermal expansion of the tip might have been expected to generate signal even if no ultrafast process was detected.

6.11. EVALUATION OF THE SPPX DESIGN

In this chapter the development of apparatus that could be used to perform SPPX has been documented. Whilst it is disappointing that no signal was detected that could be attributed to an ultrafast tunnelling process in graphite, it does not preclude its existence.

The system suffered from an intolerable level of noise at the STM junction. This was due largely to the environment in which it operated. STM images of an acceptable quality could only

be obtained when the STM was covered with a grounded metal cylinder. This stopped both air currents and reduced electrical noise, as the metal cylinder or a vacuum chamber would act as a faraday cage. It was not possible to shield the STM in this way for the SPPX measurements, as the optical microscope needed physical access to the STM junction. The Viton stack vibration isolation used by the Omicron Micro STM was not designed to and could not deal with the air currents which existed in the room. The environment also had large number of electrical devices that used air cooling, generating warm currents of air. One of these was the cooling system for the pump laser and could not be switched off or moved to a different location.

As with the confocal work, this system suffered from the problems associated with the laser being in a different room, on a different optical table to the STM. This was detrimental to the pointing stability of the laser.

In spite of these difficulties, significant progress has been made in the area of the shaker stage development and the delay stage. The shaker stage can achieve large displacement amplitudes whilst isolating the vibration from the STM. Also a custom micro-stepping delay stage controller has been developed that offers some useful features which were not available from the commercial micro-step controllers.

6.11.1.   FUTURE WORK

Ultimately the noise in the STM proved too great to make high quality measurements. This needs to be resolved. The STM controller and computer are also becoming prone to equipment failure. During this work, the computer suffered two hard disk failures necessitating replacement of the disk. No modern disk is compatible and the replacement had to be sourced second hand - this also failed at a later date. It is no longer economical to continue to repair and maintain this computer. The controller is also no longer supported by the manufacturer, so this will need to be replaced as well.

The STM head does not appear to having anything wrong with it and, perhaps with a new controller, it could be usefully applied elsewhere but its vibration isolation makes it unsuitable for use on the bench top unless it is in an acoustically dampened enclosure. Its prolonged exposure to a relatively dirty environment would also make reintroduction to UHV a difficult task, but not impossible if sufficient time and care were applied. The main problem with the STM head for the LA-STM application was the vibration isolation and the fact that the reflected beam was inaccessible.

The following recommendations and improvements are suggested for any further work taking this project forward:

- A STM with good optical access for both the incident and reflected beam would allow conventional time resolved femtosecond optical spectroscopy to be conducted in situ.

- The STM should have excellent drift stability. SPPX measurements take a long time to acquire and if the lateral resolution of SPPX is to be investigated then drift stability is crucial to such a measurement.

- The Laser should be on the same table as the STM: fluctuations in laser intensity caused by continuous variation of the position of the laser lead to an intolerable level of thermal expansion or loss of the signal altogether.

- The laser should have as high a repetition rate as possible. There is considerable experimental dead time between the excitation relaxing and the next pulse pair arriving. This may achieved with an external resonant cavity or the construction of a Ti:sapphire laser with a shortened cavity.

- A laser with shorter pulse duration of around 15 to 20fs should be used as this will provide access to many of the ultrafast chemical processes that now being investigated by optical femtosecond reflection spectroscopy. Pulses much short than 15fs, required short wavelengths and the correspondingly higher energy photons could cause a significant photoemission current which may swamp any tunnelling signals and so these should be avoided.

Although the shaker stage has been successfully used to generate large displacements of a retroreflector, using a simpler mirror with a smaller mass would allow KHz frequencies to be attained. It would make the alignment of the interferometer more difficult and would necessitate a wide band STM pre-amplifier such as one of those suggested by Demming or Jersch [88, 89].

Future SPPX experiments might consider using pump and probe pulses that are plane polarised to the sample but arriving at 90° to each other. This would reduce the thermal instability Takeuchi et al experienced at low delay times. They have already investigated the possibility of rotating the polarisation of the probe beam by 90° with respect to the pump beam, however field enhancement at the STM tip provides a polarisation mixing capability which renders this approach ineffective [85].

Gernstner et al [82] suggested the use of a fibre to couple the light to the STM, but discounted this method due to the pulse dispersion created by optical material in the fibre. However with the advent of hollow fibres [101-103] that have been used successfully to carry ultrashort pulses with near zero dispersion, this could now be considered again. It may be

especially useful if the laser must be located on a different optical table, or an STM on an eddy damped spring suspension system is used.

CHAPTER 7.

7. Summary and Future Work

7.1. OVERVIEW

This thesis has sought to investigate selected applications of femtosecond pulses in confocal microscopy and scanning tunnelling microscopy. The benefits of ultrashort pulses open up new possibilities in both these fields but their success is critically dependent on having well characterised pulses and a good understanding of the underlying processes involved in ultrafast light-matter interactions.

Ultrafast pulses were used to induce 3 photon DNA damage in live cells with greater sensitivity than any previous measurement. Studies of the concentration of the fluorescently tagged repair protein, PCNA, following damage allowed the cellular repair response time to be assessed and evidence for remote intra-cell signalling was found.

The measurement of PCNA foci in live cells required the development of a foci tracking procedure to accommodate the movement of live cells over the duration of the measurement. This led to the development of a generic algorithm for the automated counting of large numbers of foci in 3 dimensions which could be applied to high-content screening. One of the algorithms developed accurately and consistently measured foci number and properties in 3D. These properties could be easily aggregated to facilitate biological studies. An investigation was conducted into the dependence of the numbers of γ-H2AX foci in radiation dosed cells on the dose of radiation received.

Finally, progress towards the development of an SPPX apparatus similar to that reported by Takeuchi et al [7] has been reported. Although a time dependant tunnelling signal has not yet been detected, many of the challenges associated with this demanding experiment have been investigated, resulting the development of a novel shaker stage. This uses the idea of a tuned mass damper to facilitate large displacements of a moderately heavy retroreflector without transmitting the mechanical vibration to the junction of the STM. A custom step motor

controller was also developed that implemented micro-stepping and a real-time position control interface using inexpensive commercial grade integrated circuits and a microcontroller.

7.2. 3-PHOTON INDUCED DNA DAMAGE

A confocal microscope employing ultrashort pulses from the Ti:sapphire laser operating at a wavelength of 750nm and producing pulses with a duration of 86fs was used to precisely induce DNA damage by a 3-photon absorption process. The pulse broadening caused by the confocal microscope, laser scanner and the objective were established by the experimental measurement of the pulse duration and point spread function of the microscope for these pulses. It was discovered that the pulse duration had been broadened to 401fs and the point spread function was larger than might have been expected. Yet 3P DNA damage was detected at peak intensities as low as 23 ± 3 GJ/cm2.

Damaged caused by this process was observed in real time by conventional one photon fluorescence confocal microscopy and the movement and concentration of PCNA tagged with a fluorescent GFP allowed the localisation of PCNA to be measured by fitting to an exponential localisation model, analogous to a capacitor charge. Using this method, the half-time for localisation ranged from 50-260 seconds. The level of damage and the speed of localisation are thought to be related to the concentration of DNA at the damage site. The distribution of the DNA is inhomogeneous throughout the nucleus, explaining the large variation in the localisation half-times.

7.3. AUTOMATED COUNTING OF Γ-H2AX FOCI

Three foci counting algorithms were implemented, each of them in 2D and 3D. The algorithms implemented were a simple intensity threshold algorithm, the Compact Hough and Radial Mapping (CHARM) algorithm [65] and a watershed algorithm. The CHARM algorithm was extended to operate in 3D and both the 2D and 3D applications of the Meyer watershed [66] were developed from scratch. All algorithms were implemented in Matlab and the algorithms were compared and an investigation into the effects of each of the algorithms' parameters was undertaken. In 2D the CHARM algorithm performed most reliably but did not scale well to 3D. In 3D the watershed algorithm was faster and yielded additional information about the foci, including volume and effective radius.

A systematic method of optimising the algorithm parameters was developed which simultaneously reduced over-segmentation leading to a reduced false positive detection whilst reducing the likelihood that foci could be missed.

The 3D watershed algorithm with the automated parameter determination algorithm was used to conduct an investigation into radiation dosed cells. From these measurements, the number of foci has been seen to increase with the radiation dose in a broadly linear trend. However the spread on the number of foci detected at each dose of radiation is very large and further results may help to more precisely identify the function dependence of foci number on the radiation dose, and whether there is a saturation point. When average intensity and foci sizes were measured it was discovered that at the highest radiation dose tested, of 8Gy, the intensity was actually reduced compared to 6Gy. It is thought that this was because the cells were so heavily damaged at 8Gy they were dying before they were fixed and immunostained, whilst at 6Gy the high dose of radiation leads to the development of stalled replication forks in the vicinity of the damage creating larger high intensity foci.

7.4. FUTURE WORK

The work with the confocal microscope has been very successful and further work with the multiphoton absorption apparatus has already been carried out using the equipment developed this work [63]. The provision of a dedicated femtosecond source would greatly assist this work, as it would the SPPX experiments. In any case the laser should be located on the same optical table as both of these apparatus to reduce the amount of time spent routinely aligning the laser. The method of measuring pulse duration at the focus that was developed in this work would be of greater application if some form of dispersion compensation were installed prior to the microscope scanner allowing the laser pulse to be pre-chirped, reducing the pulse duration at the focus. This would permit the peak intensities produced in this work to be achieved with a fraction of the laser intensity and further reduce any thermal damage that may be caused by the IR laser beam. Plans are in place to study the effects of damage through the life cycle of the cells which will be possible once an incubator has been installed on the microscope sample stage.

The foci counting algorithms are broadly applicable to any system that handles 3D or 4D (3D time series) datasets and needs to automatically identify large numbers of aggregates. Data has been acquired for a time series of cells dosed with radiation to investigate properties of γ-H2AX foci throughout the cell repair process.

The next steps towards the development of the SPPX apparatus have been listed at the end of Chapter 6, but broadly it requires a STM with improved immunity to environmental noise, less drift and better mechanical junction stability. An STM designed for STS measurements would be ideal. If an SPPX signal could be verified on such an STM the effort and funding required to implement the other suggestions could be justified.

REFERENCES

1. Shah, J. and C. American Telephone and Telegraph, *Ultrafast spectroscopy of semiconductors and semiconductor nanostructures*. Springer series in solid-state sciences; v. 115,0171-1873. 1996, Berlin; London: Springer. xv,372p.

2. Miller, J.C., ed. *Laser Ablation: Principles and Applications*. Springer Sereis in Materials Science. 1994, Springer-Verlag: Berlin.

3. Göppert-Mayayer, M., *Ueber Elementarakte mit zzwei Quantenspruengen*. Ann. Phys., 1931. **9**: p. 273.

4. G. Binnig, H.R., *Scanning Tunneling Micrscopy*. IBM Journal of Research and Development, 1986. **30**(4).

5. Takeuchi, O., et al., *Probing subpicosecond dynamics using pulsed laser combined scanning tunneling microscopy (vol 85, pg 3268, 2004)*. Applied Physics Letters, 2004. **85**(23): p. 5790-5790.

6. Takeuchi, O., et al., *Probing subpicosecond dynamics using pulsed laser combined scanning tunneling microscopy*. Applied Physics Letters, 2004. **85**(15): p. 3268-3270.

7. Takeuchi, O., et al., *Development of time-resolved scanning tunneling microscopy in femtosecond range*. Japanese Journal Of Applied Physics Part 1-Regular Papers Short Notes & Review Papers, 2002. **41**(7B): p. 4994-4997.

8. Diels, J.-C. and W. Rudolph, *Ultrashort Laser Pulse Phenomena: Fundamentals, Techniques, and Applications on a Femtosecond Time Scale*. Optics and Photonics. 1995, London: Academic Press Limited. 600.

9. Diels, J.-C. and W. Rudolph, *Ultrashort laser pulse phenomena: fundamentals, techniques, and applications on a femtosecond time scale*. 2nd ed. Optics and photonics. 2006, Amsterdam; London: Academic Press. xxi, 652 p.

10. Fork, R.L. and C.V. Shank, *Generation of optical pulses shorter than 0.1ps by colliding pulse mode-locking*. Applied Physics Letters, 1981. **38**: p. 671.

11. *TSunami Users' Manual (Rev D)*: Spectra Physics.

12. Minsky, M., *Memoir on inventing the confocal scanning microscope*. Scanning, 1988. **10**: p. 128-138.

13. Melet, R., et al., *Resonant emission of a single InAs/GaAs quantum dot in a waveguiding configuration*, in *Physics Of Semiconductors, Pts A And B*. 2007, Amer Inst Physics: Melville. p. 913-914.

14. Palomba, S., *Nanophotonics and biophysics with size-selected clusters*, in *Nanophysics*. 2007, The University of Birmingham: Birmingham.

15. Chansin, G.A.T., et al., *Single-molecule Spectroscopy using nanoporous membranes*. Nano Letters, 2007. **7**(9): p. 2901-2906.

16. Olympus, *http://www.olympusfluoview.com/theory/confocalintro.html*.

17. Born, M. and E. Wolf, *Principles of Optics*, ed. 6th. 1980, Oxford: Pergamon Press.

18. Stamnes, J.J., *Waves in focal regions: propagation, diffraction and focusing of light, sound and water waves*. Adam Hilger series on optics and optoelectronics. 1986, Bristol: Hilger. xviii,600p,4p of plates.

19. Pawley, J.B., *Handbook of biological confocal microscopy*. 2nd ed. The language of science. 1995, New York; London: Plenum Press. xxiii,632p.,[4]p. of plates.

20. Degerman, J., et al., *A computational 3D model for reconstruction of neural stem cells in bright-field time-lapse microscopy - art. no. 64981E*. Computational Imaging V, 2007. **6498**: p. E4981-E4981.

References

21. Dusch, E., et al., *Three-dimensional point spread function model for line-scanning confocal microscope with high-aperture objective.* Journal Of Microscopy-Oxford, 2007. **228**: p. 132-138.

22. Small, A., et al., *Enhancing diffraction-limited images using properties of the point spread function.* Optics Express, 2006. **14**(8): p. 3193-3203.

23. Vicidomini, G., *Image formation in fluorescence microscopy - Three-dimensional mathematical model*, in *From Cells To Proteins: Imaging Nature Across Dimensions.* 2005. p. 371-393.

24. Zhang, B., J. Zerubia, and J.C. Olivo-Marin, *Gaussian approximations of fluorescence microscope point-spread function models.* Applied Optics, 2007. **46**(10): p. 1819-1829.

25. Huang, L., C.K. Tao, and M.H. Hu, *A blind deconvolution method in a LCSM system - art. no. 614932*, in *2nd International Conference On Advanced Optical Manufacturing And Testing Technologies: Advanced Optical Manufacturing Technologies.* 2006. p. 14932-14932.

26. Pankajakshan, P., et al., *Parametric blind deconvolution for Confocal Laser Scanning Microscopy.* 2007 Annual International Conference Of The Ieee Engineering In Medicine And Biology Society, Vols 1-16, 2007: p. 6532-6535.

27. Imaging, S.V., *Huygens Professional*, http://www.svi.nl.

28. Wilson, T. and A. Carlini, *Size of the detector in confocal imaginf systems.* Optics Letters, 1987. **12**(4): p. 227-229.

29. Svelto, O. and D.C. Hanna, *Principles of lasers.* 4th ed. 1998, New York; London: Plenum. xxi, 604 p.

30. Alfano, R.R., *The supercontinuum laser source: fundamentals with updated references.* 2006, New York; [London]: Springer. xx, 537 p. cm.

31. McConnell, G., *Confocal laser scanning fluorescence microscopy with a visible continuum source.* Opt. Express, 2004. **12**(13): p. 2844.

32. Esposito, E., J. Harris, and G. McConnell, *Fast wavelength-tunable ultra-violet laser source for confocal Fura-2AM imaging.* Optics Communications, 2007. **270**(2): p. 470.

33. Du, H., et al., *PhotochemCAD: A computer-aided design and research tool in photochemistry.* Photochemistry and Photochemistry and Photobiology, 1998. **68**: p. 141-142.

34. Hild, M., et al., *Femtosecond laser-assisted retinal imaging and ablation: Experimental pilot study.* Current Eye Research, 2008. **33**(4): p. 351-363.

35. Pike, P., et al., *Temperature distribution in dental tissue after interaction with femtosecond laser pulses.* Applied Optics, 2007. **46**(34): p. 8374-8378.

36. Török, P., personal communication with R. Meldrum.

37. Petráñ, M., et al., *Tandem Scanning Reflected Light Microscope.* Journal of the Optical Society of America, 1968. **58**(5): p. 661-664.

38. Yin, S., et al., *Kinoform-based Nipkow disk for a confocal microscope.* Applied Optics, 1995. **34**(25): p. 5695-5698.

39. Song, L.L., et al., *Photobleaching Kinetics Of Fluorescein In Quantitative Fluorescence Microscopy.* Biophysical Journal, 1995. **68**(6): p. 2588-2600.

40. Meldrum, R.A., et al., *Nanoscale spatial induction of ultraviolet photoproducts in cellular DNA by three-photon near-infrared absorption.* Embo Reports, 2003. **4**(12): p. 1144-1149.

41. Essers, J., *Images of the localisation of PCNA at different stages of the cell cycle.* 2005, Erasmus Medical Centre, Rotterdam.

42. *Autocorrelator MINI 2000 - Manual.*

43. Chen, C.J., *Introduction to scanning tunneling microscopy.* Oxford series in optical and imaging sciences; 4. 1993, New York, N.Y.: OUP. 412p.

44. Sørensen, A., et al., *Preparation of platinum/iridium scanning probe microscopy tips.* Rev. Sci. Inst., 1999. **70**(7): p. 3059-3067.

45. Lindahl, J., T. Takanen, and L. Monelius, *Easy and reproducible method fro making sharp tips of Pt/Ir.* J. Vac. Sci. Technol. B, 1998. **16**(6): p. 3077-3081.

46. Solomon, D.A., M.C. Cardoso, and E.S. Knudsen, *Dynamic targeting of the replication machinery to sites of DNA damage.* Journal Of Cell Biology, 2004. **166**(4): p. 455-463.

47.   Svoboda, K., D.W. Tank, and W. Denk, *Direct Measurement of Coupling Between Dendritic Spines and Shafts.* Science, 1996. **272**(5262): p. 716-719.

48.   Furuta, T., et al., *Brominated 7-hydroxycoumarin-4-ylmethyls: Photolabile protecting groups with biologically useful cross-sections for two photon photolysis.* Proceedings of the National Academy of Sciences of the United States of America, 1999. **96**(4): p. 1193-1200.

49.   Echevarria, W., et al., *Regulation of calcium signals in the nucleus by a nucleoplasmic reticulum.* Nature Cell Biology, 2003. **5**(5): p. 440-446.

50.   Brown, E.B., et al., *Measurement of molecular diffusion in solution by multiphoton fluorescence photobleaching recovery.* Biophysical Journal, 1999. **77**(5): p. 2837-2849.

51.   Berland, K.M., P.T. So, and E. Gratton, *Two-photon fluorescence correlation spectroscopy: method and application to the intracellular environment.* Biophysical Journal, 1995. **68**(2): p. 694.

52.   Schwille, P., et al., *Molecular Dynamics in Living Cells Observed by Fluorescence Correlation Spectroscopy with One- and Two-Photon Excitation.* Biophysical Journal, 1999. **77**(4): p. 2251.

53.   Dinant, C., et al., *Activation of multiple DNA repair pathways by subnuclear damage induction methods.* Journal Of Cell Science, 2007. **120**(15): p. 2731-2740.

54.   Williams, E.S., et al., *DNA double-strand breaks are not sufficient to initiate recruitment of TRF2.* Nat Genet, 2007. **39**(6): p. 696.

55.   Mari, P.O., et al., *Dynamic assembly of end-joining complexes requires interaction between Ku70/80 and XRCC4.* Proceedings Of The National Academy Of Sciences Of The United States Of America, 2006. **103**(49): p. 18597-18602.

56.   Tirlapur, U.K. and K. König, *Cell biology - Targeted transfection by femtosecond laser.* Nature, 2002. **418**(6895): p. 290-291.

57.   König, K., I. Riemann, and W. Fritzsche, *Nanodissection of human chromosomes with near-infrared femtosecond laser pulses.* Optics Letters, 2001. **26**(11): p. 819-821.

58.   Volker, M., et al., *Sequential assembly of the nucleotide excision repair factors in vivo.* Molecular Cell, 2001. **8**(1): p. 213-224.

59.   König, K., et al., *Pulse-length dependence of cellular response to intense near-infrared laser pulses in multiphoton microscopes.* Optics Letters, 1999. **24**(2): p. 113-115.

60.   Essers, J., et al., *Nuclear dynamics of PCNA in DNA replication and repair.* Molecular And Cellular Biology, 2005. **25**(21): p. 9350-9359.

61.   Alberts, B., et al., *Molecular Biology of the Cell.* 5th ed. 1994, New York, Abingdon: Garland Science, Taylor Francis Group.

62.   Friedberg, E.C., et al., *DNA Repair and Mutagenesis.* 2nd ed. 2005, Washington: ASM Press.

63.   Zielinska, A., et al., *Direct visualisation of repair of oxidative damage by OGG1 in the nuclei of live cells.* DNA Repair (submitted, awaiting approval), 2009.

64.   Keatings, S.R., W. Zhang, and G. McConnell, *Characterization of microscope objective lenses from 1,400 to 1,650 nm to evaluate performance for long-wavelength nonlinear microscopy applications.* Microscopy Research And Technique, 2008. **71**(7): p. 517-520.

65.   Barber, P.R., et al., *Gamma-H2AX Foci Counting: Image processing and control software for high-content screening - art. no. 64411M.* Imaging, Manipulation, And Analysis Of Biomolecules, Cells, And Tissues V, 2007. **6441**: p. M4411-M4411.

66.   Meyer, F., *Topographic Distance And Watershed Lines.* Signal Processing, 1994. **38**(1): p. 113-125.

67.   Mischo, H.E., et al., *Actinomycin D induces histone gamma-H2AX foci and complex formation of gamma-H2AX with Ku70 and nuclear DNA helicase II.* Journal Of Biological Chemistry, 2005. **280**(10): p. 9586-9594.

68.   Barber, P.R., et al., *Automated counting of mammalian cell colonies.* Physics In Medicine And Biology, 2001. **46**(1): p. 63-76.

69.   Conti, J., *vol3d command for visualisation of 3D data.* MATLAB Central - User Community File Exchange, 2004.

References

70. Bresenham, J.E., *Algorithm for computer control of a digital plotter*. IBM Systems Journal, 1965. **4**(1): p. 25-30.

71. Steeves, G.M. and M.R. Freeman, *Ultrafast scanning tunneling microscopy*, in *Advances In Imaging And Electron Physics, Vol 125*. 2002, Academic Press Inc: San Diego. p. 195-229.

72. Grafstrom, S., *Photoassisted scanning tunneling microscopy*. Journal Of Applied Physics, 2002. **91**(4): p. 1717-1753.

73. Yamashita, M., H. Shigekawa, and R. Morita, eds. *Mono-cycle photonics and optical scanning tunneling microscopy: route to femtosecond ångstrom technology*. Springer series in optical sciences; 99. 2005, Springer: Berlin; London.

74. Weiss, S., et al., *Ultrafast Scanning Probe Microscopy*. Applied Physics Letters, 1993. **63**(18): p. 2567-2569.

75. Feldstein, M.J., et al., *Femtosecond optical spectroscopy and scanning probe microscopy*. Journal Of Physical Chemistry, 1996. **100**(12): p. 4739-4748.

76. Hamers, R.J. and D.G. Cahill, *Ultrafast Time Resolution In Scanned Probe Microscopies*. Applied Physics Letters, 1990. **57**(19): p. 2031-2033.

77. Groeneveld, R.H.M., et al., *New optoelectronic tip design for ultrafast scanning tunneling microscopy*. Journal Of Vacuum Science & Technology B, 1996. **14**(2): p. 861-863.

78. Keil, U.D., et al., *Femtosecond tunneling response of surface plasmon polaritons*. Applied Physics Letters, 1998. **72**(23): p. 3074-3076.

79. anonymous, Research Disclosure, 1989(August): p. #30480.

80. Hamers, R.J. and D.G. Cahill, *Ultrafast Time Resolution In Scanned Probe Microscopes - Surface Photovoltage On Si(111)-(7x7)*. Journal Of Vacuum Science & Technology B, 1991. **9**(2): p. 514-518.

81. Pfeiffer, W., et al., *Rapid communication Photoelectron emission in femtosecond laser assisted scanning tunneling microscopy*. Applied Physics B: Lasers and Optics, 1997. **64**(2): p. 265.

82. Gerstner, V., et al., *Femtosecond laser assisted scanning tunneling microscopy*. Journal Of Applied Physics, 2000. **88**(8): p. 4851-4859.

83. Grafstrom, S., et al., *Thermal expansion of scanning tunneling microscopy tips under laser illumination*. Journal Of Applied Physics, 1998. **83**(7): p. 3453-3460.

84. Gerstner, V., A. Thon, and W. Pfeiffer, *Thermal effects in pulsed laser assisted scanning tunneling microscopy*. Journal Of Applied Physics, 2000. **87**(5): p. 2574-2580.

85. Takeuchi, O., A. Masahiro, and H. Shigekawa, *Analysis of Time-Resolved Tunnel Current Signal in Sub-Picosecond Rnage Observed by Shaken-Pulse-Pair-Excited Scanning Tunneling Microscopy*. Japanese Journal Of Applied Physics, 2005. **44**(7B): p. 5354-5357.

86. Jones, D.W., *Control of Stepping Motors*. 2004, http://www.cs.uiowa.edu/~jones/step/index.html.

87. Yeadon, W.H. and A. W, *Handbook of Small Electric Motors*. 2001: McGraw-Hill.

88. Jersch, J., et al., *Wide-band low-noise tunnel current measurements in laser assisted experiments*. Review Of Scientific Instruments, 1999. **70**(7): p. 3173-3176.

89. Demming, F., K. Dickmann, and J. Jersch, *Wide bandwidth transimpedance preamplifier for a scanning tunneling microscope*. Review Of Scientific Instruments, 1998. **69**(6): p. 2406-2408.

90. Harris, C.M. and A.G. Piersol, *Harris' shock and vibration handbook*. 2002, Norwich, NY: Knovel.

91. Thomson, W.T. and M.D. Dahleh, *Theory of vibration with applications*. 5th ed. 1998, Upper Saddle River, N.J.: Prentice Hall. xiii, 524 p.

92. Ishioka, K., et al., *Ultrafast carrier and phonon dynamics in ion-irradiated graphite*. Applied Physics Letters, 2001. **78**(25): p. 3965-3967.

93. Kitajima, M., et al., *Application of time-domain vibrational spectroscopy to the study of defects in ion-implanted materials*. Nuclear Instruments & Methods In Physics Research Section B-Beam Interactions With Materials And Atoms, 2003. **206**: p. 99-102.

94.   Moos, G., et al., *Anisotropy of Quasiparticle Lifetimes and the Role of Disorder in Graphite from Ultrafast Time-Resolved Photoemission Spectroscopy.* Physical Review Letters, 2001. **87**(26): p. 267402.

95.   Farztdinov, V.M., et al., *Ultrafast Optical Response of Carbon Films.* The Journal of Physical Chemistry B, 1999. **104**(2): p. 220.

96.   Dorough, G.D., J.R. Miller, and F.M. Heuennekens, *Spectra of Metallo-derivative of $\alpha,\beta,\gamma,\delta$-Tetraphenylporphine.* Journal Of The American Chemical Society, 1951. **73**: p. 4315-4320.

97.   Sorgues, S., et al., *Femtosecond electronic relaxation of excited metalloporphyrins in the gas phase.* Journal Of Chemical Physics, 2006. **124**(11).

98.   Boeckl, M.S., et al., *Self-assembly of tetraphenylporphyrin monolayers on gold substrates.* Langmuir, 2000. **16**(13): p. 5644-5653.

99.   Zhang, Z.J., et al., *A self-assembled monolayer of an alkanoic acid-derivatized porphyrin on gold surface: A structural investigation by surface plasmon resonance, ultraviolet-visible, and infrared spectroscopies.* Journal Of Colloid And Interface Science, 2001. **243**(2): p. 382-387.

100.   Wang, H.N., et al., *Chain-length-adjusted assembly of substituted porphyrins on graphite.* Surface And Interface Analysis, 2001. **32**(1): p. 266-270.

101.   Humbert, G., et al., *Hollow core photonic crystal fibers for beam delivery.* Optics Express, 2004. **12**(8): p. 1477-1484.

102.   Mohebbi, M., *Transmission characteristics of femtosecond optical pulses in hollow-core fibers.* Optics Communications, 2005. **253**(4-6): p. 290-300.

103.   Pearce, G.J., et al., *Hollow-core PCF for guidance in the mid to far infra-red.* Optics Express, 2005. **13**(18): p. 6937-6946.

APPENDIX A

A. Maximum Intensity Projections of γ-H2AX Foci in irradiated Cells

A.1. OVERVIEW

This appendix provides figures of the maximum intensity projections through the confocal stack for the data that was used in the analysis in section 5.3.

From each slide dosed with a different amount of radiation 6 fields of data were captured. All the images were 512x512 voxels in their X and Y dimensions. The number of voxels in the Z-direction varied so that that a full cell could be captured from top to bottom. In all measurements the size of a voxel was maintained constant, and as close to a cube as could be achieved.

It would not be beneficial or informative to present every slice of every field. The original data can be found on the cover DVD, and for this dataset alone space required is about 2.4 GB. To facilitate discussion and identification of specific nuclei they have all been assigned numbers, which are labelled on the intensity projections on the following pages. A cell may be uniquely identified by referring to its radiation dose and its cell number. For example, Cell 8Gy_3 refers to cell 3 from the 8Gy series shown in Figure A-1. Below is a list of the figures and data sets they represent.

Figure A-1   Cells Exposed to 8Gy Radiation (Maximum Intensity Projection)
Figure A-2   Cells Exposed to 6Gy Radiation (Maximum Intensity Projection)
Figure A-3   Cells Exposed to 4Gy Radiation (Maximum Intensity Projection)
Figure A-4   Cells Exposed to 2Gy Radiation (Maximum Intensity Projection)
Figure A-5   Cells Not Exposed To Radiation (Maximum Intensity Projection)

Figure A-1   ***Cells Exposed to 8Gy Radiation (Maximum Intensity Projection)***

Figure A-2   Cells Exposed to 6Gy Radiation (Maximum Intensity Projection)

Figure A-3 ***Cells Exposed to 4Gy Radiation (Maximum Intensity Projection)***

Figure A-4 ***Cells Exposed to 2Gy Radiation (Maximum Intensity Projection)***

Figure A-5   Cells Not Exposed To Radiation (Maximum Intensity Projection)

| Radiation Dose	Field No	Detection Threshold	Maxima Suppression
8Gy	1	232	81
8Gy	2	232	89
8Gy	3	231	83
8Gy	4	223	81
8Gy	5	217	82
8Gy	6	205	70
6Gy	1	257	100
6Gy	2	245	89
6Gy	3	244	88
6Gy	4	251	91
6Gy	5	245	94
6Gy	6	234	85
4Gy	1	196	60
4Gy	2	197	61
4Gy	3	203	65
4Gy	4	203	63
4Gy	5	190	57
4Gy	(Cell 13) 6	200	64
4Gy	(Cell 14&15) 6	190	57
4Gy	7	194	59
2Gy	1	184	54
2Gy	2	207	73
2Gy	3	191	61
2Gy	4	187	56
2Gy	5	189	59
2Gy	6	211	72
0Gy	1	169	45
0Gy	2	181	55
0Gy	3	154	32
0Gy	4	152	30
0Gy	5	154	33
0Gy	6	150	29

Table A-1   *Table of automatically determined foci detection parameters*

APPENDIX B

B. Electronic Appendices

During the execution of this work naturally a substantial amount was learnt about the operation of the pices of equipment used. Although most of this equipment was commercially procured and has excellent documentation as a system there is very little documentation about how it all operates together. This information is provided in an electronic appendix on the suplemental disk.

The guides contained in the electronic appendices should enable a user to quickly gain an operational knowledge of the equipment used in this work. A brief summary of the contents is included below:

B.1.   Operating the Laser System

Contains procedures for the routine operation of the femtosecond laser and its pump laser.

B.2.   Operating the Omicron STM

Contains procedures for the routine operation of the Scanning Tunnelling Microscope (STM), inlcuding tip and sample loading and a basic imaging procedure.

B.3.   Operating the Leica Confocal Microscope

Contains details of the controls provided by the leica micorscope control software. Particularly it describes the step-by-step process used to inflict DNA damage at specific location using the Leica bleaching capability.

B.4.   Schematics and PCB Artwork for LA-STM Controller

Contains schematics and PCB art work for the dealy stage controller deveoped in this work. There is also guidance on the construction techniques employed.

B.5.   SPPX Labview Data Acquisition Manual

Provides a manual for the application developed to capture SPPX data, using the the lock-in amplifier and computer controlled delay stage.

APPENDIX C

C. Supplemental Disk Contents

C.1. INTRODUCTION

Large volumes of data have been collected during this work. Also original software has been developed which is not suited to presentation in hard copy and is more usefully provided in electronic form. The data presented in this thesis can only represent a small fraction of the total information analysed. The raw data which was processed to from the results resented in this thesis is provided on a supplementary disk. The multi-dimensional nature of the data collected also lends itself to presentation in video or movie format. A few of the figures in this thesis have Movie counter parts that may help the use appreciate the data more.

Finally additional data which was not presented in this thesis is also provided. This was omitted due to a lack space and time required to perform an in depth analysis of the material. It is hoped that this data will be presented at a later date else where.

The supplemental disk is divided into three folders, and the root folder also contains an electronic copy of this thesis. These folders are:

- Data   -   containing the raw and unprocessed data from this thesis
- Movies   -   containing the video and movie file counterparts to selected figures in this thesis.
- Software -   Provides useful free software and software developed in the course of this work.
- Electronic Appendices – containing the electronic appendices described in Appendix B.

The remainder of this appendix will provide a brief guide to the contents of the supplemental disk.

C.2. DATA

Data was compressed to allow it all to be fit onto a single DVD. The Leica software save image in uncompressed Tiff format and the lossless compression provide by the ".zip" format provides considerable space savings. Once decompressed the Leica Files can be opened with the Leica Light software, provided in the software folder, or with the Matlab functions developed to open Leica Files provided in the Matlab folder. The data folder has been further divided into the relevant chapters.

C.2.1. CHAPTER 3 – PSF AND FRAC MEASUREMENTS

This folder has data from the Pulse duration Measurements captured from the APE MINI 2000. This data is stored in the *.DAT files. Each value is recorded on a separate line. The first 3 lines are header information, and the remainder are data points.

There are also two ".zip" files containing images captured from the microscope for the point spread function measurements and the in-situ fringe resolved autocorrelation.

- FRAC_Measurements.zip contains the Leica files for the Fringe resolved autocorrelation.
- PSF_Final.zip contains 3D images for the measurement of the Point Spread Function.

C.2.2. CHAPTER 4 – 3P DNA DAMAGE

This folder contains all the data presented in chapter 4. There are three zip files containing Leica images.

- 3D_Localisation_and_patterned_DNA_Damage.zip relates to section 4.2.
- Threshold_Intensity.zip relates to sections 4.3.2 and 4.3.3
- Cell_Signalling.zip relates to section 4.4.

C.2.3. CHAPTER 5 – Γ-H2AX FOCI

The data from the radiation dosed cells studied in Chapter 5 is provided in:

- Radiation_Series.zip.

There is also another zip file:

- FOCI_Repaire.zip.

This contains data not presented in this thesis. These include images captured from cells that were dosed with radiation and allowed various amounts of time to repair. The Data files have been annotated with the necessary details to permit further analysis.

C.2.4. CHAPTER 6 – SPPX

The folder contains the data showing the lack of signal detected in SPPX experiments. Data is stored as comma separated values.

C.3.   LA-STM

This folder contains electronic copies of all the source code and project files for the microcontroller firmware. They can be compiled using the Renesas "High Performance Development Environment" for the RC8 microcontroller, a copy of which is provided in the Software folder.

The Hardware folder contains the schematics and PCB artwork for the LA-STM electronics. There are graphics of the schematic and the scaled PCB artwork. The electronic schematics can also be opened with the Eagle CAD software provided in the software folder.

C.4.   MOVIES

Three Videos are provided as counter parts to three figures in this thesis.

Movie Filename		Figure	
PCNAJeroen.avi	Ref. [41]	Figure 2-18	Progression through the S-Phase.
		Figure 2-19	Progression through the M-Phase.
PCNA_3D_Loc.avi		Figure 4-2	3D visualisation showing localisation of PCNA following 3p induced DNA damage
ROI_Movie.avi		Figure 4-19	ROIs specified for the intra-cell signalling measurements.

Table C-1   Main Screens in the SPPX Data Acquisition Program

C.5.   SOFTWARE

Three pieces of freely distributable software are provided.

- Leica Light – Which is free viewer for files collected with the Leica microscope controller.

- Eagle CAD – Is freely distributable for evaluation and educational purposes. This was the software used to design the PCB and schematic for the LA-STM controller.

- Renesas – Contains a free compiler for the Renesas RC8 microcontroller, and all the software required to program the device. There is an excellent tutorial that to get started with the RC8 controller in the hobby electronics magazine "Elektor Electronics" Feb 2006 and March 2006. The LA-STM is built around the RC8 starter kit featured in the Feb 2006 issue.

- MATLAB – Contains all the foci counting and tracking code developed in chapters 4 and 5. The code is heavily commented and should be easily understood. Copy the contents of the MATLAB folder into your MATLAB user environment and configure paths to those folders.

C.6.   ELECTRONIC APPENDICIES

This folder contains the electronic appendices. See Appendix B for details of the electronic appendices and their contents.